FLOW IN CURVED DUCTS OF
VARYING CROSS-SECTION

AD-A254 660

||||||||||||||||||||||||||||||||||

F. Sotiropoulos and V. C. Patel

DTIC
S ELECTE
AUG 3 1 1992
A D

IIHR Report No. 358

July 1992

188300

92-24028

92 8 28 131

||||||||||||||||||||||||| 205P 6

FLOW IN CURVED DUCTS OF VARYING CROSS-SECTION

by

F. Sotiropoulos and V. C. Patel

DTIC QUALITY INSPECTED 5

Table of Contents

i

ii

ABSTRACT

Two numerical methods for solving the incompressible Navier-Stokes equations are compared with each other by applying them to calculate laminar and turbulent flows through curved ducts of regular cross-section. Detailed comparisons, between the computed solutions and experimental data, are carried out in order to validate the two methods and to identify their relative merits and disadvantages. Based on the conclusions of this comparative study a numerical method is developed for simulating viscous flows through curved ducts of varying cross-sections. The proposed method is capable of simulating the near-wall turbulence using fine computational meshes across the sublayer in conjunction with a two-layer k-ε model. Numerical solutions are obtained for: i) a straight transition duct geometry, and ii) a hydroturbine draft-tube configuration at model scale Reynolds number for various inlet swirl intensities. The report also provides a detailed literature survey that summarizes all the experimental and computational work in the area of duct flows.

ACKNOWLEDGEMENTS

LIST OF SYMBOLS

<u>Alphabetical Symbols</u>

A, B, C, R,	coefficients in the linearized transport equations for the finite analytic method
a,b,c	constants in the finite analytic solution of the one-dimensional equations
A_j	diagonal matrices containing the convective velocities (j = 1,2,3)
A_ϕ, B_ϕ, C_ϕ	coefficients in the linearized transport equations for ϕ
A_μ, A_ε	constants in the two-layer turbulence model
C_D, C_P, C_U,	finite-analytic coefficients
C_r	constant in two-layer turbulence model
C_{nb}	finite-analytic coefficients
C_p	pressure-coefficient ($= 2(P - P_o)/\rho U_o^2$)
C_μ, $C_{\varepsilon 1}$, $C_{\varepsilon 2}$	turbulence model constants
CFL	Courant-Friedrich-Lewis number
$\widehat{D}$	mass-source in the pressure equation of Method I
De	Dean's number
d_h	duct's hydraulic diameter
E^{ii}	coefficients in the pressure equation of Method I
E_{v_i}	viscous flux vector (i = 1,2,3)
f^i	grid control functions (i = 1,2,3)
G	turbulence generation term
g	determinant of the metric tensor g_{ij} and source function at the node P for the finite analytic discretization
G_P	source term at the node P for the finite-analytic discretization
g^{ij}	contravariant metric tensor
g_{ij}	covariant metric tensor

h, k, l	dimensions of a finite-analytic numerical element
J	Jacobian of the geometric transformation
k	turbulent kinetic energy
$\ell_\mu, \ell_\varepsilon$	length scales in the two-layer turbulence models
p	piezometric pressure, normalized by ρU_o^2
Q	velocity vector containing the three cartesian velocity components
r	radial coordinate
Re	Reynolds number
R_ϕ	effective Reynolds number including the eddy viscosity
S	inlet swirl intensity
S_ϕ	source functions in the transport equations, used in Method I
t	dimensionless time, normalized by L_o/U_o
U, V, W,	dimensionless mean velocity components in the streamwise, radial and normal directions (used for curved duct geometries) and cartesian velocity components in the x-, y-, and z-directions
U_b	bulk velocity
U_i	dimensionless mean Cartesian velocity component
U_o	free-stream (reference) velocity
u_τ	friction velocity $(= \sqrt{\tau_w/\rho}\,)$
$\overline{u_i u_j}$	dimensionless Reynolds stresses (i, j = 1,2,3)
V^i	contravariant velocity components (i = 1,2,3)
V(i)	physical contravariant velocity components (i = 1,2,3)
$\widehat{V}$(i)	pseudo-velocity of V(i)
X, Y, Z	curvilinear coordinates along the curved duct
x_i	cartesian coordinates (i = 1, 2, 3)
y^+	dimensionless wall distance $(= \dfrac{u_\tau y}{\nu})$

y^+	dimensionless wall distance ($= \dfrac{u_\tau y}{\nu}$)
z	normal coordinate

Greek Symbols

α_ℓ	Runge-Kutta coefficients
γ	artificial mass source parameter
Γ^i_{jk}	Cristoffel symbols of the second kind
δ	finite difference operator
$\Delta\xi^i$	grid spacings (i = 1,2,3)
$\Delta t, \Delta\tau$	time increments
ε	rate of turbulent energy dissipation, normalized by U_o^3 / L
θ	streamwise coordinate
κ	Von Karman constant ($= 0.42$)
ν	kinematic viscosity
ν_t	turbulent eddy-viscosity
ξ, η, ζ	general curvilinear coordinates
ξ^i	general curvilinear coordinates (i = 1, 2, 3)
σ_ϕ	turbulence model constants (ϕ = U, V, W, k, ε)
τ	time variable
τ_w	wall shear stress
ϕ	transport quantities and circumferential coordinate
ω_i	implicit residual smoothing coefficients (i = 1,2,3)
Ω	Von-Neumann stability number
Ω_x	streamwise mean vorticity component

I. INTRODUCTION

The study of flow through curved ducts, or conduits is of great importance because such flows are found in a variety of practical situations, ranging in scale from the flow through the human arterial and respiratory systems to that in the ducting of gas and hydraulic turbines. The flow in open channels and rivers is also related to duct flow, although, in these cases, both the bottom and the free surface may be free to move. An accurate description of the flow in ducts, even when the walls are rigid, poses a challenging fluid mechanics problem. There are several difficulties. One of these is the complexity of the geometries encountered in practice. Changes in cross-sectional shape and curvature of the duct axis are of particular concern because these lead to vortical motions, flow reversals, and unsteadiness. Another major difficulty is related to the fact that most flows of practical interest are turbulent, and available mathematical models cannot properly simulate all of the consequences of turbulence. To these may be added difficulties that are peculiar to specific applications, such as coupling between the flow and moving boundaries in biomedical applications, compressibility effects and shock waves in gas turbines, sediment transport in rivers, and aeration in autoventing hydraulic turbines. These, and other applications too numerous to list, have inspired many experimental, analytical and computational studies of the flow in curved ducts but, for a variety of reasons, it is still not possible to accurately predict such flows.

The work described in this report was motivated by a recently initiated joint research program between the Iowa Institute of Hydraulic Research (IIHR) and the Tennessee Valley Authority (TVA). This program aims to develop a numerical method specially for applications to the new generation of autoventing hydroturbines (AVT) that are being considered as possible replacements for conventional ones. The initial phase of the project is conducted in two parts: development of a numerical method for solution of the Reynolds-averaged Navier-Stokes (RANS) equations for single-phase flow in ducts of complex geometry is pursued at IIHR, and development of physical models and transport equations for two-phase flow, for air-water exchange, is carried out at TVA. The two phases will be integrated at an appropriate stage. This report describes the development of numerical methods for prediction of single-phase fluid flow in curved ducts.

The starting point for the research described here was provided by the two numerical methods that were available at IIHR at the beginning of the project, namely, one developed by Patel and his colleagues (see, for example, Chen, Patel and Ju (1990)), and the other developed by Sotiropoulos (1991). Both were developed for external, three-dimensional, laminar and turbulent flows, and have been extensively applied to such flows. Both methods were modified to incorporate the two-layer turbulence model of Chen and Patel (1988), and extended to internal flow

in ducts. As a preliminary step in the validation of these methods, consideration is first given to the flow in simply-curved ducts of simple cross-section. The choice of suitable test cases to evaluate the performance of these methods is not straightforward, however, because there exists an enormous amount of previous work on this subject and even a cursory review of this indicates that there are a number of issues, both numerical and physical, that are not yet fully resolved. Therefore, this report begins with a brief review of previous studies of curved duct flows with emphasis on experiments and those aspects that are still topics of active research. The two methods are then described, and their results are compared for a few relatively simple duct flows to highlight their capabilities and shortcomings. Next, a modified version of the method of Sotiropoulos is employed to study the flow in additional cases. Among these are the flow in a straight duct that changes its cross section from circular to rectangular, and the flow in a typical draft tube of a hydraulic turbine. These two examples bring forth the complexities that are present when the duct cross-section shape is changed and the area is increased for continuous diffusion. The results demonstrate that accurate numerical simulation of such practical flows is at hand provided some improvements are made in two areas, namely, in the turbulence model and in generation of grids appropriate for more complex geometries. Possible future directions of the project are outlined in the final section of the report.

II. OVERVIEW OF PREVIOUS WORK ON FLOW IN CURVED DUCTS

Before attempting to summarize previous work on flow in curved ducts, it is useful to define certain terms that are commonly used in connection with such flows. Definition of these terms aids in the classification of duct flows, in general, and provides a basis for comparing the various types of flows that have been studied.

The flow in a curved duct of finite cross-section is three dimensional insofar as the velocity vector has three non-zero components, each of which varies across the section. Whether the flow is laminar or turbulent, such a three-dimensional flow is often described in terms of primary and secondary velocities. Loosely speaking, primary refers to the velocity component along the axis of the duct and secondary flow refers to velocity components in transverse sections, orthogonal to the duct axis. For ducts whose cross-section shape and area change rapidly, these terms are not precise because these velocity components are not orthogonal and, therefore, depend on the coordinates that are chosen. The term secondary also suggests that motion is weak compared with the primary motion. This is again not true for ducts of arbitrary shape and curvature. However, most previous studies of curved-duct flow are confined to simple cross sections and moderate curvatures for which the concepts of primary and secondary flow are quite useful.

In a curved duct, the secondary flow arises quite simply as a result of the radial pressure gradient. The higher pressure at the outer radii drives the slower moving near-wall fluid towards the inner radii. This is compensated by an opposite but considerably weaker motion of the higher-velocity fluid in the duct core from the inner to the outer radii. Prandtl termed the resulting secondary flow as *secondary motion of the first kind* or pressure-driven secondary motion. In turbulent flow, another kind of secondary motion can be induced, even in straight ducts, by the gradients of the Reynolds stresses in the plane normal to the primary flow. Prandtl called this *secondary motion of the second kind*. This stress-driven secondary motion is absent in laminar flow, but in turbulent flow, both are present. For an overview of the theory of secondary motion in turbulent flows, reference should be made to the recent article by Bradshaw (1987).

The magnitude of the pressure-driven secondary motion depends on a number of factors, including the section shape, the Reynolds number, the Dean number, and the flow conditions at the beginning of curvature. In general, Reynolds-stress driven secondary motion is much weaker than pressure-driven secondary motion but the two are not easily separated because of the coupling between the mean flow and the Reynolds stresses. Secondary motions of both kind have a significant impact on the distribution of the wall shear, heat transfer at the wall, and related properties.

A review of previous work on curved ducts leads to the following general observations. Most studies have dealt with ducts of simple shape, such as a circular or square section, with constant cross-sectional area, turning through either 90 or 180 degrees with a constant radius. Ducts with two bends, the so-called S-shaped ducts, also fall in this category. There are very few investigations in ducts with section and area changes, or in ducts with axis curved in more than one plane. Secondly, there are many more studies of laminar flow, at necessarily low Reynolds numbers, than with turbulent flow. Transitional flows have not been investigated. Thirdly, fully-developed entry flow is more common than developing boundary-layer flow at entry. The former leads to rapidly developing and stronger secondary motions. Fourth, in spite of extensive experimental investigations, the data base is still limited, particularly with regard to the distribution of the Reynolds stresses in turbulent flow.

The better documented experiments in laminar and turbulent flows have been used to test computations using a variety of numerical methods and turbulence models. Of course, there are many computations for each experimental condition, and the results have been rather mixed. Differences among numerical methods and turbulence models will be discussed in the text as the results of the present methods are presented and compared with previous ones. For the present purposes, it is more useful to provide a summary of some of the most commonly cited experiments. This summary is not intended to be exhaustive, however. We have selected the most recent experiments, performed with advanced instrumentation to obtain the most detailed data.

3

II.1   Experiments in laminar flow

Laminar flow through curved pipes have been studied extensively during the past fifteen years, primarily because of their relevance to biomedical problems. Measurements for steady and unsteady flows have been reported by, among others, Agrawal et al. (1978), Chandran et al. (1979, 1981), Enayet et al. (1982b), Talbot and Gong (1983), Bovendeerd et al. (1987) and Rindt et al. (1991). There are several other experiments in curved ducts of different shapes but none provide data that are comparable in detail to the experiments summarized in Table 1. Together, these experiments provide a data base for the development of secondary motion in laminar flow with developed and developing flow at entry.

II.2   Reynolds-stress driven secondary motion: experiments in turbulent   flow in straight ducts

Secondary motions of the second kind were first observed by Nikuradse (1926) who made careful measurements of mean velocity in turbulent flow in a series of straight, non-circular ducts. His measurements indicated that the isovels (or isotachs, contours of constant axial velocity) were distorted near the corner region in a manner that suggested the existence of secondary motion. This situation is depicted in Figure 1, taken from Gessner and Jones (1965), where a typical isovel pattern for laminar flow is compared with the corresponding one for turbulent flow. Recall that there is no secondary motion in laminar flow. This has been shown analytically by Moissis (1957) and Maslen (1958). It is seen that in the turbulent case the isovels are displaced towards the corner and away from the mid-point of the walls. Prandtl (1926) suggested that the distortion of the isovels is the result of a secondary motion towards the corner, which is accompanied by a return flow at the mid-points of the walls for continuity to be satisfied. Moreover, he postulated that this secondary motion is generated by velocity fluctuations tangential to the isovels in regions where the curvature of the isovel changes.

Due to the small magnitude of the secondary-flow velocity components, approximately one percent of the average or bulk velocity, quantitative measurements for developing turbulent flows in square ducts were not reported until Hoagland (1960) developed a hot-wire technique. Subsequently, hot-wire measurements of increased accuracy were reported by Leutheusser (1963), Brundrett and Baines (1964), Gessner (1964), Gessner and Jones (1965), Ahmed (1971), Thomas and Easter (1972), and Launder and Ying (1972). The first attempt to provide a comprehensive explanation of the physics of stress-driven secondary flow was that of Brundrett and Baines who measured the three mean-velocity components and the six Reynolds-stress components. In their analysis, they employed the equation for the mean streamwise vorticity along with the symmetry properties the Reynolds-stress tensor, and showed that: (i) streamwise vorticity is produced in the

4

region near the corner bisector by the gradients of the Reynolds stresses, (ii) the corner bisectors separate independent secondary flow circulation zones (as seen in figure 1b), and (iii) the main contribution to streamwise vorticity production comes from the gradients of the normal Reynolds stresses. The validity of their last conclusion, however, was later challenged by Perkins (1970) and Gessner (1973). Perkins, for instance, pointed out that the experimental apparatus of Brundett and Baines could lead to ±100% error in the shear stress measurement, while Gessner (1973) claimed that the gradients of the normal Reynolds stresses do not play a major role in the streamwise vorticity production and it is rather the transverse gradients of the shear stress that drive the secondary motion in the corner region. In a more recent work, Demuren and Rodi (1984) reviewed all the above experimental findings and concluded that both the gradients of normal and shear Reynolds stresses are of the same order of magnitude and that it is their difference that drives the secondary motion.

In most of the above experimental efforts the emphasis was placed in understanding the physical mechanism that generates and sustains the secondary motion, rather than in providing a reliable data base suitable for validating turbulence models. In many of these studies, for instance, the symmetry of the flow about the corner bisector was either not checked (since measurements were carried out in only one octant), or the check was not thorough enough to guarantee reliability of the measurements. In a more recent study, Melling and Whitelaw (1976) attempted to obtain better quality measurements in the entrance region of square ducts using Laser-Doppler Velocimetry (LDV). They made measurements in a quadrant of the flow at several cross-sections and reported high levels of symmetry in the streamwise mean velocity and normal Reynolds-stress components (the maximum asymmetry was found to be about 3 percent in the near wall region and 1 percent elsewhere). The same degree of symmetry, however, was not achieved in their secondary flow velocities and transverse Reynolds-stress components, and their data indicate significant asymmetries about the wall bisector. Another set of measurements in developing turbulent flow in the entrance region of a square duct was reported by Gessner et al. (1977); see also Po (1975). They carried out detailed mean velocity (in a quadrant of the flow) and turbulence (in an octant of the flow) measurements at several cross-sections in the developing and fully-developed flow regions. Their mean velocity data exhibit high levels of symmetry, but the quality of their turbulence data can not be readily evaluated. The measurements of Gessner et al. constitute a complete and comprehensive data set which is detailed enough to assist in the development and validation of turbulence models. A detailed review of experiments and computations for straight ducts of regular cross-section can be found in Demuren and Rodi (1984). Additional experimental data for ducts with arbitrary cross-sections have been reported by Rodet (1960), Aly et al. (1978) and Seale (1982) for trapezoidal, triangular, and simulated rod-bundle-type cross-sections, respectively.

5

As already noted, the driving force for secondary motions of the second kind is the anisotropy of the Reynolds stresses and, thus, any attempt to calculate such motions should utilize a turbulence model which can predict turbulence anisotropy. It has been demonstrated computationally (see Demuren and Rodi, 1984) that the isotropic k-ε model does not predict any secondary motion of second kind and fails, consequently, to predict the important features of straight duct flows. For that reason all the computational efforts in the area of stress-driven secondary motions have focused on developing algebraic Reynolds stress (ASM), or full Reynolds stress (RSM) models. The first calculation of secondary motion of the second kind, in straight non-circular ducts, was reported by Launder and Ying (1973). They employed an ASM model (LY model, say) based on a simplification of the model of Hanjalic and Launder (HL) (1972). The LY model, or some variant of it, was subsequently used by Gessner and Emery (1981), Trupp and Aly (1979), Rapley and Gosman (1986), and Nakayama et al. (1983) to calculate flows through straight ducts of regular and irregular cross-sections. All the above calculations yielded fairly good results for the magnitude of the secondary flow but failed to yield accurate predictions for the Reynolds stress distributions. Naot and Rodi (NR) (1982) were able to obtain better overall predictions, for both the crossflow and the Reynolds stress distributions, by utilizing an ASM model which they developed from the Reynolds stress model of Launder, Reece and Rodi (LRR) (1975). A more refined version of the NR model was proposed by Demuren and Rodi (DR) (1984, 1987) and used to calculate the flow in ducts with simple cross-sections. Recently, Demuren (1991) has extended both the NR and DR models to generalized curvilinear coordinates and applied them to calculate flows in straight ducts of arbitrary cross-sections. Most of his computations demonstrate correct trends but are, at best, in qualitative agreement with the experimental data. It should be pointed out that all of the above described computational methods utilize the wall-function approach which, as indicated by the limited success of even the most advanced methods, is inadequate for complex shear flows (Demuren, 1991).

II.3 Experiments in turbulent flow in curved ducts of regular cross-sectional shape

Turbulent flow measurements in curved ducts of square or rectangular cross-section have been reported by Joy (1950), Eichenberger (1952, 1953), Squire (1954), Bruun (1979), Humphrey et al. (1981), Taylor et al. (1982), Enayet et al. (1982a), Chang (1983), Iacovides et al. (1990) and Kim (1991). The early works of Joy, Eichenberger and Squire provided evidence of the oscillatory nature of the secondary flow in 180° square bends. The turbulent flow measurements of Joy, for instance, indicate that the secondary flow was reversed at a bend angle of 135°. Bruun (1979) studied the effect of inlet boundary-layer thickness on the development of the secondary flow and on the pressure losses in a 120° square bend. He presented data for the

mean total pressure, static pressure and velocity field as well as some limited turbulence intensity data.

Table 2 summarizes the most detailed experiments in turbulent flow in curved ducts. A significant contribution in the understanding of the physics of curved-duct flow came from Humphrey et al. (1981) who presented detailed measurements inside a highly curved 90° square bend. They employed LDV to measure the mean-velocity components and components of the Reynolds-stress tensor at several cross sections inside the bend. Their data indicates that the Reynolds-stress driven secondary motion, measured in the inlet tangent of the bend, was quickly taken over by the pressure-driven motion, in which the secondary velocities attain values up to 28 percent of the mean bulk velocity, during the first half of the bend. This latter secondary motion was found to be responsible for strong cross-stream convection of the Reynolds stresses inside the bend which, in conjunction with the curvature effects, resulted in a high level of anisotropy of the turbulence. Furthermore, the production of turbulent kinetic energy predominated near the outer wall (destabilization due to concave curvature) but regions of negative production were observed near the inner wall (stabilization by convex curvature). To study the effect of the inlet boundary-layer thickness on the flow structure, Taylor et al. (1982) carried out measurements in exactly the same bend but with developing flow, compared to the nearly fully-developed flow in the experiments of Humphrey et al., at the inlet to the bend. They concluded that the thinner inlet boundary layer results in weaker crossflow and lower overall turbulence intensities.

The effect of bend curvature on the crossflow and the turbulence structure was studied by Enayet et al. (1982a) who carried out measurements inside a 90° bend of milder curvature with a partially developed flow (relatively thick boundary layer) at inlet. Their data shows that, due to the milder curvature the streamwise pressure gradient is small and less important. Also, unlike observations in strongly curved ducts, there appears to be no evidence of significant damping or amplification of turbulence due to longitudinal curvature. Taylor et al. compared their measurements with the data of Enayet et al. and concluded that the milder curvature results in much weaker crossflow velocities which are confined to a smaller region near the wall. However, due to the small streamwise pressure gradient, in the case of mild curvature, the effect of the crossflow in the streamwise flow development was found to be dominant.

The flow through a strongly curved 180° square bend was studied by Chang (1983). His detailed measurements (wall pressures, mean velocity components and Reynolds stresses) revealed rather complicated flow patterns, with the secondary motion dominating the dynamics of the flow development. Between 0° and 45°, for instance, destabilizing and stabilizing curvature effects in conjunction with the strong secondary motion--primarily pressure driven except in the inlet straight tangent, where Reynolds stress driven secondary currents are present--cause large levels of turbulence anisotropy. As a result, a region of negative production of turbulent kinetic energy

exists near the inner wall, indicating flow of energy from the large eddies back to the mean flow (recall that a similar trend was observed by Humphrey et al. (1981) in their 90° bend experiment). The anisotropy of the turbulence field is reduced, however, for bend angles greater than 130°, due to the mixing effect of the crossflow. Apart from influencing the dynamics of turbulence, the secondary motion has a significant impact on the mean flow development as well. For bend angles less than 90° the strong secondary currents convect low momentum fluid from the side walls to the core of the cross-section, resulting in S-shaped axial and radial mean velocity profiles. The same phenomenon was observed by Humphrey et al. (1977) in their laminar flow measurements, but it was not present in the turbulent flow measurements of Humphrey et al. (1981) despite the fact that the same bend was used in both experiments. For angles greater than 90°, however, the crossflow starts decreasing and high speed fluid is restored back in the core of the flow. In a more recent study, Iacovides et al. (1990) carried out turbulent flow measurements through a 180° square bend whose geometry was similar to that used by Chang (1983) except that the inlet section was shortened to six hydraulic diameters (as compared to some thirty diameters in the experiment of Chang)--the short inlet tangent resulted to a developing flow at the beginning of the bend with the thickness of the boundary layer being approximately 15 percent of the hydraulic diameter. Their data indicates that, despite the thinner boundary layer, the S-like structure of the streamwise velocity profiles were as notable in their measurements as in those of Chang. They also reported the generation of a very strong secondary motion, which, by 135° around the bend, appeared to have broken down into a chaotic pattern.

Data from most of the above described experiments have been used, over the last ten years, as test cases for validating numerical methods and turbulence models. Humphrey et al. (1981) presented calculations for their experimental configuration using the standard k-ε model in conjunction with the wall-functions approach. The same configuration was one of the test cases selected for the 1980-81 Stanford Conference on Complex Turbulent Flows (Kline et al., 1981) and was computed by several participants. In most cases good agreement between computed and measured mean-velocity components was obtained for the first half of the bend but significant deviations were present farther downstream. The configuration of Taylor et al. (1982) has been computed by Buggeln et al. (1980) (one-equation turbulence model), Govindan et al. (1991) (algebraic turbulence model) and Kunz and Lakshminarayana (1991) (k-ε model with wall-functions). All the numerical predictions for this case are in better overall agreement with the measurements than the corresponding results for the configuration of Humphrey et al., despite the fact that the same bend was used for both cases. This is mainly due to the thinner boundary layer present at the inlet of the bend in the study of Taylor et al. which resulted in weaker secondary motion than measured by Humphrey et al. The 180° bend configuration of Chang has been studied computationally by Chang (1983), Johnson (1984), Birch (1984) and, more recently, by

Choi et al. (1990). Chang, Johnson, and Birch used in their calculations the standard two-equation k-ε turbulence model in conjunction with wall functions; Chang also carried out calculations using an algebraic Reynolds stress model but he was unable to obtain a converged solution. All three computations failed to reproduce significant features of the flow field, such as the S-shaped profiles of the mean axial velocity component caused by the strong secondary motion. In the more recent study, Choi et al. showed that the inability of the computations to reproduce correctly the strength of the secondary flow and its interaction with the axial flow can be attributed primarily to the inadequacy of the wall-function approach for complex, three-dimensional, non-equilibrium shear flows. They carried out calculations all the way to the wall by replacing the wall functions with a fine mesh across the sublayer and tested both the k-ε model and an algebraic Reynolds-stress (ASM) model. For both models, the near-wall region was modeled by the van Driest mixing-length formula. Their k-ε calculations showed significant improvements, as compared to previous computations (Chang, Johnson, Birch), in the agreement between measurements and computations. Better agreement for the axial velocity profiles and the distribution of the Reynolds stresses was obtained, however, when the algebraic Reynolds-stress model was employed. Despite marked improvements in their results, significant discrepancies between experiment and calculations still remained. However, the success of their modelling refinement sequence indicates that, for future improvements in the modelling of such flows, research efforts should focus in the development of turbulence models which account for non-isotropic effects and at the same time provide accurate resolution of the near-wall layer.

The most recent experiment listed in Table 2 is that of Kim (1991), who made measurement of pressure, mean velocity, and Reynolds stresses in developing boundary-layer flow in a rectangular duct, of aspect ratio six, turning through an angle of 90°. There are, to be sure, several previous measurements in rectangular ducts of different aspect ratio but, to the authors' knowledge, most of these were concerned with secondary motion (of the second kind) in fully-developed flow in straight ducts. In particular, none has considered developing flow in a curved duct. Kim's measurements are particularly noteworthy because they document the development of the pressure-driven secondary motion in boundary layers, and the formation of longitudinal vortices within the boundary layers as a result of this secondary motion. His data also reveal the action of the concave and convex surface curvatures on the boundary layer velocity and turbulence profiles. Kim made extensive comparisons between measurements and calculations. The calculations were performed with one of the numerical methods used in the present work. As the method will be described in this report, discussion of Kim's results is postponed until a later section.

Measurements in turbulent flow in curved circular ducts appear to be relatively sparse in spite of the varied practical applications. The first detailed measurements were reported by Rowe

(1970) who used Pitot probes to measure the total pressure, mean velocity, and yaw angles in several cross-sections of a 180° pipe bend of mild curvature. His data indicate that the crossflow reaches a maximum at a bend angle of 30° and then decreases to a near constant value. Rowe explained this phenomenon by examining the gradients of the total pressure and using inviscid theories to predict the evolution of the secondary motion. In a later work, Enayet et al. (1982b) used LDV to measure the streamwise components of the mean and fluctuating velocity in a 90° strongly curved pipe bend. A very detailed set of data for turbulent pipe-bend flow was reported by Azzola and Humphrey (1984) who measured both the streamwise and circumferential components of the mean and fluctuating velocity in a 180° bend. The major features of this flow are the reversals that the secondary motion undergoes for bend angles larger than 90°, a phenomenon which was found to be essentially independent of the Reynolds number, and the large levels of turbulence anisotropy arising everywhere in the bend and in the downstream tangent. Comparison of this pipe-bend flow with the corresponding square-duct flow (Chang, 1983) reveals that the magnitudes of the secondary motion are in general lower for the pipe bend. Moreover, there are no crossflow reversals in the square bend case which demonstrates that, despite superficial similarities, the two flows may be quite different. The most recent set of measurements was reported by Anwer et al. (1989) who carried out mean flow and turbulence measurements through a 180° pipe bend and in the downstream tangent. Their measurements include the three components of the mean velocity and the six Reynolds stress components.

The first turbulent flow calculation of a curved pipe flow was reported by Patankar et al. (1975), who presented solutions for the mildly curved bend measured by Rowe. Their solutions, obtained with the standard k-ε model with wall functions, were quite successful in reproducing the general features of the flow observed in the measurements. However, the shapes of the computed contours of constant velocity head, which are not as distorted as the corresponding measured ones, indicate that the calculations did not predict accurately the development and decay of the secondary motion. It should be pointed out, however, that the data of Rowe do not include quantitative measurements of the secondary motion and thus no direct comparisons could be made. In a more recent study, Iacovides and Launder (1984) calculated the 90° pipe bend of Enayet et al. (1982b). They employed a two-layer, k-ε model with van Driest's eddy-viscosity formula for the near-wall layer. The agreement of their calculations with the experimental data was broadly satisfactory for the streamwise velocity profiles, but the boundary layer on the inside of the bend did not proceed as far toward separation as indicated by the measurements. Moreover, the calculated rate of recovery of the flow in the downstream tangent was slower than measured. The 180° pipe bend of Azzola and Humphrey (1984) was computed by Azzola et al. (1986), using the same method as in Iacovides and Launder (1984). Their calculations for the development of the streamwise mean velocity component through the bend, along the radius at 90° from the symmetry plane, were in

10

good agreement with the measurements. However, significant discrepancies between experiment and calculations were present in the corresponding profiles of the circumferential mean velocity component between bend angles of 45° and 180°, as well as in the rate of recovery of the flow in the downstream tangent. In a very recent study, Lai (1990) computed the 180° pipe bend of Anwer et al. (1989) using a full Reynolds-stress transport model including the direct modelling of the near wall flow. His calculations emphasized the secondary flow patterns in curved-pipe flows. Based on analytical arguments with the vorticity transport equation, as well as on his numerical calculations, he showed that a turbulence-driven secondary motion is present near the outer bend of the curved pipe.

II.4   Experiments in turbulent flow in transition ducts

The term transition duct denotes an internal flow configuration whose cross-sectional shape changes in the streamwise direction, for example, from circular to rectangular (CR), or vice versa. Transition ducts can be either straight or curved and are encountered in aircraft propulsive systems (as inlet and exhaust nozzles of jet engines), wind tunnels (wind tunnel contractions and diffusers), and hydraulic turbine systems (draft tubes). Turbulent flow measurements through transition ducts have been reported by Mayer (1939), Taylor et al. (1981), Burley and Carlson (1985), Patrick and Mc Cormick (1987, 1988) and, more recently, by Miau et al. (1990), and Davis and Gessner (1992). All these experiments, which have focused exclusively on straight transition ducts, are summarized in Table 3.

The first turbulent flow measurements in a transition duct were reported by Mayer (1939) who measured the flow through two rectangular-to-circular (and vice versa) transition ducts of constant cross-sectional area. His measurements included streamwise static pressure variations along the duct walls, total pressure contours and mean velocity components. The next set of measurements was reported four decades later by Taylor et al. (1981) who carried out mean velocity measurements through a square-to-circular transition duct whose cross-sectional area reduced by 21.5% over the transition length. These two experimental studies demonstrated the impact of the transition length on the streamwise flow development and showed that a moderate secondary motion (not exceeding 10% of the bulk velocity) can induce significant distortion of the streamwise flow. In a more recent study, Burley and Carlson (1985) carried out pressure loss tests for transonic flow through five different CR transition ducts in order to study the effect of transition length, cross-sectional shape and inlet swirl on the duct's performance. Their measurements indicated that short transition lengths (less than 0.75 hydraulic diameters) can induce large regions of separated flow. They also found that the inlet swirl can enhance the performance of low pressure ratio transition ducts.

The first turbulence measurements for transition duct configurations were reported by Patrick and McCormick (1987, 1988). They carried out measurements for two CR transition ducts: i) the first with an aspect ratio of three and transition length equal to one diameter, and ii) the second with an aspect ratio of six and transition length equal to three diameters. The cross-sectional area ratio remained constant for the first duct but it increased to 1.1 at the midpoint and then decreased back to 1.0 for the second duct. Their measurements include mean velocity components and normal Reynolds stresses at the inlet and exit planes. More recently Miau et al. (1990) carried out turbulent flow measurements through three CR transition ducts of constant cross-sectional area. They reported measurements of mean velocity components, static pressure distributions and normal Reynolds stress distributions. Miau et al. used their data to evaluate the different terms in the transport equation for the mean streamwise vorticity component and showed that the generation of the secondary motion is due to the transverse pressure gradients induced by the rapid geometrical changes. Perhaps the most complete set of measurements for a transition duct configuration is the very recent work of Davis and Gessner (1992) who measured the flow through a CR transition duct (overall length-to-diameter ratio of 4.5, aspect ratio of 3.0 at the exit plane, cross-sectional area ratio increasing to 1.15 at midpoint and then decreasing back to 1.0 at exit). They made very detailed mean flow and turbulence measurements (including all the six components of the Reynolds stress tensor) at several cross-sections within the transition region as well as at the exit plane of the duct. Their results show that the curvature of the duct walls induces a relatively strong pressure-driven secondary motion which significantly distorts both the streamwise mean-velocity and Reynolds-stress fields. In addition, careful analysis of their near-wall data indicated that the extent of the law-of-the-wall behavior is diminished in regions where streamwise wall curvature effects influence the flow development.

Finally, we note that data on turbulent flow in curved transition ducts, with significant area changes, such as a hydroturbine draft tubes, are quite sparse, and certainly neither well documented nor detailed enough to serve the purpose of evaluating numerical methods. Nevertheless, we shall refer to the available data in a later section.

III. SCOPE OF THE PRESENT WORK

The foregoing review of previous research on flow in curved ducts clearly indicates that the related literature is vast and still growing. The subject continues to be of great current interest because there are a number of issues that remain to be settled. In the case of laminar flow, the central concern is that of developing numerical methods for the solution of the Navier-Stokes equations that can accurately capture the various phenomena that are observed in the experiments. There exist significant differences among calculations made by different numerical methods with

identical geometries as well as initial and boundary conditions. Such differences are also observed in turbulent flow. In this case, however, experiments reveal a much more complex response of the flow to curvature, and the numerical problem is compounded by the differences in turbulence models that are used for closure of the Reynolds-averaged Navier-Stokes equations. The initial and boundary conditions employed for the additional turbulence-model equations, and the manner in which these equations are solved, influence the results. In both laminar and turbulent flows, there are a number of other problems, such as grid topology and grid generation, that must be resolved when existing methods are extended and applied to complex duct geometries of practical interest. Thus, current research is driven by the need for accurate numerical methods, on the one hand, and improved turbulence models, on the other. These two aspects become even more critical when numerical methods are used for the prediction of the flow in curved ducts of arbitrary and changing cross section.

The present work represents the first phase of a broad research effort that aims to develop numerical methods suitable for predicting the flow through the passages of hydraulic turbomachinery. Passages such as turbine scrolls and draft tubes are strongly curved ducts of arbitrary and changing cross-section. In view of the inadequacy of state-of-the-art numerical methods and turbulence models to predict flows through simply-curved ducts of square and circular cross section, it is not surprising that the flow in ducts with the geometric complexity of a typical hydroturbine lies beyond present capabilities. Our initial objective herein is to assess the performance of the numerical methods and turbulence models currently available at the Institute in the context of curved duct flows and identify the focal areas of our subsequent research efforts.

We first present the Reynolds averaged Navier-Stokes equations, along with the turbulence closure equations, in Cartesian coordinates. Subsequently, we describe and examine in parallel two numerical methods, namely, the one developed by Patel and his co-workers (see Kim, 1991), which will be referred to as Method I, and the other developed by Sotiropoulos (1991), referred to as Method II. We then proceed to carry out a series of laminar and turbulent flow calculations in ducts of regular (square, rectangular, and circular) cross-section and to compare the results with experimental data. The laminar calculations offer a very good indication of the spatial resolution of the numerical methods while the turbulent calculations allow the evaluation of the turbulence model of Chen and Patel (1988) which is incorporated in both methods. Finally, we report results of calculations made for the straight transition duct of Davis and Gessner (1992), and a draft tube configuration derived from the one at the Norris Dam in Tennessee. These are perhaps the first such results to be obtained with a fine grid, resolving the flow all the way to the wall. In the case of the draft tube, qualitative comparisons are made between the present results and those of some recent calculations for similar draft tubes made by Vu and Shyy (1990) and Agouzoul et al. (1990), who have employed rather coarse grids. The present solutions reveal a wealth of detail that is

difficult to capture with coarse-grid calculations, and offer the opportunity to speculate on advances that must be made to develop a predictive capability for turbulent flow in hydroturbine ducts and similar geometries encountered in numerous other applications.

IV. GOVERNING EQUATIONS IN CARTESIAN COORDINATES

The Reynolds-averaged Navier-Stokes equations for an incompressible fluid, non-dimensionalized by the fluid density ρ, reference velocity U_0, and reference length L_0, in Cartesian coordinates x_i ($= x_1, x_2, x_3$) are

$$\frac{\partial V_i}{\partial t} + V_j \frac{\partial V_i}{\partial x_j} = -\frac{\partial p}{\partial x_i} + \frac{1}{Re} \frac{\partial^2 V_i}{\partial x_j \partial x_j} + \frac{\partial}{\partial x_j} (\overline{v_i v_j}) \tag{1}$$

and the conservation of mass (continuity) condition is

$$\frac{\partial V_i}{\partial x_i} = 0 \tag{2}$$

Here, V_i is the mean velocity component in x_i direction, v_i denotes the corresponding fluctuating component, an overbar denotes an ensemble average, and Re is the Reynolds number ($Re = U_0 L_0 / v$), where v is molecular viscosity. The Reynolds stresses are related to the mean flow through the eddy viscosity v_t by

$$-\overline{v_i v_j} = v_t \left[\frac{\partial V_i}{\partial x_j} + \frac{\partial V_j}{\partial x_i} \right] - \frac{2}{3} k \, \delta_{ij} \tag{3}$$

where the Kronecker delta function is given by

$$\delta_{ij} = \begin{array}{ll} 1, & i = j \\ 0, & i \neq j \end{array}$$

The eddy viscosity v_t is related to the turbulent kinetic energy k and its rate of dissipation ε by the Prandtl-Kolmogoroff formula

$$v_t = C_\mu \frac{k^2}{\varepsilon} \tag{4}$$

and k and ε are determined by the modelled transport equations

$$\frac{\partial k}{\partial t} + V_j \frac{\partial k}{\partial x_j} = \frac{\partial}{\partial x_j}\left[\left(\frac{1}{Re} + \frac{v_t}{\sigma_k}\right)\frac{\partial k}{\partial x_j}\right] + G - \varepsilon \tag{5}$$

$$\frac{\partial \varepsilon}{\partial t} + V_j \frac{\partial \varepsilon}{\partial x_j} = \frac{\partial}{\partial x_j}\left[\left(\frac{1}{Re} + \frac{v_t}{\sigma_\varepsilon}\right)\frac{\partial \varepsilon}{\partial x_j}\right] + C_{\varepsilon 1}\frac{\varepsilon}{k}G - C_{\varepsilon 2}\frac{\varepsilon^2}{k} \tag{6}$$

where the generation of turbulent kinetic energy, G, is

$$G = -\overline{v_i v_j}\frac{\partial V_i}{\partial x_j} = v_t\left[\frac{\partial V_i}{\partial x_j} + \frac{\partial V_j}{\partial x_i}\right]\frac{\partial V_i}{\partial x_j} \tag{7}$$

The constants used in this "standard" k-ε model are $C_\mu = 0.09$, $C_{\varepsilon 1} = 1.44$, $C_{\varepsilon 2} = 1.92$, $\sigma_k = 1.0$ and $\sigma_\varepsilon = 1.3$.

In the two-layer turbulence model of Chen and Patel (1988), which is employed in both methods here, the flow domain is divided into two regions -- the inner layer and the outer layer. The inner layer includes the sublayer, the buffer layer and a part of the fully-turbulent or logarithmic layer. The simple one-equation model of Wolfshtein (1969) is modified and employed to account for the wall-proximity effects, whereas the standard, two-equation k-ε model is used in outer layer.

The one-equation near-wall model requires the solution of only the turbulent kinetic energy equation (5) in inner layer. The rate of energy dissipation in this region is specified by

$$\varepsilon = \frac{k^{3/2}}{\ell} \tag{8}$$

and the eddy viscosity is obtained from

$$v_t = C_\mu \sqrt{k}\, \ell_\mu \tag{9}$$

where the length scales ℓ_ε and ℓ_μ contain the damping effects in the near-wall region in terms of the turbulence Reynolds number R_y $(= \frac{\sqrt{k}\, y}{v})$:

$$\ell_\mu = C_\ell\, y\left[1 - \exp\left(-\frac{R_y}{A_\mu}\right)\right] \tag{10}$$

$$\ell_\varepsilon = C_\ell\, y\left[1 - \exp\left(-\frac{R_y}{A_\varepsilon}\right)\right] \tag{11}$$

15

Note that both ℓ_μ and ℓ_ε become linear, and approach $C_\ell\, y$ with increasing distance from the wall. The constant C_ℓ is given by

$$C_\ell = \kappa\, C_\mu^{-3/4} \tag{12}$$

κ (=0.418) being the von Karman constant, to ensure a smooth eddy-viscosity distribution at the junction of the inner and outer layer. In addition, $A_\varepsilon = 2C_\ell$ is assigned so as to recover the proper asymptotic behavior

$$\varepsilon = \frac{2\nu}{y^2}\, k \tag{13}$$

in the sublayer. The third parameter $A_\mu = 70$ was obtained from numerical tests to recover the additive constant $B = 5.45$ in the logarithmic law in the case of a flat-plate boundary layer. In the outer layer, beyond the near-wall layer, the standard k-ε model is employed to calculate the velocity field as well as the eddy viscosity.

V. DESCRIPTION OF METHOD I

The numerical method developed by Patel and his co-workers (see, for instance Kim, 1991), which for convenience will be referred to as Method I, is described first. Method I utilizes the *full transformation* approach, which transforms both dependent (velocity and Reynolds stress components) and independent (spatial coordinates) variables to generalized curvilinear components. In the following sections, the governing equations in generalized curvilinear coordinates, expressed in terms of the physical contravariant velocity components, are presented and the overall solution procedure is described.

V.1 Governing equations in general curvilinear coordinates

The transformation of the equations from Cartesian coordinates, x^i, to the general nonorthogonal coordinates, ξ^i, is facilitated by the use of the metric tensor in the ξ^i coordinates

$$g_{ij} = \delta_{rs}\, \frac{\partial x^r}{\partial \xi^i}\, \frac{\partial x^s}{\partial \xi^j} \tag{14}$$

and its inverse matrix g^{ij} given by

$$g^{ij} = \frac{1}{g}\left(g_{km}g_{ln} - g_{kn}g_{lm}\right)$$

(15)

where the indices, grouped as (i,k,l) and (j,m,n), follow a cyclic order. The Jacobian of the transformation is the square root of the determinant of the g_{ij} matrix, $J^2 = |g_{ij}| = g$, and the Christoffel symbols of the second kind are related to the metric coefficients by

$$\Gamma^i_{mn} = \frac{1}{2} g^{ij}\left(\frac{\partial g_{jm}}{\partial \xi^n} + \frac{\partial g_{nj}}{\partial \xi^m} - \frac{\partial g_{mn}}{\partial \xi^j}\right)$$

(16)

To carry out the transformations, the partial derivatives are first changed into covariant derivatives. Next, the vector components of velocity are replaced by the contravariant components, and the indices of covariant terms, like the gradient of a scalar, are raised by multiplying by the geometric coefficient g^{ij}. The resulting equations, in general curvilinear coordinates, are:

continuity equation

$$V^m_{,m} = 0$$

(17)

momentum equation

$$\frac{\partial V^i}{\partial t} + \left(V^m - g^{mn} v_{t,n}\right)V^i_{,m} - v_{t,n}g^{im}V^n_{,m}$$

$$= -g^{im}\left(\frac{p}{\rho} + \frac{2k}{3}\right)_{,m} + \left(\frac{1}{Re} + v_t\right) g^{mn}\left(V^i_{,m}\right)_{,n}$$

(18)

where use is made of the eddy-viscosity relation

$$\overline{v^i v^m} = v_t\left(g^{ir}V^m_{,r} + g^{ms}V^i_{,s}\right) - \frac{2k}{3} g^{im}$$

(19)

k-ε model equations

$$\frac{\partial k}{\partial t} + \left(V^m - \frac{1}{\sigma_k} g^{mn}v_{t,n}\right) k_{,m} = \left(\frac{1}{Re} + \frac{v_t}{\sigma_k}\right) g^{mn}\left(k_{,n}\right)_{,m} + G - \varepsilon$$

(20)

$$\frac{\partial \varepsilon}{\partial t} + \left(V^m - \frac{1}{\sigma_\varepsilon} g^{mn}v_{t,n}\right) \varepsilon_{,m} = \left(\frac{1}{Re} + \frac{v_t}{\sigma_\varepsilon}\right) g^{mn}\left(\varepsilon_{,n}\right)_{,m} + C_{\varepsilon 1}\frac{\varepsilon}{k} G - C_{\varepsilon 2}\frac{\varepsilon^2}{k}$$

(21)

17

in which

$$G = - g_{ij} \overline{v^i v^m} \, V^j_{,m} = v_t \left(V^m_{,i} V^i_{,m} + g_{ij} g^{mn} V^i_{,m} V^j_{,n} \right)$$

(22)

In the above, the covariant derivative of a scalar is defined by

$$k_{,m} = \frac{\partial k}{\partial \xi^m}$$

(23)

the covariant derivative of a contravariant component of a vector is given by

$$V^i_{,m} = \frac{\partial V^i}{\partial \xi^m} + \Gamma^i_{mk} V^k$$

(24)

and the covariant derivative of a covariant component of a vector is given by

$$(k_{,m})_{,n} = \frac{\partial (k_{,m})}{\partial \xi^n} - \Gamma^s_{mn}(k_{,s}) = \frac{\partial}{\partial \xi^n} \left(\frac{\partial k}{\partial \xi^m} \right) - \Gamma^s_{mn} \frac{\partial k}{\partial \xi^s}$$

(25)

The covariant derivative of a mixed second-order tensor is given by

$$\left(V^i_{,m} \right)_{,n} = \frac{\partial \left(V^i_{,m} \right)}{\partial \xi^n} + \Gamma^i_{ns} \left(V^s_{,m} \right) - \Gamma^s_{mn} \left(V^k_{,s} \right)$$

(26)

which results in

$$g^{mn} \left(V^i_{,m} \right)_{,n} = \nabla^2 V^i + 2 C^{im}_s \frac{\partial V^s}{\partial \xi^m} + V^s \left[\frac{\partial C^{im}_s}{\partial \xi^m} + C^{im}_s \Gamma^n_{mn} + C^{im}_n \Gamma^n_{ms} \right]$$

(27)

where $C^{im}_s = g^{mn} \Gamma^i_{ns}$, and ∇^2 is the Laplacian of a scalar, defined by

$$\nabla^2 = g^{mn} \frac{\partial^2}{\partial \xi^m \xi^n} + f^m \frac{\partial}{\partial \xi^m}$$

(28)

and

$$f^m = - g^{rs} \Gamma^m_{rs} = \frac{1}{J} \frac{\partial}{\partial \xi^r} (J g^{rm})$$

(29)

The contravariant components of velocity vectors do not, in general, have measurable dimensions. Therefore, following Trusdell (1953), the so-called physical components of the contravariant components, defined by

$$V(i) = \sqrt{g_{ii}}\, V^i \qquad (30)$$

are introduced. Then, the final equations, which are solved, are obtained by substituting (30) into equations (17) through (21). Thus, we have the

continuity equation

$$\frac{1}{J} \frac{\partial\left[J g_{ii}^{-1/2} V(i) \right]}{\partial \xi^i} = 0 \qquad (31)$$

momentum equation

$$\frac{\partial V(i)}{\partial t} + g_{mm}^{-1/2}\left[V(m)\frac{\partial V(i)}{\partial \xi^m} + D_m(i)V(m)V(i) + g_{ii}^{1/2}g_{nn}^{1/2}\Gamma_{mn}^i V(m)V(n) \right]$$

$$- \frac{\partial v_t}{\partial \xi^n}\left[g_{mn}\frac{\partial V(i)}{\partial \xi^m} + g_{nn}^{-1/2}g_{ii}^{1/2}g^{im}\frac{\partial V(n)}{\partial \xi^m} + E^m(i)V(i) + g_{nn}^{-1/2}g_{ii}^{1/2}E^i(n)V(n) \right.$$

$$+ g_{ii}^{1/2}g_{ss}^{-1/2}\{C_s^{in} + C_s^{ni}\}V(s)] = - g_{ii}^{1/2}g_{im}\frac{\partial}{\partial \xi^n}\left[\frac{p}{\rho} + \frac{2k}{3} \right]$$

$$+ \left(\frac{1}{Re} + v_t\right)\left[\nabla^2 V(i) + 2 E^m(i)\frac{\partial V(i)}{\partial \xi^m} + P(i)V(i) + g_{ii}^{1/2}g_{nn}^{-1/2}\left\{ 2\, C_n^{im}\frac{\partial V(n)}{\partial \xi^m} + Q_n^i V(n)\right\}\right]$$

(no sum on i)   (32)

κ-ε mode quations

$$\frac{\partial k}{\partial t} + g_{mm}^{-1/2}\left[V(m) - \frac{1}{\sigma_k} g^{mn}\frac{\partial v_t}{\partial \xi^m}\right]\frac{\partial k}{\partial \xi^m} = \left(\frac{1}{Re} + \frac{v_t}{\sigma_k}\right)\nabla^2 k + G - \varepsilon \qquad (33)$$

$$\frac{\partial \varepsilon}{\partial t} + g_{mm}^{-1/2}\left[V(m) - \frac{1}{\sigma_\varepsilon} g^{mn}\frac{\partial v_t}{\partial \xi^m}\right]\frac{\partial \varepsilon}{\partial \xi^m} = \left(\frac{1}{Re} + \frac{v_t}{\sigma_\varepsilon}\right)\nabla^2 \varepsilon + C_{\varepsilon 1}\frac{\varepsilon}{k} G - C_{\varepsilon 2}\frac{\varepsilon^2}{k} \qquad (34)$$

where

$$G = - g_{ij}\overline{v^i v^m}\, V^j{}_{,m} = v_t\left(V^m{}_{,i}V^i{}_{,m} + g_{ij}g^{mn}\, V^i{}_{,m}V^j{}_{,n}\right)$$

19

with

$$V^i_{,m} = g_{ii}^{-1/2} \frac{\partial V(i)}{\partial \xi^m} + g_{ii}^{-1/2} D_m(i)V(i) + g_{ss}^{-1/2} \Gamma^i_{ms}V(s)$$

(35)

and other geometry-related terms are

$$D_m(i) = -\frac{1}{2g_{ii}} \frac{\partial g_{ii}}{\partial \xi^m}$$

$$E^m(i) = g^{mn} D_n(i)$$

$$C^{in}_s = g^{mn} \Gamma^i_{ms}$$

$$P(i) = \frac{\partial[E^m(i)]}{\partial \xi^m} + [D_m(i) + \Gamma^n_{nm}] E^m(i)$$

$$Q^i_n = \frac{\partial C^{im}_n}{\partial \xi^m} + [2D_m(i) + \Gamma^s_{sm}] C^{im}_n + \Gamma^s_{mn}C^{im}_s$$

V.2 Discretization of the transport equations

The three-dimensional form of the transport equations of momentum and turbulence properties are discretized using the finite-analytic method developed by Chen and Chen (1984) and modified by Patel, Chen and Ju (1988). The dimensionless forms of the momentum and k-ε equations are arranged into the form of a general convection-diffusion equation as follows:

$$g^{11}\phi_{\xi\xi} + g^{22}\phi_{\eta\eta} + g^{33}\phi_{\zeta\zeta} = 2C_\phi\phi_\xi + 2B_\phi\phi_\eta + 2A_\phi\phi_\zeta + R_\phi\phi_t + S_\phi$$

(36)

where the subscript indicates a partial derivative with respective to time or one of the general coordinates $(\xi^1,\xi^2,\xi^3) \equiv (\xi,\eta,\zeta)$. The variable ϕ represents one of the following quantities: [V(1), V(2), V(3), k, ε].

When ϕ represents one of the velocity components, $[V(1),V(2),V(3)] \equiv (U,V,W)$, say, the coefficients and source terms derived from the momentum equations are

$$2C_\phi = R_\phi \left[g_1^{-1/2}V(1) - g^{1n}\frac{\partial v_t}{\partial \xi^n} - g^{i1}\frac{\partial v_t}{\partial \xi^i} \right] - [f^1 + 2E^1(i) + 2C^{i1}_i]$$

(37)

20

$$2B_\phi = R_\phi \left[g_{22}^{-1/2} V(2) - g^{2n} \frac{\partial v_t}{\partial \xi^n} - g^{i2} \frac{\partial v_t}{\partial \xi^i} \right] - \left[f^2 + 2E^2(i) + 2C_i^{i2} \right] \tag{38}$$

$$2A_\phi = R_\phi \left[g_{33}^{-1/2} V(3) - g^{3n} \frac{\partial v_t}{\partial \xi^n} - g^{i3} \frac{\partial v_t}{\partial \xi^i} \right] - \left[f^3 + 2E^3(i) + 2C_i^{i3} \right] \tag{39}$$

$$R_\phi = R_{V^1} = R_{V^2} = R_{V^3} = \frac{1}{\dfrac{1}{Re} + v_t} \tag{40}$$

$$S_\phi = - NO[V(i)] + R_\phi \, g_{ii}^{1/2} \left[g^{im} \frac{\partial}{\partial \xi^m} \left(p + \frac{2k}{3} \right) \right]$$

$$- R_\phi \left[g_{jj}^{-1/2} g_{ii}^{1/2} g^{im} \frac{\partial v_t}{\partial \xi^j} \frac{\partial V(j)}{\partial \xi^m} + g_{kk}^{-1/2} g_{ii}^{1/2} g^{im} \frac{\partial v_t}{\partial \xi^k} \frac{\partial V(k)}{\partial \xi^m} \right]$$

$$- R_\phi \frac{\partial v_t}{\partial \xi^m} \left[E^m(i) V(i) + g_{mm}^{-1/2} g_{ii}^{1/2} E^i(m) V(m) + g_{nn}^{-1/2} g_{ii}^{1/2} \left(C_n^{im} + C_n^{mi} \right) V(n) \right]$$

$$- \left[P(i) V(i) + g_{ii}^{1/2} g_{mm}^{-1/2} Q_m^i V(m) + g_{ii}^{1/2} g_{jj}^{-1/2} 2C_j^{im} \frac{\partial V(j)}{\partial \xi^m} + g_{ii}^{1/2} g_{kk}^{-1/2} 2C_k^{im} \frac{\partial V(k)}{\partial \xi^m} \right]$$

$$+ R_\phi g_{mm}^{-1/2} \left[D_m(i) V(i) V(m) + g_{ii}^{1/2} g_{nn}^{-1/2} \Gamma_{mn}^i V(m) V(n) \right] \tag{41}$$

where (i,j,k) are in cyclic order and the diffusion terms arising due to the nonorthogonal coordinates are given by the operator

$$NO(\phi) = 2 \left[g^{12} \phi_{\xi\eta} + g^{13} \phi_{\xi\zeta} + g^{23} \phi_{\eta\zeta} \right] \tag{42}$$

The various geometric coefficients were defined in the previous section. Note that they involve sums over the indices m and n. The coefficient required for each component of the momentum equation can be found using

$$\phi = V(1) = U \quad (i=1, j=2, k=3)$$

$$\phi = V(2) = V \quad (i=2, j=3, k=1)$$

$$\phi = V(3) = W \quad (i=3, j=1, k=2)$$

The coefficients for $\phi = k$ or ε are derived from their corresponding non-dimensional equations and arranging them in the form of equations (37) to (39) and (41). This yields

21

$$2C_\phi = R_\phi \left[g_{11}^{-1/2} V(1) - \frac{1}{\sigma_\phi} g^{1n} \frac{\partial v_t}{\partial \xi^n} \right] - f^1 \tag{43}$$

$$2B_\phi = R_\phi \left[g_{22}^{-1/2} V(2) - \frac{1}{\sigma_\phi} g^{2n} \frac{\partial v_t}{\partial \xi^n} \right] - f^2 \tag{44}$$

$$2A_\phi = R_\phi \left[g_{33}^{-1/2} V(3) - \frac{1}{\sigma_\phi} g^{3n} \frac{\partial v_t}{\partial \xi^n} \right] - f^3 \tag{45}$$

$$S_k = -NO(k) - R_k (G - \varepsilon) \tag{46}$$

$$S_\varepsilon = -NO(\varepsilon) - R_\varepsilon \frac{\varepsilon}{k} (C_{\varepsilon 1} G - C_{\varepsilon 2} \varepsilon) \tag{47}$$

where R_ϕ is the effective Reynolds number defined by

$$\frac{1}{R_k} = \frac{1}{Re} + \frac{v_t}{\sigma_k} \tag{48}$$

$$\frac{1}{R_\varepsilon} = \frac{1}{Re} + \frac{v_t}{\sigma_\varepsilon} \tag{49}$$

Now, introducing the coordinate stretching

$$\xi^* = \frac{\xi}{\sqrt{g_P^{11}}}, \quad \eta^* = \frac{\eta}{\sqrt{g_P^{22}}}, \quad \zeta^* = \frac{\zeta}{\sqrt{g_P^{33}}} \tag{50}$$

equation (36) reduces to the standard three-dimensional, convective-diffusive transport equation described in Chen and Chen (1984), i.e.,

$$\phi_{\xi^*\xi^*} + \phi_{\eta^*\eta^*} + \phi_{\zeta^*\zeta^*} = 2C\phi_{\xi^*} + 2B\phi_{\eta^*} + 2A\phi_{\zeta^*} + R\phi_t + (S_\phi)_P \tag{51}$$

with

22

$$C = \frac{(C_\phi)_P}{\sqrt{g_P^{11}}}, \quad B = \frac{(B_\phi)_P}{\sqrt{g_P^{22}}}, \quad A = \frac{(A_\phi)_P}{\sqrt{g_P^{33}}}, \quad R = (R_\phi)_P$$

(52)

for a numerical element with dimensions

$$\Delta\xi^* = \ell = \frac{1}{\sqrt{g_P^{11}}}, \quad \Delta\eta^* = k = \frac{1}{\sqrt{g_P^{22}}}, \quad \Delta\zeta^* = h = \frac{1}{\sqrt{g_P^{33}}}$$

(53)

shown in figure 2, where subscript P denotes a quantity evaluated at a point (node) P.

In applying the finite-analytic method of Chen and Chen (1984) to the linearized equation (51), the most general version for a three-dimensional element results in a 28-point discretization formula. While such a scheme will, in principle, yield better results, for a wide class of problems it suffices to use a simplified method to save computational effort. Here the hybrid method, which combines a two-dimensional local solution in the $\eta\zeta$-plane with a one-dimensional solution in the ξ-direction, is employed. A brief description is given below.

In the hybrid scheme, equation (51) is decomposed into one- and two-dimensional partial differential equations as follows

$$2C\phi_{\xi^*} - \phi_{\xi^*\xi^*} + R\phi_t + (S_\phi)_P = G(\xi^*, \eta^*, \zeta^*, t)$$

(54)

$$\phi_{\eta^*\eta^*} + \phi_{\zeta^*\zeta^*} - 2B\phi_{\eta^*} - 2A\phi_{\zeta^*} = G(\xi^*, \eta^*, \zeta^*, t)$$

(55)

If G is assumed to be constant in each local element, and if the time derivatives are approximated by backward finite-difference formulas, equations (54) and (55) reduce, respectively, to the standard one- and two-dimensional convection-diffusion equations described in Chen and Chen (1984).

The general solution of the one-dimensional equation (54) can be readily obtained as

$$\phi = a\left(e^{2C\xi^*} - 1\right) + b\xi^* + c$$

(56)

where a, b, c are constants to be determined from the boundary conditions. By substituting equation (56) into (54), the source function G at the center node P is obtained as

$$G_P = g = G(0,0,0,0) = \left(2C\phi_{\xi^*} - \phi_{\xi^*\xi^*} + R\phi_t + S_\phi\right)_P$$

$$= (C_U + C_D) \phi_P - C_U \phi_U - C_D \phi_D + \frac{R}{\Delta \tau} \left(\phi_P - \phi_P^{n-1} \right) + (S_\phi)_P \tag{57}$$

with

$$C_U = \frac{C \, e^{C\ell}}{\ell \sinh C\ell}, \quad C_D = \frac{C \, e^{-C\ell}}{\ell \sinh C\ell} \tag{58}$$

where the subscripts P, U, and D denote the center, upstream and downstream nodes, respectively, as shown in figure 2. The superscript (n-1) refers to the value at the previous time step, and $\Delta \tau$ is the time step.

By specifying boundary conditions for each element, equation (55) can be solved analytically by the method of separation of variables. The boundary conditions on all four boundaries, $\eta^* = \pm k$ and $\zeta^* = \pm h$ of the transverse section ($\eta\zeta$-plane) of each local element are specified as a combination of exponential and linear functions, which are the natural solutions of the governing equation, i.e.,

$$\phi(k, \zeta^*) = a_n \left(e^{2A\zeta^*} - 1 \right) + b_n \zeta^* + c_n$$

$$\phi(-k, \zeta^*) = a_s \left(e^{2A\zeta^*} - 1 \right) + b_s \zeta^* + c_s$$

$$\phi(\eta^*, h) = a_e \left(e^{2B\eta^*} - 1 \right) + b_e \eta^* + c_e$$

$$\phi(\eta^*, -h) = a_w \left(e^{2B\eta^*} - 1 \right) + b_w \eta^* + c_w$$

where a, b, c are again constants determined by the nodal values along the boundaries of the element. When the local solution thus derived is evaluated at the center node P of the element, the following nine-point discretization formula is obtained:

$$\phi_P = C_{NE} \phi_{NE} + C_{NW} \phi_{NW} + C_{SE} \phi_{SE} + C_{SW} \phi_{SW}$$

$$+ C_{EC} \phi_{EC} + C_{WC} \phi_{WC} + C_{NC} \phi_{NC} + C_{SC} \phi_{SC} + C_P \, g \tag{59}$$

where

$$C_{SC} = \frac{e^{Bk}}{2 \cosh Bk} P_A$$

$$C_{NC} = e^{-2Bk} C_{SC}$$

$$C_{WC} = \frac{e^{Ah}}{2 \cosh Ah} P_B$$

$$C_{EC} = e^{-2Ah} C_{WC}$$

$$C_{SW} = \frac{e^{Bk + Ah}}{4 \cosh Bk \cosh Ah} (1 - P_A - P_B)$$

$$C_{SE} = e^{-2Ah} C_{SW}$$

$$C_{NW} = e^{-2Bk} C_{SW}$$

$$C_{NE} = e^{-2Bk - 2Ah} C_{SW}$$

$$C_P = \frac{h \tanh Ah}{2A} (1 - P_A) = \frac{k \tanh Bk}{2B} (1 - P_B)$$

with

$$P_A = 4E_2 \, Ah \cosh Ah \cosh Bk \coth Ah$$

$$P_B = 1 + \frac{Bh \coth Bk}{Ak \coth Ah} (P_A - 1)$$

and

$$E_2 = \sum_{m=1}^{\infty} \frac{-(-1)^m \lambda_m h}{\left[(Ah)^2 + \lambda_m^2\right]^2 \cosh \sqrt{A^2 + B^2 + \lambda_m^2} \, k}$$

$$\lambda_m = \left(m - \frac{1}{2}\right) \pi$$

Finally, by substituting the inhomogeneous term g from equation (57) into equation (59), the following discretization formula is obtained for an unsteady, three-dimensional flow:

$$\phi_P = \frac{1}{1 + C_P\left(C_U + C_D + \frac{R}{\Delta\tau}\right)} \left\{ C_{NE}\phi_{NE} + C_{NW}\phi_{NW} + C_{SE}\phi_{SE} + C_{SW}\phi_{SW}\right.$$

$$+ C_{EC}\phi_{EC} + C_{WC}\phi_{WC} + C_{NC}\phi_{NC} + C_{SC}\phi_{SC}$$

$$\left. + C_P\left(C_U\phi_U + C_D\phi_D + \frac{R}{\Delta\tau}\phi_P^{n-1}\right) + C_P(S_\phi)_P\right\}$$

(60)

or

$$\phi_P = \frac{1}{1 + C_P\left(C_U + C_D + \frac{R}{\Delta\tau}\right)} \left\{ \sum_{nb=1}^{8} C_{nb}\phi_{nb}\right.$$

$$\left. + C_P\left[C_U\phi_U + C_D\phi_D + \frac{R}{\Delta\tau}\phi_P^{n-1}\right] + C_P(S_\phi)_P\right\}$$

(61)

where the subscript nb denotes "neighboring" nodes (NE, NW, etc.). It is seen that ϕ_P depends on all eight neighboring nodal values in the transverse plane as well as the values at the upstream and downstream nodes (ϕ_U, ϕ_D) and the previous time step ϕ_P^{n-1}. When the cell Reynolds number 2C becomes large, C_U approaches $2C/\ell = 2(C_\phi)_P$ and C_D goes to zero so that the coefficients of discretized equations turn windward. Similarly, all finite-analytic coefficients of transport equations automatically control the direction of difference and weighting of neighboring nodes.

As equations (61) are implicit in time and space, their assembly for all elements in the solution domain results in a system of simultaneous algebraic equations. These equations are solved by the tridiagonal-matrix algorithm in conjunction with an Alternating-Direction-Implicit (ADI) scheme. For steady-flow calculations, where it is not necessary to obtain a fully converged solution at intermediate stages, only ten internal iterations are used during each time step.

V.3 Continuity equation and pressure-velocity coupling

If the pressure is known, equation (61) can be employed to solve equations (32) for three velocities, and (33) and (34) for k and ε. However, the pressure is not known *a priori* and must be determined by requiring the velocity field to satisfy the continuity equation (31). In the method of Chen and Patel (1989), the pressure equation is derived by introducing pseudo-velocities at staggered locations while maintaining the regular grid arrangement for all the transport quantities. Figure 2 shows the locations of nodes in the regular grid in the $\eta\zeta$ plane.

26

In the regular grid arrangement, the twelve-point discretization formula (61) for the momentum equations gives the contravariant physical velocity component V(i) at P as

$$[V(i)]_P = \frac{1}{1 + C_P\left(C_U + C_D + \frac{R}{\Delta\tau}\right)} \left\{ \sum_{nb=1}^{8} C_{nb}V(i)_{nb} \right.$$

$$\left. + C_P\left\{C_U V(i)_U + C_D V(i)_D + \frac{R}{\Delta\tau} V(i)_P^{n-1}\right\} + C_P\left(S_{V(i)}\right)_P \right\} \tag{62}$$

Note that these equations contain the pressure gradient terms inside the source terms; see equations (41).

The actual velocity field V(i) in the momentum equation (32) is decomposed into a modified pseudo-velocity $\widehat{V}(i)$ plus the pressure gradient terms acting in the direction of the velocity component, i.e.,

$$V(i) = \widehat{V}(i) - \frac{C_P R\, g_{ii}^{1/2}}{1 + C_P\left(C_U + C_D + \frac{R}{\Delta\tau}\right)}\, g^{ii}\, \frac{\partial p}{\partial \xi^i} \tag{63}$$

or

$$V(i) = \widehat{V}(i) - E^{ii}\, \frac{\partial p}{\partial \xi^i} \qquad \text{(no sum on i)} \tag{64}$$

The continuity equation (31) yields

$$\left[Jg_{11}^{-1/2}V(1)\right]_d - \left[Jg_{11}^{-1/2}V(1)\right]_u$$

$$+ \left[Jg_{22}^{-1/2}V(2)\right]_e - \left[Jg_{22}^{-1/2}V(2)\right]_w$$

$$+ \left[Jg_{33}^{-1/2}V(3)\right]_n - \left[Jg_{33}^{-1/2}V(3)\right]_s = 0 \tag{65}$$

Substitution of (64) into (65) gives

$$\left\{\left[Jg_{11}^{-1/2}E^{11}\right]_d + \left[Jg_{11}^{-1/2}E^{11}\right]_u + \left[Jg_{22}^{-1/2}E^{22}\right]_e + \left[Jg_{22}^{-1/2}E^{22}\right]_w\right.$$

$$\left. + \left[Jg_{33}^{-1/2}E^{33}\right]_n + \left[Jg_{33}^{-1/2}E^{33}\right]_s\right\} p_P$$

$$= \left[Jg_{11}^{-1/2}E^{11}\right]_d p_D + \left[Jg_{11}^{-1/2}E^{11}\right]_u p_U + \left[Jg_{22}^{-1/2}E^{22}\right]_e p_{EC}$$

$$+ \left[Jg_{22}^{-1/2}E^{22}\right]_w p_{WC} + \left[Jg_{33}^{-1/2}E^{33}\right]_n p_{NC} + \left[Jg_{33}^{-1/2}E^{33}\right]_s p_{SC} - \widehat{D} \tag{66}$$

where

$$\hat{D} = \left[Jg_{1\bar{1}}^{1/2}\hat{V}(1)\right]_d + \left[Jg_{1\bar{1}}^{1/2}\hat{V}(1)\right]_u + \left[Jg_{2\bar{2}}^{1/2}\hat{V}(2)\right]_e$$
$$+ \left[Jg_{2\bar{2}}^{1/2}\hat{V}(2)\right]_w + \left[Jg_{3\bar{3}}^{1/2}\hat{V}(3)\right]_n + \left[Jg_{3\bar{3}}^{1/2}\hat{V}(3)\right]_s \qquad (67)$$

With a regular grid, the modified pseudo-velocities at the staggered locations cannot be obtained directly. Therefore, a simple one-dimensional linear interpolation is used to obtain the modified pseudo-velocities at the required staggered nodes, i.e.,

$$\left[\hat{V}(1)\right]_d = \frac{1}{2}\left\{\left[\hat{V}(1)\right]_D + \left[\hat{V}(1)\right]_P\right\}$$

$$\left[\hat{V}(2)\right]_e = \frac{1}{2}\left\{\left[\hat{V}(2)\right]_{EC} + \left[\hat{V}(2)\right]_P\right\}$$

$$\left[\hat{V}(3)\right]_n = \frac{1}{2}\left\{\left[\hat{V}(3)\right]_{NC} + \left[\hat{V}(3)\right]_P\right\} \qquad \text{etc.} \qquad (68)$$

so that $\hat{D}$ of equation (67) can be expressed in terms of the pseudovelocities at regular nodes as follows:

$$\hat{D} = \frac{1}{2}\left\{\left[\hat{V}(1)\right]_D - \left[\hat{V}(1)\right]_U + \left[\hat{V}(2)\right]_{EC} - \left[\hat{V}(2)\right]_{WC} + \left[\hat{V}(3)\right]_{NC} - \left[\hat{V}(3)\right]_{SC}\right\}$$

The coefficients $(Jg_{11}^{-1/2}E^{11})_d$, $(Jg_{22}^{-1/2}E^{22})_e$, etc. in equation (66) are also calculated by one-dimensional interpolation in the same way as in equation (68).

The solution of the coupled momentum and continuity equations involves a global iteration process, in which the velocity-pressure coupling is effected by predictor-corrector steps. In the predictor step, the pressure field at the previous time step is used in the solution of the implicit momentum equations to obtain the corresponding velocity field. Since this velocity field does not satisfy mass conservation, a corrector step is needed. In the corrector step, the explicit momentum equations and the implicit pressure equation are solved iteratively to ensure that the continuity equation is satisfied. This procedure is almost the same as the PISO algorithm of Issa (1985) except for some minor details. In the PISO algorithm, the pressure equation in an incremental form is solved in two correction steps. The present procedure, however, solves the absolute (nonincremental) pressure equation in several correction steps, the number of which is specified a priori. In the present algorithm, the finite-analytic coefficients are not updated during the corrector steps, while in the PISO algorithm the corresponding convection-diffusion coefficients based on finite-difference formulation are updated in the corrector steps.

28

V.4 Solution procedure

The system of algebraic equations formed by (61) for transport quantities and (66) for pressure is solved by the tridiagonal matrix algorithm in conjunction with the ADI (Alternating-Direction-Implicit) scheme. For transient problems, where the initial and boundary conditions are properly specified, the overall numerical solution procedure may be summarized as follows.

1. Read in the grid and calculate the geometric coefficients and related terms.
2. Specify the initial conditions for velocity and turbulence fields.
3. Give an initial guess for pressure.
4. Calculate the finite-analytic coefficients for the transport equations.
5. Solve equations (33) and (34) for turbulence parameters by tridiagonal matrix algorithm. Update the eddy-viscosity using the two-layer turbulence model.
6. Solve the momentum equations (32) using the previous pressure field. This step constitutes the predictor step for velocity field.
7. Calculate modified pseudovelocities from equation (64) and solve the pressure equation (66).
8. Using the newly obtained pressure, calculate the new velocity field explicitly from equation (64). This completes the corrector step.
9. Repeat steps 7 and 8 a specified number of times to obtain a converged solution.
10. Return to step 4 for the next time step.

VI. DESCRIPTION OF METHOD II

Method II is based on the one developed by Sotiropoulos (1991). However, during the course of this work, a number of new features and capabilities have been added, including an implicit solution procedure for the pressure equation and the two-layer turbulence model of Chen and Patel (1988). As this method utilizes the *partial transformation* approach, with the velocity components expressed in Cartesian coordinates, the appropriate forms of the Reynolds-averaged Navier-Stokes equations, and the equations for the turbulence model, in generalized curvilinear coordinates are presented once again. The spatial and temporal discretization of the governing equations, pressure-velocity coupling algorithm, and convergence acceleration techniques are then described in turn.

VI.1 Governing equations

The Reynolds-averaged Navier-Stokes equations (1) and the equation of continuity (2), are transformed to generalized curvilinear coordinates by invoking the *partial transformation*, i.e., x_i

$\rightarrow \xi^i$, but leaving the velocity components V_i in Cartesian coordinates, but now denoted V^i. The transformed governing equations, of continuity and momentum, read as follows:

continuity equation

$$\frac{1}{J}\frac{\partial(JV^i)}{\partial\xi^i} = 0 \tag{69}$$

momentum equation

$$\frac{\partial Q}{\partial t} + A_j\frac{\partial Q}{\partial\xi^j} - \frac{1}{J}\frac{\partial E_{v_j}}{\partial\xi^j} + H = 0 \tag{70}$$

In the above equation, Q is the velocity vector $Q = (V_1, V_2, V_3)^T$. The matrices A_j in equation (70), are diagonal matrices defined as follows

$$A_j = \text{diag}(V^j, V^j, V^j) \tag{71}$$

The viscous flux vectors E_{v_j} which appear in the momentum equation (70) are

$$E_{v_j} = \left(E_{v_j}^1,\ E_{v_j}^2,\ E_{v_j}^3\right)^T$$

where

$$E_{v_j}^k = J\left(\frac{1}{Re} + v_t\right)\left[\left(\xi_{x_k}^p\xi_{x_k}^j + g^{pj}\right)\frac{\partial V_k}{\partial\xi^p} + S_{kj}\right]$$

$$S_{1j} = \xi_{x_2}^j R_{21} + \xi_{x_3}^j R_{31}$$
$$S_{2j} = \xi_{x_1}^j R_{12} + \xi_{x_3}^j R_{31} \tag{72}$$
$$S_{3j} = \xi_{x_1}^j R_{13} + \xi_{x_2}^j R_{23}$$

$$R_{ij} = \frac{\partial V_i}{\partial\xi^k}\xi_{x_j}^k$$

The source vector H in the momentum equation (70) is given by

$$H = \left(\frac{\partial P}{\partial \xi^k} \xi_{x_1}^k, \quad \frac{\partial P}{\partial \xi^k} \xi_{x_2}^k, \quad \frac{\partial P}{\partial \xi^k} \xi_{x_3}^k \right)^T \tag{73}$$

The equations for the turbulent quantities k and ε are written in generalized curvilinear as follows:

$$\frac{\partial k}{\partial t} + V^j \frac{\partial k}{\partial \xi^j} - \frac{1}{J} \frac{\partial}{\partial \xi^j} \left[\left(\frac{1}{Re} + \frac{v_t}{\sigma_k} \right) J \, g^{ij} \frac{\partial k}{\partial \xi^i} \right] - G + \varepsilon = 0 \tag{74}$$

$$\frac{\partial \varepsilon}{\partial t} + V^j \frac{\partial \varepsilon}{\partial \xi^j} - \frac{1}{J} \frac{\partial}{\partial \xi^j} \left[\left(\frac{1}{Re} + \frac{v_t}{\sigma_\varepsilon} \right) J \, g^{ij} \frac{\partial \varepsilon}{\partial \xi^i} \right] - C_{\varepsilon 1} \frac{\varepsilon}{k} G + C_{\varepsilon 2} \frac{\varepsilon^2}{k} = 0 \tag{75}$$

The production term G can be expressed in generalized curvilinear coordinates as

$$G = \frac{1}{2} v_t \, (R_{ij} + R_{ji})^2 \tag{76}$$

where repeated indices imply summation and R_{ij} is defined in equation (72).

VI.2 Spatial discretization of continuity and momentum equations

The momentum equations (70) are discretized in space, on a non-staggered mesh, using three-point central finite differencing for the pressure gradient and viscous terms, and second order upwind finite differencing for the convective terms. The upwind differencing of the convective terms eliminates the need for adding artificial dissipation terms, to the right hand side of the momentum equations, to stabilize the numerical algorithm. This is due to the fact that a fixed amount of dissipation is inherent in the upwind differencing.

Referring to the computational cell of figure 3, discrete approximations of convective, pressure gradient and viscous terms in equations (70) are as follows:

$$\left[V^l \frac{\partial V_1}{\partial \xi^l} \right]_{i,j,k} = V_{i,j,k}^{l+} \delta_{\xi^l}^- (V_1)_{i,j,k} + V_{i,j,k}^{l-} \delta_{\xi^l}^+ (V_1)_{i,j,k} \tag{77}$$

$$\left[\xi_{x_1}^l \frac{\partial P}{\partial \xi^l} \right]_{i,j,k} = (\xi_{x_1}^l)_{i,j,k} \, \delta_{\xi^l} \, P_{i,j,k} \tag{78}$$

$$\left\{ \frac{\partial}{\partial \xi^1} \left[J \ (v+v_t) \left(\xi_{x_1}^1 \xi_{x_1}^1 + g^{11} \right) \frac{\partial V_1}{\partial \xi^1} \right] \right\}_{i,j,k} = \tilde{\delta}_{\xi^1} \left[J \ (v+v_t) \left(\xi_{x_1}^1 \xi_{x_1}^1 + g^{11} \right) \tilde{\delta}_{\xi^1} (V_1)_{i,j,k} \right]$$

(79)

where

$$V^{i\pm} = \frac{1}{2} \left[V^i \pm \left| V^i \right| \right], \text{ (for } i = 1,2,3)$$

$$\delta_{\xi^1}^{\pm} ()_{i,j,k} = \pm \frac{1}{2\Delta\xi^1} \ [-3()_{i,j,k} + 4()_{i\pm1,j,k} - ()_{i\pm2,j,k}]$$

$$\delta_{\xi^1} ()_{i,j,k} = \frac{1}{2\Delta\xi^1} [()_{i+1,j,k} - ()_{i-1,j,k}]$$

(80)

$$\tilde{\delta}_{\xi^1} ()_{i,j,k} = \frac{1}{\Delta\xi^1} \ [()_{i+1/2,j,k} - ()_{i-1/2,j,k}]$$

Similar expressions are used to discretize derivatives with respect the other two spatial directions. In all the above equations, the metrics and the Jacobian of the geometric transformation are computed at the (i,j,k) nodes using three-point central differences. To compute the metrics and the Jacobian at the half nodes ((i+1/2,j,k) and etc.), where they are needed for the discretization of the viscous terms, a simple averaging procedure is employed.

The continuity equation (69) is discretized using three-point central differences. For convenience we define the discrete divergence operator as follows:

$$DIV [Q_{i,j,k}] = \frac{1}{J} \left[\delta_{\xi^q} \ (JV^q)_{i,j,k} \right]$$

(81)

where Q is the cartesian velocity vector and V^q are the contravariant components of the velocity.

VI.3 Temporal discretization of continuity and momentum equations

The system of the discrete continuity and momentum equations is integrated in time using the four-stage, explicit Runge-Kutta scheme. Although explicit in time, the Runge-Kutta scheme--first used by Jameson (1981) to solve the compressible Euler equations--is known to have very good error damping properties, which can be further enhanced by employing convergence acceleration techniques as discussed later on. Particularly in complex three-dimensional flow applications, the Runge-Kutta scheme can be very competitive to approximate-factorization techniques, since it is fully vectorizable and can easily take advantage of parallel processing capabilities of today's supercomputers. The Runge-Kutta scheme has been adopted by several researchers and applied, with a great deal of success, to solve compressible viscous and inviscid

flows (Jameson and Baker (1983), Chima and Yokota (1990)). Merkle et al. (1986) used the four-stage Runge-Kutta scheme in conjunction with the artificial compressibility method to solve the incompressible Euler equations, while Sotiropoulos (1991) applied it in conjunction with the pressure-Poisson approach to calculate incompressible turbulent flows past ship hulls.

Following Sotiropoulos (1991), the Runge-Kutta scheme is applied to the system of the governing equations (69) and (70) as follows (for $\ell = 1,2,3,4$):

$$DIV \; [Q^\ell_{i,j,k}] = 0 \tag{82}$$

$$Q^\ell_{i,j,k} = Q^n_{i,j,k} - \alpha_\ell \; \Delta t_{i,j,k} \; RHS^{\ell-1}_{i,j,k} \tag{83}$$

In the above equations, the superscript "n" denotes the time step at which the solution is known, while the superscript "ℓ" denotes an intermediate time level (or iteration level) used to advance the solution from time step "n" to time step "n+1" (we designate $Q^\ell = Q^n$ for $\ell=0$ and $Q^\ell = Q^{n+1}$ for $\ell=4$). For the four-stage scheme, the coefficients α_ℓ's are: 1/4, 1/3, 1/2 and 1 for $\ell = 1,2,3,4$, in sequence. The RHS in equation (83) denotes the discrete approximation of the right-hand side of the momentum equations (70) at the node (i,j,k):

$$RHS = A_j \frac{\partial Q}{\partial \xi_j} - \frac{1}{J} \frac{\partial E_{v_j}}{\partial \xi_j} + H \tag{84}$$

Also, $\Delta t_{i,j,k}$ in equation (83) is the time increment which, for reasons discuss later on, varies in space (local time stepping). For the sake of convenience, however, in the rest of the analysis the (i,j,k) subscript has been dropped.

VI.4 Pressure-velocity coupling algorithm

The system of discrete governing equations (82) and (83) can not be integrated in time in its current form due to the lack of an evolution equation for the pressure field. The discrete momentum equation (83), however, can be substituted in the discrete continuity equation (82) to obtain a Poisson equation for the pressure field at the intermediate stage (ℓ-1). As discussed in Sotiropoulos (1991), on a non-staggered grid layout, the so resulting pressure equation would be exactly equivalent to the discrete continuity equation--since, at steady state the pressure equation reduces to the continuity equation (82)--but it would yield oscillatory solutions for the pressure field (odd-even decoupling). To overcome this difficulty, it was proposed by Sotiropoulos (1991) to derive the discrete pressure equation starting from a modified form of the discrete continuity equation. More specifically, the proposed discrete "continuity equation" reads as follows:

$$\text{DIV } [Q^\ell_{i,j,k}] = \gamma \frac{1}{J} (\widetilde{L} - L) [P^{\ell-1}_{i,j,k}] \tag{85}$$

where

$$\widetilde{L}[\ ] = \{\ \widetilde{\delta}_{\xi^1}(\ J\ g^{11}\Delta t\ \widetilde{\delta}_{\xi^1}\ ) + \widetilde{\delta}_{\xi^2}(\ J\ g^{22}\Delta t\ \widetilde{\delta}_{\xi^2}\ ) + \widetilde{\delta}_{\xi^3}(\ J\ g^{33}\Delta t\ \widetilde{\delta}_{\xi^3}\ )\}[\ ] \tag{86}$$

$$L[\ ] = \{\ \delta_{\xi^1}(\ J\ g^{11}\Delta t\ \delta_{\xi^1}\ ) + \delta_{\xi^2}(\ J\ g^{22}\Delta t\ \delta_{\xi^2}\ ) + \delta_{\xi^3}(\ J\ g^{33}\Delta t\ \delta_{\xi^1}\ )\}[\ ] \tag{87}$$

The detailed reasoning behind the selection of the source term in the right hand side of equation (85) can be found in Sotiropoulos (1991). Herein, it suffices to note that the source term in equation (85)--which is necessary to guarantee the smoothness of the computed pressure field--is proportional to the difference between the orthogonal parts of two discrete approximations of the Laplace pressure operator: the one that results by discretizing over $2\Delta\xi$ and the one that results by discretizing over $4\Delta\xi$. The positive constant γ is introduced to control the size of the source term and minimize the error in the satisfaction of the discrete continuity equation. Numerical experimentation with a variety of three-dimensional flows has shown that values of γ between 0.01 and 0.1 are sufficient to eliminate the odd-even decoupling of the pressure nodes.

By incorporating the discrete momentum equation (83) into the discrete "continuity equation" (85), the following equation is obtained for the pressure field at the (ℓ-1) stage (for the sake of convenience we set m=ℓ-1):

$$(1-\gamma)\ L[P^m] + \gamma \widetilde{L}[P^m] + N[P^m] = \frac{1}{\alpha_1} \text{DIV}[Q^n] - \sigma^m_{i,j,k} \tag{88}$$

where

$$N[P] = \{\delta_{\xi^1}[J\Delta t\ (g^{12}\delta_{\xi^2}+g^{13}\delta_{\xi^3})] + \delta_{\xi^2}[J\Delta t\ (g^{12}\delta_{\xi^1}+g^{23}\delta_{\xi^3})]$$

$$+ \delta_{\xi^3}[J\Delta t\ (g^{13}\delta_{\xi^1}+g^{23}\delta_{\xi^2})]\}[P] \tag{89}$$

and

$$\sigma = \delta_{\xi^1}(J\Delta t\ \xi^j_x f^{\xi^j}) \tag{90}$$

where f^{ξ^j} contains discrete approximations of the convective and viscous terms which appear in the ξj-momentum equation.

In Sotiropoulos (1991), the pressure equation (88) was solved using the point successive relaxation method. In the present work, however, in order to accelerate the convergence of the pressure equation as well as that of the global time marching procedure, equation (88) is solved using the Alternate Direction Implicit (ADI) method. For that reason, a time derivative of the pressure is introduced in equation (88) transforming the pressure-Poisson equation into a diffusion-like evolution equation:

$$-\beta \frac{\partial P}{\partial t} + (1-\gamma) L[P^m] + \gamma \widetilde{L}[P^m] + N[P^m] = \cdots \tag{91}$$

where β, in equation (91), is a positive preconditioning constant introduced to accelerate the convergence to steady state as discussed in a later paragraph. Incorporating the first-order accurate Euler implicit temporal linearization scheme

$$P^m = P^{m-1} + \frac{\partial P}{\partial t} \Delta t + \theta(\Delta t^2) = P^{m-1} + \Delta P$$

in equation (91), one obtains

$$\Delta P - \frac{\Delta t}{\beta} \{(1-\gamma) L[\Delta P] + \gamma \widetilde{L}[\Delta P]\} = -\frac{\Delta t}{\beta} PRHS \tag{92}$$

where

$$PRHS = (1-\gamma) L[P^{m-1}] + \gamma \widetilde{L}[P^{m-1}] + N[P^{m-1}] - \frac{1}{\alpha_1} DIV[Q^n] - \sigma_{i,j,k}^m \tag{93}$$

Note that the non-orthogonal pressure terms (N[ ]) in equation (92) are being treated explicitly in order to preserve the tridiagonal character of the resulting system. Also the dissipation term for the pressure equation (source term in equation (85)) is treated implicitly in equation (92). Such treatment, however, would result (for the general case of $\gamma \neq 1$) to a pentadiagonal system--in the i-sweep, for instance, the points i-2, i-1,i, i+1 and i+2 would be involved. To avoid the inversion of a pentadiagonal system, the L[ ] operator, which introduces the i-2 and i+2 off-diagonal terms, is eliminated from the left-hand side of equation (92) by setting the γ parameter equal to one--only, of course, in the left-hand side of equation (92). Obviously, this step has no effect on the steady state solution of the pressure equation since its left-hand side vanishes at convergence. Application of the ADI approximate factorization method to equation (92) gives:

$$[1 - \frac{\Delta t}{\beta} \tilde{\delta}_{\xi^1}(Jg^{11}\Delta t\, \tilde{\delta}_{\xi^1})][1 - \frac{\Delta t}{\beta} \tilde{\delta}_{\xi^2}(Jg^{22}\Delta t\, \tilde{\delta}_{\xi^2})][1 - \frac{\Delta t}{\beta} \tilde{\delta}_{\xi^3}(Jg^{33}\Delta t\, \tilde{\delta}_{\xi^3})]\, \Delta P$$

$$= -\frac{\Delta t}{\beta}\, PRHS$$

$$(94)$$

Equation (94) is solved, in three consecutive sweeps, using the Thomas algorithm. It is important to point out that the implicit solution of the pressure equation (94) increases the overall CPU requirement no more than five percent, mainly because: i) the three tridiagonal matrices to be inverted in equation (94) depend only on the metrics of the geometric transformation (the three diagonals of each matrix can be computed once, at the beginning of the calculation, and stored for subsequent use); and ii) the Thomas algorithm can be vectorized by solving simultaneously for all the points on a plane perpendicular to the current sweep direction.

It is well known that the ADI factorization is unconditionally stable (Anderson et al., 1984) when applied to the parabolic-in-time heat equation. Of course, the same argument can not be readily extended to the pressure equation without rigorous stability analysis of the system of governing equations. Numerical experimentation has shown, however, that stable solutions for the pressure equation (94) can be obtained for time steps much larger than those used for the momentum equations. More specifically, values of the preconditioning constant β of the order of 0.1 have been used in all the calculations reported in the following sections. This allows the pressure equation to operate with an effective time step one order of magnitude higher than the momentum equations, and this results in significant convergence acceleration of the overall time marching procedure.

VI.5 Solution of the k and ϵ equations

The k and ϵ equations (74) and (75) are discretized in space using second-order upwind differencing for the convective terms, and three-point central differencing for the viscous terms. Equations (74) and (75) are of the same type as the momentum equations (parabolic in time, elliptic in space) and, thus, the Runge-Kutta scheme could be applied to integrate them in time. The k–ϵ equations, however, contain source terms which are stiff--the production term G, for instance, is very large near solid boundaries while it decays rapidly to zero in the outer part of the boundary layer. The use of an explicit time-marching algorithm to integrate a stiff set of equations may impose severe time step limitations and have overall stability problems. To avoid such undesirable complications, equations (74) and (75) are solved by employing the ADI approximate factorization scheme.

The ε-equation (75) is used to demonstrate the linearization and approximate factorization procedure (a similar procedure is employed for the k-equation). Using the Euler implicit temporal discretization scheme, equation (75) is linearized in time as follows:

$$\Delta\varepsilon + \Delta t \, [\, -C_{\varepsilon 1} \frac{G}{k} + C_{\varepsilon 2} \frac{2\varepsilon}{k} + V^{i+} \, \widehat{\delta}_{\xi^i}^{-} + V^{i-} \, \widehat{\delta}_{\xi^i}^{+}$$

$$- \frac{1}{J} \, \widetilde{\delta}_{\xi^i} \, (Jv^{\varepsilon} g^{ii} \, \widetilde{\delta}_{\xi^i}) \,] \, \Delta\varepsilon = -\Delta t \, RHS_{\varepsilon}^{n} \tag{95}$$

where

$$RHS_{\varepsilon} = V^{i+} \, \widehat{\delta}_{\xi}^{-} \varepsilon + V^{i-} \, \widehat{\delta}_{\xi}^{+} \varepsilon \, - \frac{1}{J} \, \widetilde{\delta}_{\xi^i} \, (Jv^{\varepsilon} g^{ij} \, \widetilde{\delta}_{\xi^i} \varepsilon) - C_{\varepsilon 1} \frac{\varepsilon}{k} G + C_{\varepsilon 2} \frac{\varepsilon^2}{k} \tag{96}$$

$$\widehat{\delta}_{\xi^i}^{\pm}(\,) = \pm \frac{(\,)_{i\pm1,j,k} - (\,)_{i,j,k}}{\Delta\xi^1} \tag{97}$$

$$v^{\varepsilon} = \frac{1}{Re} + \frac{v_t}{\sigma_{\varepsilon}} \tag{98}$$

The source terms of equation (75) have been linearized in time as

$$\frac{\varepsilon^{n+1}}{k} G = \frac{\varepsilon^n}{k} G + \frac{\Delta\varepsilon}{k} G$$

$$\frac{(\varepsilon^{n+1})^2}{k} = \frac{(\varepsilon^n)^2}{k} + \frac{2\varepsilon^n}{k} \Delta\varepsilon \tag{99}$$

In order to preserve the tridiagonal character of the resulting system, the non-orthogonal terms of the diffusion operator have been treated explicitly in equation (95). For the same reason, the convective terms in the left-hand side of equation (95) have been discretized using first-order upwind differencing. This less accurate spatial discretization does not have any effect on the steady state solution--the left hand side of equation (95) vanishes at convergence--since the standard second-order upwind differencing has been employed in the right-hand side. Finally, applying the ADI approximate factorization, equation (95) reads as follows:

$$\left\{ 1 + \Delta t^* \left[V^{1+} \, \widehat{\delta}_{\xi^1}^{-} + V^{1-} \, \widehat{\delta}_{\xi^1}^{+} - \frac{1}{J} \, \widetilde{\delta}_{\xi^1} \left(Jv^{\varepsilon} g^{11} \, \widetilde{\delta}_{\xi^1} \right) \right] \right\}$$

37

$$\left\{1 + \Delta t^*\left[V^{2+}\,\widehat{\delta}_\xi^- + V^{2-}\,\widehat{\delta}_\xi^+ - \frac{1}{J}\,\widetilde{\delta}_{\xi^2}\left(Jv^\varepsilon g^{22}\,\widetilde{\delta}_{\xi^2}\right)\right]\right\}$$

$$\left\{1 + \Delta t^*\left[V^{3+}\,\widehat{\delta}_{\xi^3} + V^{3-}\,\widehat{\delta}_\xi^+ - \frac{1}{J}\,\widetilde{\delta}_{\xi^3}\left(Jv^\varepsilon g^{33}\,\widetilde{\delta}_{\xi^3}\right)\right]\right\}\Delta\varepsilon = -\Delta t^*\,RHS_\varepsilon \qquad (100)$$

where

$$\Delta t^* = \frac{\Delta t}{1 + \Delta t\left(C_{\varepsilon 2}\frac{2\varepsilon}{k} - C_{\varepsilon 1}\frac{G}{k}\right)} \qquad (101)$$

Equation (100) is solved using a vectorized version of the Thomas algorithm, in a similar fashion as described in the previous section for the pressure equation. The k-equation is linearized and solved in an identical manner as described above. The only difference, of course, being that, in the context of the two-layer model, the k-equation is solved all the way to the wall while the ε-equation is solved only in the outer layer.

Due to the rapid changes in the cross-sectional shape and area of some of the duct configurations to be considered herein, care must be exercised when specifying the matching boundary for the two-layer k-ε turbulence model. In all the previously reported calculations with the two-layer model (see, for instance, Kim, 1991) the approach followed is to match the one- with the two-equation model along a pre-selected coordinate surface which is broadly located within what is normally the logarithmic region. This approach, although it works well for ducts of constant cross-section (and is adopted herein for similar configurations), is obviously not adequate for transition ducts where the cross-section changes from circular at the inlet to rectangular at the exit. For that reason, in the calculations with transition ducts we choose to follow a more rigorous approach, that is to match the two models at points where the turbulence Reynolds number Re_y (= $\sqrt{k}y/\nu$) is approximately equal to 250 in order to ensure that the wall damping effects are negligible (Chen and Patel, 1988) beyond that distance.

VI.6 Summary of algorithm and convergence acceleration techniques

Assuming that the solution at the "n" time level is known, the solution at the "n+1" time level is obtained through the following steps:

1. Solve the k and ε equations (74) and (75), as described in section 5, and calculate the new eddy-viscosity field.

2. Using the currently known pressure field, calculate the artificial mass source term for the pressure equation (right-hand side of equation (85)). To save computational time the artificial dissipation term is frozen in all subsequent Runge-Kutta stages.

3. For $\ell=1$ to 4 ($Q^\ell = Q^{n+1}$ for $\ell = 4$):

   (a) Compute the right-hand side of the pressure equation as given by equation (93).

   (b) Solve the pressure equation (94) to obtain the pressure field at the "ℓ-1" stage. Since, the steady state solution is of interest, only one ADI iteration is performed on the pressure.

   (c) Using equation (83) compute the velocity field at the "ℓ-stage" and return to step (a).

4. Repeat steps 1 to 3, until convergence is reached.

The convergence rate of the time marching procedure is enhanced by employing the local time-stepping technique along with implicit residual smoothing. The time increment is computed and stored for every node as follows (see Martinelli (1987), Kunz and Lakshminarayana (1991)):

$$\Delta t_{i,j,k} = \min (\Delta t^I_{i,j,k}, \Delta t^v_{i,j,k}) \tag{102}$$

where

$$\Delta t^I = CFL \min(\sqrt{g_{11}}, \sqrt{g_{22}}, \sqrt{g_{33}})$$

$$\Delta t^v = \frac{\Omega}{(\frac{1}{Re} + v_t) (g^{11}+g^{22}+g^{33})}$$

In the above equations, CFL and Ω denote the Courant-Friedrich-Lewis number (hyperbolic stability criterion) and the von Neumann number (parabolic stability criterion), respectively. The CFL number, used herein, is an approximate one, since it is based only on the local length scales of the computational grid. Although an exact CFL number should involve the local velocity scales as well, we chose to use this approximate formulation in order to avoid the calculation of Δt^I at every new iteration level--this purely geometric variation of Δt^I has been found adequate on highly stretched meshes (Sotiropoulos, 1991). Typically, the parabolic stability constraint dominates only in the near-wall region where the grid spacing, the velocity and the eddy viscosity approach zero. Sufficiently far from the wall, however, the hyperbolic stability criterion dictates the choice of a stable time increment. In the present calculations, the selection of the local time increment based on

both the hyperbolic and parabolic stability criteria (equation (102)) was found necessary for stability only for Reynolds numbers of the order of 10^6 or greater. At lower Reynolds numbers, the hyperbolic stability criterion was sufficient for obtaining converged solutions.

The implicit residual smoothing was first proposed by Lerat (see, for example, Hollanders et al., 1985) for use with the Lax-Wendroff scheme and was later adopted by Jameson (1983) to accelerate the convergence of Runge-Kutta schemes. In the present study, the implicit residual smoothing is applied to the right-hand side of the momentum equation as in Sotiropoulos (1991). More specifically, the residual calculated in equation (84) is smoothed by the constant coefficient implicit operator to define a new residual:

$$(1- \omega_1\delta_{\xi^1\xi^1})(1- \omega_2\delta_{\xi^2\xi^2})(1- \omega_3\delta_{\xi^3\xi^3}) \ \overline{RHS}^r = RHS^r \qquad (104)$$

where

$$\delta_{\xi^1\xi^1}(\ )_{i,j,k} = \frac{(\ )_{i+1,j,k} - 2(\ )_{i,j,k} + (\ )_{i-1,j,k}}{(\Delta\xi^1)^2}$$

The constants ω_1, ω_2 and ω_3 are smoothing parameters which are of the order of one and their subscripts indicate that they can be chosen differently for each spatial direction. Equation (104) is solved using the Thomas algorithm and the smoothed residual replaces the residual RHS in equation (83). The residual smoothing is applied at every stage between steps (3.b) and (3.c) in the solution procedure described in the beginning of this section . The implementation of the implicit residual smoothing in the four stage procedure allows the use of higher CFL numbers and consequently leads to a significant acceleration of the convergence rate--Sotiropoulos (1991) reported a fifty percent gain in convergence speed. Moreover, the vectorized version of the Thomas algorithm, used for inverting the three linear operators in equation (104), increases the overall CPU time by no more than five percent.

The smoothing coefficients in equation (104) are constant in each spatial direction and, therefore, one can expect this formulation to be optimal for grids that are not highly stretched. Surprisingly though, equation (104) has worked quite well (Sotiropoulos, 1991) for highly stretched grids with large aspect ratios. For further acceleration of the convergence rate, however, Martinelli (1987) proposed a formulation--for the two-dimensional compressible Navier-Stokes equations--where the smoothing coefficients in equation (104) are functions of characteristic wave speeds. The idea behind Martinelli's suggestion is that, since the minimum local grid spacing dictates the maximum allowable local time step for stable calculations, more smoothing should be

40

applied in the direction of that minimum spacing. If the same smoothing is applied in the other spatial directions--where the grid spacing is coarser and the time step, as computed by equation (104), is much smaller than the local stability limit--the damping properties of the scheme are impaired. Martinelli's formulation was extended to three-dimensions by Radiespiel et al. (1989) and Liu and Jameson (1992). In the present study a formulation similar to that of Liu and Jameson is adopted as follows:

$$\omega_1 = \max \left\{ 0, \frac{1}{4} \left[\left(\frac{CFL}{CFL^*} \frac{1}{1 + r_{12} + r_{13}} \right)^2 - 1 \right] \right\}$$

(105)

$$\omega_2 = \max \left\{ 0, \frac{1}{4} \left[\left(\frac{CFL}{CFL^*} \frac{1}{1 + r_{21} + r_{23}} \right)^2 - 1 \right] \right\}$$

(106)

$$\omega_3 = \max \left\{ 0, \frac{1}{4} \left[\left(\frac{CFL}{CFL^*} \frac{1}{1 + r_{31} + r_{32}} \right)^2 - 1 \right] \right\}$$

(107)

$$r_{ij} = \sqrt{\frac{g_{ii}}{g_{jj}}}$$

In the above equations, CFL^* denotes the CFL number of the unsmoothed scheme while CFL denotes the desirable CFL number. It can be easily seen that, for non-equal grid spacings, larger smoothing will be applied in the direction of smaller spacing, while for uniform grid the three smoothing coefficients are equal. In addition, these equations involve only geometric quantities and, consequently, the smoothing coefficients need to be computed only once at the beginning of the calculation.

VII. THE DISCRETE CONTINUITY EQUATION IN METHODS I & II

It is well known that on a non-staggered computational grid--which is used by both methods employed here--the discrete continuity equation cannot be satisfied to machine zero with the resulting pressure field being smooth (Strikwerda (1984), Sotiropoulos (1991)). In general, a smooth pressure field can be obtained only at the expense of accuracy of the discrete continuity equation. Thus, a successful non-staggered grid, primitive variable method must have built into it a dissipative mechanism that eliminates the pressure decoupling and, at the same time, a mechanism that minimizes any errors introduced in the discrete incompressibility condition.

Method II was specifically tailored to account for the ambiguities associated with the non-staggered grid. The artificial mass source term, introduced in the discrete continuity equation (85),

41

eliminates the decoupling of the pressure nodes but at the same time its size is controlled via the constant γ. An estimate for the size of this source term can be easily obtained if we consider its form for the case of uniform cartesian grid (see Sotiropoulos, 1991):

$$DIV[Q_{i,j,k}] = -\gamma_{II}\frac{\Delta t}{4} [\Delta x^2 \frac{\partial^4 P}{\partial x^4} + \cdots] \tag{108}$$

where the subscript II is used to differentiate from an equivalent parameter which will be subsequently used for Method I. Also the dots in equation (108) imply similar terms in the other spatial directions, which are omitted for convenience. Recall now that Method II employs the local time stepping technique according to which the local time increment is proportional to the grid spacing, with the constant of proportionality being the CFL number ($\Delta t = CFL \, \Delta x$). Incorporating this in equation (108), we obtain

$$DIV[Q_{i,j,k}] = -\gamma_{II}\frac{CFL}{4} \Delta x^3 \frac{\partial^4 P}{\partial x^4} + \cdots \tag{109}$$

This shows that the error in the satisfaction of the discrete incompressibility condition is third order in space (lower than the truncation error of the second-order accurate finite difference approximations). Also, it is important to note that the use of the local time stepping scales the time increment out of equation (109) and makes the steady state solution independent of the time step. Moreover, the CFL number in equation (109) does not have any significant effect in the steady state solution, since its maximum allowable value for stability is 4 ($CFL/4 \le 1$). All the herein reported calculations performed with Method II use $\gamma_{II} = 0.01\div0.1$.

Let us examine now the accuracy of Method I insofar as the satisfaction of the discrete continuity is concerned. For convenience, but without loss of generality, we use only the ξ^1-derivatives in the pressure equation (66). First recall that the ξ^1-momentum equation at the (i,j,k) node reads (equation (64)):

$$V_i(1) = \widehat{V}_i(1) - E^{11}\left(\frac{\partial P}{\partial \xi^1}\right)_i \tag{110}$$

with the pressure gradient term computed as

$$\left(\frac{\partial P}{\partial \xi^1}\right)_i = \frac{P_{i+1} - P_{i-1}}{2\Delta \xi^1} \tag{111}$$

42

The pressure equation is derived from the discrete continuity equation

$$[Jg_{11}^{-1/2}V(1)]_{i+1/2} - [Jg_{11}^{-1/2}V(1)]_{i-1/2} + \cdots = 0$$

by substituting in this equation (110), using simple linear interpolation to compute the pseudovelocities at the cell interfaces (equation (68)), and calculating the pressure gradient terms as follows:

$$\left(\frac{\partial P}{\partial \xi^1}\right)_{i \pm 1/2} = \pm \frac{P_{i \pm 1} - P_i}{\Delta \xi^1} \tag{112}$$

The resulting pressure equation (66) reads

$$\frac{[Jg_{11}^{-1/2}\widehat{V}(1)]_{i+1} - [Jg_{11}^{-1/2}\widehat{V}(1)]_{i-1}}{2\Delta \xi^1} + \cdots = C_{i+1/2}^{11}\frac{P_{i+1}-P_i}{\Delta \xi^1} - C_{i-1/2}^{11}\frac{P_i-P_{i-1}}{\Delta \xi^1} + \cdots \tag{113}$$

where for convenience $C^{11} = Jg_{11}^{-1/2}E^{11}$. By simply adding and subtracting appropriate terms and using linear interpolation to compute the coefficients of the pressure derivatives at the interfaces, the right-hand side of the pressure equation (113) can be rearranged as follows:

$$\frac{[Jg_{11}^{-1/2}\widehat{V}(1)]_{i+1} - [Jg_{11}^{-1/2}\widehat{V}(1)]_{i-1}}{2\Delta \xi^1} + \cdots = \frac{1}{2\Delta \xi^1}[C_{i+1}^{11}\frac{P_{i+2}-P_i}{2\Delta \xi^1} - C_{i-1}^{11}\frac{P_i-P_{i-2}}{2\Delta \xi^1}]$$

$$- \frac{1}{2\Delta \xi^1}[C_{i+1}^{11}\frac{P_{i+2}-2P_{i+1}+P_i}{2\Delta \xi^1} - C_i^{11}\frac{P_{i+2}-2P_i+P_{i-1}}{2\Delta \xi^1} + C_{i-1}^{11}\frac{P_i-2P_{i-1}+P_{i-2}}{2\Delta \xi^1}] + \cdots$$

or, equivalently

$$\frac{1}{2\Delta \xi^1}\{(Jg_{11}^{-1/2})_{i+1}[\widehat{V}(1)_{i+1} - E_{i+1}^{11}\frac{P_{i+2}-P_i}{2\Delta \xi^1}]$$

$$- (Jg_{11}^{-1/2})_{i-1}[\widehat{V}(1)_{i-1} - E_{i-1}^{11}\frac{P_i-P_{i-2}}{2\Delta \xi^1}]\} + \cdots =$$

$$-\frac{1}{2\Delta\xi^1}[C_{i+1}^{11}\frac{P_{i+2}-2P_{i+1}+P_i}{2\Delta\xi^1} - C_i^{11}\frac{P_{i+2}-2P_i+P_{i-1}}{2\Delta\xi^1} + C_{i-1}^{11}\frac{P_i-2P_{i-1}+P_{i-2}}{2\Delta\xi^1}] + \cdots \qquad (114)$$

Note that equation (114) is identical to the original pressure equation (113). Assuming that convergence is reached for the pressure and the momentum equations, equation (110) implies that the two bold-faced terms in the left side of equation (114) reduce identically to the velocity components at the i+1 and i-1 nodes. Thus, at convergence, the pressure equation (114) can be written as follows:

$$\frac{1}{2\Delta\xi^1}[(Jg_{11}^{-1/2}V(1))_{i+1} - (Jg_{11}^{-1/2}V(1))_{i-1}] + \cdots = \frac{(\Delta\xi^1)^2}{4}\delta_{\xi^1\xi^1}(C^{11}\delta_{\xi^1\xi^1})P_i + \cdots \qquad (115)$$

with

$$\delta_{\xi^1\xi^1}(\ )_i = \frac{1}{(\Delta\xi^1)^2}[(\ )_{i+1} - 2(\ )_i + (\ )_{i-1}]$$

The right-hand side of equation (115) is the artificial mass source term introduced by the pressure-velocity coupling formulation of Method I in the continuity equation. This artificial source term is responsible for eliminating the odd-even decoupling of the pressure nodes on the non-staggered grid arrangement. It is interesting to point out that, using straightforward algebraic manipulations, the artificial source term (pressure dissipation) used in Method II (see equation (85)) can be rearranged (Sotiropoulos, 1991) in a form similar to the right-hand side of equation (115)--the difference being that the C^{11} coefficients in equation (115) depend on geometric quantities and the velocity field (see definition of E^{11}) while the corresponding coefficients in Method II depend on geometric quantities only. Note, however, that in Method II the source term (see equation(85)) was added explicitly in the discrete continuity equation before deriving the equation for the pressure. In Method I, on the other hand, the mass source is implicitly introduced in the discrete continuity equation because two different approaches are used to calculate the pseudovelocities and the pressure gradient terms at the cell interfaces. Recall, that linear interpolation is used to obtain the velocities at the cell interfaces (equations (68)) while the pressure gradient is discretized using equation (112). If the same interpolation procedure used for the pseudovelocities were to be used for the pressure gradient terms, no error would be introduced in the discrete continuity equation but the resulting pressure equation would yield oscillatory solutions for the pressure. Assuming now a uniform cartesian grid, equation (115) can take the following approximate form:

$$\text{DIV}[Q_{i,j,k}] = -\varepsilon_I \frac{\Delta\tau}{4} [\Delta x^2 \frac{\partial^4 P}{\partial x^4} + \cdots]$$ (116)

where

$$\varepsilon_I = \frac{C_P Re}{\Delta\tau [1 + C_P(C_U + C_D)] + C_P Re}$$ (117)

Note that equation (116) is only an approximation--as opposed to equation (108) for Method II which is exact on a uniform cartesian grid--because the part of the C^{11} coefficient that contains the finite analytic coefficients (ε_I term) has been locally linearized and taken out of the derivative. Although only approximate, equation (116) shows that Method I satisfies the discrete equation to accuracy comparable to that of Method II (equation (108)). The difference between the two formulations, however, is in the size and form of the dissipation coefficients ε_I and ε_{II}. The coefficient in Method I (equation (117))--and consequently the computed solution--is a function of the Reynolds number of the flow, the time step and the local velocity field (a dependency introduced via the finite analytic coefficients in equation (117)), while the ε_{II} coefficient in equation (108) is a user specified constant. It is interesting to point out, however, that for sufficiently large Reynolds numbers, the ε_I coefficient is of the order of one (see equation (117)), while it approaches zero with the Reynolds number. It can be deduced, therefore, that in the general case of any finite Reynolds number--and assuming that the left term in the denominator of equation (117) is always positive--the ε_I term is positive and less or equal to one.

VIII. A COMPUTATIONAL COMPARISON OF METHODS I & II

In this section a computational comparison of Methods I and II is made in order to identify their relative merits and weaknesses, and decide on an optimal numerical approach best suited to the problems under consideration. For this purpose, both methods are employed to calculate the following three cases (see also table 1 for more details on each case):

(i) *laminar flow* (Re = 790) through a 90° square bend with *fully-developed entry flow* (Humphrey et al., 1977),

(ii) *laminar flow* (Re = 790) through a 90° square bend with *developing entry flow* (Taylor et al., 1982), and

(iii) *turbulent flow* (Re = 224,000) through a 90° rectangular duct of aspect ratio six with *developing entry flow* (Kim, 1992).

The two laminar flow cases--both very well documented in experiments--are selected in order to assess the accuracy of the numerics without the uncertainties of a turbulence model. The third test case, on the other hand, is selected to evaluate the combined performance of the numerics with the same turbulence model. To establish a basis for meaningful and fair comparison, all subsequently reported calculations were performed with identical computational meshes, starting from the same initial conditions, using the same boundary conditions, and with the same convergence criteria for both methods. The relative performance of the methods is discussed with emphasis on numerical accuracy and overall computational efficiency.

VIII.1 Fully-developed laminar flow through a 90° square bend

The measurements of Humphrey et al. (1977) were carried out at Reynolds number, Re = 790, with a corresponding Dean number, De = 368. In the experiment, a long straight entry duct was used to realize fully-developed flow at the entrance of the bend (see table 1). In the present calculations, however, the solution domain starts five hydraulic diameters upstream of the bend and fully-developed flow conditions are prescribed there using the analytical solution given in White (1974).

Calculations are carried out on two numerical grids, namely, grid A with 74x41x21 nodes, and grid B with 99x41x21 nodes, in the streamwise, radial and normal directions, respectively. The streamwise spacing inside the bend is 2° for grid A and 1.5° for grid B. The grid nodes in the cross-sectional plane are distributed using a hyperbolic tangent stretching function with stretching ratios, in all spatial directions, nowhere exceeding 1.3. The exit boundary for both grids is located seven hydraulic diameters downstream of the bend. The physical and computational domains, along with the coordinate systems, are shown in figure 4. Typical views of the grid in the symmetry plane and the cross-section are also shown. As the duct geometry is symmetric with respect to the z-axis and as the entry flow profile is also symmetric, only one-half of the duct was considered.

As mentioned above, the same set of boundary conditions is employed for both methods. More specifically, Dirichlet conditions are used for the velocity components at the inlet (analytical solution) and on the solid walls (no-slip, no-flux condition), while at the exit the three velocity components are computed by assuming zero streamwise diffusion ($\phi_{\xi\xi} = 0$). The pressure at the inlet, exit and solid boundaries is computed using linear extrapolation from within the solution domain. Finally, on the symmetry plane (z = 0), the governing equations are solved in exactly the same way as for every internal computational node using mirror-image reflection for the grid and the flow variables.

The convergence histories, with grid A, are shown in figure 5 for both methods. The vertical axis in this figure is the logarithm of a residual defined as:

$$RESIDUAL = \left\{ \left[\frac{1}{N} \sum_{i,j,k} \Delta u_{i,j,k} \right]^2 + \left[\frac{1}{N} \sum_{i,j,k} \Delta v_{i,j,k} \right]^2 + \left[\frac{1}{N} \sum_{i,j,k} \Delta w_{i,j,k} \right]^2 \right\}^{1/2}$$

where N is the total number of grid nodes, Δ denotes changes between iterations and u, v and w denote the physical contravariant velocity components for Method I and the Cartesian velocity components for Method II. The horizontal axis in figure 5 is the computational work expressed in terms of Cray-2 CPU minutes. It is seen that Method II converges twice as fast as Method I. This result, however, is to be expected because Method I utilizes the full-transformation approach which increases considerably the computational work per grid node per iteration. The increased effort is associated with discretization of the additional grid-related terms introduced in the governing equations to account for the spatial variations of the contravariant base vectors (see Section V.1). Recall also that Method II is a mixed explicit-implicit method and, therefore, the computational work required per grid node per iteration is, by default, considerably less than that of an implicit method, such as Method I. Moreover, in the implicit parts of Method II (implicit residual smoothing and solution of the pressure equation) the operators to be inverted are linear and thus they are computed only once, at the beginning of the iterative procedure, and stored for subsequent use. In Method I, on the other hand, the operators to be inverted (momentum and pressure equations) are nonlinear and they need to be re-computed every iteration.

The effect of grid refinement on the computed solutions is shown for both methods in figure 6, where the computed streamwise velocity profiles--on grid A (dashed line) and grid B (solid line)--are plotted along the radial direction (from the inner to the outer wall) for several axial locations at z = 0. and z = -0.25. The comparison between grid A and grid B solutions is very good for Method I, since only some minor changes occur at $\theta = 60^o$ and 90° near the duct centerline. The same overall trend is also observed in the solutions obtained by Method II, except the centerplane profiles at $\theta = 60^o$ and 90° where a local maximum of the velocity appears clearly near the inner convex wall in the fine-grid solution.

The fine-grid solutions of the two methods are compared with the experimental data of Humphrey et al. (1977) in figures 7 and 8. In figure 7 the computed (dashed line for Method I and solid line for Method II) and measured (symbols) streamwise velocity profiles are plotted in the same fashion as in figure 6. The calculations are in good agreement with each other and with the experimental data at $\theta = 0^o$ and 30°. Some discrepancies exist, however, at the more downstream locations. More specifically, at $\theta = 60^o$ Method I yields lower, than measured, velocities near the bend centerline, while at $\theta = 90^o$ it underpredicts the slope of the streamwise velocity profile at the

47

z = -0.25 plane near the inner wall and fails to capture the local velocity maximum near the inner wall at z = 0. The computed lower velocities near the bend centerline at θ = 60° are even more pronounced in the solutions obtained with Method II. Note that Method II predicts two well-defined peaks in the velocity profile at z = -0.25 and 0, in contrast with the Method I solutions where two velocity peaks appear only at z = -0.25. At the θ = 90° plane, on the other hand, Method II correctly predicts the slope of the velocity profile near the inner wall at z = -0.25 and captures also the velocity maximum near the inner wall at z = 0.

Figure 8 compares the computed streamwise velocity profiles and the corresponding experimental data at θ = 30°, 60° and 90°. For each axial location the velocity profiles are plotted along the z-direction (from bottom wall to symmetry plane) for five different radial locations. As can be seen, both methods yield very similar solutions at θ = 30° and 60° but some discrepancies exist between experiment and calculations, particularly near the inner wall. At θ = 90° Method II agrees very well with the experimental data, while Method I appears to grossly underpredict the streamwise velocity at r* = 0.9. Figure 9, which is of the same format as figure 8, compares profiles of the radial velocity component calculated by the two methods; no experimental data for the radial velocity component are available. As expected, differences between the two calculations occur at the same locations where discrepancies were observed in the streamwise velocity component (figure 8). Finally, a more global picture of the computed solutions can be obtained from figure 10 where contours of the calculated streamwise velocity component are compared with measurements at θ = 60° and 90°.

VIII.2 Developing laminar flow through a 90° square bend

The measurements of Taylor et al. (1983) were made at Re = 790 and De = 368. The duct and bend geometry was almost identical to that of Humphrey et al. (1977), the only difference being a shorter entry length in order to obtain a thin boundary layer at the entrance to the bend. The calculations are carried out on a single computational grid with 69x41x21 nodes in the axial, radial and normal directions (with a streamwise spacing inside the bend of 3°). No grid refinement study is carried out for this case since the response of each method to a finer grid was established in the previous calculation. It should be pointed out, however, that the grid size employed here, particularly the number of planes in the streamwise direction, is probably not sufficient for grid independent solutions to be established.

The computations started 7.5 hydraulic diameters upstream of the bend entrance to match the experimental configuration, and a uniform (plug) inflow velocity profile was specified. Starting, however, with uniform flow at this location does not exactly represent the experimental conditions because, in reality, a boundary layer has already started forming at that location. Govindan et al. (1991) reported that in order to match the experimentally observed thickness of the

boundary layer at entrance of the bend they had to start their calculations 8.5 diameters upstream with a very thin boundary layer. No such effort is made in the present study but, as the subsequently presented results indicate, the effect of this inaccurate inlet condition is small and limited to the first one-third of the bend only. The exit boundary is located 7 hydraulic diameters downstream of the bend. The boundary conditions are applied as discussed in the previous section.

The contours of streamwise velocity component computed by the two methods are compared with experimental data at several axial locations, inside the bend and in the upstream and downstream tangents, in figure 11. The effect of the inlet conditions in the flow development can be seen primarily at $x = -0.25d_h$ and $\theta = 30^o$, where the computed velocities in the region near the bend centerline are lower than the measured ones. This trend--which implies that the core flow has not accelerated as much as the experimental data indicate--can be attributed to the specification of a plug flow profile at the inlet of the computational domain, as previously discussed. At subsequent axial locations, the distortion of the measured isovels indicates the development of a strong secondary motion which increases the velocity near the outer wall and decreases it near the inner wall. Method II appears to capture, with reasonable accuracy, the major features of the flow field. The isovels computed by Method I, on the other hand, are not distorted to the extent indicated by the experimental data, a trend which implies that the strength of the secondary motion is not correctly predicted (see, for example, the calculated 0.6 isovel in figure 11c which intersects the centerplane at the same point as the measured 0.4 isovel).

In order to assess the results of the calculations in more detail, the computed streamwise velocity profiles are compared with the experimental data at $\theta = 30^o$, 60°, 77.5^o and $x = 0.25d_h$ and $2.5\ d_h$, in figure 12. For every axial location the velocity profiles are plotted along the z-direction (from the bottom wall to the symmetry plane) at five radial locations. Both methods yield satisfactory results at $\theta = 30^o$ and 60°. At the next two downstream locations, however, significant differences appear between the two numerical solutions. More specifically, Method II agrees very well with the experimental data except, perhaps, near the inner wall at $0.25d_h$ where the velocity is underpredicted. Method I, however, significantly underpredicts the velocity near the inner wall at $\theta = 77.5^o$ and at $x = 0.25d_h$; note that this trend was also present in the fully-developed entry flow case at approximately the same locations. Figure 13 compares the computed radial velocity profiles with the experimental data. It is seen that the two numerical solutions are in much closer agreement in this case. Differences, however, do exist at the same locations where the disagreements in the axial velocity component also occur. For instance, Method I underpredicts the crossflow near the inner wall at $\theta = 77.5^o$ while it overpredicts it at $0.25d_h$. Also Method I fails to capture the experimentally observed structure of the radial velocity profiles (see profiles at $r^* = 0.7$ for $\theta = 77.5^o$ and for $0.25d_h$). It would appear, therefore, that the observed differences

49

in the predicted strength of the secondary motion, no matter how small they may be, are responsible for the significant differences in the distribution, within a cross-section, of the streamwise momentum.

VIII.3 Turbulent flow in a 90° rectangular bend with developing entry flow

These calculations correspond to the recent experiment of Kim (1992), who carried out detailed mean flow and turbulence measurements--as well as numerical calculations using Method I-- through a 90° rectangular duct, of aspect ratio 6, at Reynolds number Re = 224,000 (based on the duct width and the mean bulk velocity). An overall view of the wind tunnel and duct geometry, as well as the sections at which measurements were reported (U1, U2, 15, 45, 75, D1 and D2), are shown in figure 14. As can be seen in this figure, the flow enters the inlet tangent of the curved duct through a short transition duct (a two-dimensional 6:1 contraction). The transverse pressure gradients on the top wall of the contraction induce a pair of vortices inside the top-wall boundary layer resulting in three-dimensional flow at the inlet of the upstream straight tangent. Figure 15 shows the measured mean velocity, turbulent kinetic energy and transverse Reynolds stress fields at station U1. The apparent complexity of the inlet flow requires a careful specification of inlet conditions for the numerical calculations in order to properly represent the experimental situation. For that reason, following Kim (1992), the experimental data at station U1 are used to construct appropriate inlet distributions for the mean velocity components and the turbulent quantities.

The computational domain starts 4.5H upstream from the inlet of the bend (section U1) and extends up to 30H downstream from the exit of the bend. A numerical grid with 62x69x52 nodes, in the streamwise, radial and normal directions, respectively, is used for the subsequently reported calculations with both Methods I and II. The streamwise spacing inside the bend is 3°, while the first coordinate surface just off the duct walls is located well within the laminar sublayer, around $y^+ = 0.75$, almost everywhere. Method I requires approximately 2 hours of Cray-YMP CPU time to reduce the residuals by three orders of magnitude, while the same level of convergence is achieved in 75 minutes of CPU time by Method II.

Measured and computed profiles of the three mean velocity components at several sections through the bend and in the upstream and downstream tangents are shown in figure 16. Both numerical methods yield identical results at section 15, which are in good overall agreement with the experimental data. At the next downstream station (45) the two computed solutions are still in very close agreement with each other but discrepancies between experiment and calculations appear near the outer concave wall of the duct. As indicated by the computed velocity profiles, the predicted boundary layer is somewhat thicker than the measured one. This discrepancy should be attributed to the well known inability of k-ε based models to capture the effects of concave

50

curvature--that is increased levels of turbulent mixing which result in fuller velocity profiles near concave walls--rather than to numerical inaccuracies (Kim, 1992). The discrepancies between experiment and calculations in the prediction of the boundary layer thickness near the concave wall persist in the following downstream stations 75, D1 and D2 even after the removal of the curvature. The agreement between the two computed solutions is still quite close at sections 75 and D1 but additional discrepancies between experiment and calculations appear near the inner wall. More specifically, as indicated by the shape of the measured velocity profiles, a pressure-driven longitudinal vortex develops near the inner wall which transports low momentum fluid from the top wall boundary layer towards the inner side wall. As a result, the measured streamwise velocity profiles exhibit an S-shaped pattern as seen in sections 75 ($Z = 0.5$) and D1 ($Z = 0.5$ and 0.75). Both numerical methods fail to mimic the shape of the measured profiles, a trend which implies that the strength of the secondary motion is underpredicted. This can be seen by inspecting the measured and computed W-velocity profiles. Note, however, that at sections 75 and D1 Method II predicts peak values of the W-velocity (parallel to the vertical walls, see figure 14) component which are consistently higher--and consequently closer to the measurements--than those predicted by Method I. The same trend in the prediction of the secondary motion continues in the next downstream station D2 which is the last station at which measurements were taken. At station D2, the U-velocity profiles calculated by Method II exhibit a much more pronounced S-shaped structure than those calculated by Method I. Naturally, the differences in the computed streamwise velocity field are induced by the differences in the corresponding transverse velocity components, since Method II consistently predicts significantly higher peak values of the W-velocity profile. More specifically, at $Z = 0.5$ and 0.75, Method II overpredicts somewhat the measured W-component but good agreement between measurement and calculation is achieved at $Z = 1.00$. Method I, on the other hand, underpredicts the magnitude of the secondary motion by as much as 50 percent at $Z = 1.0$. It should be pointed out, however, that the shape and magnitude of the U and W velocity profiles at $Z = 0.5$ and 0.75 computed by Method II imply that the predicted longitudinal vortex is located at a lower position (nearer to the top wall) as compared to the measured one. In other words, Method II yields a better prediction for the strength of the secondary motion but fails to accurately capture its spatial evolution.

Figure 17 depicts the calculated, by both Methods I and II, and measured profiles of the turbulent kinetic energy at stations 45 and D1. Both methods predict very similar k-distributions which are, however, in gross disagreement with the measurements. Particularly near the concave wall, the calculations consistently underpredict the level of the turbulent kinetic energy by as much as 80 percent. As already discussed previously, these discrepancies underline the inherent inadequacy of the k-ε model to predict the high levels of production of k along concave walls.

Finally, figures 18 and 19 show, respectively, the computed and measured contours of streamwise velocity and vorticity at several locations. These figures demonstrate in a more global sense the trends discussed in the previous paragraphs as far as the discrepancies between experiments and calculations as well as those between the two numerical methods are concerned. The vorticity contours in particular (figure 19) reveal clearly the differences between the two numerical methods. Although both methods yield similar vorticity fields at stations 75 and D1, the vorticity computed by Method I appears to diffuse more rapidly in the next downstream station D2. Note, for instance, that Method II yields a core vorticity value of -0.9 which is more than twice the corresponding core value in the solution obtained by Method I.

VIII.4 Discussion

The calculations presented in the previous three sections reveal significant discrepancies between the steady-state solutions obtained by each numerical method, despite the fact that identical computational grids, solution domains and boundary conditions were employed. For the two laminar flow cases computed, it is seen that Method I tends to underpredict the magnitude of the streamwise velocity component near the inner (convex) wall for bend angles larger than 60° and that this trend does not seem to be affected by grid refinement. Method II, on the other hand, appears to capture correctly most of the flow features observed in the experimental data. The differences in the computed axial velocity field are accompanied, as one would anticipate, by qualitative and quantitative differences in the corresponding computed crossflow velocities. Method I, for instance, tends to underpredict the strength of the secondary motion inside the bend and overpredict it near the end of the bend and in the downstream tangent.

Similar trends, as far as the prediction of the secondary motion is concerned, are observed in the turbulent flow case as well since the longitudinal vortex computed by Method I diffuses more rapidly in the downstream straight tangent. However, it should be noted that, in contrast with the laminar flow cases, the discrepancies between the two computed solutions become pronounced only several duct widths downstream from the end of the bend. Unfortunately, it is not possible at this stage to separate the effect of the turbulence model from that of the numerical scheme. Certain deficiencies of the two-layer k-ε models--such as those associated with the prediction of turbulence along concave walls--have already been discussed. In addition, the present study (see also all subsequently reported calculations) confirms the results of Kim (1992) and W. J. Kim (1992) who employed the same turbulence model insofar as they indicate the inadequacy of isotropic model to accurately predict the origin, growth and decay of complex vortical flows. Therefore, it is concluded that the turbulence model is responsible for introducing a large amount of "false eddy viscosity" into the numerical solution, and this apparently overshadows the effect of any numerical dissipation and discretization errors associated with the

52

numerical methods. This conclusion by no means undermines the importance of an accurate numerical discretization. Rather, it emphasizes the fact that the numerics become crucially important (as our laminar-flow calculations clearly demonstrate) when the turbulence model has been sufficiently refined to accurately represent real flow phenomena.

The discrepancies between the two numerical solutions are certainly more dist rbing than those between the calculations and the experimental data--particularly for the laminar fl w cases where no turbulence model related uncertainties are present in the calculations. For a given mesh size (and the same turbulence model, for a turbulent flow case) one would, in general, anticipate differences between solutions computed by two numerical methods, mainly due to differences in the order of the truncation error inherent in the numerical discretization of continuous differential operators. Any such differences, however, should decrease with increasing grid resolution and eventually approach zero in the continuum limit, provided that each discretization scheme is consistent (Peyret and Taylor, 1983). Note that recent calculations carried out with very different numerical methods for both the laminar fully-developed entry flow case (Rogers et al. (1991) with an artificial compressibility method and a non-staggered grid; Rosenfeld et al. (1991) with a fractional-step method and staggered mesh), and the laminar developing entry flow case (Williams, 1991), have yielded results which are in close agreement with those of Method II. The cause for the discrepancies between the present numerical Methods I and II could be attributed to the different approaches each method adopts to formulate and discretize the flow equations--such as the type of the coordinate transformation, the accuracy in the satisfaction of the discrete continuity equation, and the resolution of the spatial discretization scheme. These factors are considered below.

Generalized coordinate transformation approach: Method I utilizes the full- transformation approach with the physical contravariant components as independent variables as opposed to the partial-transformation approach used by Method II. As already discussed, the full transformation approach introduces additional terms in the governing equations to account for the spatial variation of the coordinate base vectors (Cristoffel symbols) and imposes, consequently, additional smoothness requirements on the computational grid. As a result, Method I is expected to be more sensitive to grid discontinuities which, if large, could deteriorate the accuracy of the computed solution. It should be recalled, however, that in all the herein reported calculations: i) the configurations under consideration are geometrically very simple, and ii) particular care has been exercised to construct smooth numerical grids by keeping the grid stretching ratio less than 1.3 everywhere. Moreover, the full-transformation approach was also adopted by Rosenfeld et al. (1991), in conjunction with a finite-difference, non-staggered grid, fractional-step method, but, as mentioned above, their results (for the fully-developed entry flow case) are in very good agreement with those of Method II. Therefore, the full- transformation approach, although it may have some

53

impact on the accuracy of Method I, would not appear to be the major cause for the observed differences between the two methods.

Satisfaction of the discrete continuity equation: As shown in section V, both methods satisfy the discrete continuity equation up to dissipative terms which are proportional to fourth order derivatives of the pressure. There are two major differences between the two methods: i) the dissipative term in Method I is nonlinear in the geometrical quantities as well as the velocity field, while in Method II the corresponding term is nonlinear only in the geometrical quantities; and ii) the coefficient of the dissipative term in Method I (see equations (116) and (117)) is, for sufficiently high Reynolds number, of the order of one, while the corresponding coefficient used in Method II is a user specified constant, typically set equal to 0.01. These differences in the accuracy with which each method satisfies the discrete continuity equation suggest that, for a given mesh size, differences in the overall accuracy of the computed solutions are to be expected. Sotiropoulos (1991) showed that, while this is in general true, accuracy differences between solutions computed with different values of the γ_{II} coefficient in equation (108) decrease with grid refinement. This is also to be expected since the error in the discrete continuity equation for both methods is proportional to the grid spacing. In the present calculations, however, a 34 percent increase in the number of grid nodes (grid B for the first laminar flow case computed) did not have any significant effect on the solution computed by Method I and certainly did not appear to minimize the differences between the two methods.

Spatial discretization scheme: Method I utilizes a hybrid finite-analytic discretization scheme, while Method II uses an upwind finite-difference scheme which is formally second order accurate provided the grid stretching ratios are kept close to unity everywhere. The accuracy of the hybrid finite-analytic scheme, on the other hand, can not be readily estimated--using standard techniques such as Taylor series expansion--due to the complexity of the finite-analytic discretization coefficients which involve hyperbolic functions and exponentials. Note, however, that the hybrid finite-analytic scheme employed here is a simplified (for reasons of computational efficiency) 9-point version of the more general--and consequently more accurate--28-point scheme. This 9-point scheme has worked quite well for three-dimensional flows where the streamwise direction is the dominant flow direction (Patel et al., 1988; Kim, 1991) but it may be inadequate for highly swirling flows such as those considered in the present work. In the laminar fully-developed entry flow case, for instance, there are regions of the flowfield where the radial velocity component is as high as 50-60 percent of the streamwise component. In a very recent work, Yeo et al. (1991) calculated the duct flow of Humphrey et al. (1977), the first case computed in the present study (section VIII.1), using three different finite-difference schemes for discretization of the convective terms, namely, the first-order upwind differencing, the second-order upwind differencing, and the QUICK scheme. Interestingly enough, a comparison of their first-order

upwind solutions with the present Method I (finite-analytic discretization) solutions reveals very similar trends in the region between the middle of the cross-section and the inner wall, although Method I is more accurate near the outer wall. The similarities and differences between the first-order upwind solution of Yeo et al. and the present Method I solution would suggest that the hybrid finite-analytic discretization switches to first-order upwinding near the inner wall while it maintains higher accuracy elsewhere. The switch to first-order upwind could be probably attributed to high values of the local cell Reynolds number caused by the very large secondary velocity components--recall that the finite-analytic method automatically becomes one sided for large cell Reynolds numbers. Another interesting point regarding the calculations of Yeo et al.-- which is not addressed at all by the authors--is the fact that, as the grid is refined, the second-order upwind and QUICK solutions tend to approach each other, as it should be the case for consistent finite-difference schemes, while the first-order upwind solution improves only near the outer wall and maintains essentially the same trends near the inner wall. Similarly, the grid refinement in the present calculations did not seem to bring Methods I and II closer to each other (see figure 6). An explanation for this rather odd and unexpected behavior may be found in the recent work of Brandt and Yaneh (1991). They proved, mathematically and computationally, that when the grid lines are not aligned with the streamlines, which is usually the case except for some very cases such as boundary-layer flows, the first-order upwind difference is inadequate regardless of the grid spacing. To be more precise, their analysis assumes that the grid spacing tends to zero but it always remains bounded from below by a certain relation which involves the Reynolds number (cell Reynolds number constraint) so that the upwind differencing is necessary for stability; for sufficiently small grid spacing no such problems arise since centered schemes can be employed without stability problems. The use of the first-order upwind scheme to discretize the convective terms introduces nonisotropic artificial viscous terms which, even when their coefficients tend to zero, may effect the solution significantly.

In summary, it appears that the discrepancies between the two numerical methods used here may be primarily attributed to the different discretization schemes that are employed. Improvements in the spatial resolution of Method I could be achieved by replacing the 9-point hybrid finite-analytic scheme with a more general one involving perhaps the corner points at the upstream and downstream faces of the solution element.

IX. SOME ADDITIONAL CALCULATIONS OF FLOW IN DUCTS OF SIMPLE CROSS-SECTIONS

In this section we report a series of laminar and turbulent flow calculations for flow in curved ducts of square and circular cross-sections. All calculations were performed with Method II. The following cases are computed:

i) laminar flow through a strongly curved 90° pipe bend, with fully-developed entry flow, measured by Bovendeerd et al. (1987);

ii) laminar flow through a strongly curved 90° pipe bend, with developing entry flow, measured by Enayet et al. (1983);

iii) turbulent flow through a mildly curved 180° pipe bend, with fully-developed entry flow, measured by Rowe (1970);

iv) turbulent flow through a strongly curved 180° pipe bend, with fully-developed entry flow, measured by Azzola and Humphrey (1984);

v) turbulent flow through a strongly curved 90° square bend, with fully-developed entry flow, measured by Humphrey et al. (1981); and

vi) turbulent flow through a strongly curved 180° square bend, with fully-developed entry flow, measured by Chang (1983).

IX.1 90° pipe bend of Bovendeerd et al. (1987)

The measurements of Bovendeerd et al. (1987) were carried out at Reynolds number, Re = 700 (based on the bulk velocity and the diameter D of the pipe) and Dean number, De = 286. The radius of curvature of the bend is 3D, and the length of the upstream tangent is 50D to ensure fully-developed flow at the entrance of the bend.

In the present study, the calculations start 5D upstream of the bend where a fully-developed velocity profile is specified. The exit boundary is located 7D downstream the end of the bend. The grid topology and the related nomenclature are depicted in figure 20. Note that the bend is symmetric with respect to the z-axis and since the inlet flow is also sym ic, only one-half of the bend needs to be computed. The curvilinear coordinates (ξ, η, ζ) are aligned with the centerline, the circumferential direction, and the tangential direction, respectively. This choice of coordinates facilitates the description of the pipe bend geometry at the expense of making all the points on the bend axis singular. In the transformed domain, the bend centerline is mapped into a plane (ABCD), as shown in figure 20. The boundary conditions at the exit (GLCB plane), the solid wall (FGKE plane) and the symmetry boundaries (AFGB and DEKC planes) are applied as described

for the previous square-bend calculations, while a simple averaging is used to obtain all dependent variables on the singular plane ABCD. Note that the grid topology depicted in figure 20 is used through out in all calculations with pipe bends. The results for this case are obtained with 69x33x31 grid nodes in the axial, circumferential and radial directions; finer grid calculations yielded solutions almost identical with this grid. Typical views of the algebraically generated grid are shown in figure 21.

The computed contours of the streamwise velocity component are compared with the experimental data, at several planes inside the bend, in figure 22. It is seen that the calculations reproduce with remarkable accuracy the development of the streamwise flow as it passes through the bend. In figure 23, the computed streamwise velocity profiles on the symmetry plane are compared with the experimental data at several streamwise locations. Again, excellent agreement is observed between calculation and experiment.

IX.2 90° pipe bend of Enayet et al. (1983)

Enayet et al. (1983) carried out measurements at Re = 1096 and De = 693. The radius of curvature of their bend was 2.8D and the length of the upstream tangent was only 5D so that the flow at the entrance of the bend was still developing.

The calculations start 5D upstream of the entrance to the bend with a uniform inlet velocity distribution. The exit boundary is located 7D downstream of the exit from the bend. Grid refinement studies showed that a grid with 89x43x41 points in the streamwise, circumferential and radial directions, respectively, is necessary to obtain grid independent solutions. Note that, for the pipe bend of Bovendeerd et al., a much coarser grid (69x33x31) yielded a grid independent solution. This is attributed to the fact that, in the present case, the boundary layer entering the bend is much thinner--as compared to the fully- developed profile in the previous case--and consequently, finer grids are required to accurately resolve the steep velocity gradients in the near-wall region.

The calculated contours of streamwise velocity are compared with the experimental data at four streamwise locations in figure 24. At the θ = 30°, 60° and 75° cross-sections, the calculations reproduce quite well the overall features of the flowfield. Some discrepancies observed between experiment and calculations, primarily in the high velocity region, are probably caused by the specification of the plug-flow inlet profile at a location where the boundary layer in the experiment has already started to develop. As the secondary motion takes over the dynamics of the flow development inside the bend, however, the effect of the inlet flow profile is significantly reduced. This can be seen from the results at the last downstream station where the calculations reproduce the experimental data with remarkable accuracy.

IX.3 180° pipe bend of Rowe (1970)

Rowe (1970) carried out measurements in turbulent flow, at Re= 236,000 and De = 68,127, in a 180° mildly-curved pipe bend, with radius of curvature of 12D. The upstream tangent was 69D long and sufficiently rough to ensure that the pipe inlet had an axisymmetric and fully-developed turbulent velocity profile.

A grid with 96x33x41 points in the axial, circumferential and radial directions, respectively, is used for the present calculations. Grid dependence studies with coarser grids indicate that this grid is sufficient for grid independent solutions. The first ζ = constant coordinate surface of the solid wall is located at $y^+ = 1$ almost everywhere. To obtain the necessary inlet conditions, the flow through a very long straight pipe is calculated and the resulting fully-developed profiles of velocity and turbulence parameters are specified one pipe diameter upstream of the entrance to the bend.

Figure 25 depicts the computed and measured contours of the velocity head, $\frac{1}{2}\rho U^2$, at several cross-sections within the bend--the velocity head is nondimensionalized with $\frac{1}{2}\rho U_0^2$, where U_0 is the centerline velocity at the inlet. At the $\theta = 0°$ plane, the measured velocity contours--which should correspond to fully developed turbulent pipe flow--imply smaller than the calculated velocities in the core region. This discrepancy indicates that the flow in the experiment was still developing at the entrance of the bend (such a conclusion is also supported by the calculations presented in the next section, where a straight pipe calculation is also carried out, although at a lower Reynolds number, and the computed fully-developed axisymmetric velocity profile is in very good agreement with the measurements). The inlet velocity profile affects the predicted streamwise flow development inside the bend, since the velocities in the core are consistently higher than the measurements. Overall, however, the calculations predict fairly well the shifting of the maximum of the velocity towards the outer radii and the accumulation of low speed fluid near the inner radii. But the latter process is not as pronounced in the calculations, as the experimental data indicates, since higher velocities are predicted near the inner radii. Although no crossflow measurements were reported by Rowe, we can speculate that this trend is due to an underestimation of the strength of the secondary motion which is responsible for the distribution of the streamwise momentum within the cross-section.

IX.4 180° pipe bend of Azzola and Humphrey (1984)

Azzola and Humphrey measured the flow through a 180° strongly curved pipe bend (R_c = 3.375D) at two Reynolds numbers, Re = 57,400 and 110,000, corresponding to De = 31,300 and 59,900. The entrance length of their bend was 54.7D to ensure axisymmetric fully-developed flow at the inlet to the bend.

Calculations are carried out only for the low Reynolds number case. The computational grid comprises 154x41x23 nodes in the streamwise, radial and circum-ferential directions, respectively. The first ζ = constant coordinate surface just off the pipe wall is located at $y^+ = 0.6$ almost everywhere. The inlet profiles, for the velocity and turbulent quantities, are obtained by solving the developing flow through a long straight pipe. The calculations start two diameters upstream of the entrance to the bend and continued until eight diameters downstream.

The computed profiles of the longitudinal (u_θ) and circumferential (u_ϕ) velocity components are compared with the measurements at several streamwise locations in figure 26 (the profiles are plotted from the symmetry plane to the wall along the radius located 90° from the symmetry plane). The calculations capture well the development of the longitudinal velocity component inside the bend and in the downstream tangent--some differences exist only at $\theta = 90°$ where the measurements indicate a larger dip in the velocity profile near the symmetry plane. This is not the case, however, with the profiles of the circumferential velocity component. The calculations underpredict the secondary motion in the first quarter of the bend with the maximum discrepancy occurring at 45° in the near-wall region. Further downstream, the measurements indicate a reversal of the secondary motion near the symmetry plane at approximately 90°. This process is predicted qualitatively by the calculations, but it is weaker and somewhat delayed since it occurs after 90°. Moreover, the calculations indicate two more crossflow reversals occurring at 177° and at one diameter downstream of the end of the bend. The measured crossflow, on the other hand, exhibits a trend to reverse direction, decreases between 135° and 177° and increases between 177° and one diameter downstream the bend, but remains always positive near the symmetry plane. The two additional crossflow reversals near the symmetry plane were also predicted (at the same locations as the present calculations) by Azzola et al. (1986), who calculated the same bend on a mesh of similar size using the standard k-ε model.

The effect of the crossflow on the streamwise flow development can be seen in figures 27, where the calculated contours of streamwise velocity component and the cross-flow velocity vectors are plotted at several longitudinal locations inside the bend and in the downstream tangent. At 90° and 135°, for instance, the strong secondary motion has displaced the maximum of the velocity in the interior of the cross-section, while the effect of the crossflow reversal near the symmetry plane is clearly visible at 177° and x=+1 (see, for example, the change in the shape of the U = 1.0 isovel between these two locations).

IX.5 90° square bend of Humphrey et al. (1981)

Humphrey et al. (1981) carried out turbulent flow measurements in a square bend geometrically identical to that used by Humphrey et al. (1977) and Taylor et al. (1982). Their measurements were made at Re = 40,000, corresponding to De = 26,000. The length of the entry

tangent was 45 hydraulic diameters so that fully-developed flow was expected at the entrance of the bend.

This experiment of Humphrey et al. (198[1]) was one of the test cases selected for the 1980-81 Stanford Conference on Complex Turbulent Flows (Case 0512) (Kline et al., 1981) and for which numerical solutions were submitted by six computor groups. The turbulence models used for the calculations by the various computors included: i) an algebraic eddy-viscosity model (one computor); ii) the standard k-ε model with wall functions (three computors); iii) a k-l model with wall functions (one computor); and iv) an algebraic Reynolds-stress model (one computor). These calculations were started 7.5 hydraulic diameters upstream of the entrance of the bend where the experimental data of Melling and Whitelaw were used to obtain inlet profiles for the flow variables. A sample of the calculations is shown in figure 28 (taken from Vol. II, pp. 942-943, of the Conference Proceedings). Figure 28a shows general agreement on the streamwise velocity component at the inlet plane but significant disagreement at the exit. On the other hand, the predictions of the radial velocity component (Figure 28b) are, with one exception, reasonable at both the inlet and exit planes. Overall, however, none of the six computers produced results that could be characterized as satisfactory. Note that in assessing the performance of the numerical methods applied to incompressible duct flows in the Stanford Conference, J. B. Jones concluded that (Vol. II, pp. 914-918): "among all the cases involving secondary flow of the second kind, Case 0512 has produced the least satisfactory results."

The present calculations are carried out on a 54x49x26 mesh which is found to be adequate for grid independent solutions. The inlet conditions are obtained by performing a developing flow calculation through a long, straight, square duct. The fully-developed solution is then used to set the inlet profiles of the velocity components and the turbulent quantities, 2.5 hydraulic diameters upstream of the inlet of the bend; the experimental data of Humphrey et al. (1983) indicate that the flow at that location corresponds to fully-developed square duct flow with no influence of the downstream bend. The calculated fully-developed mean velocity profile is compared with the measurements of Humphrey et al. (at x=-2.5 d$_h$) in figure 29. The calculated isovels do not mimic the shape of the measured ones which appear to be bulging towards the corners of the cross-section. Recall, however, that the distortion of the measured isovels is caused by the existence of secondary motion of the second kind which is induced by the anisotropy of the Reynolds stresses. The inability of the calculations to reproduce this behavior is due to the isotropic eddy-viscosity model employed in the present calculations. The present model implies equal normal Reynolds stresses and, therefore, cannot predict the stress-driven secondary motion.

The computed and measured contours of streamwise mean-velocity component, at several cross-sections within the bend, are shown in figure 30. At the inlet of the bend, the calculations indicate that the high speed core of the flow shifts towards the inner wall. This trend is broadly

consistent with the data but the measured velocities in the high speed core are higher than the calculated and also the velocity maximum stays closer to the centerline of the bend. Moreover, as indicated by the shape of the measured isovels near the corners, the effect of the stress-driven secondary motion is still present in the measurements at that location. At the $\theta = 45^{\circ}$ cross-section, the calculations imply that the high speed core continues to move towards the inner wall while in the measurements this trend has been reversed, since the velocity maximum appears to be shifting towards the centerline. At the two subsequent cross-sections the calculations predict in general, although not to the extent indicated by the data, the accumulation of low speed fluid near the inner wall and the shifting of the high speed core towards the outer wall. But the predicted velocities in the high speed core are significantly lower than the measured. Finally, the predicted and measured contours of radial velocity component at $\theta = 90^{\circ}$ are shown in figure 31. The computed radial velocity contours are in good agreement with the measurements except near the endwall of the duct, where the calculations predict somewhat higher crossflow velocities.

The reason for the significant disagreement between the calculations and measurements is not altogether clear although, as noted earlier in the case of the rectangular duct flow (section VIII.3), the turbulence model must be suspected. To some extent, and particularly near the inlet of the bend, the disagreement can be attributed to the simple inlet conditions used in the present calculations. The flow through the bend undergoes very rapid changes over a short distance (the bend under consideration is strongly curved) and, thus, one would anticipate the inlet conditions to be of major importance. Recall, however, that all the calculations for the 1980 Stanford Conference started with the measured inlet flow conditions. As a result (see figure 28a) almost all the predictions were quite satisfactory at $\theta = 0^{\circ}$ but major disagreements were observed at $\theta = 90^{\circ}$. Interestingly enough, at the exit of the bend, most of the Stanford Conference calculations exhibit the same general features as the present results. For instance, most of the methods predicted reasonably well the radial velocity component, but did not predict as high streamwise mean velocities in the core as indicated by the experimental data (only one method predicted velocities of the correct magnitude but then the predicted high speed core was displaced close to the outer wall). The common factor between the present numerical method and most of the methods used in the 1980 Stanford Conference is the use of the isotropic k-ε model. We should point out, of course, that in the present method the calculations are carried out all the way to the wall, while all the Stanford Conference methods employed the wall-function approach to bridge the gap between the logarithmic layer and the wall. For the flow under consideration, high levels of turbulence anisotropy are present throughout the bend. Near the inlet of the bend, for instance, the stress-driven secondary motion, generated in the straight entry tangent, affects the dynamics of the flow development but only locally, since it is been quickly taken over by the pressure-driven secondary motion. On the other hand, near the exit of the bend, Humphrey et al. (1983) reported high levels

of turbulence anisotropy, caused by the redistribution of the Reynolds stresses by the secondary motion, as well as regions of negative turbulent kinetic energy production near the inner convex wall. These phenomena cannot be accounted for by an isotropic eddy viscosity model and, therefore, the failure to accurately simulate this flow must be attributed largely to the turbulence model.

IX.6 180° square bend of Chang (1983)

This test case corresponds to the measurements of Chang (1983) who carried out detailed mean and turbulent flow measurements through a strongly-curved 180° square bend and its downstream tangent at Re = 56,700 and De = 21,900. An inlet tangent of 31 hydraulic diameters long was used in order to ensure nearly fully-developed flow at the entrance to the bend.

The calculations are carried out on a numerical grid with 119x41x22 nodes in the streamwise, radial and normal directions, respectively. The streamwise spacing inside the bend is 2° while the first coordinate surface just off the duct walls is located at $y^+ = 2$ almost everywhere. The computational domain starts 5 hydraulic diameters upstream of the inlet to the bend and extends 7 diameters downstream of the end of the bend. The inlet distributions of the mean velocity and turbulence quantities are specified from a straight duct calculation as in the previous test case.

The calculated velocity profiles at several streamwise locations are compared with the measurements in figure 32. The discrepancies between experiment and calculations observed at the upstream station -1d_h are due to the inaccuracies in the inlet conditions caused by the inability of the turbulence model to predict the stress-driven secondary motion. At the next downstream station, $\theta = 3°$, the calculations are in good overall agreement with the measurements, although discrepancies associated with the prediction of the boundary layer thickness on the concave wall, the reasons for which have already been discussed, can be clearly seen, particularly near the bottom wall of the duct (see profiles at D and E). Further downstream, however, large discrepancies between experiment and computations, similar to those encountered in previous turbulent flow calculations, appear in the region between the duct centerline and the inner wall. More specifically, at $\theta = 90°$ the pressure-driven secondary motion transports fluid from the boundary layer of the convex wall towards the duct centerplane, resulting in the big "holes" in the streamwise velocity observed in the A, B and C profiles. The calculations fail completely to reproduce this feature of the flow field, a trend which, once more, indicates that the strength of the secondary motion is grossly underpredicted. Similar discrepancies between experiment and calculations, although not as severe due, perhaps, to the reduction of the strength of the secondary motion, persist at the next station, $\theta = 130°$.

In a recent study, Choi et al. (1989) have calculated the same bend geometry using a anisotropic, algebraic Reynolds-stress closure and a computational grid of similar size as the one used in the present calculations. Their calculations were certainly more successful than the present ones in predicting at least qualitatively the shapes of the streamwise velocity profiles, although significant quantitative differences remained between the experiment and their computation. They also reported a multi-cellular structure of the calculated secondary motion at the $\theta = 130^o$ station with the main vortex breaking down into three smaller vortices. No definite conclusion can be drawn, however, about how successful their calculations were as far as the prediction of the secondary motion is concerned since no detailed comparisons with the data were reported.

X. FLOW IN STRAIGHT AND CURVED TRANSITION DUCTS

In this section we report a series of laminar and turbulent flow calculations with typical transition duct configurations. Two test cases are studied: i) turbulent flow through a straight circular-to-rectangular transition duct for which detailed turbulent flow measurements have been recently reported by Davis and Gessner (1992), and ii) laminar and turbulent flow through a typical hydroturbine draft tube. The draft tube is a strongly curved diffuser whose cross-sectional shape also changes from circular at the inlet to rectangular at the exit. No measurements are available for the latter geometry. Although some measurements in a similar geometry have been reported, it has not been possible to acquire the necessary geometrical details to carry out a meaningful calculation.

X.1 Turbulent flow in a straight circular-to-rectangular transition duct

The measurements of Davis and Gessner (1992) were carried out at a Reynolds number, $Re = 3.9 \times 10^5$, based on the bulk velocity and the inlet diameter. The circular-to-rectangular (CR) duct configuration chosen for their experiment has an exit aspect ratio of 3.0 and a transition length of 1.5 inlet diameters over which changes in the cross-sectional shape occur. At each streamwise location, the cross-sectional shape is defined by the equation of a super-ellipse. Details about the precise geometry definition can be found in Davis (1992). The geometry of the CR duct along with the stations where measurements were carried out are shown in figure 33.

The computational domain extends from station 1 to station 6 and a grid topology similar to that used for pipe bend calculations is employed. The numerical grid, generated algebraically using the EAGLE grid generation code (Thompson, 1987), consists of 46x51x27 grid nodes in the axial, radial and tangential directions, respectively. The grid lines are concentrated near the duct wall using hyperbolic tangent stretching functions. The first coordinate surface just off the solid wall is located, almost everywhere, at $y^+ = 0.5$ with 8 to 10 points within the sublayer and the buffer layer. Typical cross-sectional views of the numerical mesh, as well as a view of the mesh on the

63

duct wall, are given in figure 34. Due to the symmetry of the duct and symmetric inlet-flow conditions, only one quadrant of the duct is simulated.

Inlet conditions are specified at station 1 using the very detailed data of Davis and Gessner (1992); they reported mean velocity measurements up to the edge of the sublayer and turbulence measurements up to $y^+ = 200$. Detailed discussion of the flow conditions at station 1 can be found in Davis (1992). Here it suffices to say that the inflow conditions correspond to developing pipe flow with a boundary layer thickness of approximately 14 percent of the inlet diameter and a friction velocity of 0.0406.

Computed and measured distributions of wall static pressure coefficient around the perimeter at stations 3 to 6 are shown in figure 35. In this figure, S is distance along the wall along the perimeter, and S_{ref} is one quarter of the duct perimeter at each station. The calculations are in fair agreement with the experiment since they reproduce all the measured trends. However, the calculated pressures are somewhat higher than the measured ones at stations 3 and 4 with this trend reversing at the exit of the duct (station 6). This indicates that the pressure gradients are not being accurately resolved.

The calculated contours of mean streamwise velocity are compared with the measurements at stations 3, 4, 5 and 6 in figure 36. At station 3, both the calculated and measured contours follow the general shape of the wall and are in good agreement with each other. At the next downstream station (station 4), the thickening of the measured boundary layer near the shorter wall indicates that a pressure-driven secondary motion (induced by the rapid geometrical changes) starts to develop. The calculations, although in fair agreement with the measurements, predict a significantly fuller boundary layer in the vicinity of the side wall. The distortion of the measured isovels at stations 5 and 6 is due to a secondary flow pattern which develops into a pair of vortices along the shorter sidewall. The calculations fail to reproduce the measured isovel shapes, a trend which, as in previously reported calculations with ducts of regular cross-section, indicates that the predicted secondary motion is much weaker than the measured one.

The extent to which the present calculations resolve the near-wall region is demonstrated in figure 37, where measured and computed velocity profiles are plotted in wall coordinates at stations 5 and 6 along the vertical (Y1-profiles) and horizontal (Y2-profiles) planes of symmetry at each station. The solid line in these figures corresponds to the sublayer and logarithmic portions of the usual law of the wall. It is seen that, for all profiles shown in figure 37, the calculations exhibit the correct asymptotic behavior in the sublayer. Moreover, the calculated profiles are in good agreement with the measurements along the vertical plane of symmetry (Y1-profiles) where the boundary layer is thin. Along the horizontal plane of symmetry, however, the calculations agree with the experiment only in the inner layer, up to about $y^+ = 1000$, but significant discrepancies

appear farther away from the wall. These discrepancies underscore the failure of the calculations to reproduce the region of low streamwise momentum within the developing vortical flow.

X.2 Laminar and turbulent flow in a typical hydroturbine draft tube

The draft tube is a strongly curved diffuser located right beneath the turbine in a hydropower plant. Its role is to deliver the exhaust water from the turbine to the tailwater basin at a reduced speed in order to recover part of the velocity head that is not recovered by the turbine. The velocity head recovered within the draft tube represents a significant portion of the total effective head of the turbine and, therefore, the design of the tube is of crucial importance for the overall efficiency of the hydropower plant. A typical draft tube consists of a short conical diffuser followed by a strongly curved 90° elbow of varying cross-section and then a rectangular diffuser section. Its cross-sectional shape changes continuously from circular, at the inlet, to elliptical within the elbow, and finally to rectangular at the exit. The flow that enters the draft tube--the wake of the turbine blades--is turbulent and three dimensional with high levels of swirl. The already complex inlet flow undergoes additional straining as it passes through the tube, induced by the rapid area changes and the very strong longitudinal curvature, resulting in an extremely complicated shear flow with very strong vortical motions, which are often accompanied by regions of streamwise flow reversal at off-design operating conditions.

Here we report laminar and turbulent flow calculations for a typical draft tube configuration. Our objective, herein, is twofold: i) to demonstrate the feasibility of carrying out turbulent flow calculations all the way to the wall for complex, three-dimensional geometries of practical interest, and ii) to identify areas upon which future research efforts should concentrate in order to improve the numerical and physical modelling of such flows. It is important to point out that recent attempts to numerically simulate the flow in a draft tube (Vu and Shyy (1990), Camarero et al. (1991)) have been restricted to the use of very coarse grids in conjunction with the wall-function approach for the treatment of the near-wall flow. As a result, and given the inherent complexity of the flow, the so obtained solutions have provided only limited information about the structure of the flowfield. The calculations to be subsequently reported, however, constitute the first attempt to model the details of the flow through a draft tube using fine numerical meshes.

X.2.1 Draft tube geometry and computational grid

The draft tube configuration, used for the present computations, is based on one of the draft tubes at the Norris Power Plant in Tennessee, which is designed to operate with 66,000 H.P. turbines. The geometry of the draft tube was made available by the Tennessee Valley Authority (Waldrop, 1991b). The neat lines of the tube along with its plan and elevation views are shown in figures 38 and 39. The area expansion ratio for this draft tube (ratio of the exit over the inlet cross-

sectional area) is approximately 4.5:1 while the radius of curvature of the elbow is 1.34 diameters of the inlet circular cross-section. The configuration shown in figures 38 and 39 has two piers, symmetrically placed about the centerline, supporting the downstream rectangular diffuser. For simplicity, particularly in grid generation, the piers are omitted in the present calculations but their effect is accounted for by appropriately scaling the dimensions of the cross-sections such that the longitudinal variation of the net flow area remains the same. The various cross-sections of the scaled draft tube, without the piers, are shown in figure 40.

A grid topology similar to that used for the pipe-bend calculations (see figure 20) is also adopted for the draft tube. The physical and transformed domains along with the associated coordinate systems are shown in figure 41. Note that, for the present applications--unlike all our previous pipe calculations--the inlet velocity profile is not in general symmetric and thus the entire tube geometry has to be considered. The transformation of the physical to the computational domain is achieved by introducing an artificial cut along the symmetry plane of the tube and mapping it into two planes (ABCD and HGFE in figure 41) where periodic conditions are applied. With reference to figure 41, the overall computational domain consists of the inlet (ABHG) and exit (DCFE) planes, the solid wall boundary (BCFG), the two periodic boundaries (ABCD and HGFE) and the tube centerline singular boundary (ADEH).

The computational grid for each cross-section is generated algebraically using the EAGLE grid generation code (Thompson, 1987). The grid lines are concentrated near the walls using the hyperbolic tangent stretching function. As in all previous calculations, particular care is exercised to keep the maximum stretching ratio near 1.3 everywhere. The cross-sectional grids are then stacked along the centerline of the tube to complete the three-dimensional grid. A view of the three-dimensional grid on the surface of the draft tube is shown in figure 42, while typical cross-sectional views are shown in figure 43.

X.2.2 Boundary conditions

With reference figure 41, the boundary conditions for the calculations are applied as follows:

Inlet: The distributions of the three velocity components, and the turbulence parameters (k, ε) in the case of turbulent flow, are specified at the inlet plane (ABGH). For the laminar flow calculations, a plug flow profile with zero swirl is specified for the velocity field. For the turbulent calculations, several velocity profiles with and without inlet swirl are considered (see subsequent sections). The pressure is computed from the interior nodes using linear extrapolation.

Periodic boundaries: The governing equations are solved on the periodic boundaries (planes ABCD and HGFE) in a similar fashion as for any interior node by appropriately introducing fictitious periodic lines.

Solid wall: No-slip, no-flux conditions for the velocity components, k = 0, and linear extrapolation for the pressure are employed.

Exit boundary: To facilitate the application of outflow boundary conditions the computational domain is extended by adding a straight tangent (3 to 4 inlet diameters long) at the end of the draft tube. At the end of this straight tangent, the velocity components and the turbulence quantities are computed by assuming zero streamwise diffusion while the pressure is computed using linear extrapolation. The downstream extension of the computational domain was found necessary in order to ensure that no reverse flow reaches the exit boundary, in which case the calculations become unstable and eventually fail to converge.

X.2.3 Laminar flow

The laminar flow calculations are carried out at Reynolds number Re = 1,000, based on the bulk velocity and the diameter of the circular inlet cross-section. A plug flow profile without swirl is specified at the inlet. Since the inlet profile is symmetric only half of the draft tube needs to be computed. Two numerical grids are used for the calculations in order to study the grid dependency of the computed solutions: i) a coarse grid with 43x47x51 (13 planes in the elbow) nodes, and ii) and a fine grid with 64x47x51 (31 planes in the elbow) nodes in the streamwise, tangential and radial directions, respectively. The minimum grid spacing, just off the solid wall, is 4×10^{-5} inlet diameters for both grids. Note that the near-wall resolution of the two grids is the same as that used for the subsequently reported turbulent flow calculations in order to test the robustness of the numerical method on highly stretched grids.

The solutions obtained with the coarse and fine grids are compared in figures 44 and 45. In figure 44, the streamwise velocity profiles at the end of the elbow (section XV in figure 38) are plotted along the horizontal and vertical cross-sectional axes of symmetry, while figure 45 depicts the contours of constant static pressure on the symmetry plane. The agreement between the coarse and fine grid solutions is good, since only relatively small discrepancies can be observed. All the subsequently reported results have been obtained on the fine grid.

The computed velocity vectors on the symmetry plane of the draft tube, along with a blow up of the downstream region, are shown in figure 46. The flow in the first half of the elbow exhibits all the typical features of a plug flow entering a strongly curved passage. More specifically, the flow is accelerated near the inner (top) side of the tube since it is driven by the, initially, favorable longitudinal pressure gradient. Along the outer side (bottom wall), on the other hand, the initially adverse longitudinal pressure gradient induces a small region of reversed flow. Further downstream, however, a strong secondary motion develops--driven by the transverse pressure gradients--which transports high momentum fluid towards the outer (bottom) wall of the elbow (see figure 48). As a result, the flow is accelerated along the outer wall while it is retarded

along the inner (top) wall. This process, in conjunction with the continuous increase of the cross-sectional area in the streamwise direction, leads to a large region of reversed flow at the top of the draft tube. This originates near the end of the elbow and extends all the way to the exit from the tube.

Figures 47 and 48 show the contours of streamwise velocity and the cross-flow vectors at sections IX, XV and XXXI (see figure 41). At section IX (located at $\theta = 45°$) a very strong secondary motion develops with two distinct swirls near the left and right side walls. The secondary motion tends to sweep the flow away from the vertical axis of symmetry and as a result the maxima of the streamwise velocity appear in the vicinity of the side walls. At the exit of the elbow (section XV) the magnitude of the secondary motion is significantly reduced and the two swirls shift towards the corner between the inner (top) and end walls. A region of reversed flow appears in the vicinity of the top wall which induces the acceleration of the flow observed near the outer wall. At the exit of the draft tube (section XXXI) the secondary motion--although very weak--sweeps the high speed fluid towards the two side walls while a large separated region is still present near the top wall.

X.2.4 Turbulent flow

A series of calculations was carried out at a typical model-scale Reynolds number, Re = 1.1×10^6 (based on the bulk velocity and the inlet diameter of the draft tube), in order to investigate the effect of the inlet velocity profile on the flow development through the draft tube. Two different inlet conditions were simulated: i) a fully-developed pipe-flow profile (obtained from a straight pipe computation), combined with a free-vortex with an axial-velocity defect (case FV), which approximates the real flow situation since it accounts for the wake-like outflow from the turbine runner; and ii) the fully-developed pipe-flow profile for the streamwise velocity combined with a solid-body rotation swirl . In both cases, the swirl velocity at the wall is reduced to zero using the inner leg of Johnston's (1960) triangular model relating the secondary and primary velocity components in a three-dimensional turbulent boundary layer. The swirl intensity S is defined, in the present study, as the ratio of the area average swirl velocity at the inlet divided by the bulk velocity (for solid body rotation this definition yields $S = 0.66V_m$, where V_m is the maximum swirl velocity). According to this definition, solid-body swirl intensities of S = 0, 0.33 and 0.66 (cases S1,S2,S3, respectively) were investigated in the present study. The inlet velocity profiles for all the cases computed are shown in figure 49. In the following sections we discuss the grid sensitivity of the computed solutions and compare the computed flow structures corresponding to different inlet velocity profiles and swirl intensities.

68

Grid dependence study

The grid dependence study was performed only for the case FV, since this corresponds to the real life flow situation through the draft tube. The calculations were carried out on two numerical grids, a coarse one with 45x94x51 nodes, and a fine one with 64x94x51 nodes in the streamwise, circumferential and radial directions, respectively. The streamwise spacing inside the elbow is 7.5° for grid A and 3.75° for grid B. For both grids, the first coordinate surface just off the solid wall is located everywhere such that $1 < y^+ < 4$, with at least 4 coordinate surfaces placed within the sublayer and the buffer layer. Approximately 4000 iterations are required for three orders of magnitude reduction of the velocity and pressure residuals, which, for the fine grid, take about 4.5 hours of CRAY-YMP CPU time.

The solutions computed on the coarse and fine grids are compared in figures 50 to 53. The piezometric pressure coefficient on the wall, around the perimeter at the end of the elbow (section XV), is plotted in figure 5ᴐ ι ι both grids. Here, S is the distance along the wall and S_{ref} is the total perimeter at that station. It is seen that both solutions exhibit similar trends, but the finer grid predicts higher overall pressures as well as a steeper pressure gradient along the inner wall of the bend (the midpoint of the inner wall is located at $S/S_{ref} = 0.5$). The contours of piezometric pressure in the plane symmetry of the draft tube are shown in figure 51. The general features of both solutions are very similar in the region between the inlet and the beginning of the elbow. Note, for instance, the sharp rise of pressure in the inlet conical diffuser as indicated by the closely spaced pressure contours--in fact most of the pressure recovery appears to take place in this inlet region. Further downstream, however, and towards the end of the elbow, the fine grid solution predicts steeper streamwise pressure gradients as well as higher pressures near the outer wall.

In figure 52 the streamwise velocity profiles, computed on both grids, are plotted along the horizontal and vertical axes of symmetry at the end of the elbow. Along the horizontal line of symmetry (figure 52a) both solutions are in close agreement, although the fine grid solution predicts somewhat lower velocities near the left endwall. Significant discrepancies between the two computed solutions appear, however, along the vertical axis of symmetry (figure 52b) and particularly in the vicinity of the inner wall where the coarse grid solution predicts a much thicker boundary layer as compared to the fine grid prediction. A more global picture of the computed solutions is given in figure 53, where the contours of constant streamwise velocity are plotted at the end of the elbow and the end of the draft tube (sections XV and XXXI). The general structure of the isovels appears to be the similar for both grids at both sections but a closer look reveals significant differences. At the end of the elbow (figure 53a), for instance, the closely spaced isovels near the inner wall, computed on the fine grid, indicate fuller velocity profiles in that region (compare, for example, the 0.5 and 0.6 isovels in both solutions). This trend implies that the fine

grid solution predicts a stronger secondary motion than the corresponding prediction on the coarse grid, and this tends to sweep the isovels closer to the inner wall, resulting in the fuller velocity profiles in that region. At the exit of the draft tube (figure 53b), the coarse grid solution predicts lower velocities in the center of the cross-section with regions of reversed flow both on the inner and outer walls. The fine grid solution, on the other hand, predicts only one small region of reversed flow near the inner wall.

Finally, figure 54 depicts the calculated velocity vectors on the plane of symmetry as well as a blow up of the downstream diffuser region. The two solutions exhibit similar overall features through the elbow and in the downstream diffuser. The coarse grid solution, however, predicts a much larger region of reversed flow near the inner wall of the downstream diffuser which is accompanied--for continuity to be satisfied--by higher velocities in the vicinity of the outer wall. This trend is consistent with the discrepancies between the two solutions already observed in the streamwise velocity contours and profiles. Also, the reduction of the separated flow region in the fine grid solution is consistent with the steeper streamwise pressure gradients, observed in the pressure contours computed on the fine grid (figure 51).

The above comparisons clearly indicate that, unlike the laminar flow calculations where the coarse and fine grid solutions were quite similar, the streamwise resolution of the coarse grid is not sufficient to capture the evolution of the streamwise and secondary flow through the elbow and in the downstream diffuser (recall that the coarse grid has only 13 planes within the elbow). The coarse grid solution, however, exhibits all the general features observed on the fine grid and can, thus, be used to predict quantitatively the flow field. For that reason and in order to save computer resources, all the subsequently reported calculations with different inflow conditions are carried out on the coarse grid. Note that the main objective of these calculations is to get an overall idea about the impact that the inflow conditions have on the flow development through the draft tube rather than to perform detailed comparisons with experimental data, which are not available at this time.

Effect of inflow conditions on the flow development

The velocity distributions in the symmetry plane of the draft tube computed with the four different inflow conditions are shown in figure 55. The figure also includes an enlargement of the exit region of the draft tube so that the effects of inflow conditions can be easily identified. For case S1 (no inlet swirl, figure 55a), the maximum of the velocity profile initially shifts towards the inner wall of the elbow (due to the initially favorable pressure gradient along this wall) but this trend is reversed half way through the elbow by the strong pressure-driven secondary motion. Note that this behavior is consistent with experimental data for curved ducts of regular cross-section. Towards the exit from the elbow, the strong adverse pressure gradient, induced by the continuous area increase, results in a large recirculation or reverse axial-flow zone covering the

70

area between the centerline and the inner wall, with reverse-flow velocities as high as 30 percent of the bulk velocity. The favorable effect of a solid-body swirl on the flow development can be seen in the subsequent figures 55b and 55c. For case S2, for instance, the extent of the recirculation zone in the downstream diffuser is significantly reduced and the maximum backflow velocities do not exceed 15 percent of the bulk velocity, while for case S3 the recirculation zone disappears entirely. For this latter case it is interesting to note that, starting half way through the elbow, the flow bifurcates towards the inner and outer walls and, as a result, the minimum of the velocity appears near the centerline of the draft tube. For the FV case, shown in figure 55d, a region of very low velocity appears near the centerline (due to a combination of the adverse pressure gradient and the wake-like inlet velocity profile) and the maximum of the velocity remains near the inner wall throughout the elbow. In the downstream diffuser, a small recirculation zone also appears near the inner wall but the velocity profiles between the centerline and the outer wall tend to be more uniform as compared to the corresponding profiles of cases S1 and S2.

The effect of the inflow conditions on the pressure field is depicted in figure 56, where contours of constant piezometric pressure are plotted in the symmetry plane for all four cases. The pressure in these figures has been referenced with respect to the pressure at the center of the inlet cross-section. For cases S1, S2 and S3 it is seen that the overall pressure rise between the inlet of the draft tube and the end of the elbow increases with increasing swirl intensities. In addition, for case S3, almost 50 percent of the overall pressure rise takes place within the inlet conical diffuser. For the FV case the pressure rises very rapidly in the inlet region and almost 70 percent of the overall pressure rise is achieved within the inlet conical diffuser.

The contours of streamwise velocity and the associated secondary flow vectors at stations IX, XV and XXXI are shown in figures 57 to 59 (the inner wall of the draft tube is at the top). It can be seen that the inlet swirl has a dramatic effect on the flowfield through the elbow and in the downstream diffuser. At station IX, the two curvature-induced swirls located near the inner (top) wall, symmetrically about the vertical centerplane in case S1 (figure 57a), transport high momentum fluid towards the outer (bottom) wall along the centerplane, and this results in the low velocity regions observed near the inner wall. The imposition of an inlet swirl which counteracts the pressure-driven secondary motion, however, tends to reverse this trend. In case S2, for instance (figure 57b), the maximum of the streamwise velocity has shifted near the inner wall while, for the S3 case (figure 57c), the maximum velocity also appears near the inner wall but a region of high velocity has appeared near the outer wall as well. This accumulation of high momentum fluid near the inner wall increases the resistance of the flow against the adverse pressure gradient and, thus, results in the reduction of the recirculation zone in the downstream diffuser as discussed above. A similar trend is also observed in case FV (figure 57d).

71

At the end of the elbow (figure 58), a large region of reversed flow appears near the inner wall in case the S1. As the swirl intensity increases, however, the separated flow region is significantly reduced and eventually eliminated for sufficient high swirl intensities (cases S3 and FV). For case S2, the maximum of the velocity is located in the vicinity of the inner wall to the right of the vertical axis of symmetry. For the S3 case, on the other hand, the bifurcation of the high speed flow towards the inner and outer walls, observed in figure 55c, persists in this station as well. In addition, a core of low speed fluid is seen to develop near the junction between the inner wall and the left endwall. For the FV case, the maximum of the velocity is also located near the inner wall and to the right but now a larger cross-sectional area near the right endwall is occupied by high speed fluid.

At the exit from the draft tube (figure 59), zero inlet swirl (figure 59a) results in a large region of reversed flow, near the inner wall, and in a secondary motion that sweeps the high speed flow towards the two end walls. For the S2 case, the separated flow region is significantly reduced and a single swirl appears near the right endwall. High velocity fluid is accumulated near both the left and the right endwalls but the maximum velocity occurs in the vicinity of the right endwall. Further increase of the swirl intensity (case S3) results in an accumulation of high speed fluid almost exclusively near the right endwall with a small region of reversed flow at the junction between the inner and left end walls. A flow pattern somewhat similar to that of case S2 is also observed at the exit of the tube in case FV (figure 59d). More specifically, high speed fluid is found in the vicinity of both endwalls with the maximum velocity near the right endwall. However, a region of low velocity, with two separation bubbles near the inner and outer walls, is found in the middle of the cross-section.

Finally, the near-wall resolution achieved by the present numerical method and turbulence model is demonstrated in figure 60, where velocity profiles are plotted in wall coordinates for cases S1, S2 and S3, and compared with the universal law of the wall. The profiles shown in these figures are plotted at two axial locations, at the exit from the elbow and the at the end of the draft tube, on the symmetry plane from the outer wall towards the centerline. At the exit from the elbow, all three velocity profiles collapse into a single curve and conform with the law of the wall up to $y^+ < 80$, approximately. This behavior is consistent with the conclusions of the recent experimental work of Davis and Gessner (1992). Their data indicate that at the end of the transition duct the measured velocity profiles exhibit logarithmic behavior for values of y^+ less than 80, but they fall below the logarithmic curve for greater values of y^+. At the end of the draft tube, however, the computed velocity profiles conform with the law of the wall only within the sublayer but none of them appears to exhibit a logarithmic region. More specifically, the velocity profile for S1 (no swirl) falls well below the logarithmic curve while increased swirl intensities tend to reverse that trend. This latter behavior is consistent with the strong adverse pressure gradient which the

flow experiences in the downstream diffuser. The behavior of the near-wall flow for case S1, on the other hand, can be attributed to the strong divergence of the flow away from the centerplane towards the left and right endwalls (a divergence induced by the pressure-driven secondary motion). As the inlet swirl intensity increases it counteracts the secondary motion and, as a result, the effects of the adverse pressure gradient dominate in the near-wall region. The velocity plots clearly show the location of the near-wall grid points and the resolution that is achieved in the sublayer.

XI. SUMMARY AND CONCLUSIONS

Two numerical methods were described and their results compared with each other in order to identify the relative merits and disadvantages of these methods when applied to calculate laminar and turbulent flows in curved ducts with varying cross-section. Method I employs the finite-analytic discretization for the convective and viscous terms and solves the fully-transformed governing equations in generalized curvilinear coordinates using the ADI method. Method II, on the other hand, is a finite-difference method which integrates in time the partially-transformed governing equations (with the cartesian velocity components retained as unknowns in generalized curvilinear coordinates) using the four-stage, explicit Runge-Kutta algorithm, enhanced with local time stepping and implicit residual smoothing. For turbulent flows, both methods employ the two-layer, two equation k-ε model of Chen and Patel (1988). The methods were applied--on the same numerical grid, with identical boundary conditions, starting from the same initial conditions, and using the same convergence criteria--to calculate laminar and turbulent flows through strongly curved ducts of regular cross-section. The computed solutions were compared with each other and with experimental data in order to assess the spatial resolution of each method.

Method II was subsequently applied to calculate laminar and turbulent flows in several curved ducts of square and circular cross-sections, as well as turbulent flow in a straight circular-to-rectangular transition duct, and a curved circular-to-rectangular transition duct, namely a hydroturbine draft tube. The objective of these calculations was twofold: i) to further validate the spatial resolution and numerical performance of Method II; and ii) to validate the ability of the two-layer turbulence model to predict the origin, growth and decay of pressure-driven vortical structures in complex, three-dimensional shear flows. To facilitate the validation process, a detailed literature survey was carried out in order to summarize all the experimental and computational work in the area of duct flows and identify, among the available experimental studies, those that are more appropriate for validating numerical methods and turbulence closures.

73

The study is concluded with application of Method II to simulate the flow through a typical hydroturbine draft tube. Unlike previous attempts to simulate such flows, the present method resolves the near-wall flow using fine computational meshes across the sublayer. Numerical solutions were obtained, at typical model-scale Reynolds numbers for various inlet swirl intensities and axial velocity profiles. for a draft-tube configuration based on the installation at the Norris Dam in Tennessee.

The following general conclusions are drawn from the present study:

i) An accurate simulation of complex, three-dimensional flows requires very careful discretization of the governing flow equations--particularly the convective terms--in order to ensure that numerical diffusion is kept to a minimum and real viscous-flow processes are not obscured. This was demonstrated in the comparison of the two numerical methods, since the finite-analytic method (Method I) appeared to consistently underpredict the strength of the secondary motion and consequently its impact on the streamwise flow development. This is attributed to the fact that the finite-analytic discretization automatically switches to a first-order accurate upwind discretization in regions of the flow where the cell Reynolds number exceeds a certain limiting value. The performance of Method I in highly three-dimensional flows considered here could be improved if the hybrid nine-point discretization formula employed in the present version of the method is replaced with a more accurate discretization involving additional points in the upstream and downstream sections of the finite-analytic element. This, however, would result in additional computational effort. Method II, which uses a second-order accurate upwind scheme, was shown to be sufficiently accurate to predict--at least for the laminar flow cases where no turbulence-model related uncertainties are present--the evolution of the streamwise and the secondary flow with remarkable accuracy.

ii) The present study indicates that isotropic eddy-viscosity based turbulence models are inadequate for resolving the origin, growth and decay of pressure-driven secondary motion in complex, three-dimensional shear flows, even when the most advanced, state-of-the-art near-wall models are used to resolve the flow all the way to the wall. In all the turbulent flow calculations performed herein, the two-layer k-ε model failed to predict the strength of the secondary motion as well as its effect on the streamwise flow development. These discrepancies cannot be attributed to numerical discretization errors since the calculations were carried out using Method II, the numerical performance of which was carefully established through a series of complex laminar-flow calculations. While it is well known that turbulence models of the type employed here cannot predict Reynolds-stress-driven secondary motion, the reasons for the failure of the two-layer model to capture the pressure-driven secondary motion are not entirely clear, particularly because it appears to resolve the important near-wall layers in even the most complex flow situations. One may only speculate that the observed discrepancies are due, at least in part, to the equally well

74

known deficiency of the k-ε model to account for the increased levels of turbulence production along concave walls. Whether it is this factor, or the general anisotropy of the Reynolds stresses, cannot be answered without further computations using turbulence models that claim greater generality. This is obviously a topic for further research. Extensions of Method II to incorporate models based on the individual Reynolds-stress transport equations are now under way.

iii) The computations with the draft tube geometry demonstrated, for the first time, the feasibility of carrying out turbulent flow calculations all the way to the wall for complex, three-dimensional configurations. The numerical method was shown to yield robust and efficient solutions on highly stretched, very fine computational grids--with as many as 310,000 grid nodes. The efficiency of the numerical method can be significantly improved, however, by implementing the multigrid acceleration technique which can reduce the overall CPU time required for convergence by a factor of four to five.

iv) The inlet swirl intensity and the axial velocity profile were found to have a dramatic effect on the flow development throughout the draft tube. The numerical results indicate that high swirl intensities tend to diminish the stalling characteristics of the flow through the elbow and to increase the overall pressure recovery. In addition, the comp˞r ˞olutions were shown to reproduce with remarkable accuracy the correct limiting behavior of the flow within the sublayer. While the present solutions are qualitatively similar to those reported by others for different draft-tube geometries, no specific conclusions can be drawn at this time insofar as the overall accuracy of the computed solutions is concerned since no experimental data is available to validate the numerical predictions. An experiment is under way at Voith Hydro Inc. to measure the flow in a scaled model of the Norris Dam draft tube, including the flow dividing piers in the downstream reach of the tube. The numerical method will be modified to handle such a geometry, and comparisons will be made between the calculations and data as they are gathered.

REFERENCES

Agouzoul, M., Regio, M. and Camarero, R. (1990), "Calculation of Turbulent Flows in a Hydraulic Turbine Draft Tube," J. Fluids Engineering, Vol. 112, pp. 257-263.

Agrawal, Y., Talbot, L. and Gong, K. (1978), "Laser Anemometer Study of Flow Development in Curved Circular Pipes," J. Fluid Mechanics, Vol. 85, pp. 497-518.

Ahmed, S. and Brundrett, E. (1971), "Turbulent Flow in Non-Circular Ducts. Mean Flow Properties in the Developing Region of a Square Duct," Int. J. Heat Transfer, Vol. 14, p. 365.

Aly, A. A. M., Trupp, A. C. and Gerrard, A. D. (1978), "Measurements and Prediction of Fully-Developed Turbulent Flow in an Equilateral Triangular Duct," J. Fluid Mechanics, Vol. 85, pp. 57-83.

Anderson, D. A., Tannehill, J. C. and Pletcher, R. H. (1984),"Computational Fluid Mechanics and Heat Transfer," McGraw Hill Book Company.

Anwer, M., So, R. M. and Lai, Y. G. (1989), "Perturbation by the Recovery from Bend Curvature of a Fully Developed Turbulent Pipe Flow," Phys. Fluids A, 1, 1387-1397.

Azzola, J. and Humphrey, J. A. C. (1984), "Developing Turbulent Flow in a 180 deg Curved Pipe and its Downstream Tangent," Report LBL-17681, Materials and Molecular Research Division, Lawrence Berkeley Laboratory, Uni. California, Berkeley, CA.

Azzola, J., Humphrey, J. A. C., Iacovides, H. and Launder, B. E. (1986), "Developing Turbulent Flow in a U-Bend of Circular Cross-Section: Measurements and Computation," J. Fluids Engineering, Vol. 108, pp. 214-226.

Birch, N. (1984), "The Calculation of 3D Flow in Curved Ducts Using Q385," Report TSG0161, Rolls-Royce Theoretical Science Group, Derby, U.K.

Bovendeerd, P. H. M., Steenhoven, A. A., Vosse, F. N. and Vossers, G. (1987), "Steady Entry Flow in a Curved Pipe," J. Fluid Mechanics, Vol. 177, pp. 233-246.

Bradshaw, P. (1987), "Turbulent Secondary Flows," Ann. Review of Fluid Mechanics, Vol. 19, pp. 53-74.

Brandt, A., and Yavneh, I. (1991), "Inadequacy of First-Order Upwind Difference Schemes for Some Recirculating Flows," J. Comp. Phys., Vol. 93, pp. 128-143.

Brundrett, E. and Baines, W. D. (1964), "The Production and Diffusion of Vorticity in Duct Flow," J. Fluid Mechanics, Vol. 19, pp. 375-394.

Buggeln, R. C., Briley, W. R. and McDonald, H. (1980), "Computation of Laminar and Turbulent Flow in Curved Ducts, Channels, and Pipes using Navier-Stokes Equations," Report R80-92C006-F.

Burley II, J. R. and Carlson, J. R. (1985), "Circular-to-Rectangular Transition Ducts for High-Aspect Ratio Nonaxisymmetric Nozzles," AIAA Paper 85-1346.

Bruun, H. H. (1979), "An Experimental Investigation of Secondary Flow Losses in Bends with Rectangular Cross Sections," CUED/A-Turbo/TR 97, Dept. of Engineering, Univ. of Cambridge, U.K.

Chandran, K. B. and Yearwood, T. L. (1981), "Experimental Study of Physiological Pulsatile Flow in a Curved Tube," J. Fluid Mechanics, Vol. 111, pp. 59-85.

Chandran, K. B., Yearwood, T. L. and Wieting, D. W. (1979), "An Experimental Study of Pulsatile Flow in a Curved Tube," J. Biomechanics, Vol. 12, pp. 793-805.

Chang, S. M. (1983), "Turbulent Flow in Passage around a 180° Bend; An Experimental and Numerical Study," Ph.D Thesis, Dept. of Mech. Eng., Univ. California, Berkeley, CA.

Chen, H. C. and Chen, C. J. (1984), "Finite Analytic Numerical Method for Unsteady Two-Dimensional Navier-Stokes Equations," J. Comp. Phy., Vol. 53, pp. 209-226.

Chen, H. C., and Patel, V. C. (1988), "Near-Wall Turbulence Models for Complex Flows Including Separation," AIAA Journal, Vol. 26, pp. 641-648.

Chen, H. C. and Patel, V. C. (1989), "The Flow Around Wing-Body Junctions," Proc. 4th Symp. Num. Phys. Aspects Aerodyn. Flows, T. Cebeci ed., Long Beach, CA.

Chen, H. C., Patel, V. C. and Ju, S. (1990), "Solutions of Reynolds-Averaged Navier-Stokes Equations for Three-Dimensional Incompressible Flows," J. Comp. Phy., Vol. 88, pp. 305-336.

Chima, R. V. and Yokota, J. W. (1990), "Numerical Analysis of Three-Dimensional Viscous Internal Flows," AIAA Journal, Vol. 28, pp. 798-806.

Choi, Y. D., Iacovides, H. and Launder, B. E. (1989), "Numerical Computation of Turbulent Flow in a Square-Sectioned 180 Deg Bend," J. Fluids Engineering, Vol. 111, pp. 59-68.

Davis, D. O. and Gessner, F. B. (1992), "Experimental Investigation of Turbulent Flow Through a Circular-to-Rectangular Transition Duct," AIAA Journal, Vol. 30, pp. 367-375.

Demuren, A. O. and Rodi, W. (1984), "Calculation of Turbulence-Driven Secondary Motion in Non-Circular Ducts," J. Fluid Mechanics, Vol. 140, pp. 189-222.

Demuren, A. O. and Rodi, W. (1987), "Three-Dimensional Calculation of Turbulent Duct Flow with Non-Uniform Inlet Conditions," Computers & Fluids, Vol. 15, pp. 47-57.

Demuren, A. O. (1991), "Calculation of Turbulence-Driven Secondary Motion in Ducts with Arbitrary Cross Section," AIAA Journal, Vol. 29, pp. 531-537.

Eichenberger, H. P. (1952), "Shear Flow in Bends," Tech. Report 2, Mass. Inst. Tech., MA.

Eichenberger, H. P. (1953), "Secondary Flow within a Bend," J. Math. & Phys., Vol. 32, p. 34.

Enayet, M. M., Gibson, M. M. and Yianneskis, M. (1982a), "Measurements of Turbulent Developing Flow in Moderately Curved Square Duct," Int. J. Heat & Fluid Flow, Vol. 3, pp. 221-224.

Enayet, M. M., Gibson, M. M. and Yianneskis, M. (1982b), "Laser Doppler Measurements for Laminar and Turbulent Flow in a Pipe Bend," Int. J. Heat & Fluid Flow, Vol. 3, pp. 213-220.

Gessner, F. B. (1964), "Turbulence and Mean-Flow Characteristics of Fully Developed Flow in Rectangular Channels," Ph.D Dissertation, Purdue University, IN.

Gessner, F. B. and Jones, J. B. (1965), "On Some Aspects of Fully Developed Turbulent Flow in Rectangular Channels," J. Fluid Mechanics, Vol. 23, pp. 689-713.

Gessner, F. B. (1973), "The Origin of Secondary Flow in Turbulent Flow along a Corner," J. Fluid Mechanics, Vol. 58, pp. 1-25.

Gessner, F. B., Po, J. K. and Emery, A. F. (1977), "Measurements of Developing Turbulent Flow in a Square Duct," Symposium on Turbulent Shear Flows, Penn. State University, University Park, Vol. 1.

Gessner, F. B. and Emery, A. F. (1981), "The Numerical Prediction of Developing Turbulent Flow in Rectangular Ducts," J. Fluids Engineering, Vol. 103, pp. 445-453.

Govindan, T. R., Briley, W. R. and McDonald, H. (1991), "General Three-Dimensional Viscous Primary/Secondary Flow Analysis," AIAA Journal, Vol. 29, pp. 361-370.

Hanjalic, K. and Launder, B. E. (1972), "A Reynolds Stress Model and its Application to Thin Shear Flows," J. Fluid Mechanics, Vol. 52, pp. 609-638.

Hoagland, L. C. (1960), "Fully Developed Turbulent Flow in Straight Rectangular Ducts," Ph.D Dissertation, Mass. Inst. Tech., MA.

Hollanders, H., Lerat, A. and Peyret, R. (1985), "Three-Dimensional Calculations of Transonic Viscous Flows by an Implicit Method," AIAA Journal, Vol. 23, p. 1670.

Humphrey, J. A. C., Taylor, A. M. K. and Whitelaw, J. H. (1977), "Laminar Flow in a Square Duct of Strong Curvature," J. Fluid Mechanics, Vol. 83, p. 509.

Humphrey, J. A. C., Whitelaw, J. H. and Yee, G. (1981), "Turbulent Flow in a Square Duct with Strong Curvature," J. Fluid Mechanics, Vol. 103, p. 443.

Iacovides, H. and Launder, B. E. (1984), "The Computation of Momentum and Heat Transport in Turbulent Flow around Pipe Bends," Proc. 1st UK National Heat Transfer Conference, Vol. 2, p. 1097, I. Chem. Engrs. Symposium Series 86.

Iacovides, H., Launder, B. E., Loizou, P. A. and Zhao, H. H. (1990), "Turbulent Boundary Layer Development around a Square-Sectioned U-Bend: Measurements and Computation," J. Fluids Engineering, Vol. 112, pp. 409-415.

Issa, R. I. (1985), "Solution of the Implicitly Discretized Fluid Flow Equations by Operator-Splitting," J. Comp. Physics, Vol. 62, pp. 40-65.

Jameson, A. (1981), "Numerical Solution of the Euler Equations by Finite Volume Methods Using Runge-Kutta Time-Stepping Schemes," AIAA Paper 81-1259.

Jameson, A. and Baker, T. J. (1983), "Solution of the Euler Equations for Complex Configurations," AIAA Paper 83-1929.

Johnson, R. W. (1984), "Turbulent Convecting Flow in a Square Duct with a 180° Bend," Ph.D Thesis, Faculty of Technology, Univ. Manchester, U.K.

Jonston, J. P. (1960), "On the Three-Dimensional Turbulent Boundary Layer Generated by Secondary Flow," J. Basic Eng., Vol. 82, pp. 233-248.

Joy, W. (1950), "Experimental Investigation of Shear Flow in Rectangular Bends," M.S. Thesis, Mass. Inst. Tech., MA.

Kim, S. E. (1991), "Numerical Studies of Three-Dimensional Flow separation," Ph.D Dissertation, Mech. Engineering, Uni. Iowa, IA.

Kim, W. J. (1991), "An Experimental and Computational Study of Longitudinal Vortices in Turbulent Boundary Layers," Ph.D Dissertation, Mech. Engineering, Uni. Iowa, IA.

Kline, S. J., Cantwell, B. J. and Lilley, G. M. (eds.) (1983), "Complex Turbulent Flows," Proc. 1980-81 AFOSR-HTTM-STANFORD Conferences, Vol. I-III.

Kunz, R. F. and Lakshminarayana, B. (1991), "Three-Dimensional Navier-Stokes Computation of Turbomachinery Flows Using an Explicit Numerical Procedure and a Coupled k–ε Turbulence Model," Int. Gas Turbine and Aeroengine Congress and Exposition, Orlando, Florida.

Lai, Y. G. (1990), "Near-Wall Modelling of Complex Turbulent Flows," Ph.D. Dissertation, Dept. of Aerospace Eng., Arizona State University, Arizona.

Launder, B. E. and Ying, W. M. (1972), "Secondary Flows in Ducts of Square Cross-Section," J. Fluid Mechanics, Vol. 54, p. 289.

Launder, B. E. and Ying, W. M. (1973), "Prediction of Flow and Heat Transfer in Ducts of Square Cross-Section," Proceedings of the Institute of Mechanical Engineers, Vol. 187, pp. 455-461.

Launder, B. E., Reece, G. J. and Rodi, W. (1975), "Progress in the Development of a Reynolds-Stress Closure," J. Fluid Mechanics, Vol. 68, p. 537.

Leutheusser, H. J. (1963), "Turbulent Flow in Rectangular Ducts," ASCE J. Hydraulics Division, Vol. 89, p. 1.

Liu, F. and Jameson (1992), "Multigrid Navier-Stokes Calculations for Three-Dimensional Cascades," AIAA Paper 92-0190.

Martinelli, L. (1987), "Calculations of Viscous Flows with a Multigrid Method," Ph.D Thesis, MAE Department, Princeton Uni., NJ.

Maslen, S. H. (1958), "Transverse Velocities in Fully-Developed Flows," Quart. Appl. Math., Vol. 16, p. 173.

Mayer, E. (1939) "Effect of Transition in Cross-Sectional Shape on the Development of the Velocity and Pressure Distribution of the Turbulent Flow in Pipes," NASA TM 903.

Melling, A. and Whitelaw, J. H. (1976), "Turbulent Flow in a Rectangular Duct," J. Fluid Mechanics, Vol. 78, pp. 289-315.

Merkle, C. H. and Tsai, Y., L. (1986), "Applications of Runge-Kutta Schemes to Incompressible Flows," AIAA Paper 86-0553.

Miau, J. J., Leu, T. S., Chou, J. H., Lin, S. A. and Lin, C. K. (1990) "Flow Distortion in a Circular-Rectangular Transition Duct," AIAA Journal, Vol. 28, pp. 1447-1456.

Moissis, R. (1957), "Secondary Flow in Rectangular Ducts, " M.S. Thesis, Mass. Inst. Tech., MA.

Nakayama, A., Chow, W. L. and Sharma, D. (1983), "Calculation of Fully Developed Turbulent Flows in Ducts with Arbitrary Cross-Section," J. Fluid Mechanics, Vol. 128, pp. 199-217.

Naot, D. and Rodi, W. (1982), "Numerical Simulation of Secondary Currents in a Channel Flow," ASCE J. Hydraulics Division, Vol. 108, pp. 948-968.

Nikuradse, J. (1926), "Untersuchungen uber die Geschwinddigkeitsvertverteilung in Turbulenten Stromungen," VDI-Forschungsheft, p. 281.

Patankar, S. V., Pratap, V. S. and Spalding, D. B. (1975), "Prediction of Turbulent Flow in Curved Pipes," J. Fluid Mechanics, Vol. 67, pp. 583-595.

Patel, V. C., Chen, H. C. and Ju, S. (1988), "Ship Stern and Wake Flows: Solutions of the Fully-Elliptic Reynolds-Averaged Navier-Stokes Equations and Comparisons with Experiments." Iowa Inst. Hydraulic Research, Uni. Iowa, IIHR Report No. 323.

Patrick, W. P. and McCormick, D. C. (1987), "Circular-to-Rectangular Transition Duct flows: A Benchmark Experimental Study," SAE Technical Paper 87-1776.

Patrick, W. P. and McCormick, D. C. (1988), "Laser Velocimeter and Total Pressure Measurements in Circular-to-Rectangular Transition Ducts, " Report No. 87-41, United Technology Research Center. East Hartford, CT.

Perkins, H. J. (1970), "The Formation of Streamwise Vorticity in Turbulent Flow." J. Fluid Mech., Vol. 44, pp. 721-724.

Peyret, R., and Taylor, D. (1983), "Computational Methods for Fluid Flow," Springer Series in Computational Physics, Springer-Verlag, New York.

Po, J. K. (1975), "Developing Turbulent Flow in the Entrance Region of a Square Duct, " M. S. Thesis, Mech. Engineering, Uni. Washington, WA.

Prandtl, L. (1926), "Uber die Ausgebildete Turbulenz," Verh. 2nd Int. Kong. Tech. Mech., Zurich, pp. 62-75. (Translation: NACA TM 435).

Radespiel, R., Rossow, C. and Swanson, R. C. (1989), "An Efficient Cell-Vertex Multigrid Scheme for the Three-Dimensional Navier-Stokes Equations," Proc. AIAA 9th Computational Fluid Dynamics Conference, Buffalo, NY, pp. 249-260.

Rapley, C. W. and Gosman, A. D. (1986), "The Prediction of Fully-Developed Axial Turbulent Flow in Rod Bundles," Nuclear Engineering and Design, Vol. 97, pp. 313-325.

Rindt, C. C., Steenhoven, A. A., Janssen, J. D. and Vossers, G. (1991), "Unsteady Entrance Flow in a 90 deg Curved Tube," J. Fluid Mechanics, Vol. 226, pp. 445-474.

Rodet, E. (1960), "Etude de l'Ecoulement d'um Fluide dans un Tunnel Prismatique de Section Trapezoidal," Publications Scientifiques et Techniques du Ministere de l's Air, Paris, No. 369.

Rogers, S. E., Kwak, D., and Kiris, C. (1991), "Steady and Unsteady Solutions of the Incompressible Navier-Stokes Equations," AIAA J., Vol. 29, pp. 603-610.

Rosenfeld, M., Kwak, D., and Vinokur, M. (1991), "A Fractional Step Method for the Unsteady Incompressible Navier-Stokes Equations in Generalized Coordinate Systems," J. Comp. Physics, Vol. 94, pp. 102-137.

Rowe, M. (1970), "Measurements and Computations of Flow in Pipe Bends," J. Fluid Mechanics, Vol. 43, pp. 771-783.

Seale, W. J. (1982), "Measurements and Predictions of Fully Developed Flow in a Simulated Rod Bundle," J. Fluid Mechanics, Vol. 123, pp. 399-423.

Sotiropoulos, F. (1991), "A Primitive Variable Method for the Solution of External and Internal Flow-Fields," Ph.D Dissertation, Aerospace Eng. and Eng. Mechanics, Uni. Cincinnati, OH.

Squire, H. B. (1954), "Note on Secondary Flow in a Curved Circular Pipe," Unpublished British Aero. Res. Council, Rep. No. 16601.

Strikwerda, J. C. (1984), "Finite Difference Methods for the Stokes and Navier-Stokes Equations," SIAM J. Sci. Stat. Comp., Vol. 5, No. 1, pp. 56-67.

Talbot, L. and Gong, K. O. (1983), "Pulsatile Entrance Flow in a Curved Pipe," J. Fluid Mechanics, Vol. 127, pp. 1-25.

Taylor, A. M. K. P., Whitelaw, J. H. and Yianneskis, M. (1981), "Turbulent Flow in a Square-to-Round Transition," NASA CR-3447.

Taylor, A. M. K. P., Whitelaw, J. H. and Yianneskis, M. (1982), "Curved Ducts with Strong Secondary Motion: Velocity Measurements of Developing Laminar and Turbulent Flow," J. Fluids Engineering, Vol. 104, pp. 350-359.

Thomas, D. L. and Easter, P. G. (1972), "Measurements of Wall Shear Stress in a Duct of Square Cross-Section," Central Electr. Gen. Board, C.E.G.B. Report RD/B/N2477, U.K.

Thompson, J. F. (1987), "A Composite Grid Generation Code for General 3-D Regions," AIAA Paper 87-0275.

Trupp, A. C. and Aly, A. A. M. (1979), "Predicted Secondary Flows in Triangular Array Rod Bundles," J. Fluids Engineering, Vol. 101, pp. 354-363.

Vu, T. C. and Shyy, W. (1990), "Viscous Flow Analysis as a Design Tool for Hydraulic Turbine Components," J. Fluids Engineering, Vol. 112, pp. 5-11.

Waldrop, W. R. (1991), private communication.

White, F. M. (1974), "Viscous Fluid Flow," Mac Graw Hill, New York.

Williams, R. W. (1991), "Computational Study of Duct and Pipe Flows Using the Method of Artificial Compressibility," AIAA Paper 91-1656.

Wolfstein, M. (1969), "The Velocity and Temperature Distribution in One-Dimensional Flow with Turbulence Augmentation and Pressure Gradient," Int. J. Heat & Mass Transfer, Vol. 12, pp. 301-318.

Yeo, R. W., Wood, P. E., and Hrymak, A. N. (1991), "A Numerical Study of Laminar 90-Degree Bend Duct Flow with Different Discretization Schemes," J. Fluids Eng., Vol. 113, pp. 563-568.

Table 1. Experiments in laminar flow

Investigator	shape	Re	De	R_c/d_h	L_u/d_h	L_d/d_h	θ_T	Entry flow	Instrument and measurements
Humphrey et al. (1977)	square	790	368	2.3	45	30	90	nearly dev.	LDV: U_θ profiles
Taylor et al. (1982)	square	790	368	2.3	7.5	50	90	developing	LDV: U_θ, U_r profiles
Agrawal et al. (1978)	circular	310	139	10.			180	developing	LDV: U_θ, U_r profiles
	circular	450	200	10.			180	developing	LDV: U_θ, U_r profiles
	circular	561	251	10.			180	developing	LDV: U_θ, U_r profiles
	circular	1260	565	10.			180	developing	LDV: U_θ, U_r profiles
	circular	242	183	3.5			180	developing	LDV: U_θ, U_r profiles
	circular	367	278	3.5			180	developing	LDV: U_θ, U_r profiles
	circular	492	372	3.5			180	developing	LDV: U_θ, U_r profiles
Enayet et al. (1983)	circular	500	212	2.8	5	10	90	developing	LDV: U_θ contours
	circular	1093	462	2.8	5	10	90	developing	LDV: U_θ contours
Bovendeerd et al. (1987)	circular	700	286	3.	50		90	developed	LDV: U_θ, U_r profiles

Nomenclature for Tables 1 and 2

R_c: bend's radius of curvature
L_u: length of upstream tangent
L_d: length of downstream tangent
θ_T: bend's turning angle in degrees

86

Table 2. Experiments in turbulent flow in curved ducts

Investigator	shape	Re	De	R_c/d_h	L_u/d_h	L_d/d_h	θ_T	Entry flow	Instrument and measurements
Humphrey et al. (1980)	square	40,000	18,650	2.3	45	30	90	nearly dev.	LDV: U_θ, U_r,u_θ, u_r, $\overline{u_\theta u_r}$
Taylor et al. (1982)	square	40,000	18,650	2.3	7.5	50	90	developing	LDV: Wall static pressures U_θ, U_r, u_θ, u_r, k, $\overline{u_\theta u_r}$
Enayet et al. (1983)	square	35,000	9,354	7	7.5	50	90	developing	LDV: U_θ, U_r, u_θ, u_r, $\overline{u_\theta u_r}$
Chang et al. (1983)	square	56,700	21,900	3.375	31	31	180	nearly dev.	LDV: Wall static pressures U_θ, U_r, u_θ, u_r, $\overline{u_\theta u_r}$
Iacovides et al. (1990)	square	58,000	22,000	3.375	6	31	180	developing	Hotwire: U_θ, U_r,u_θ, u_r, $\overline{u_\theta u_r}$
Kim (1991)	rectang. AR=6	220,000	95,000	2.04	4.38	30	90	developing	Hotwire: Wall static pressures U_θ, U_r, U_z, all six $\overline{u_i u_j}$
Rowe (1970)	circular	23,600	4,817	12	69	69	180	developed	pressure probes: Total pressure, velocity head, yaw angles
Enayet et al. (1983)	circular	43,000	18,170	2.8	5	10	90	developing	LDV: Wall static press., U_θ, u_θ
Azzola & Humphrey (1986)	circular circular	57,400 110,000	22,090 42,340	3.375 3.375	54.5 54.5	54.7 54.7	180 180	developed developed	LDV: U_θ, U_r, U_ϕ, u_θ, u_ϕ LDV: U_θ, U_ϕ, u_θ, u_ϕ
Anwer et al. (1989)	circular	50,000	13,868	6.493	96	96	180	developed	Hotwire: U_θ, U_r, U_ϕ, all six $\overline{u_i u_j}$

Table 3. Experiments in turbulent flow in straight transition ducts

Investigator	shape	Re	L_{tr}/d_h	AR at exit	Area ratio A_{exit}/A_{inlet}	Flow regime	Instrument and flow measurements
Mayer (1939)	R-to-C		0.69		1.0	Incompr.	Pitot probe: Static, total press., U,V,W
	C-to-R		2.76		1.0	Incompr.	Pitot probe: Static, total press., U,V,W
Taylor et al. (1981)	S-to-C	35,350	2.00		0.785	Incompr.	LDV: U,V,W
Burley and Carlson (1985)	C-to-R		1.00	6.16	1.0	Low subs.	Strain-gage bal.: perform. parameters
	C-to-R		0.75	6.16	1.0	Low subs.	Strain-gage bal.: perform. parameters
	C-to-R		0.50	6.16	1.0	Low subs.	Strain-gage bal.: perform. parameters
	C-to-R		0.75	6.46	0.75	Low subs.	Strain-gage bal.: perform. parameters
Patrick and McCormick (1988)	C-to-R	4.2×10^5	1.00	3.00	1.0	Low subs.	LDV:U,V,W,$\overline{uu}$,$\overline{vv}$,$\overline{ww}$, total press.
	C-to-R	4.2×10^5	3.00	6.00	1.0	Low subs.	LDV:U,V,W,$\overline{uu}$,$\overline{vv}$,$\overline{ww}$, total press.
Miau et al. (1990)	C-to-R	$10^5 \div 10^6$	1.08	2.00	1.0	Low subs.	Hot wire:U,V,W,$\overline{uu}$, static press.
	C-to-R	$10^5 \div 10^6$	0.92	2.00	1.0	Low subs.	Hot wire:U,V,W,$\overline{uu}$, static press.
	C-to-R	$10^5 \div 10^6$	0.54	2.00	1.0	Low subs.	Hot wire:U,V,W,$\overline{uu}$, static press.
Davis (1992)	C-to-R	3.9×10^5	1.5	3.00	1.0	Incompr.	Hot wire:U,V,W, all $\overline{u_i u_j}$, static press.

Nomenclature for Table 3

A	:	cross-sectional area
AR	:	aspect ratio at the exit station
C-R	:	circular-to-rectangular transition duct
R-C	:	rectangular-to-circular transition duct
S-C	:	square-to-circular transition duct
L_{tr}	:	length of transition
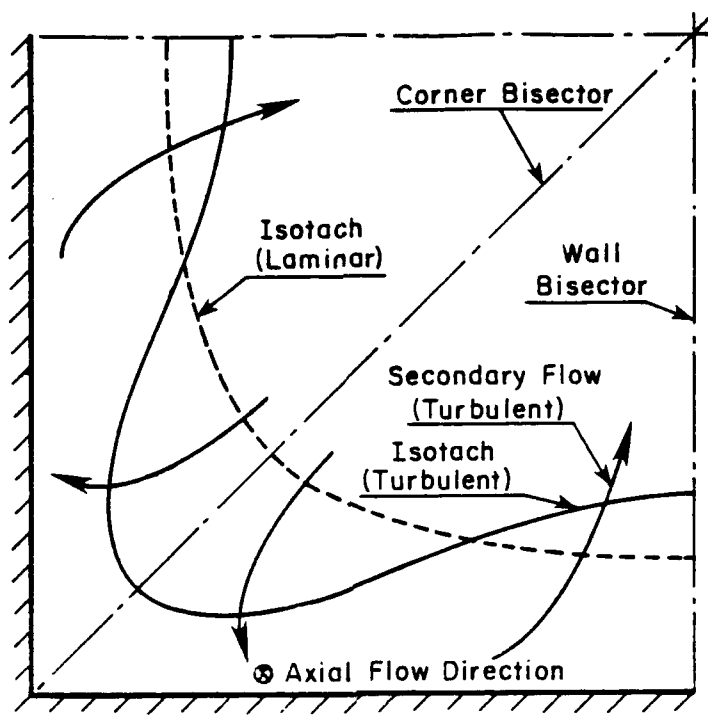
(a) Isotach pattern
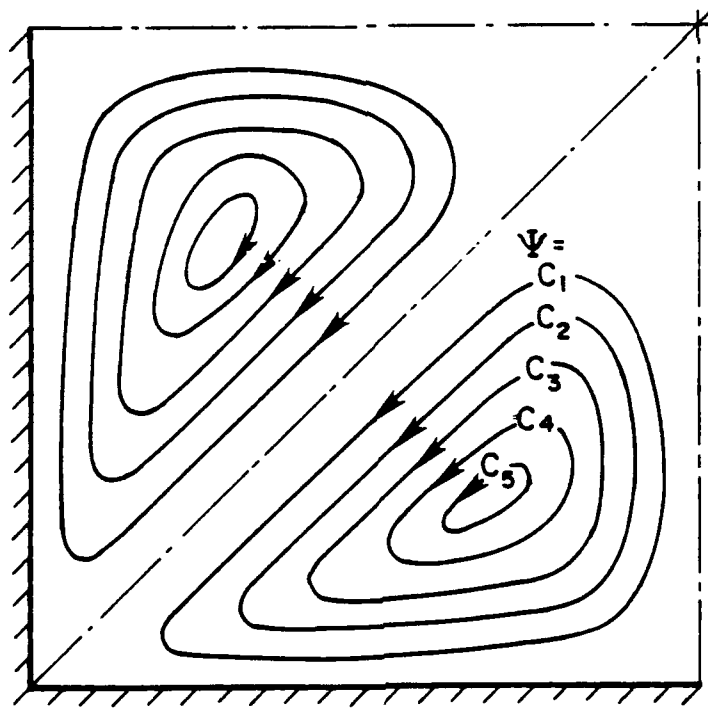
(b) Secondary flow pattern

Fig. 1   Typical flow structure in the corner region (from Gessner and Jones, 1965)
        (a) isotach pattern; (b) secondary flow pattern

89
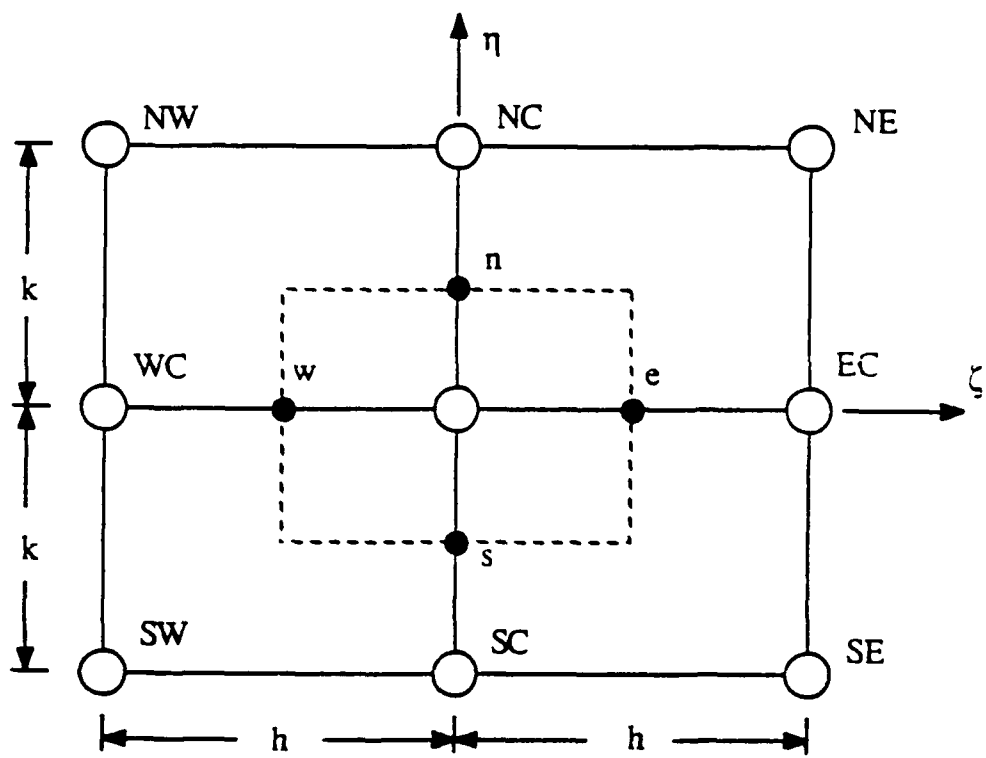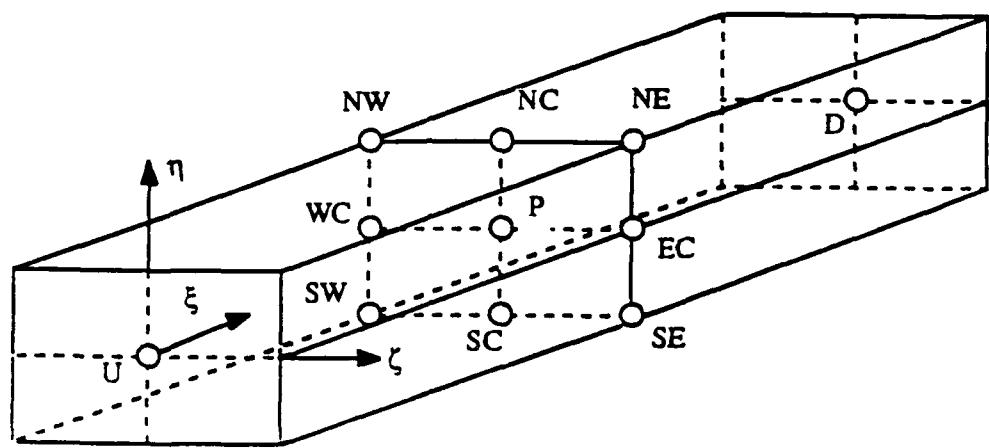
Fig. 2　Finite analytic computational cell
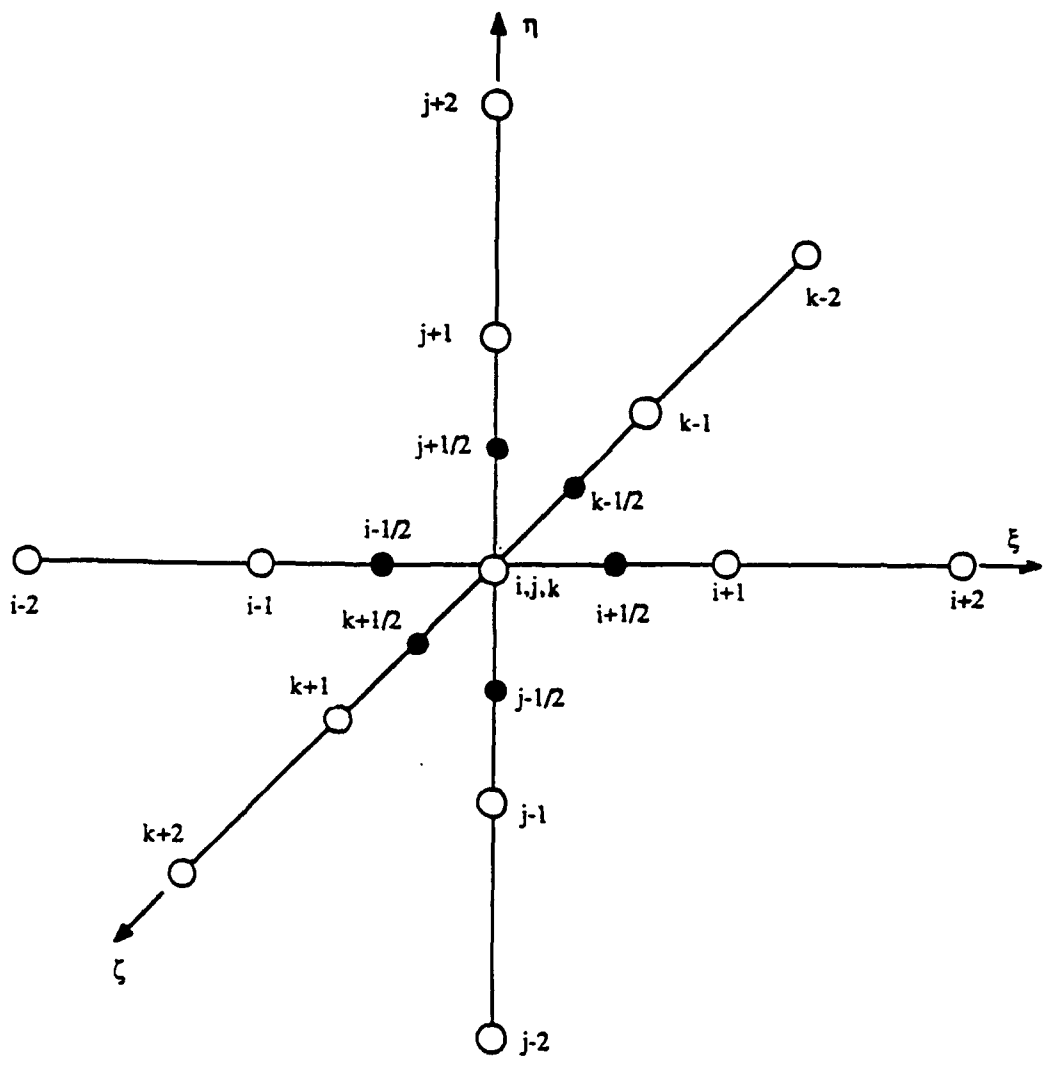
Fig. 3   Finite difference computational cell
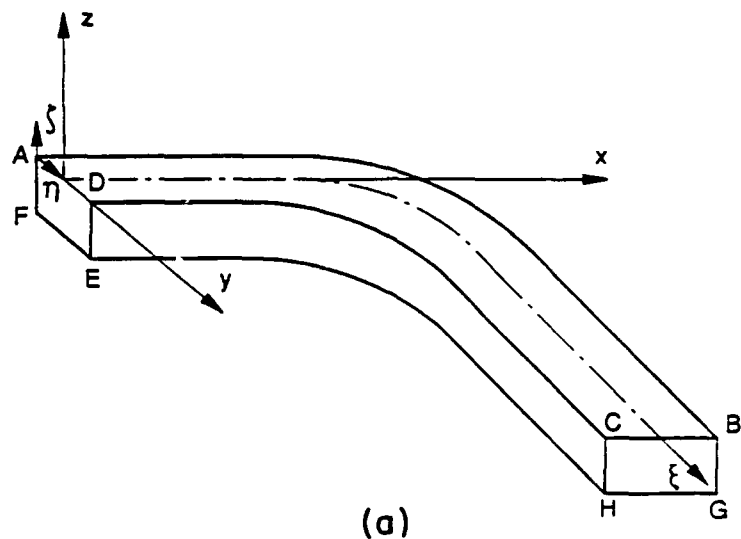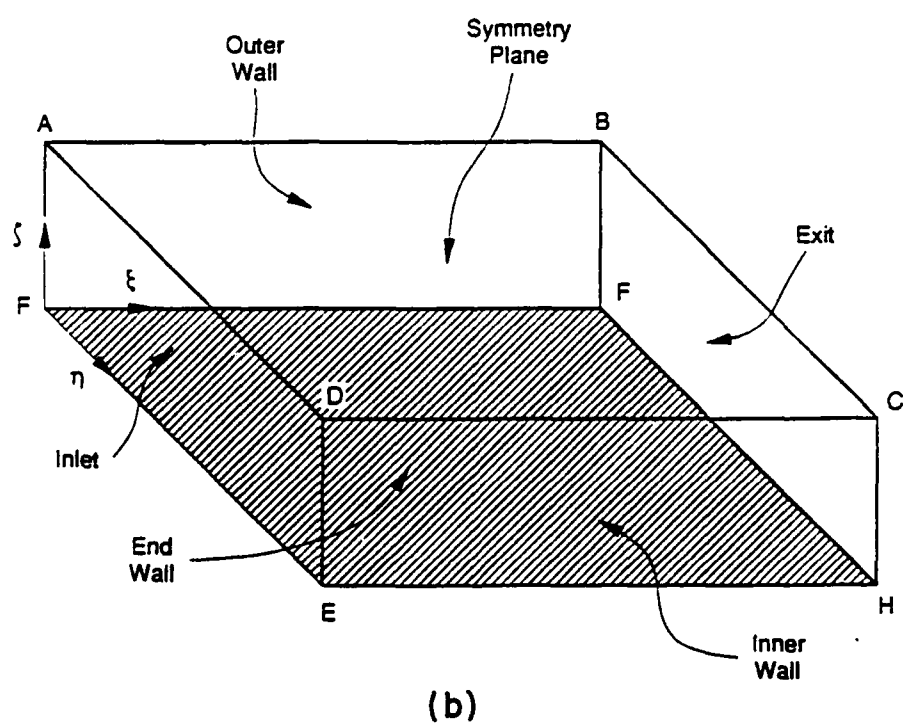
Fig. 4 Curvilinear coordinates and computational grid for a curved square duct
(a) physical solution domain; (b) transformed solution domain
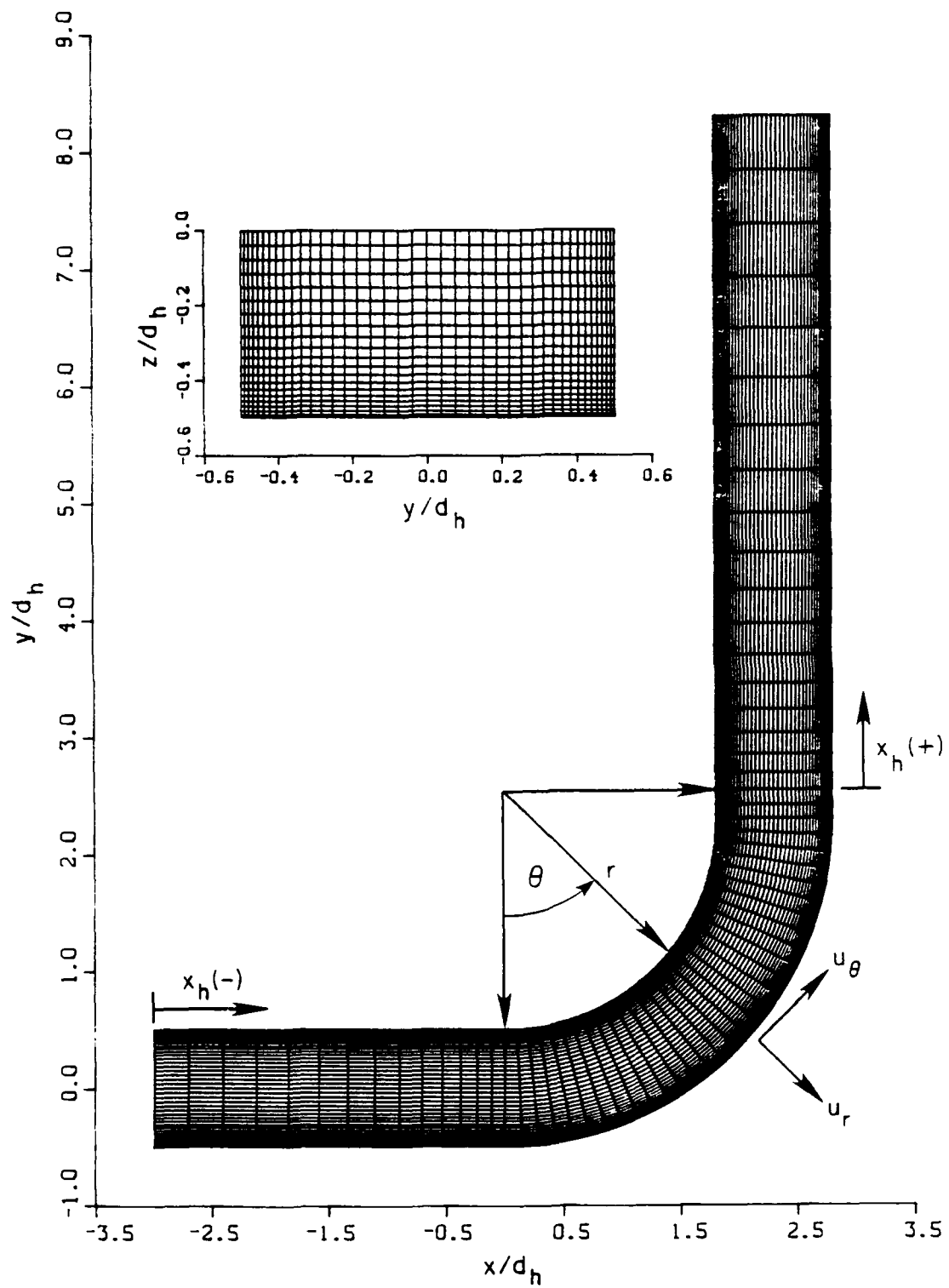
Fig. 4 Curvilinear coordinates and computational grid for a curved square duct
(c) Typical cross-sectional and plane of symmetry grid views

93
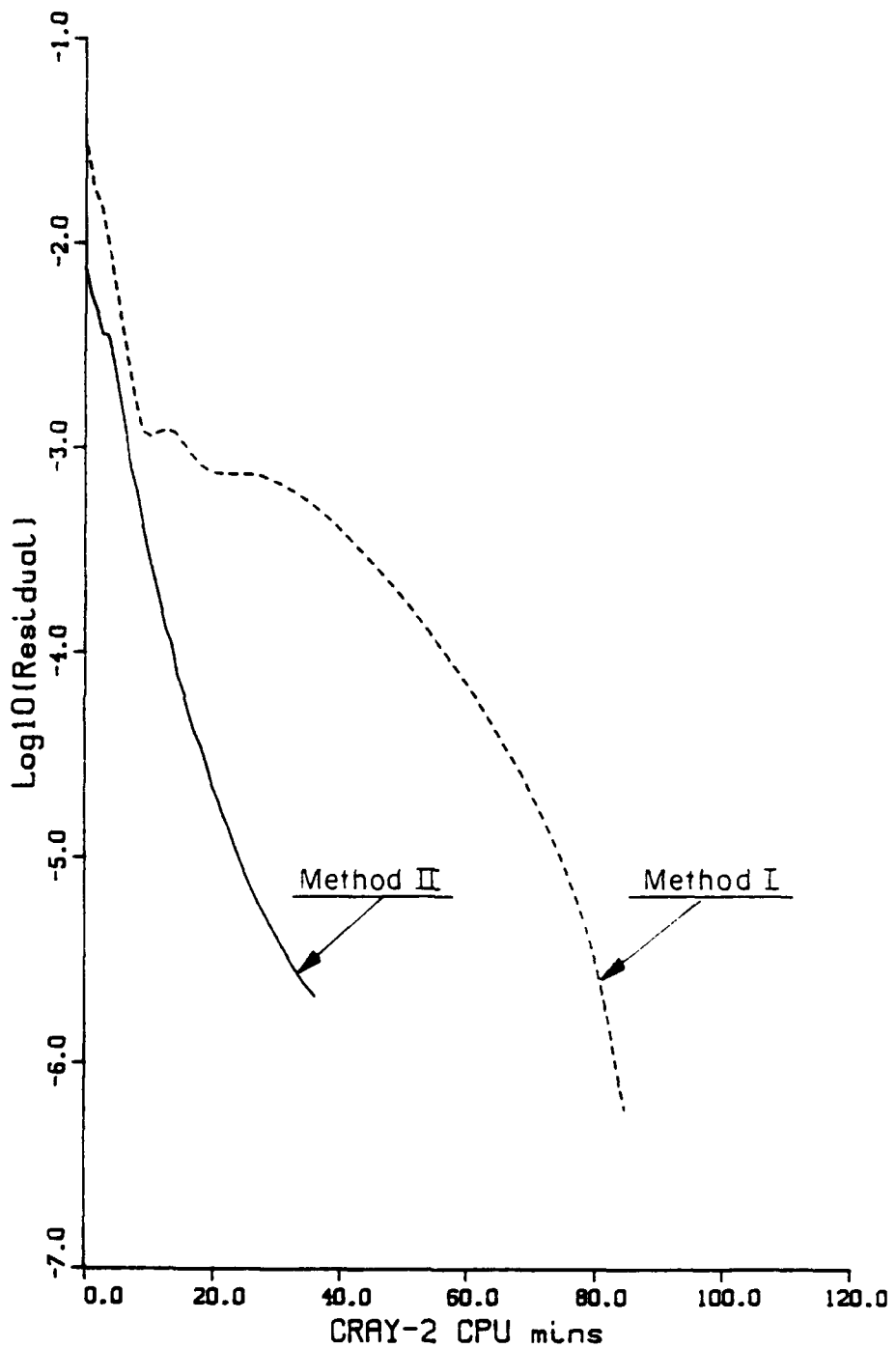
Fig. 5   Comparison of the convergence histories for Methods I and II
(Duct of Humphrey et al. (1977); Re=790; Grid A)
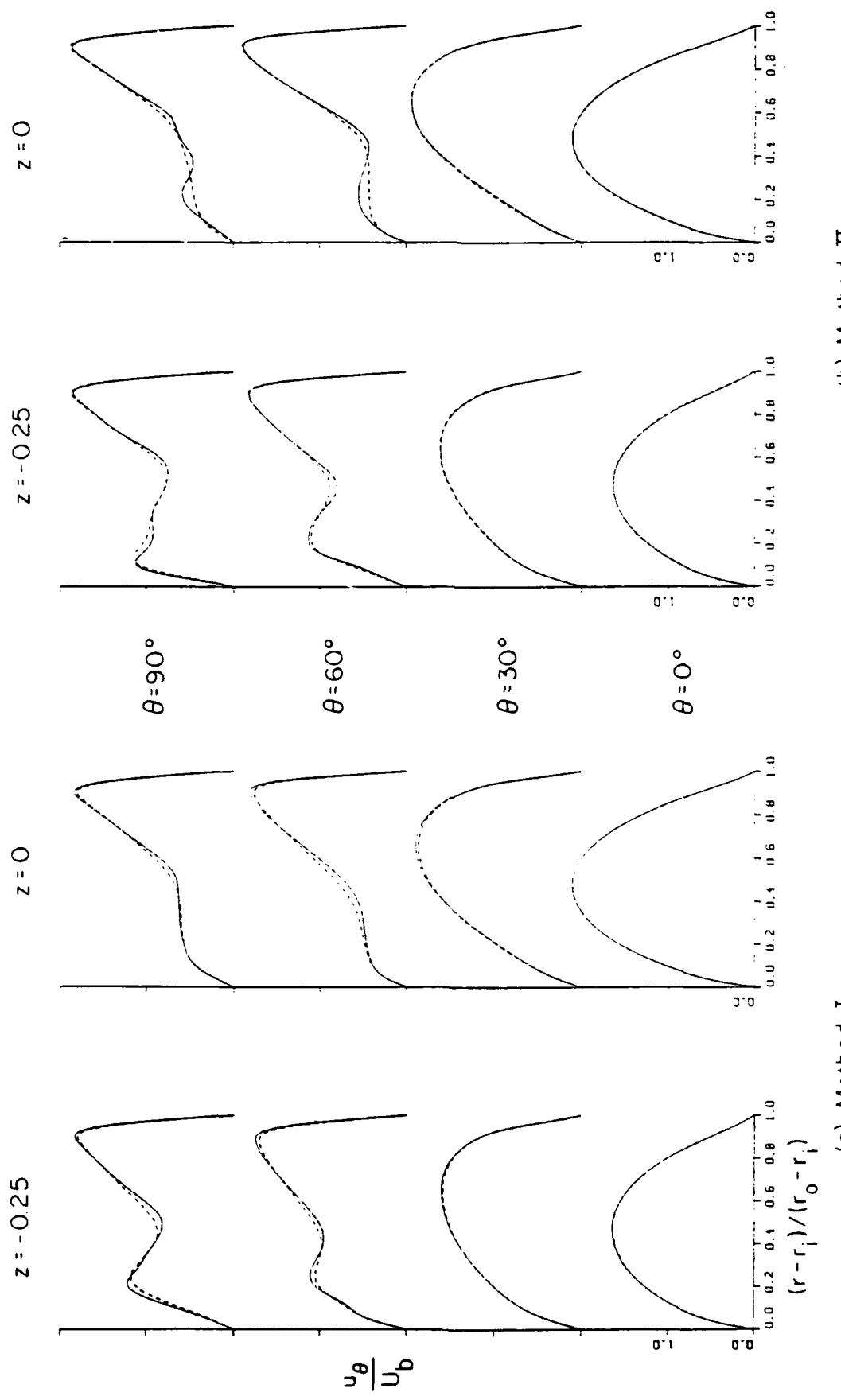
Fig. 6   Grid dependence study for the duct of Humphrey et al. (1977):
– – –, grid A; ———, grid B. (a) Method I; (b) Method II
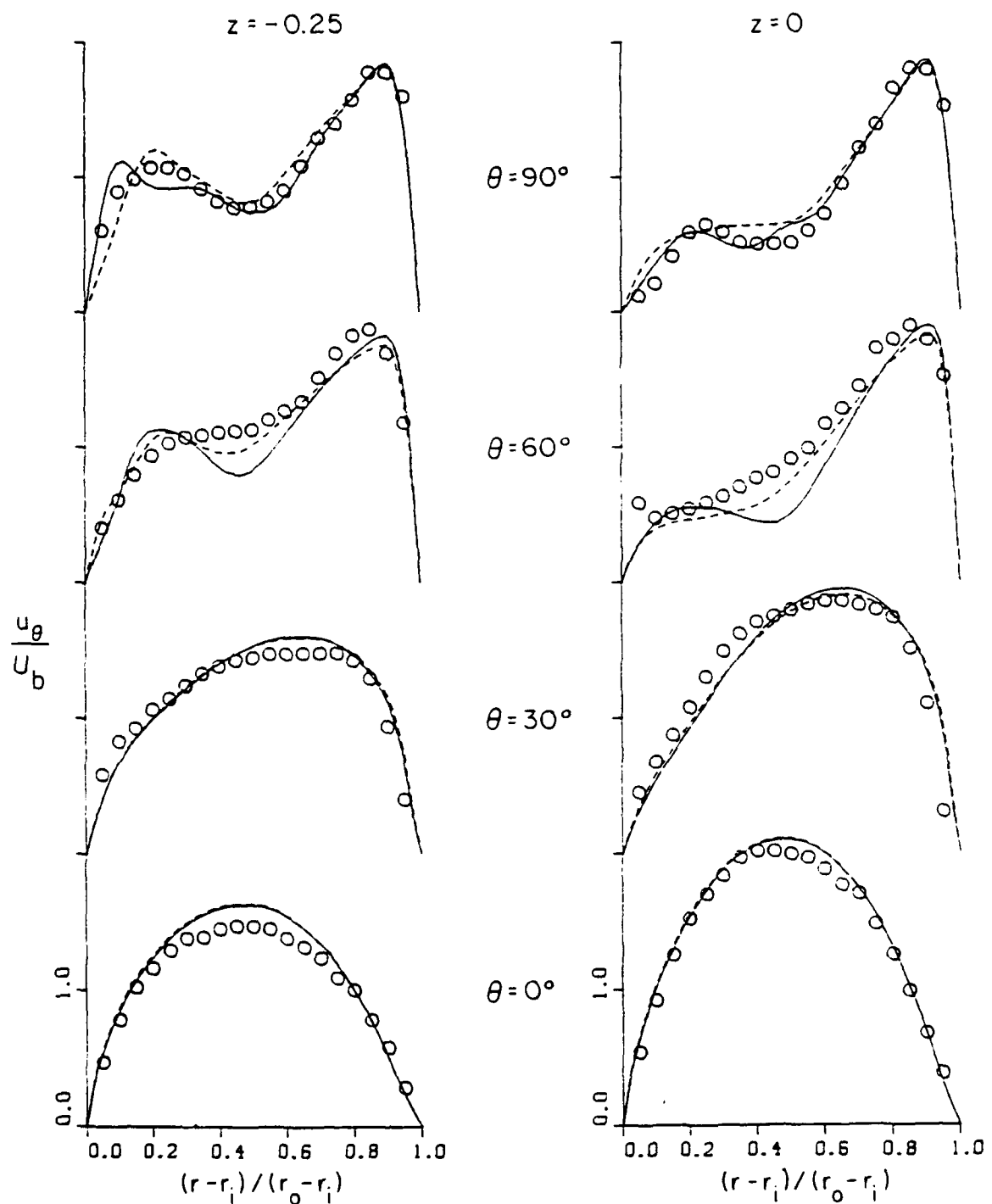
Fig. 7   Measured and calculated streamwise velocity profiles along radial lines:
o, measurements (Humphrey et al., 1977); − − −, Method I; ⎯⎯⎯, Method II
(a) z = -0.25d$_h$; (b) z = 0.0

96
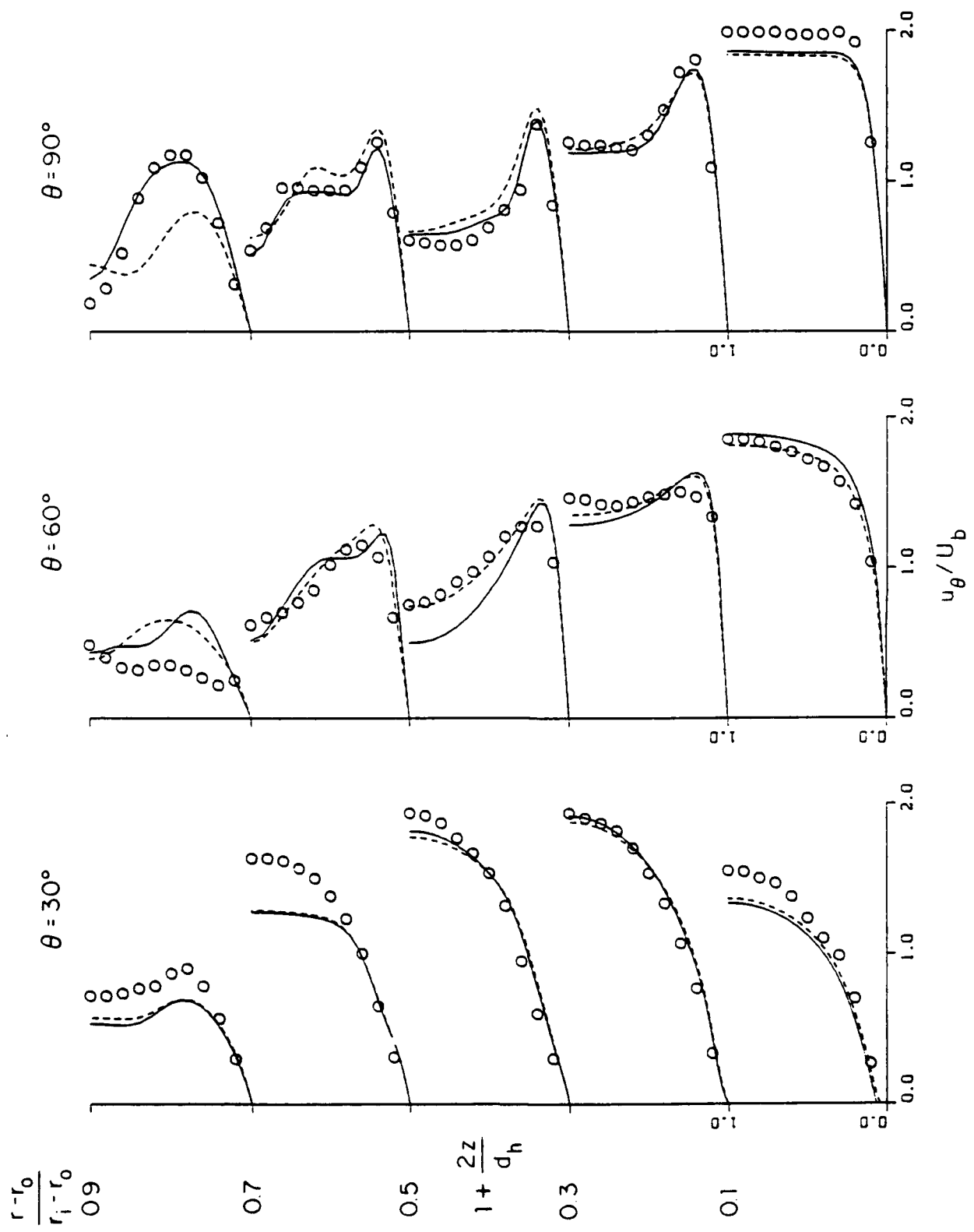
Fig. 8   Measured and calculated streamwise velocity profiles along z-lines:
o, measurements (Humphrey et al., 1977); – –, Method I; ——, Method II
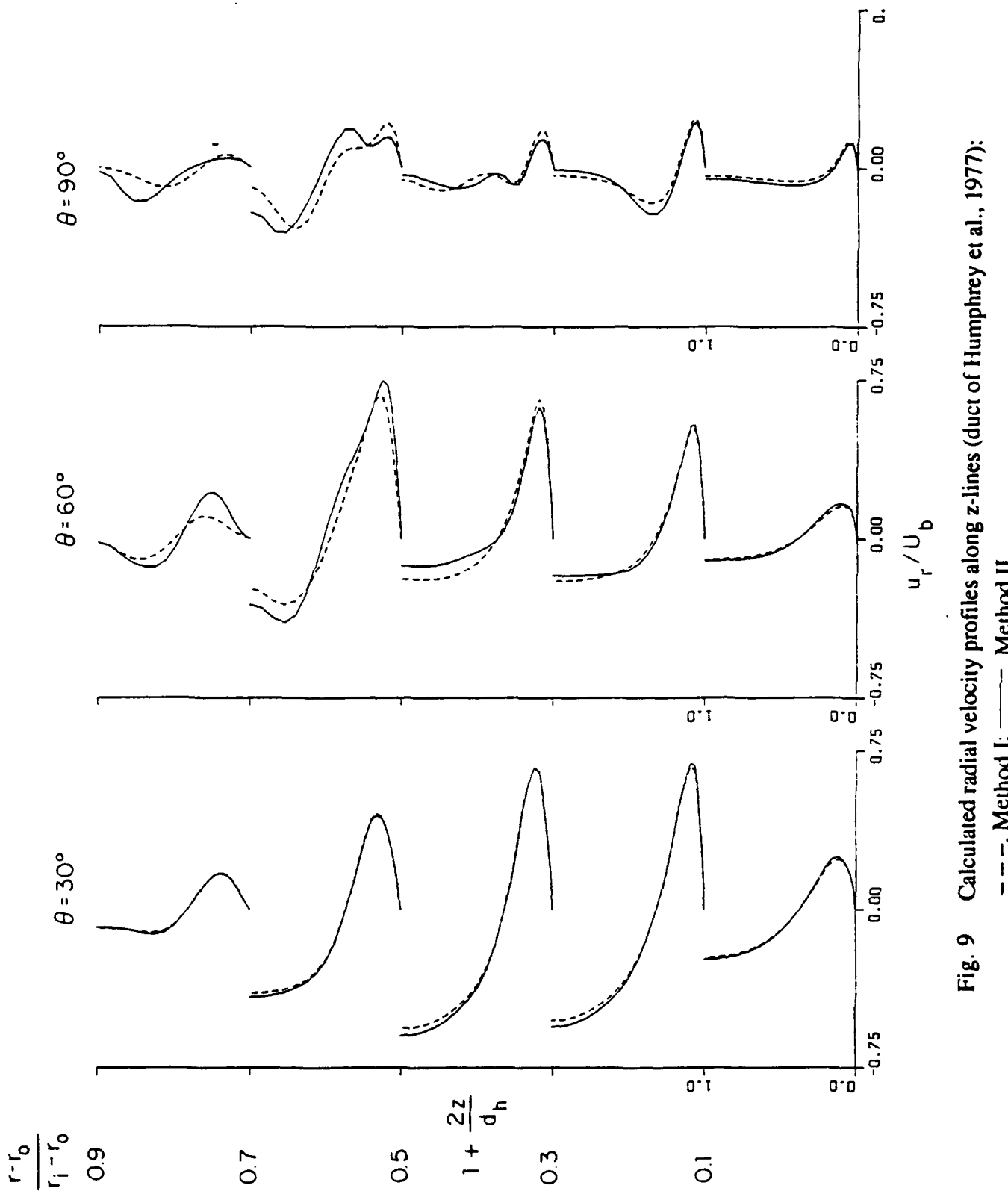
Fig. 9 Calculated radial velocity profiles along z-lines (duct of Humphrey et al., 1977): – – –, Method I; ————, Method II
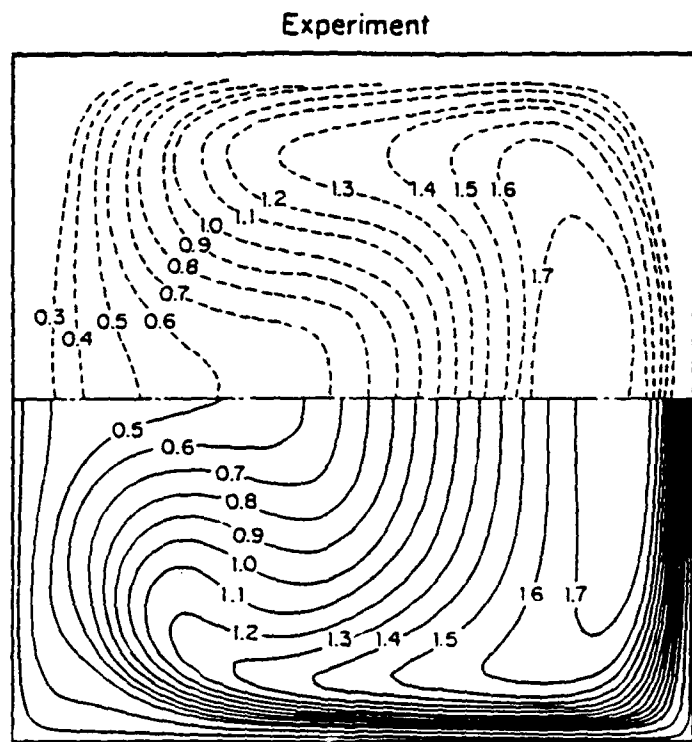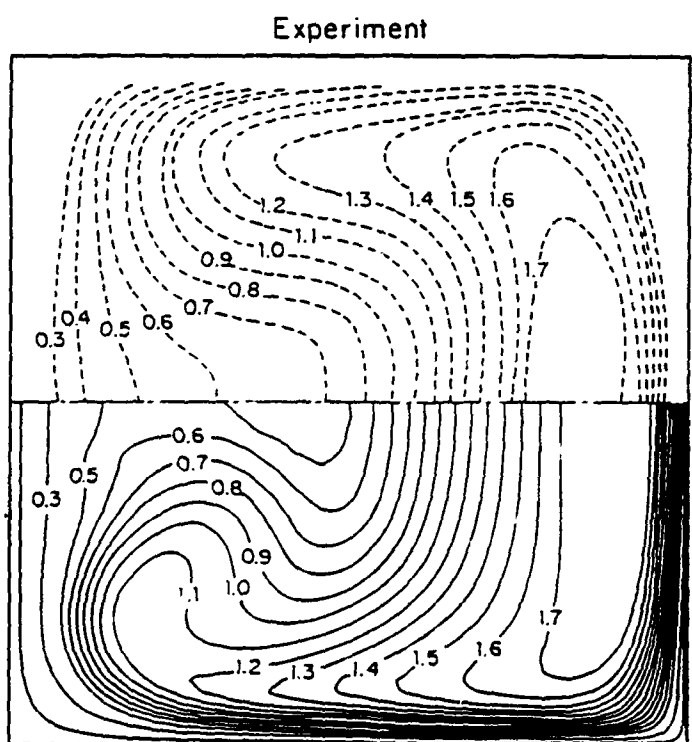
Fig. 10 Measured (Humphrey et al., 1977) and calculated streamwise velocity contours
(a) θ = 60°

Fig. 10 Measured (Humphrey et al., 1977) and calculated streamwise velocity contours
(b) θ = 90°

100

Experiment

Calculation

Method I

Experiment
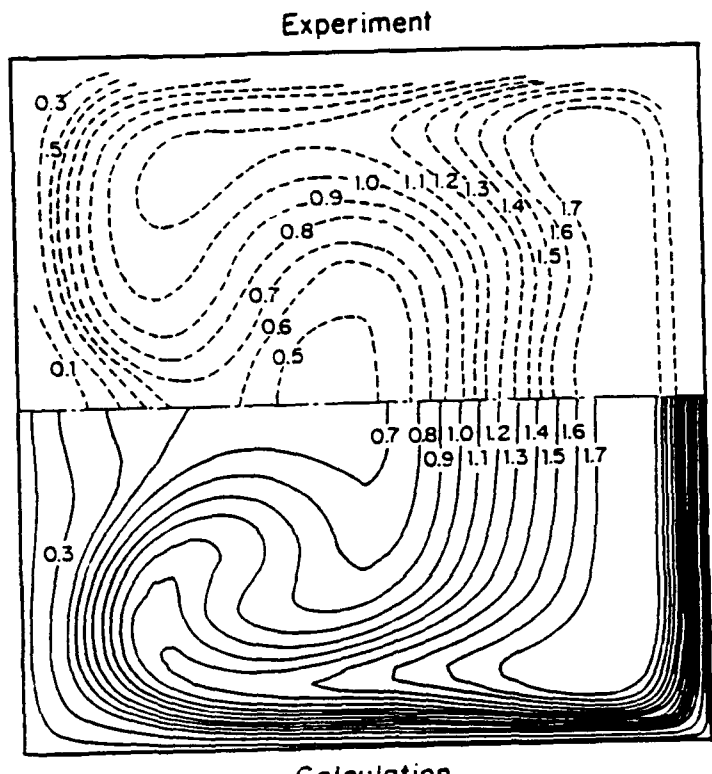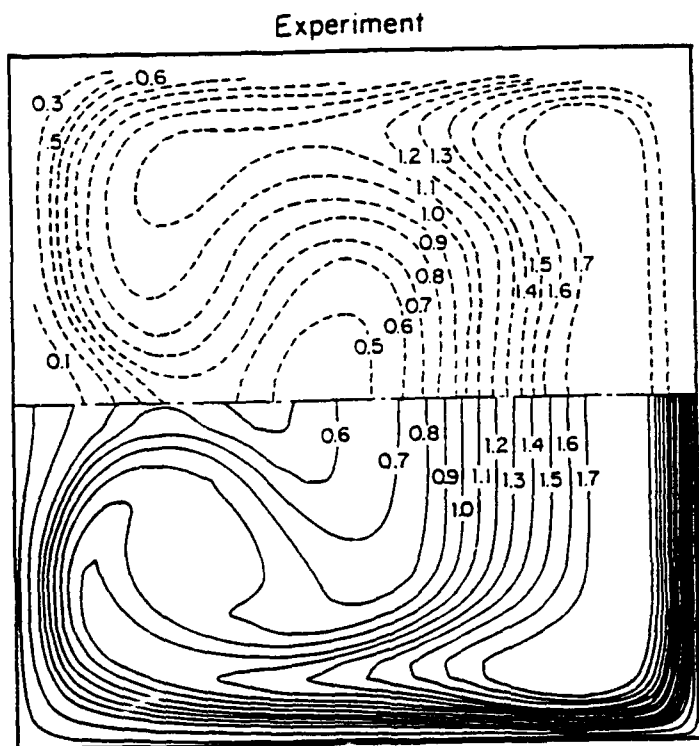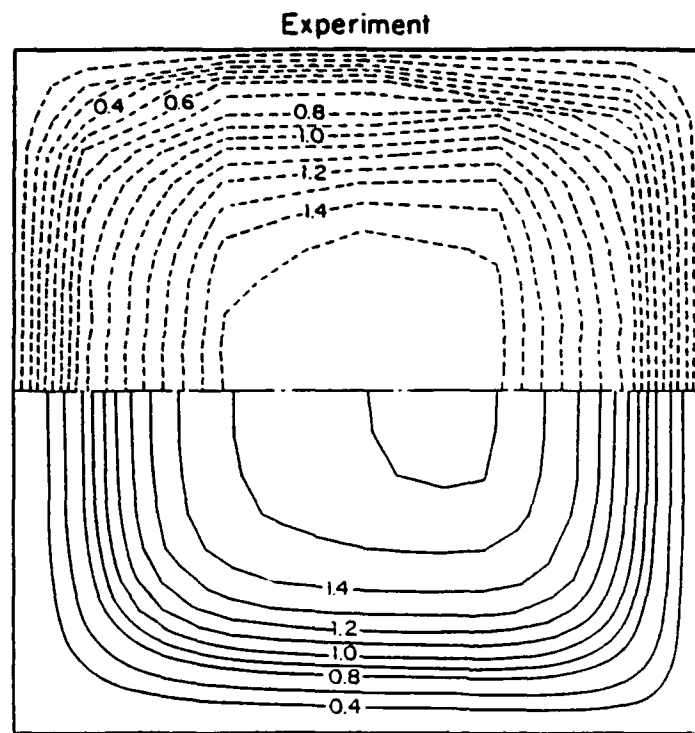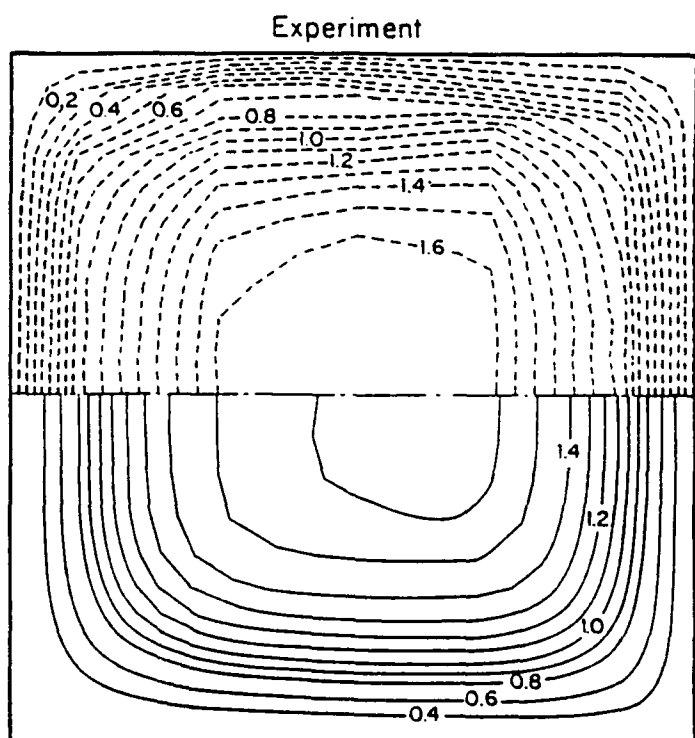
Calculation

Method II

(a) $x_h = -0.25\ d_h$

Fig. 11   Measured (Taylor et al., 1982) and calculated streamwise velocity contours
(a) $x_h = -0.25 d_h$

Experiment

Calculation

Method I

Experiment
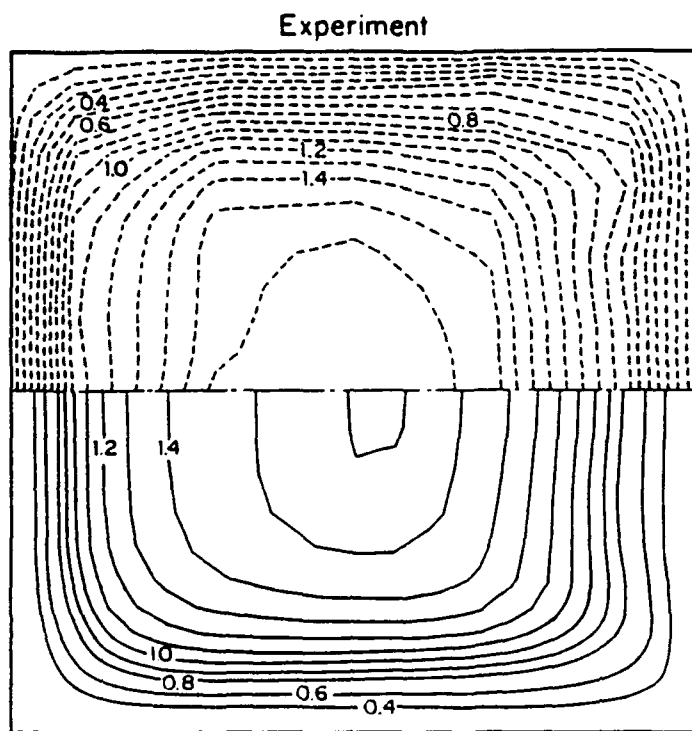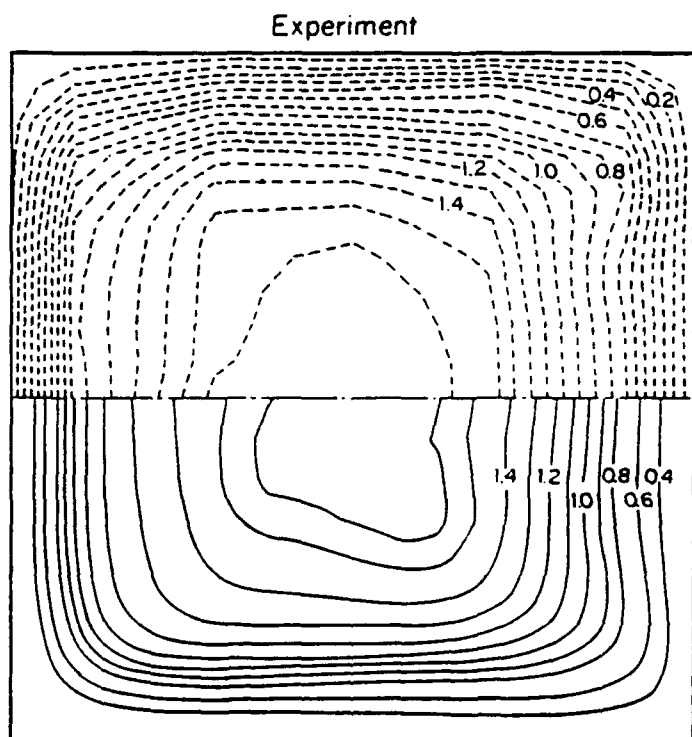
Calculation

Method II

(b) $\theta = 30°$

Fig. 11   Measured (Taylor et al., 1982) and calculated streamwise velocity contours
(b) $\theta = 30°$
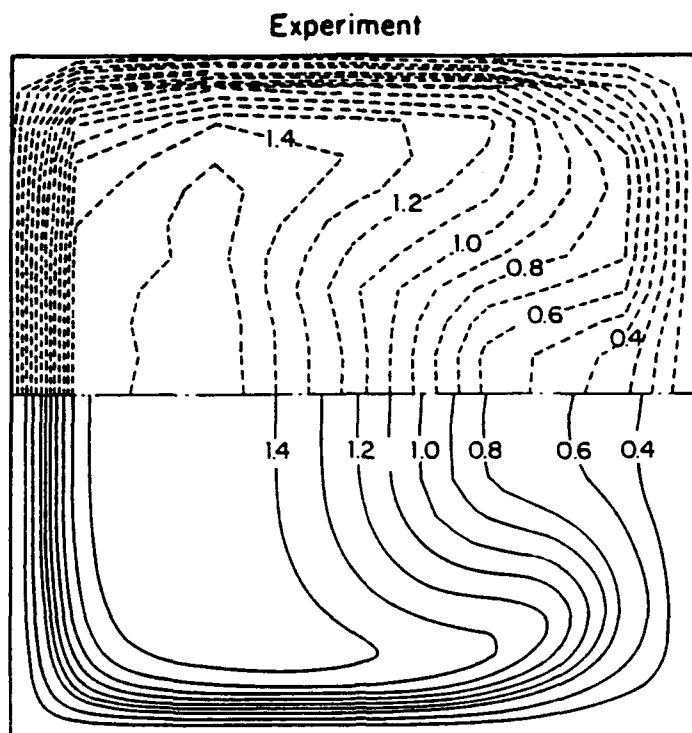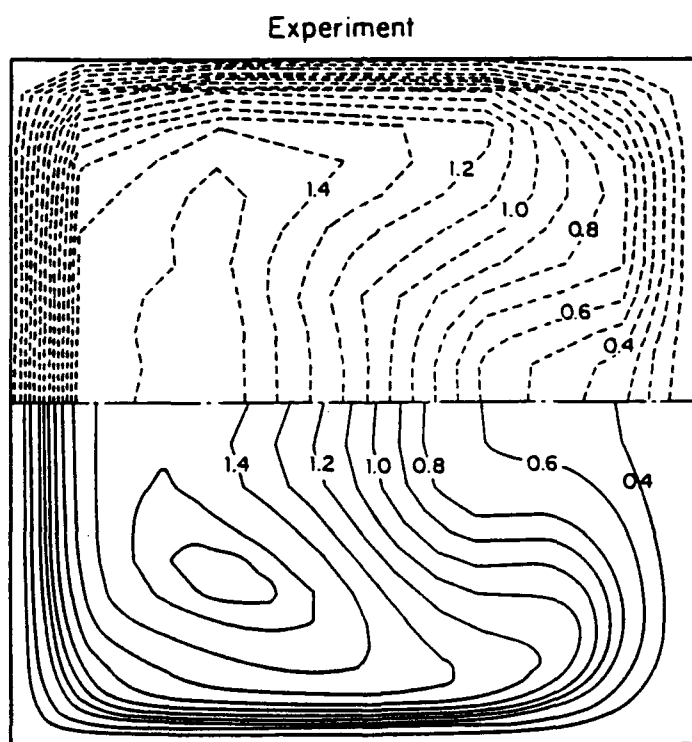
102

Experiment

Calculation
Method I

Experiment

Calculation
Method II

(c) θ = 60°

Fig. 11   Measured (Taylor et al., 1982) and calculated streamwise velocity contours
(c) θ = 60°

Experiment

Calculation

Method I

Experiment
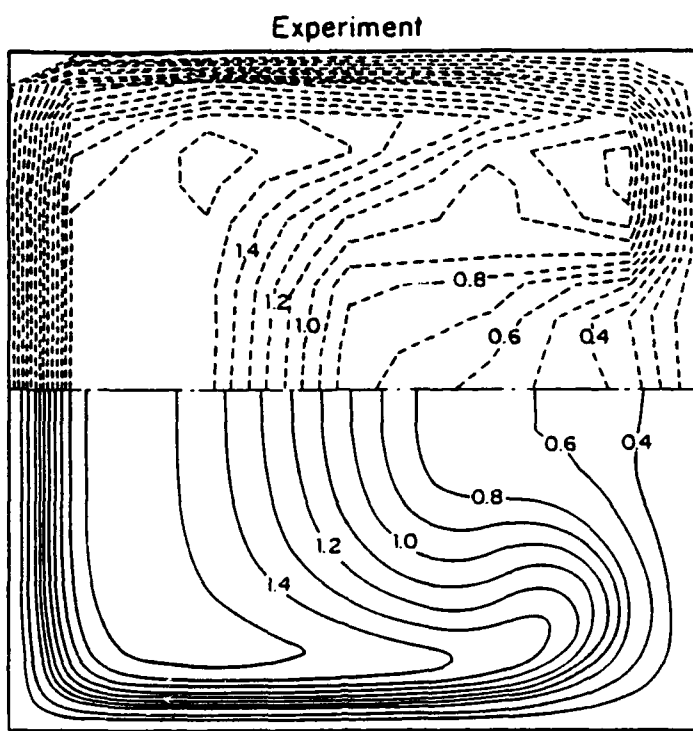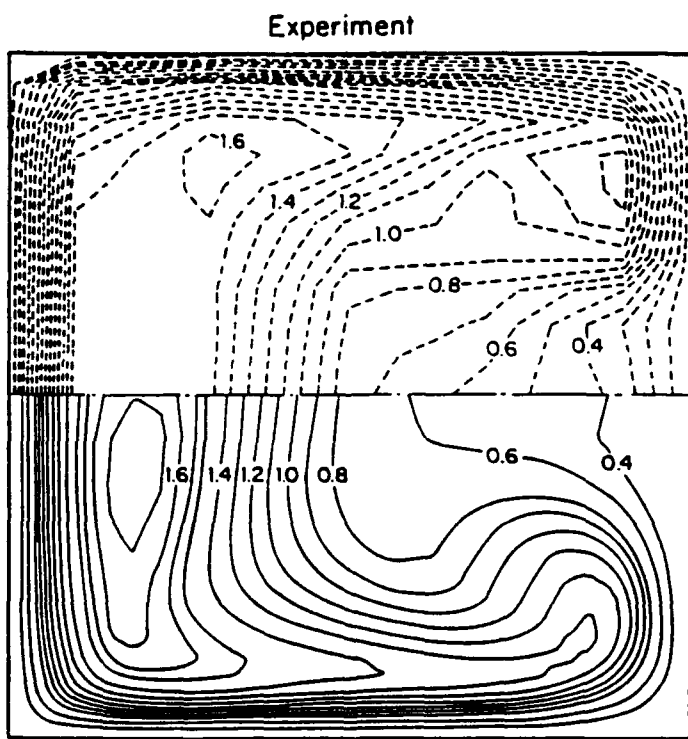
Calculation

Method II

(d) $\theta = 77.5°$

Fig. 11 Measured (Taylor et al., 1982) and calculated streamwise velocity contours
(d) $\theta = 77.5°$

Experiment

Calculation

Method I

Experiment
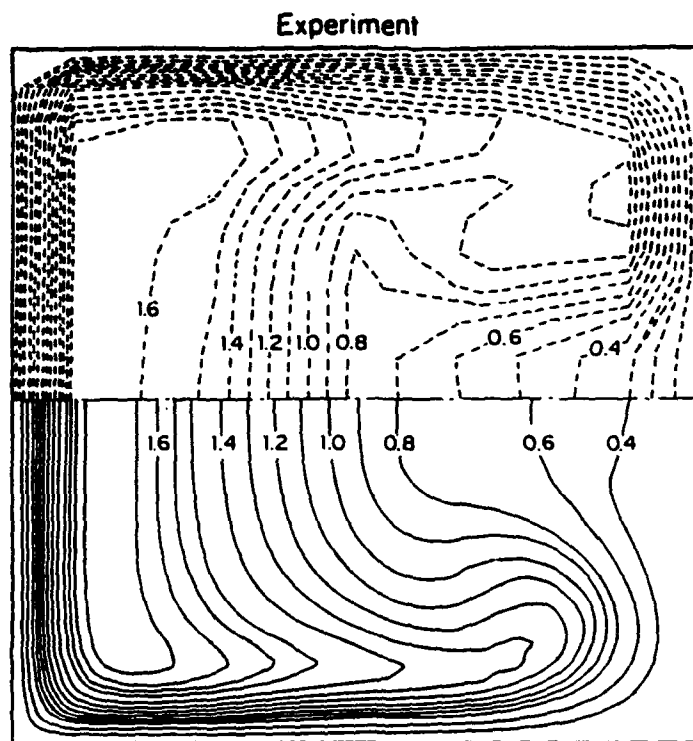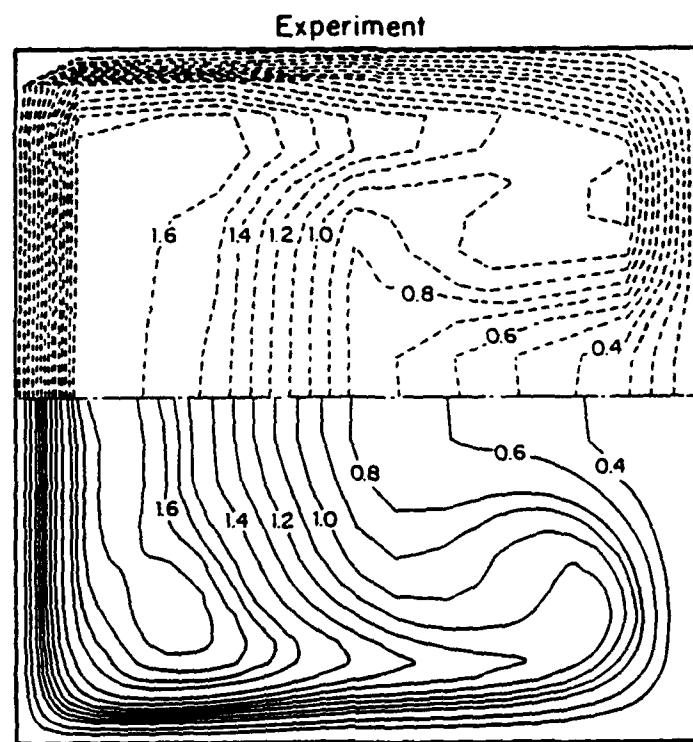
Calculation

Method II

(e) $x_h = +0.25\,d_h$

Fig. 11   Measured (Taylor et al., 1982) and calculated streamwise velocity contours
(e) $x_h = +0.25d_h$

105

Experiment

Calculation

Method I

Experiment
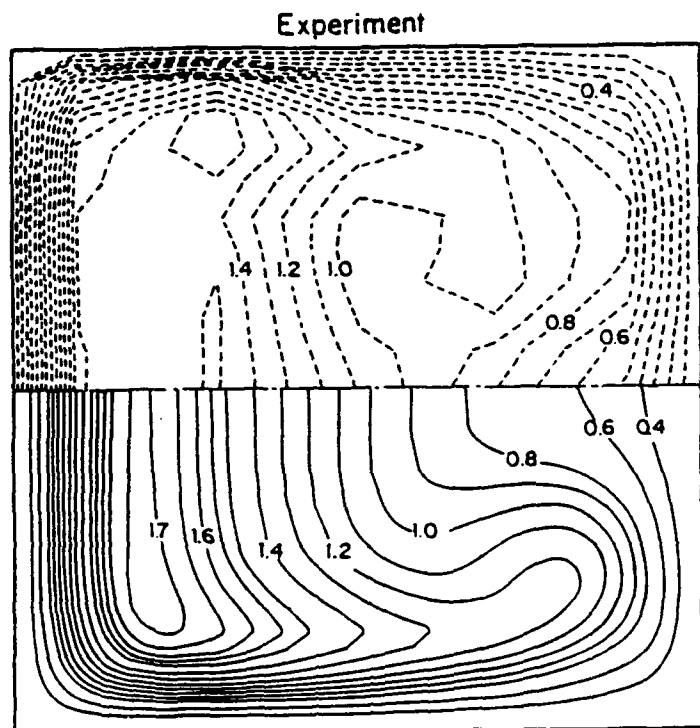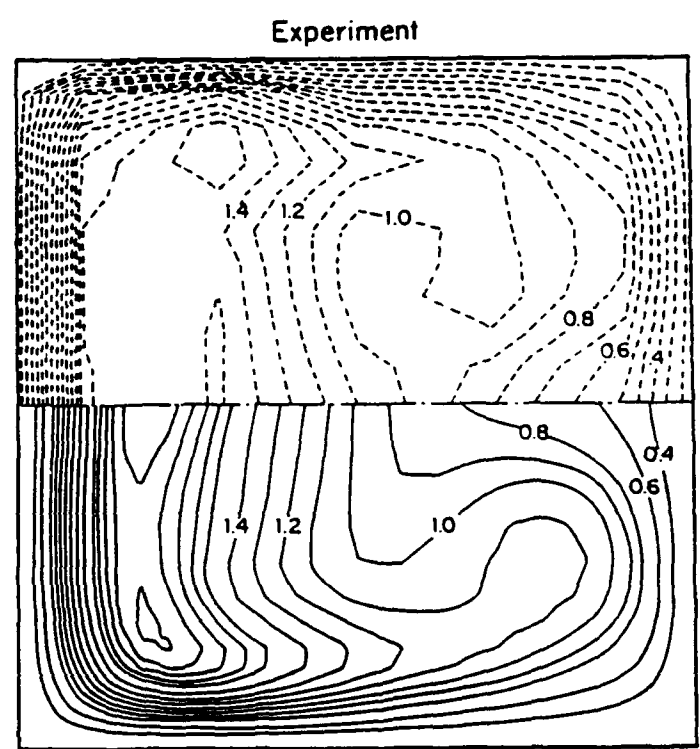
Calculation

Method II

(f) $x_h = +2.5 \, d_h$

Fig. 11 Measured (Taylor et al., 1982) and calculated streamwise velocity contours
(f) $x_h = +2.5 d_h$
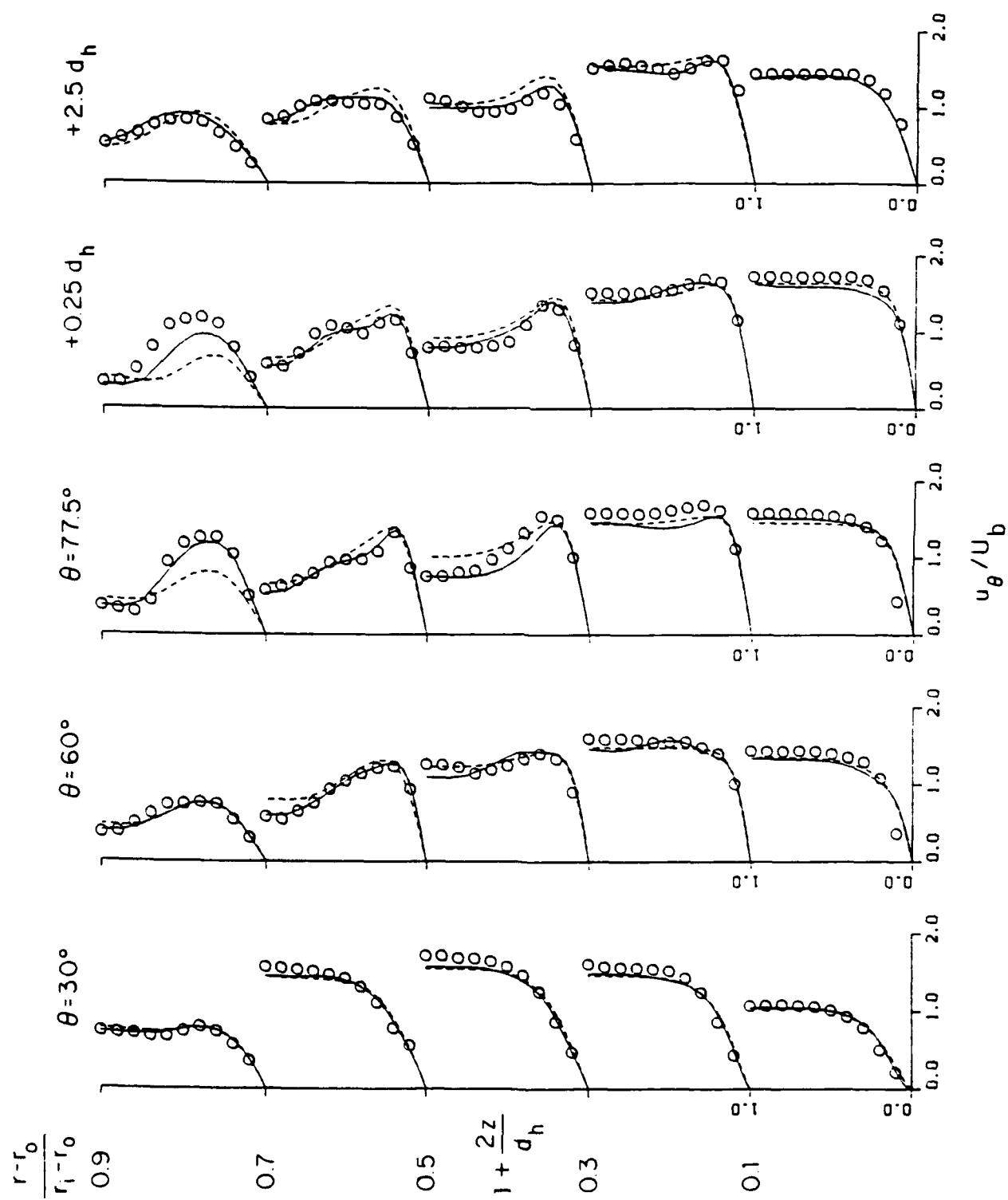
Fig. 12 Measured and calculated streamwise velocity profiles along z-lines:
o, measurements (Taylor et al., 1982); – – –, Method I; ———, Method II
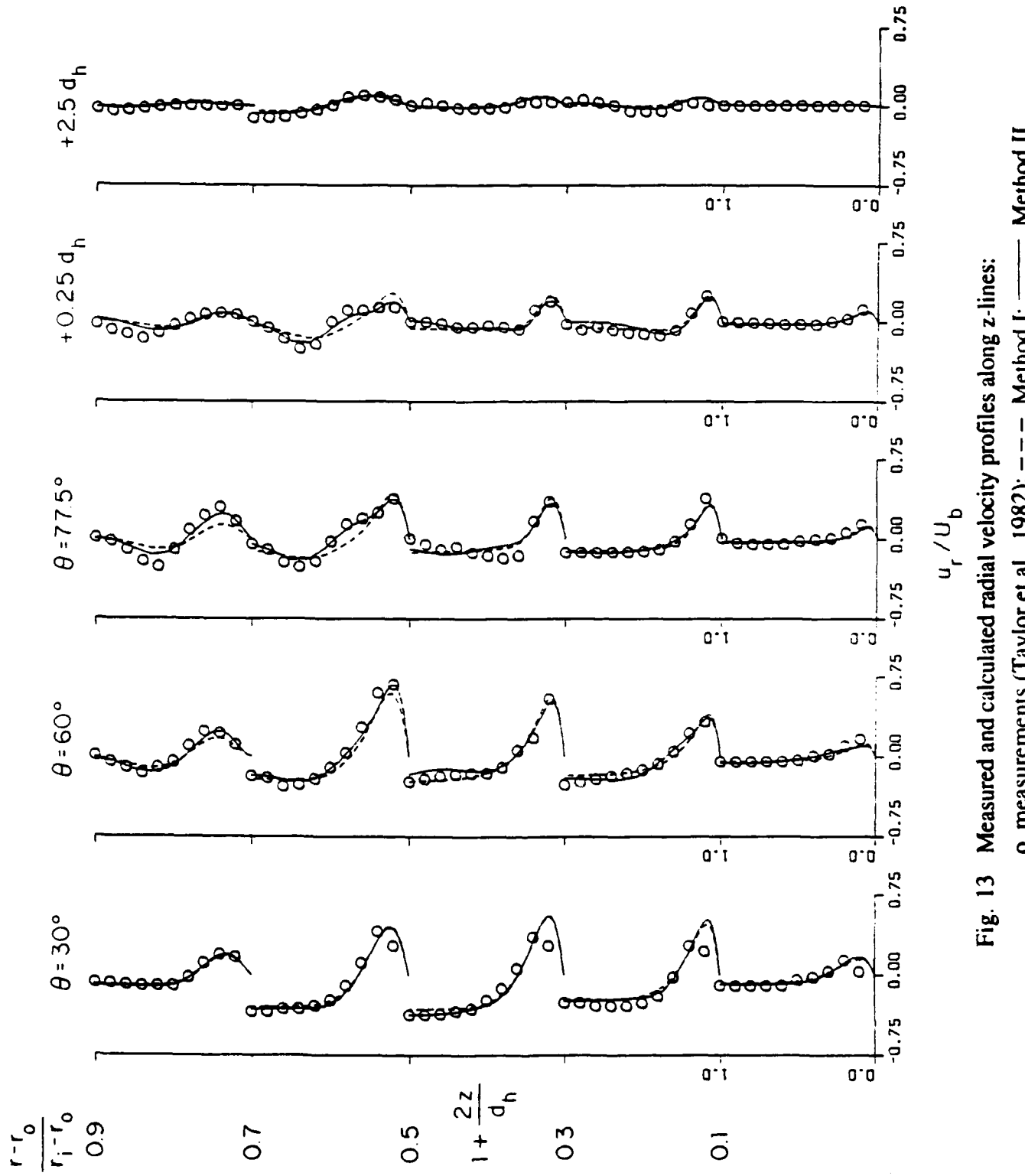
Fig. 13 Measured and calculated radial velocity profiles along z-lines:
o, measurements (Taylor et al., 1982); – – –, Method I; ———, Method II
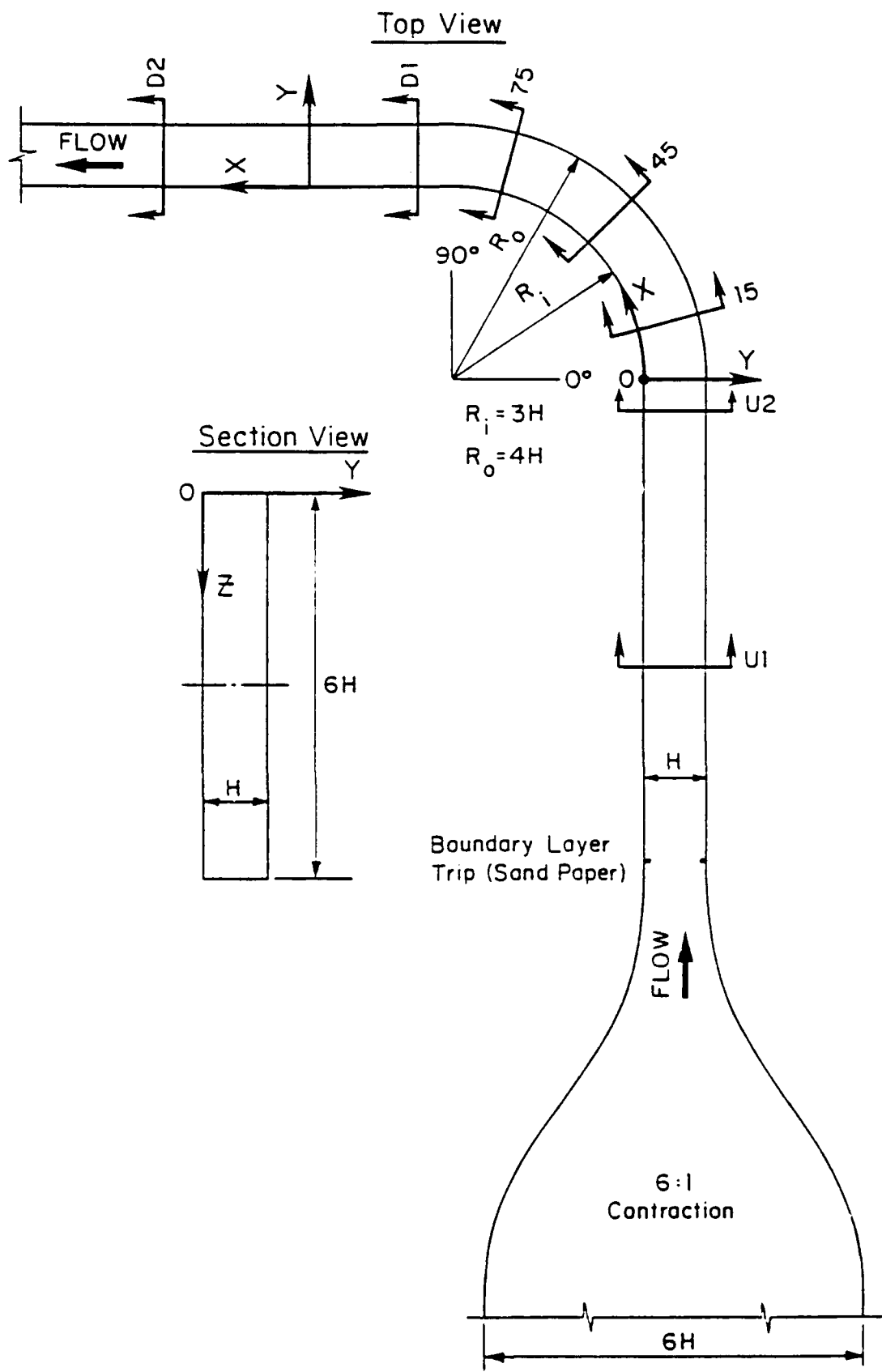
Fig. 14 Curved-wall wind tunnel, coordinates and locations of measurement stations for the duct of Kim (1991)

109
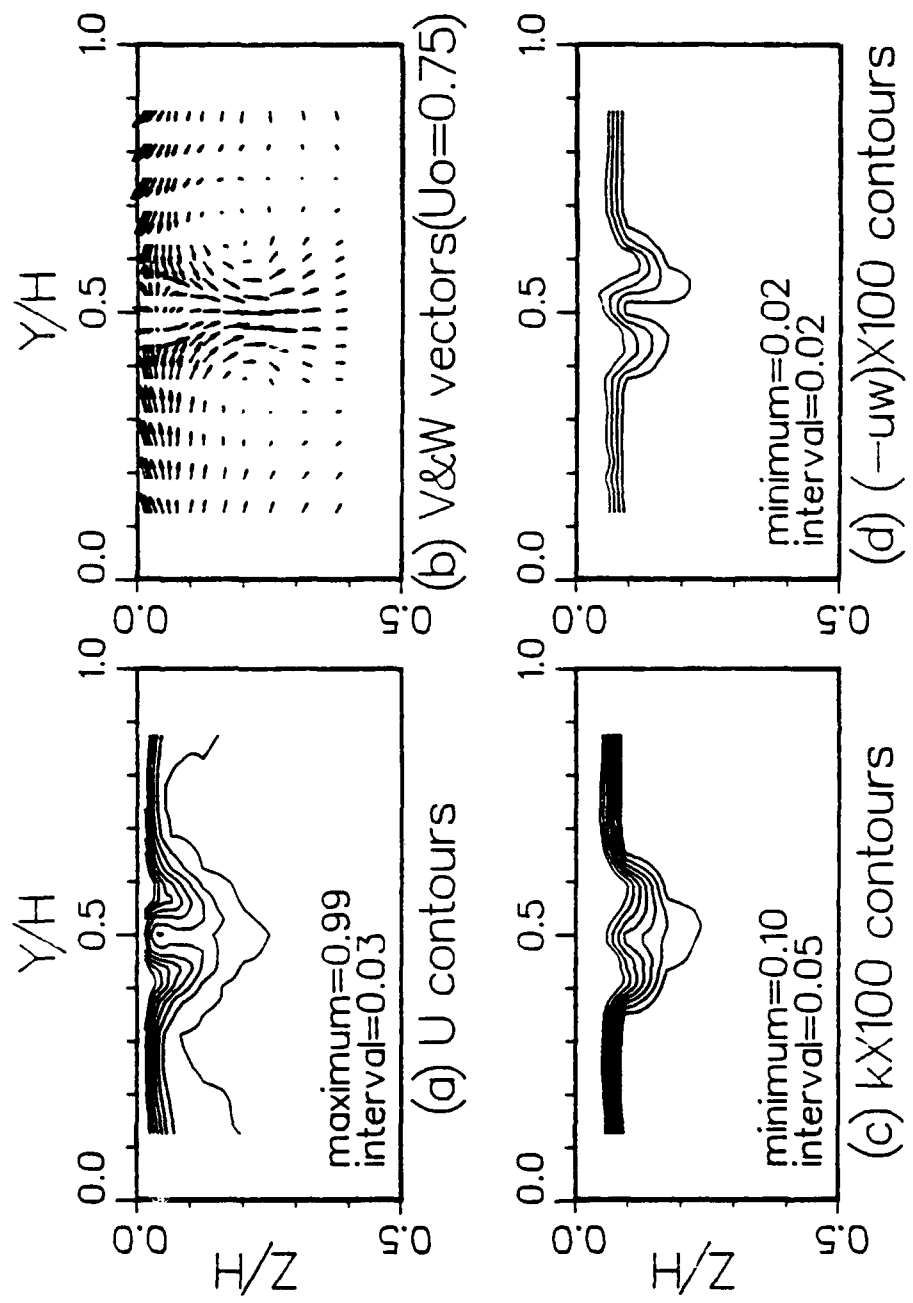
Fig. 15　Measured (Kim, 1991) top-wall boundary layer at station U1
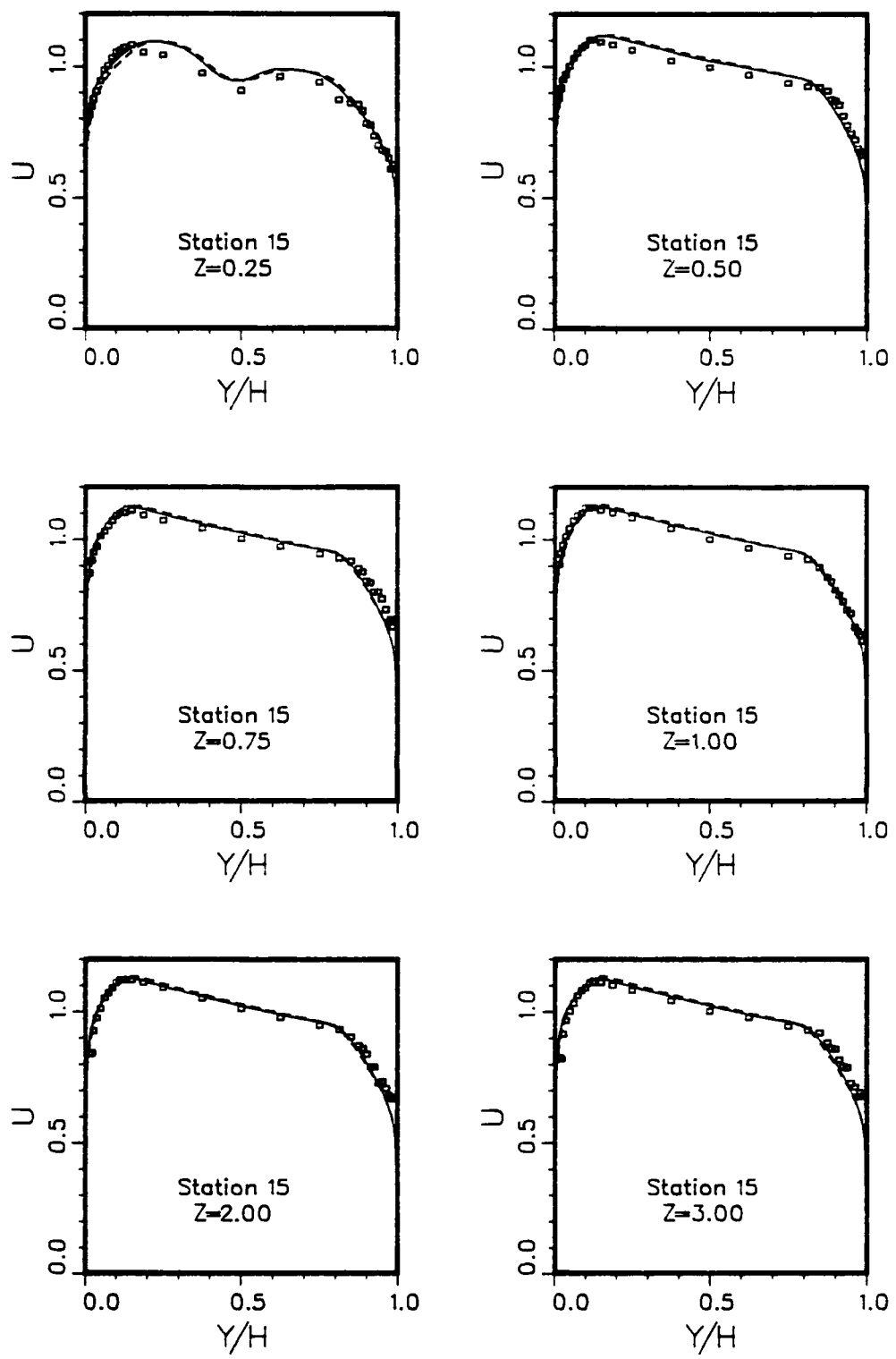
(a) U contours

maximum=0.99
interval=0.03

(b) V&W vectors(Uo=0.75)

(c) kX100 contours

minimum=0.10
interval=0.05

(d) (−uw)X100 contours

minimum=0.02
interval=0.02

Fig. 16 Measured and calculated mean velocity profiles along radial lines

□ , measurements (Kim, 1991); — — —, Method I; ————, Method II
(a) Streamwise mean velocity; Station 15
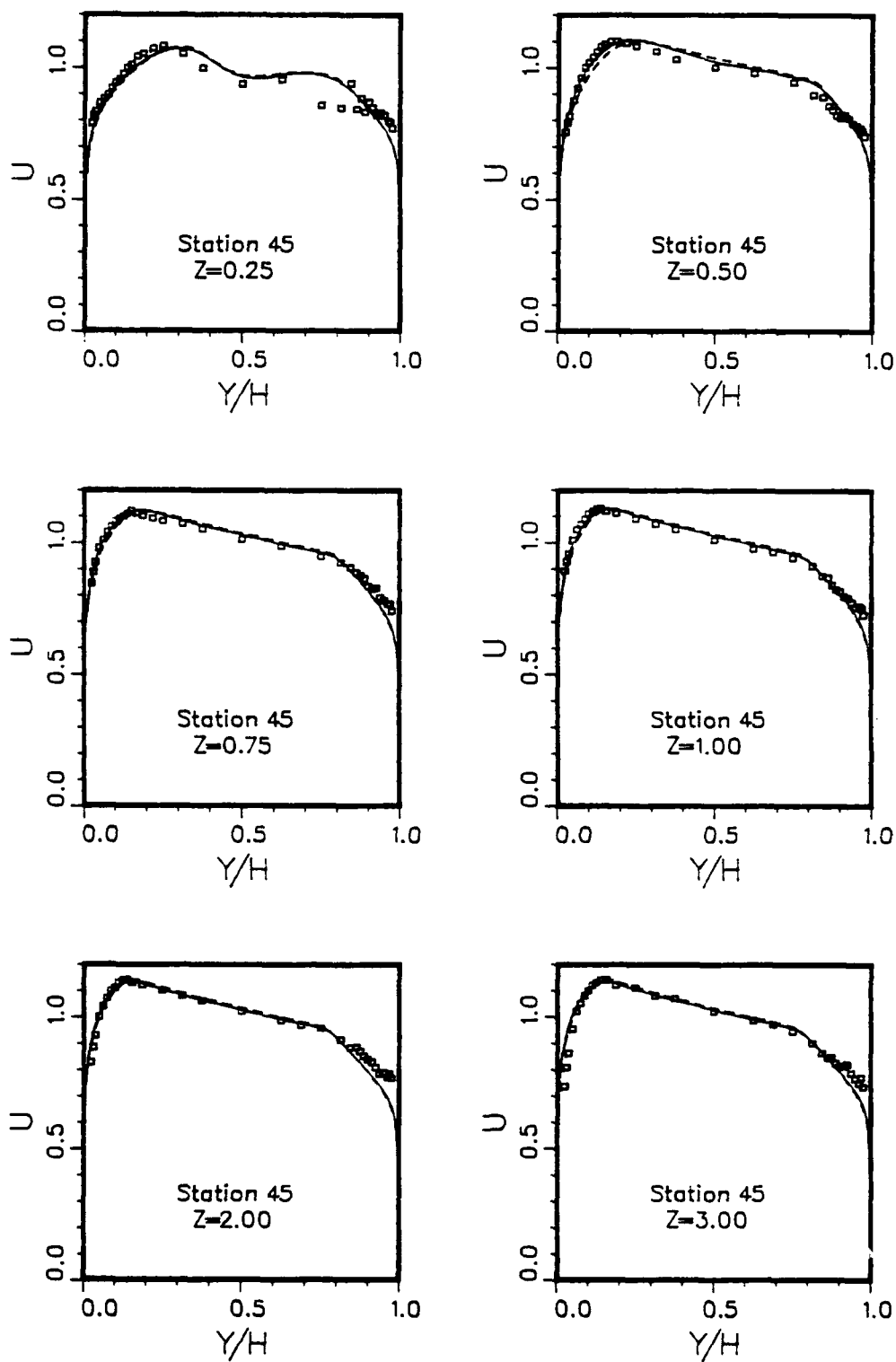
Fig. 16   Measured and calculated mean velocity profiles along radial lines

□ , measurements (Kim, 1991); − − −, Method I; ———, Method II
(b) Streamwise mean velocity; Station 45
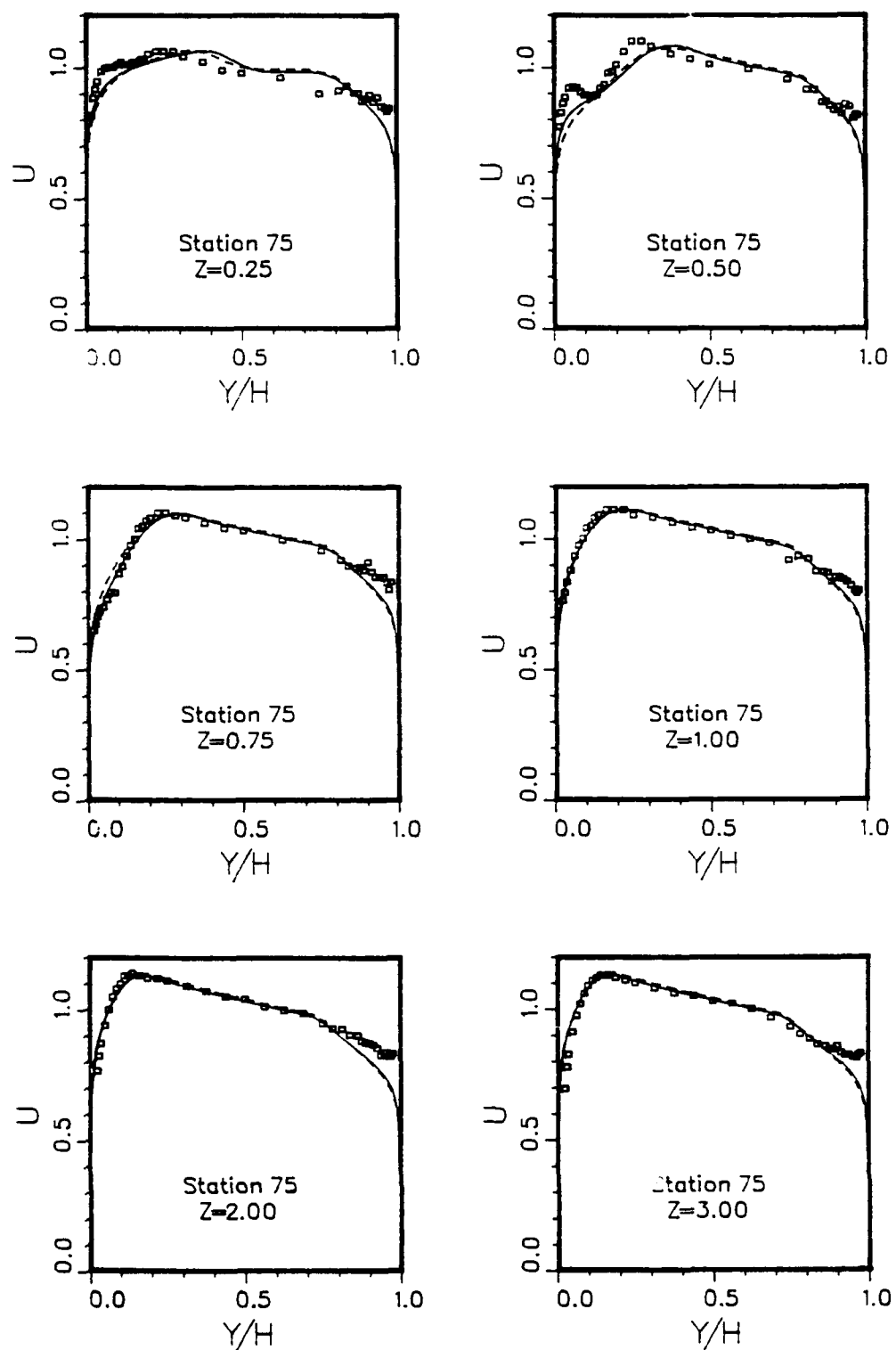
Fig. 16   Measured and calculated mean velocity profiles along radial lines

☐ , measurements (Kim, 1991);   – – –, Method I; ———, Method II
(c) Streamwise mean velocity; Station 75
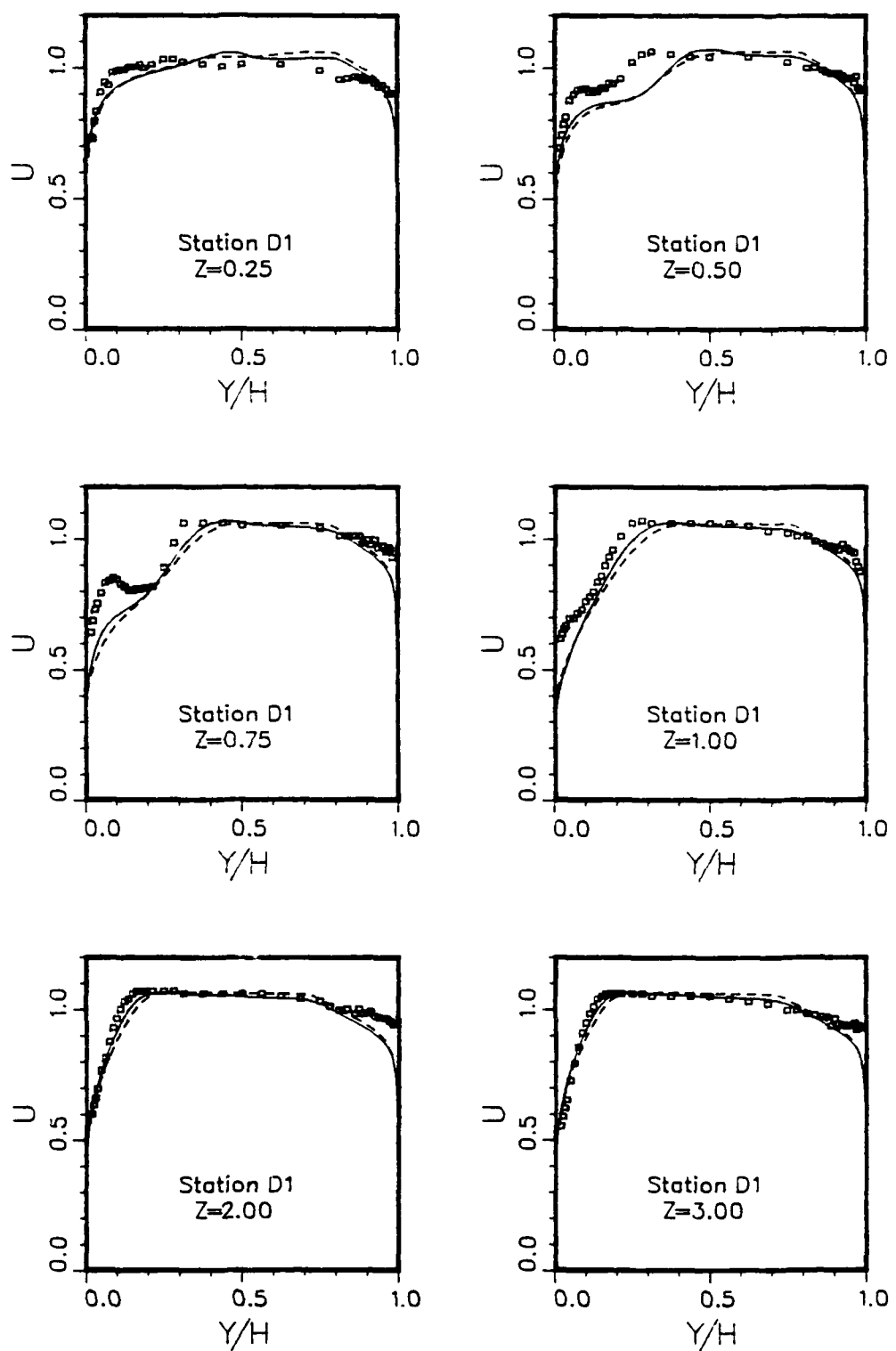
113

Fig. 16   Measured and calculated mean velocity profiles along radial lines

□, measurements (Kim, 1991); – – –, Method I; ————, Method II
(d) Streamwise mean velocity; Station D1
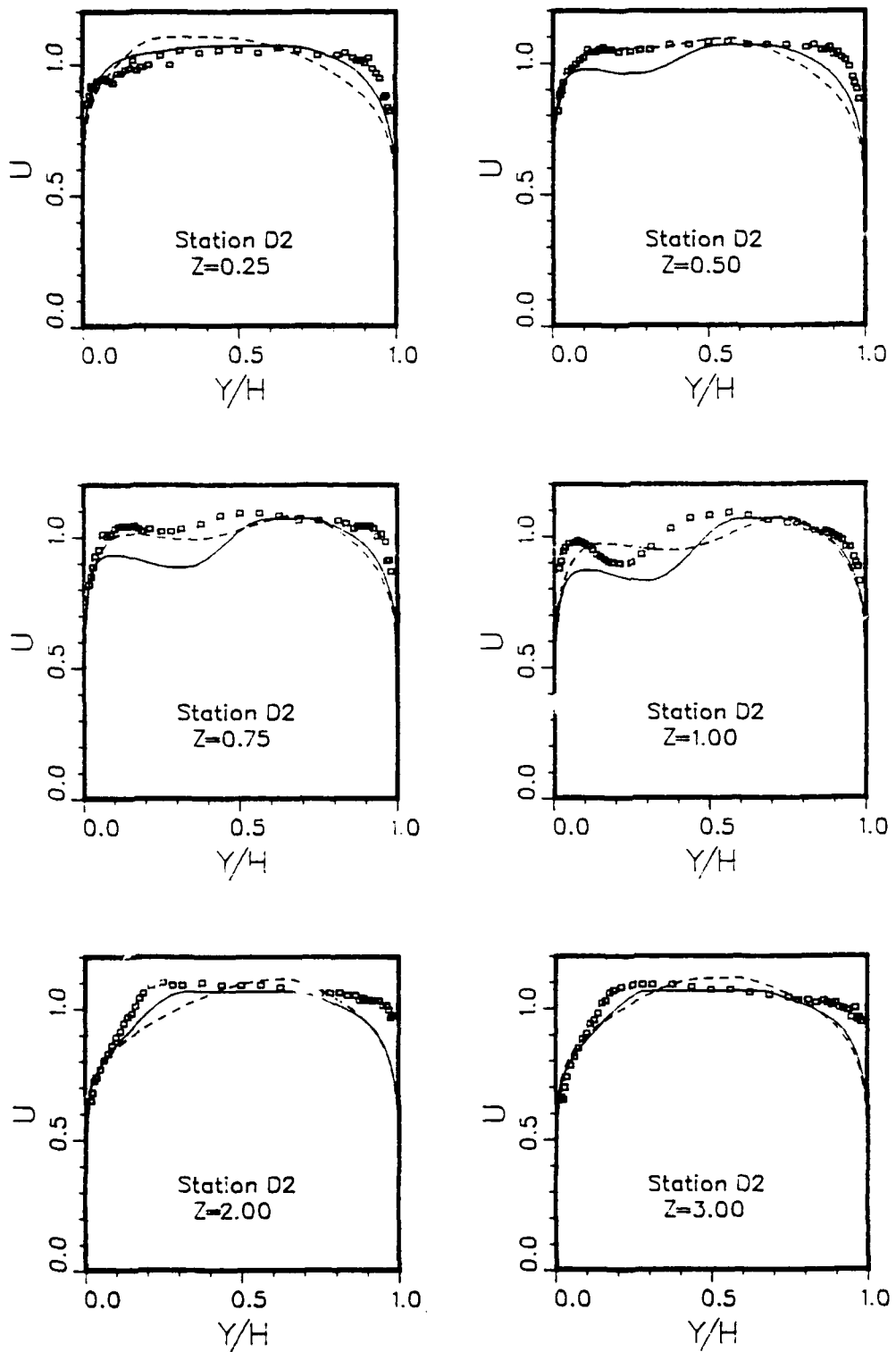
114

Fig. 16 Measured and calculated mean velocity profiles along radial lines

□, measurements (Kim, 1991); − − −, Method I; ———, Method II
(e) Streamwise mean velocity; Station D2
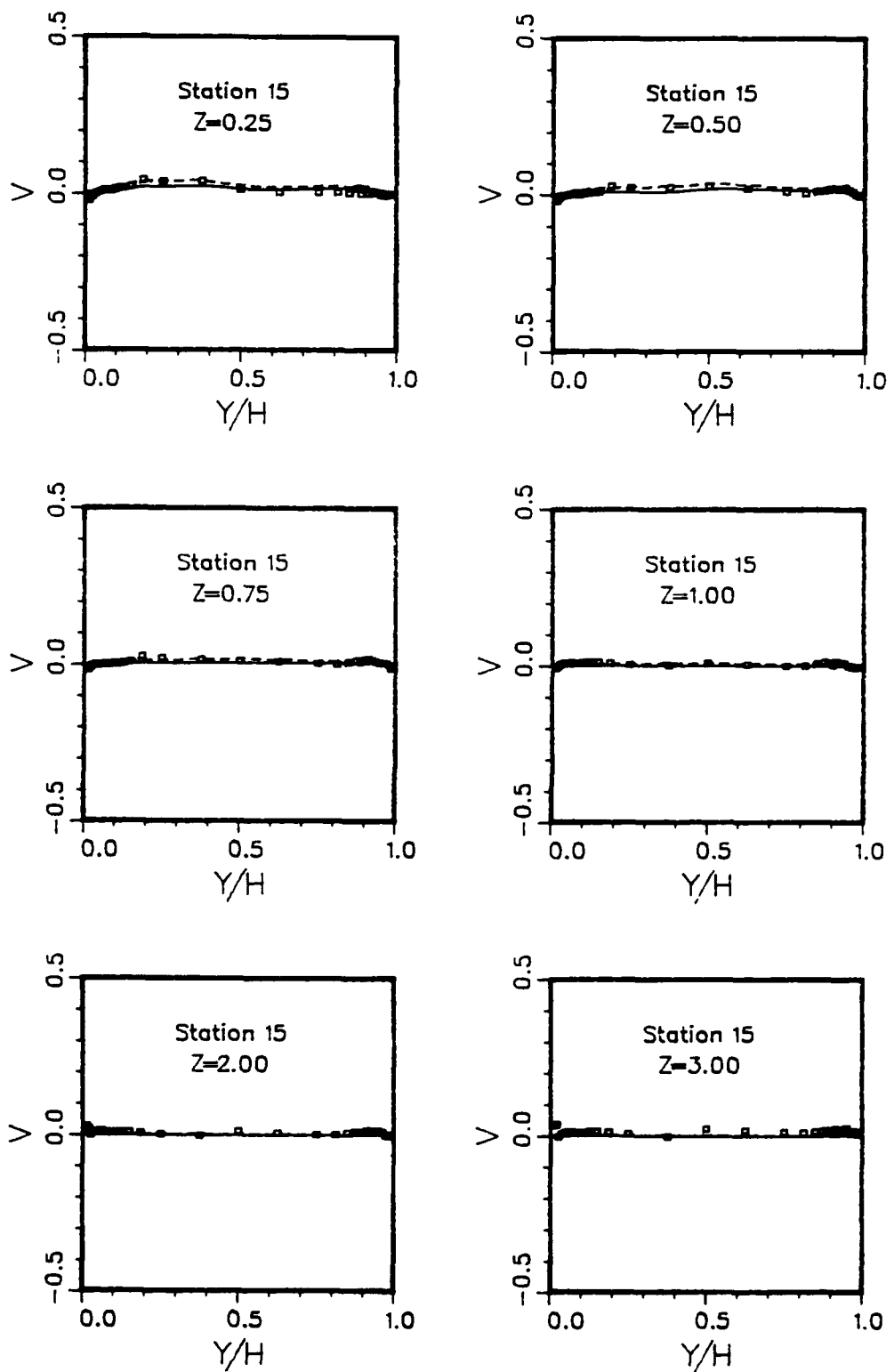
Fig. 16 Measured and calculated mean velocity profiles along radial lines

    □, measurements (Kim, 1991); – – –, Method I; ——, Method II
(f) Radial mean velocity; Station 15
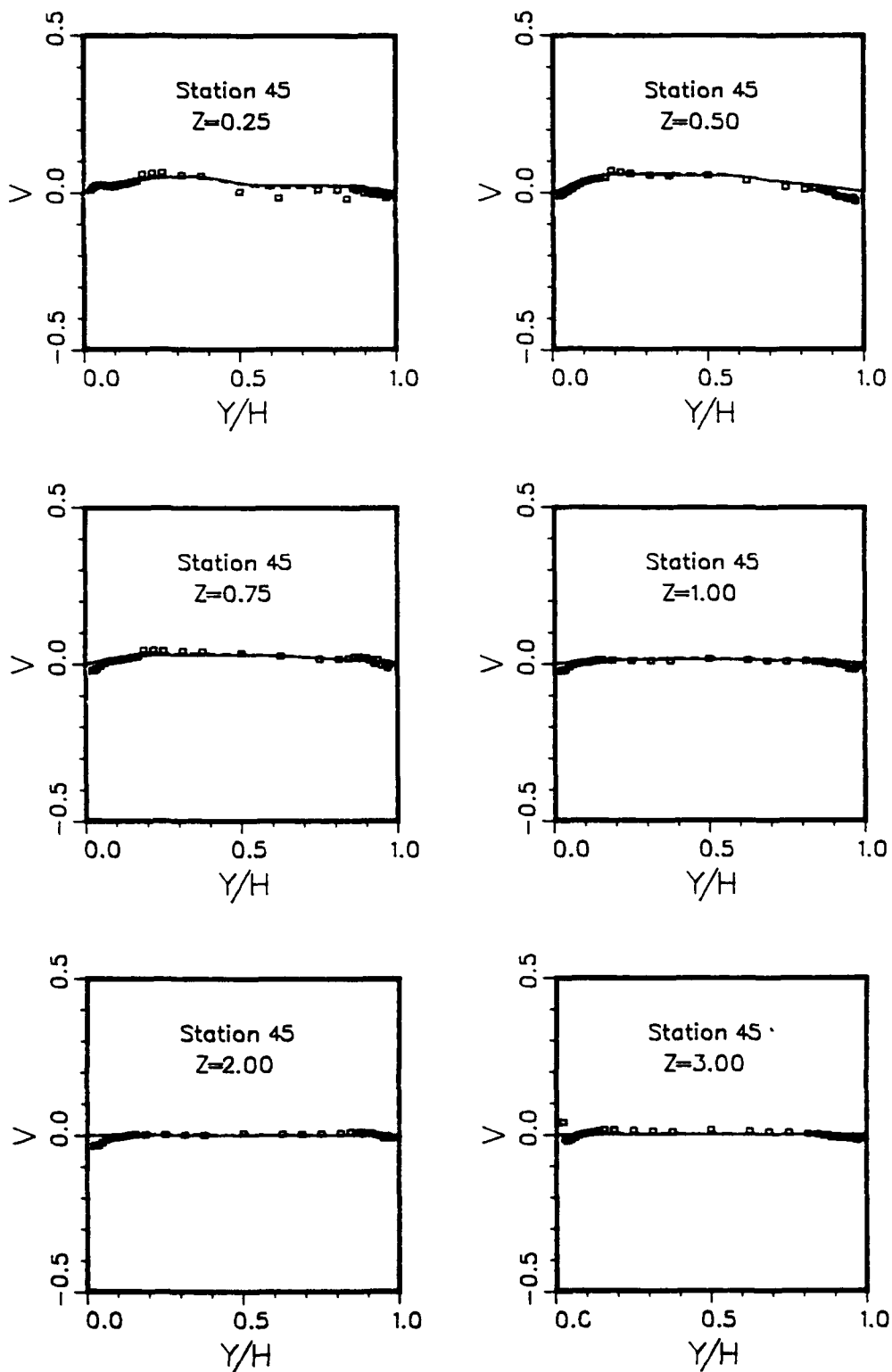
Fig. 16   Measured and calculated mean velocity profiles along radial lines

□, measurements (Kim, 1991); – – –, Method I; ———, Method II

(g) Radial mean velocity; Station 45
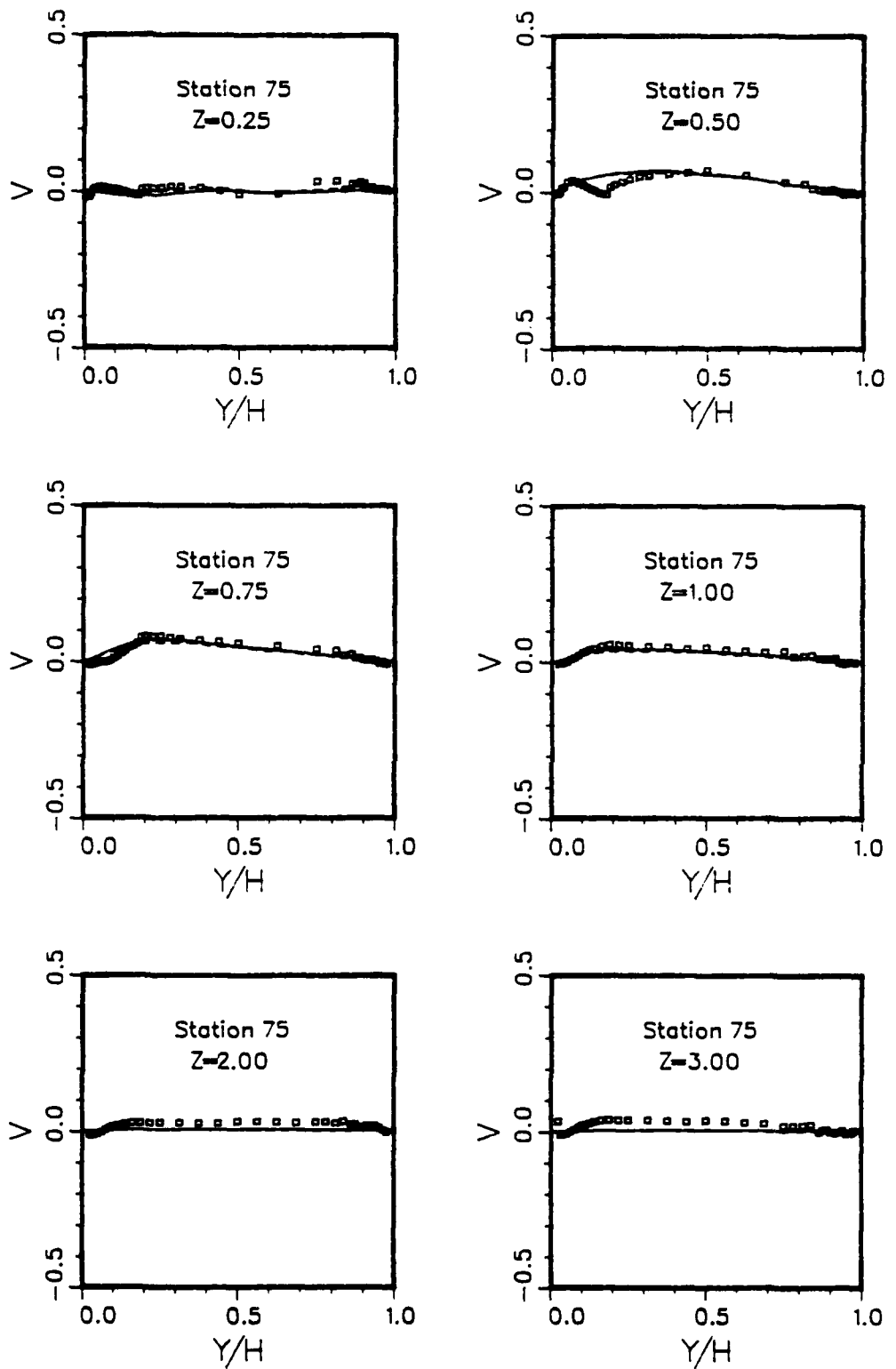
Fig. 16   Measured and calculated mean velocity profiles along radial lines

☐, measurements (Kim, 1991);   – – –, Method I; ———, Method II
(h) Radial mean velocity; Station 75
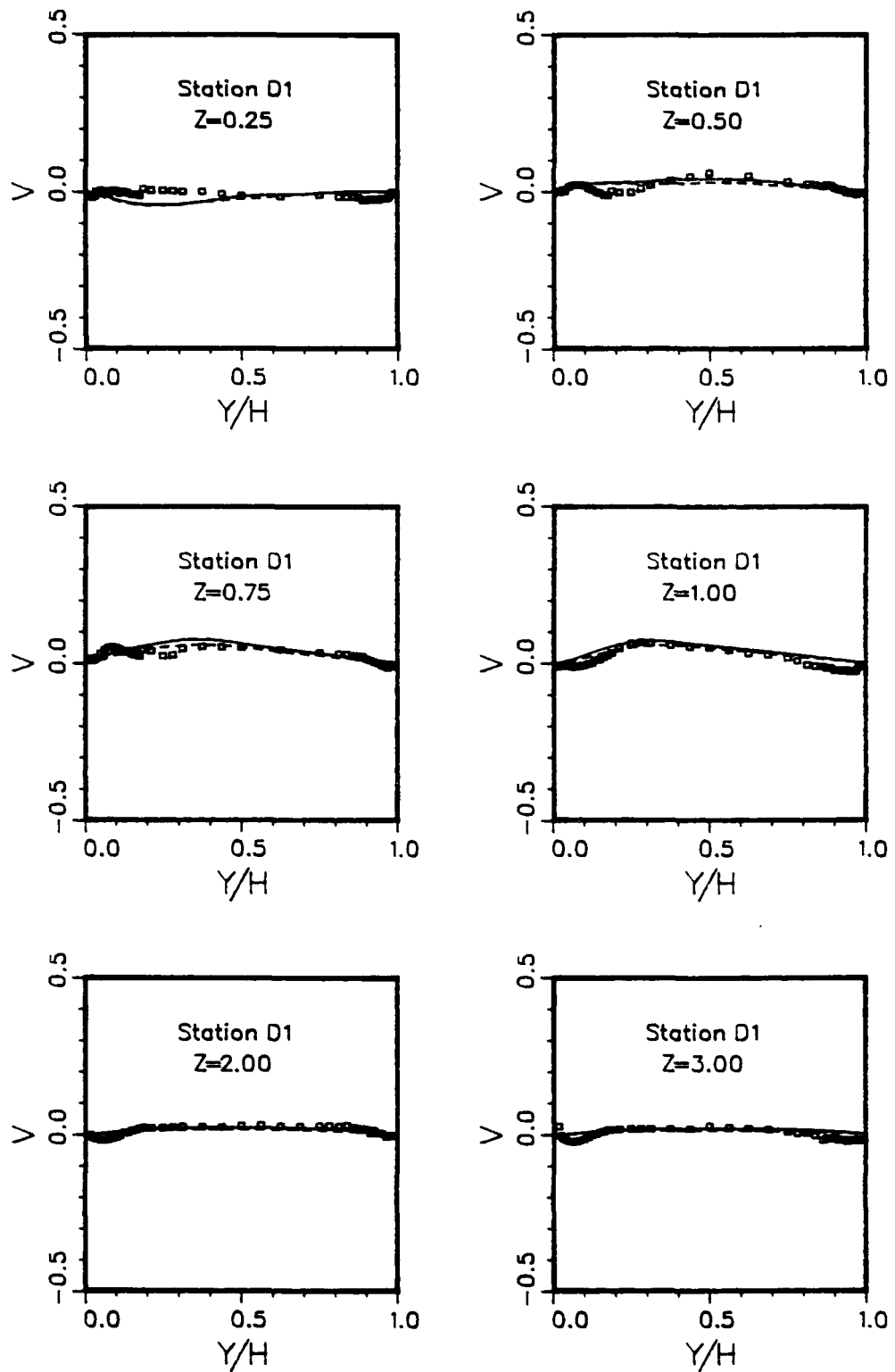
Fig. 16   Measured and calculated mean velocity profiles along radial lines
□, measurements (Kim, 1991); ‒ ‒ ‒, Method I; ————, Method II
(i) Radial mean velocity; Station D1
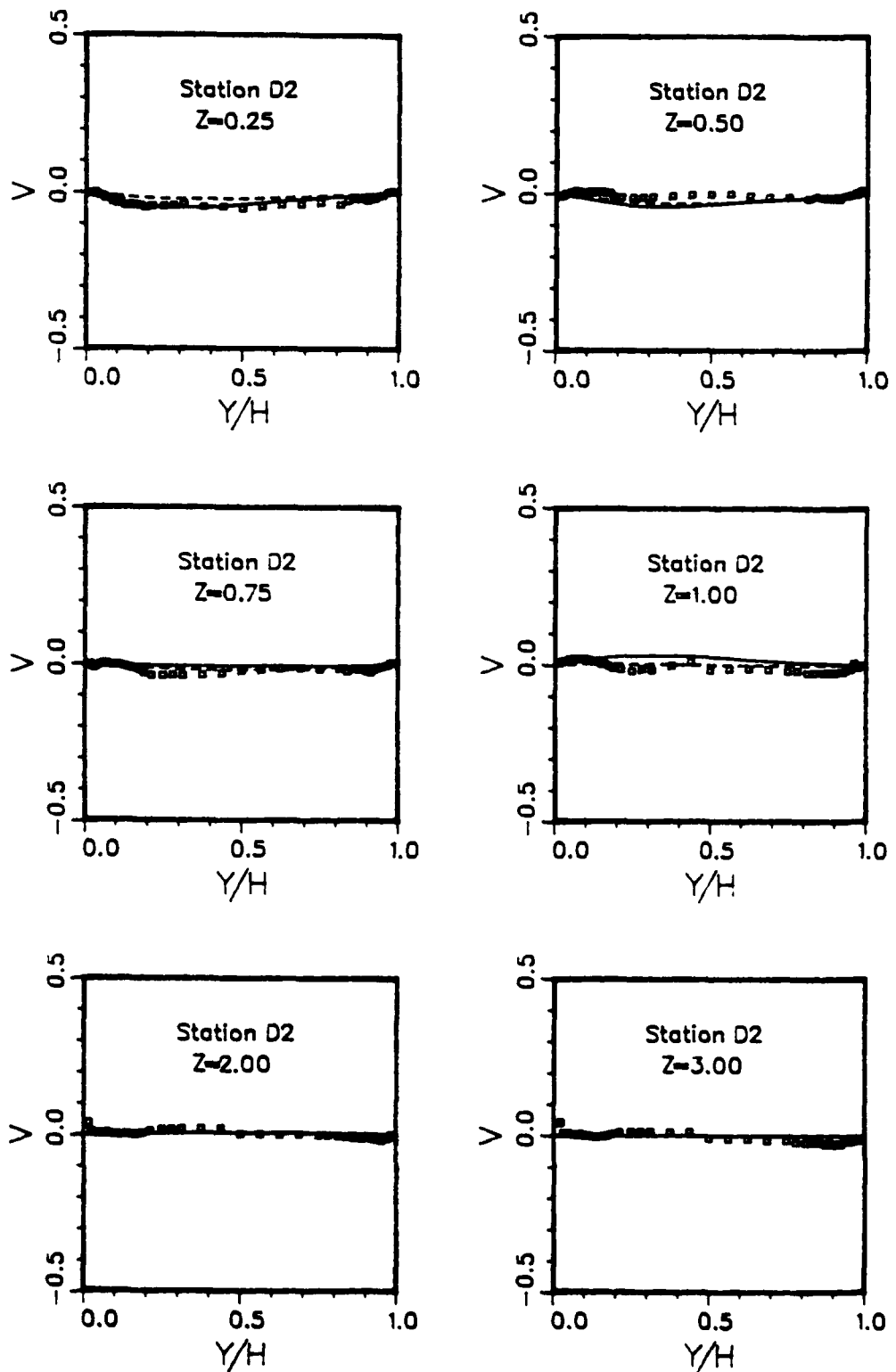
119

Fig. 16 Measured and calculated mean velocity profiles along radial lines

□, measurements (Kim, 1991); – – –, Method I; ———, Method II
(j) Radial mean velocity; Station D2
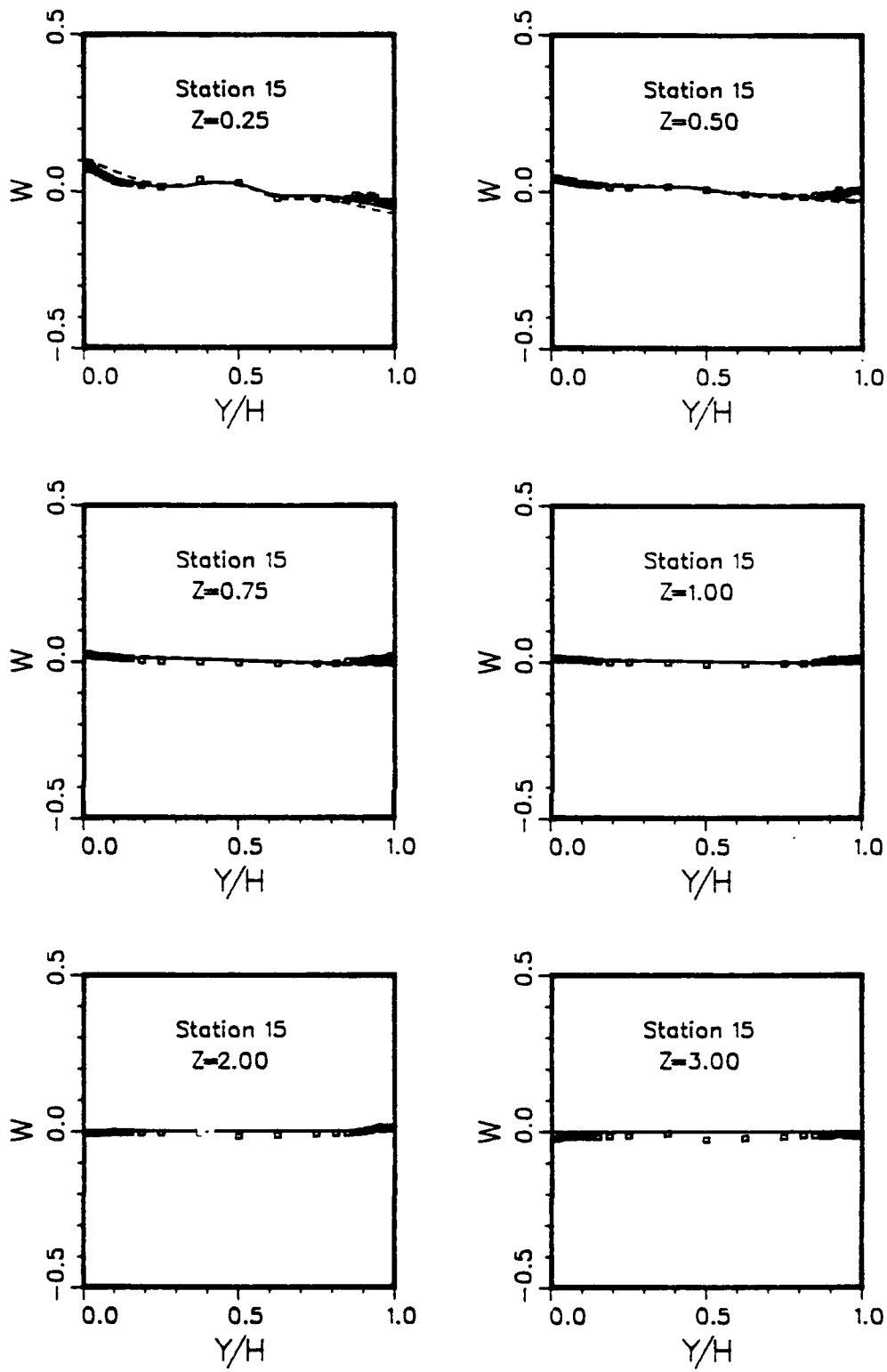
Fig. 16 Measured and calculated mean velocity profiles along radial lines

　　□, measurements (Kim, 1991); — — —, Method I; ————, Method II

　　(k) Vertical mean velocity; Station 15
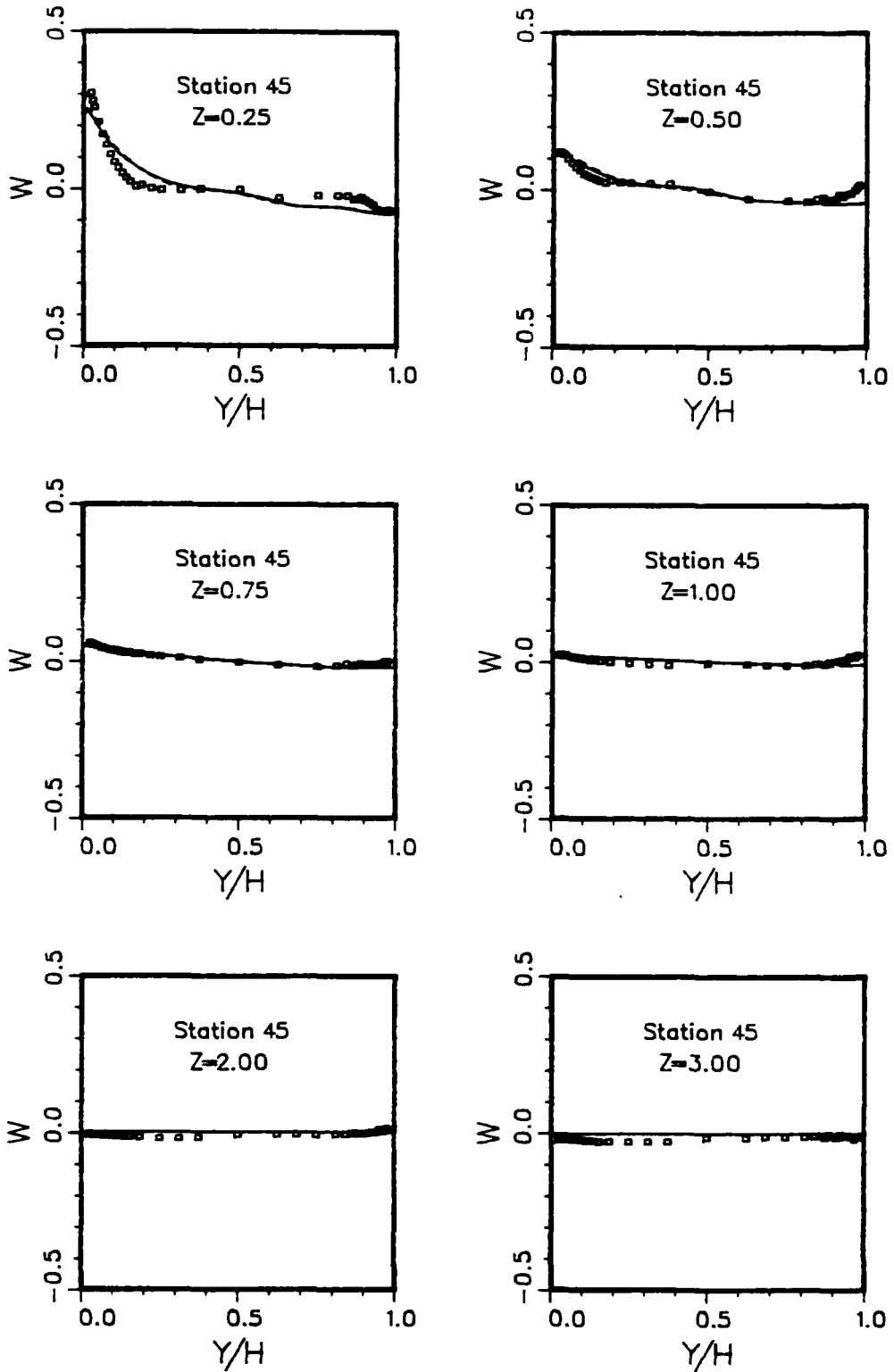
Fig. 16   Measured and calculated mean velocity profiles along radial lines

□, measurements (Kim, 1991); − − −, Method I; ────, Method II
(l) Vertical mean velocity; Station 45
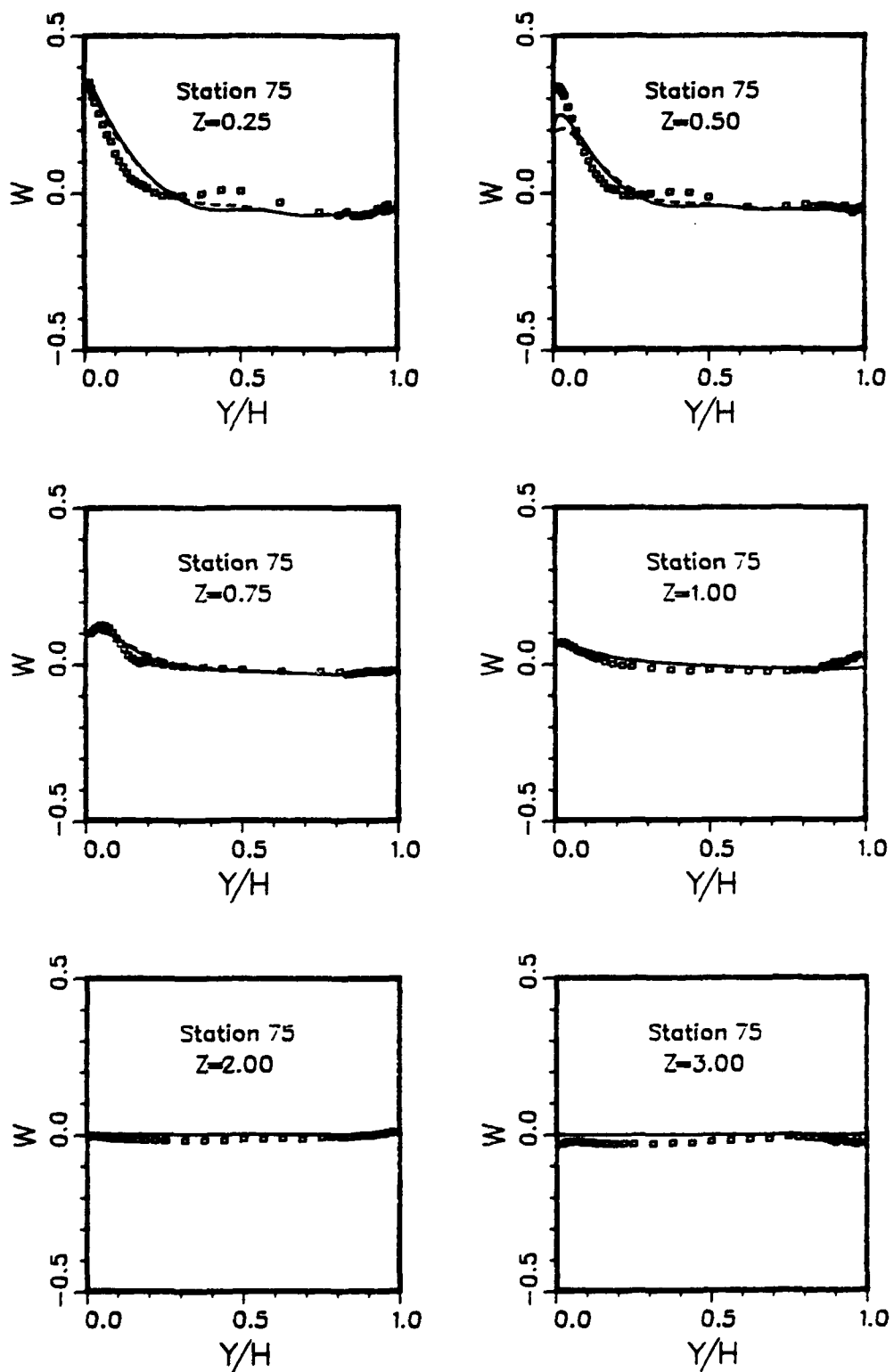
Fig. 16 Measured and calculated mean velocity profiles along radial lines

□, measurements (Kim, 1991); ─ ─ ─, Method I; ─────, Method II
(m) Vertical mean velocity; Station 75
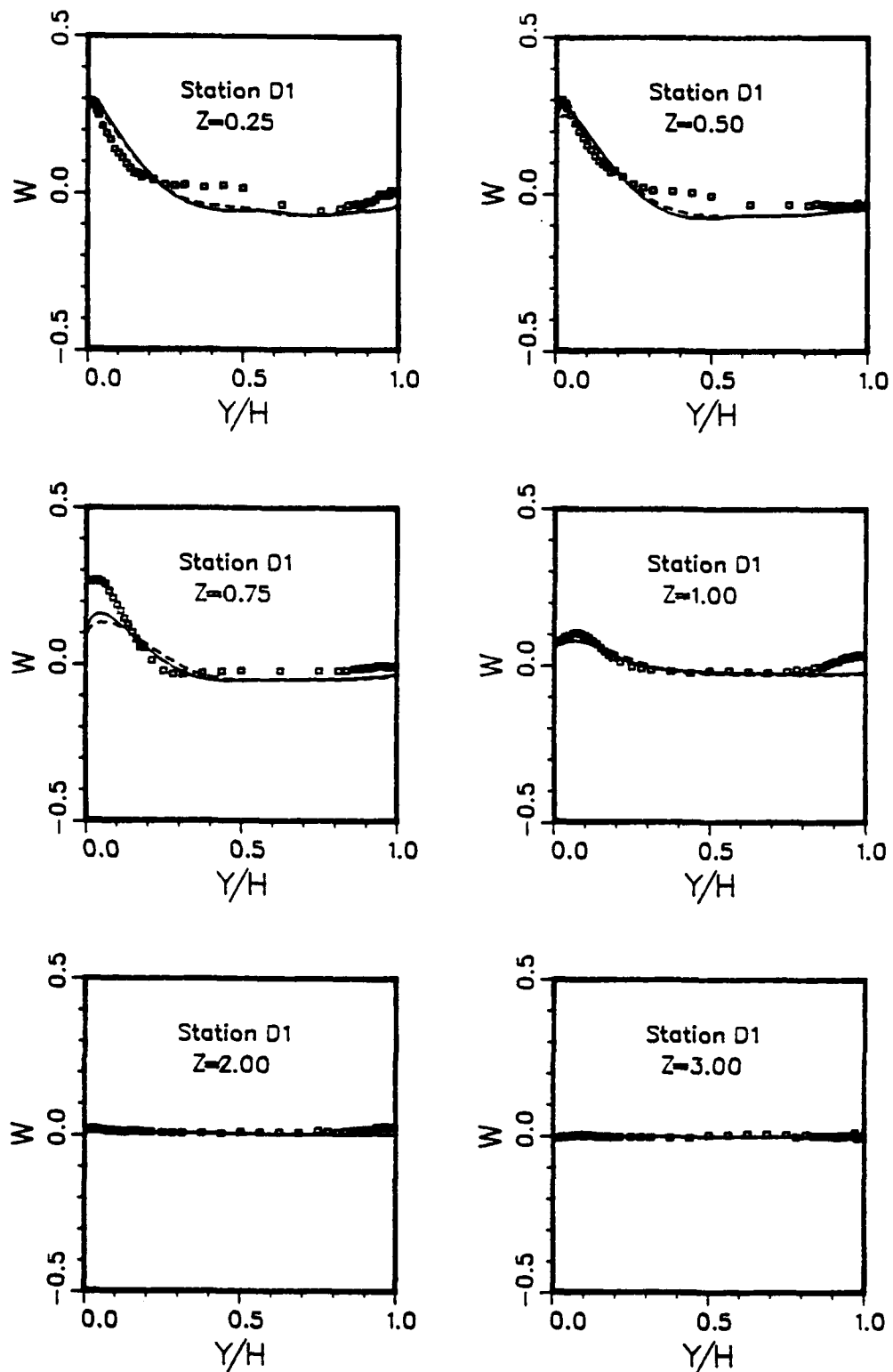
123

Fig. 16 Measured and calculated mean velocity profiles along radial lines

□, measurements (Kim, 1991); − − −, Method I; ————, Method II
(n) Vertical mean velocity; Station D1
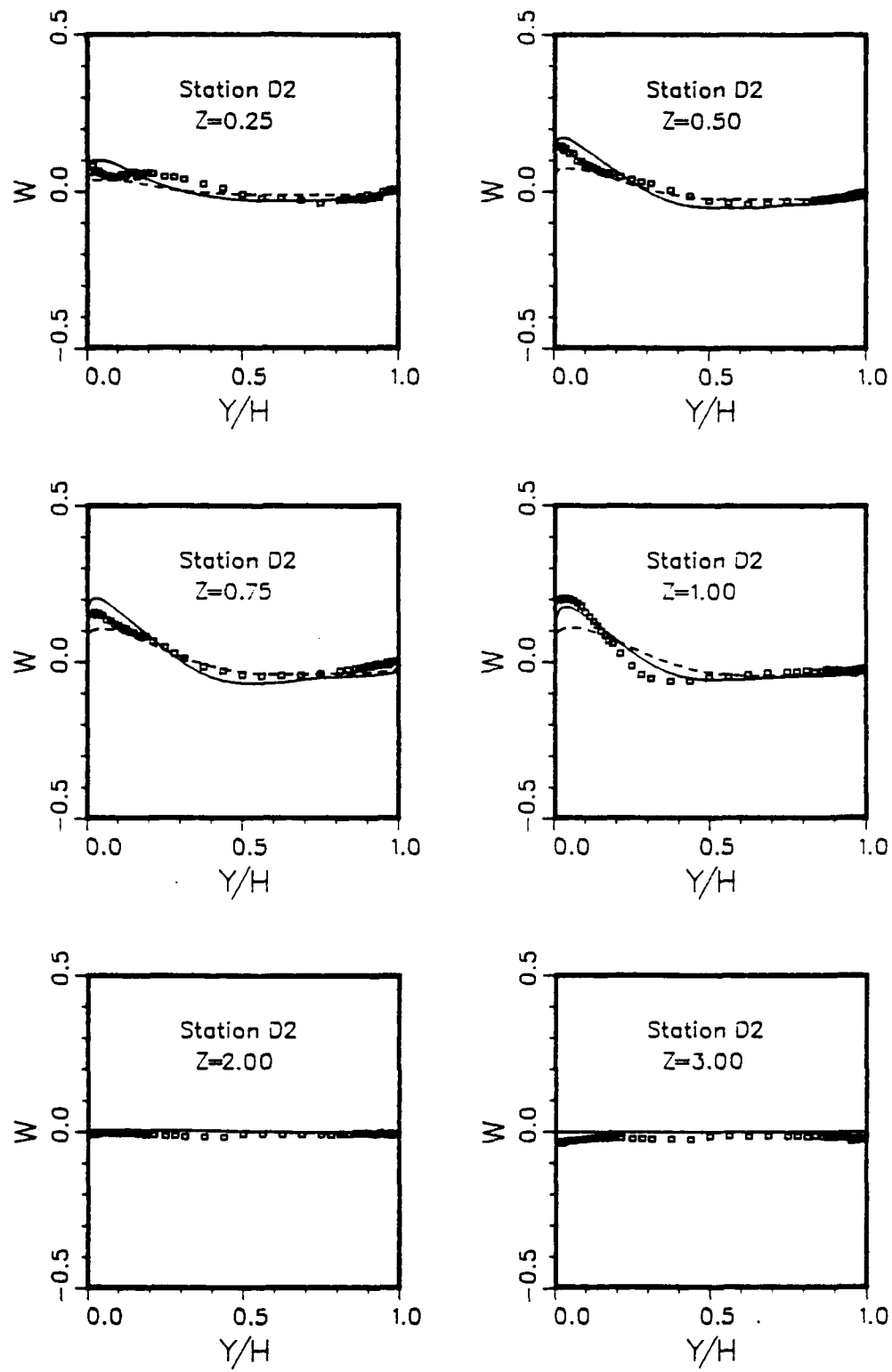
124

Fig. 16   Measured and calculated mean velocity profiles along radial lines

□, measurements (Kim, 1991); – – –, Method I; ————, Method II
(o) Vertical mean velocity; Station D2
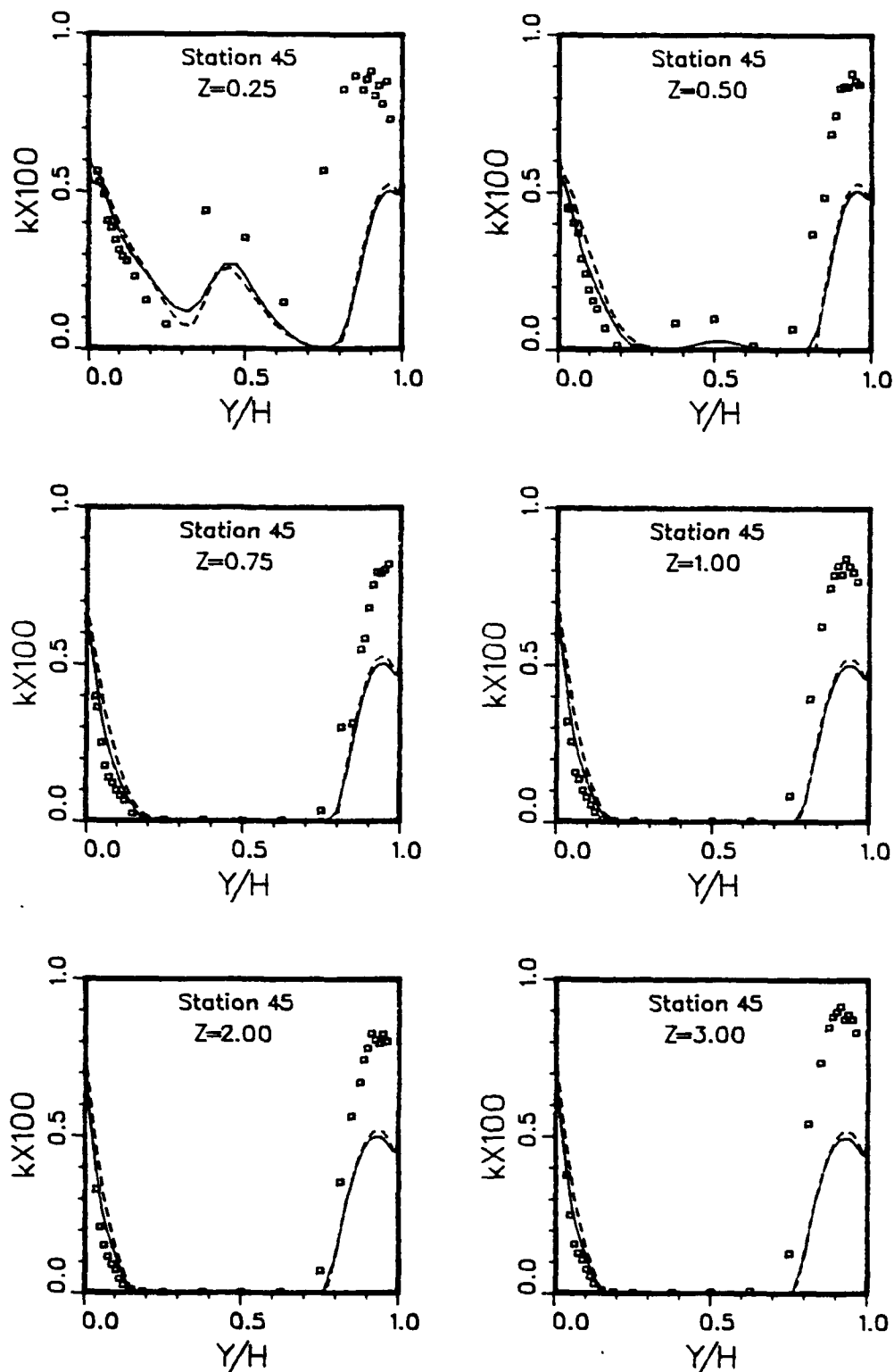
Fig. 17 Measured and calculated turbulent kinetic energy profiles along radial lines
□, measurements (Kim, 1991); – – –, Method I; ———, Method II
(a) Station 45
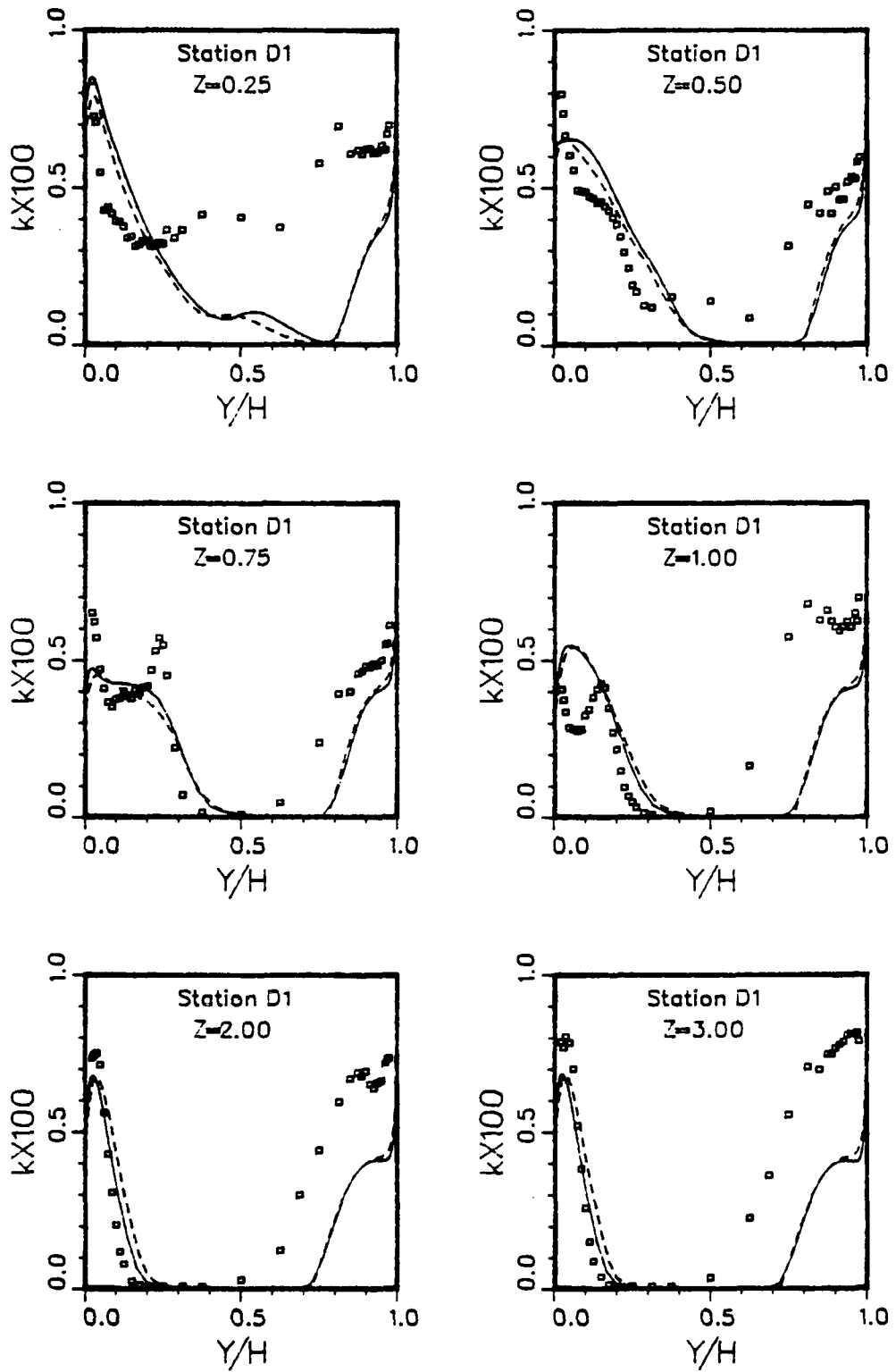
126

Fig. 17 Measured and calculated turbulent kinetic energy profiles along radial lines
□, measurements (Kim, 1991); − − −, Method I; ————, Method II
(b) Station D1

127
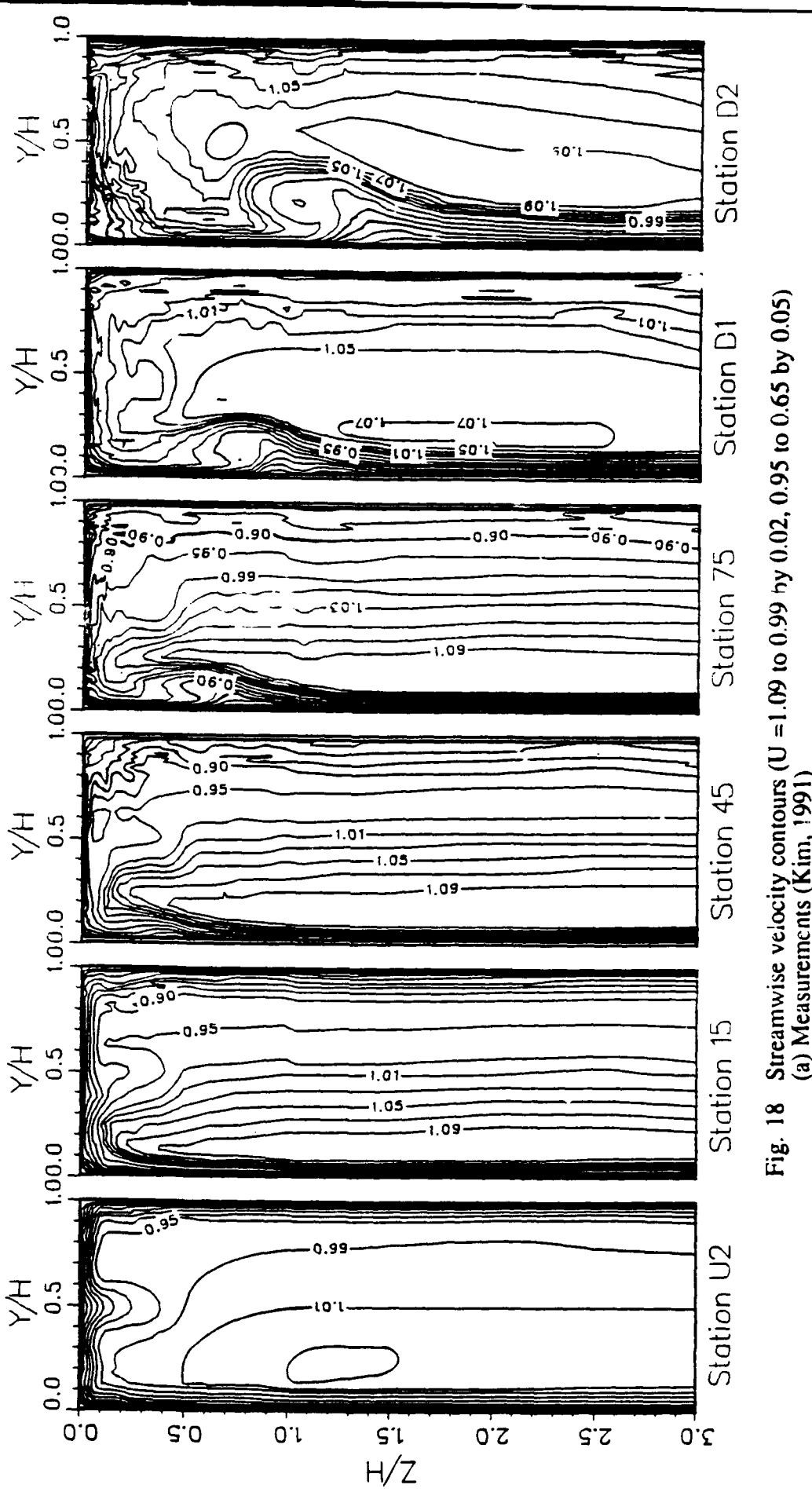
Fig. 18 Streamwise velocity contours (U =1.09 to 0.99 by 0.02, 0.95 to 0.65 by 0.05)
(a) Measurements (Kim, 1991)

128
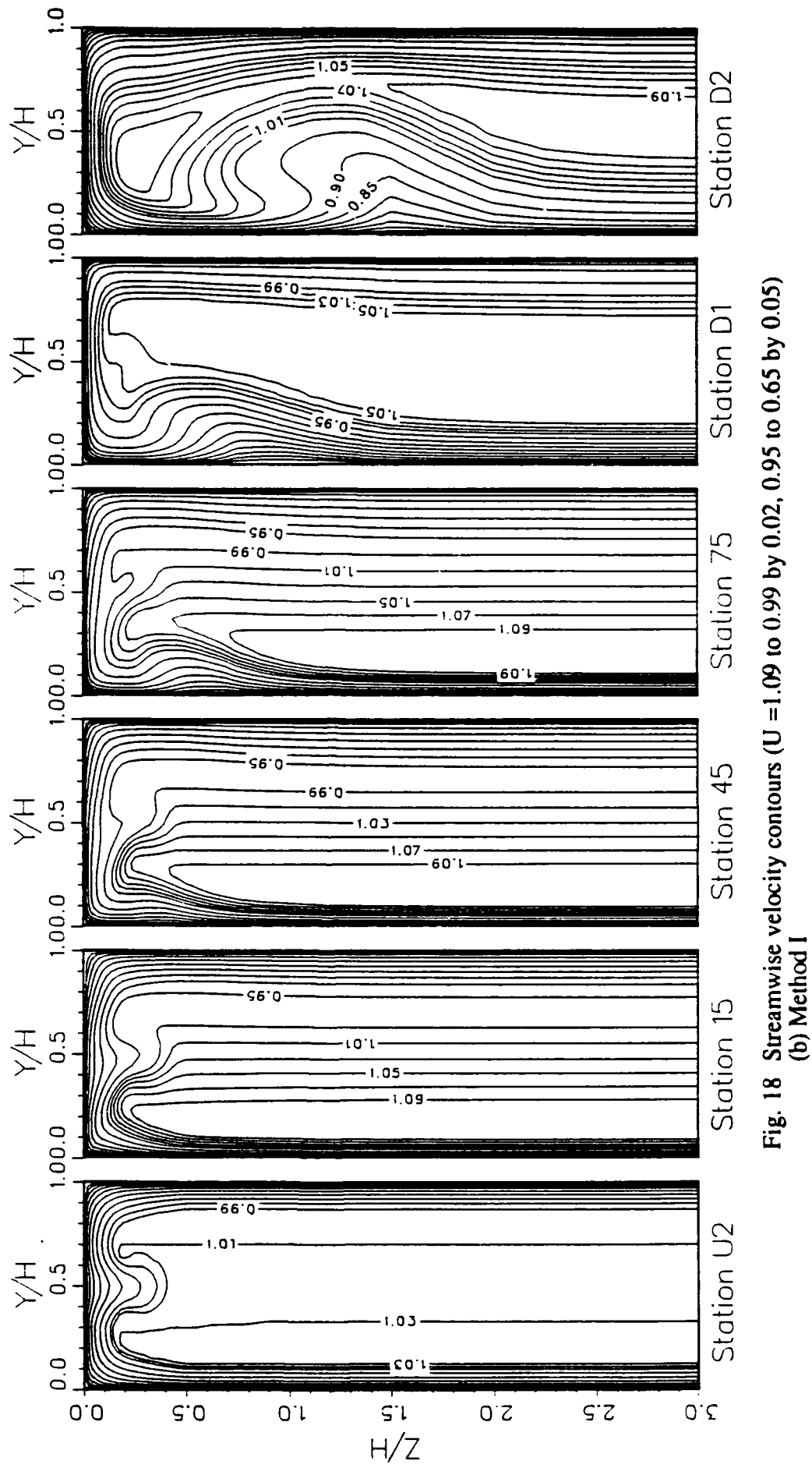
Fig. 18 Streamwise velocity contours (U =1.09 to 0.99 by 0.02, 0.95 to 0.65 by 0.05) (b) Method I

129
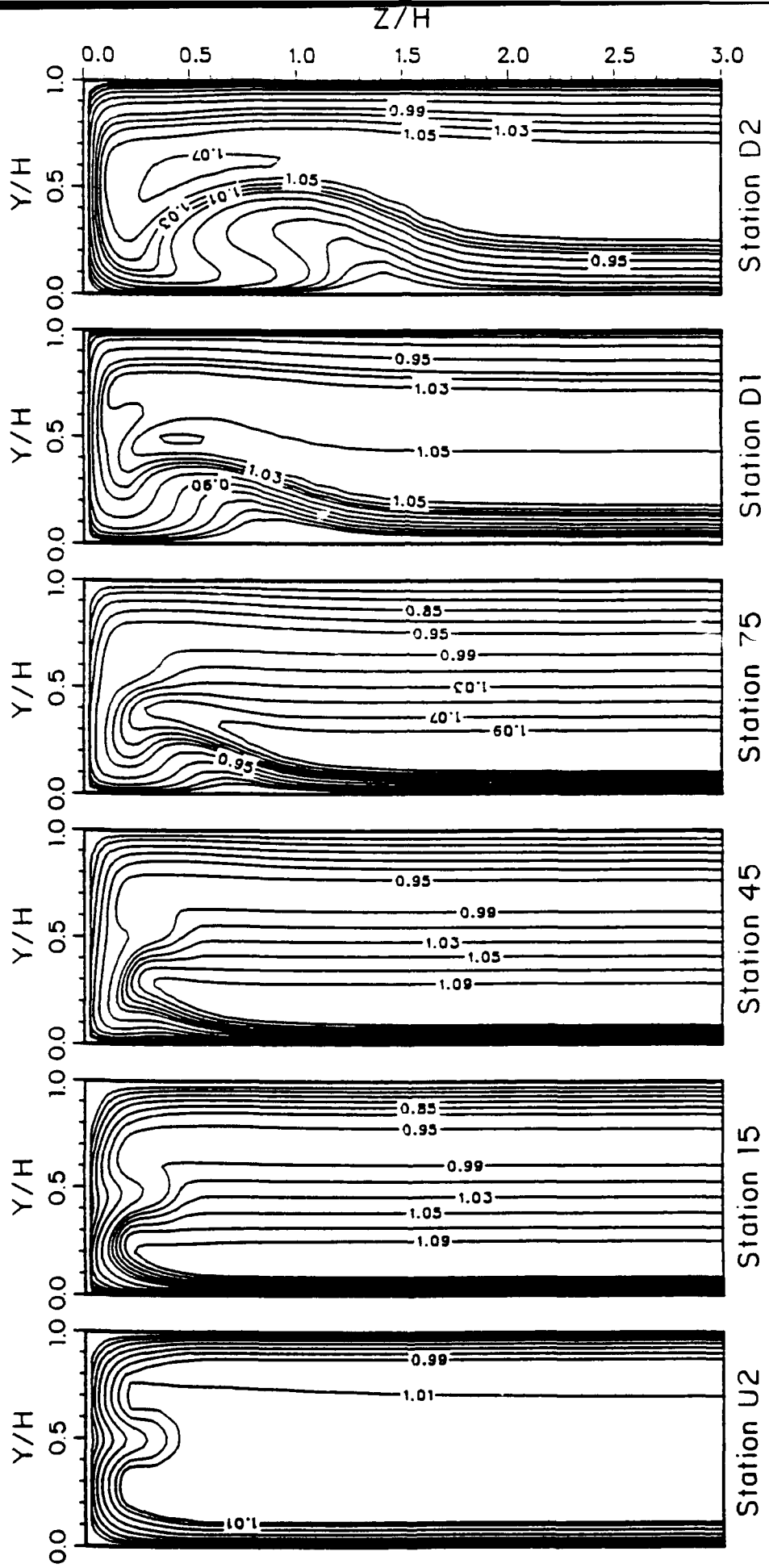
Fig. 18 Streamwise velocity contours (U = 1.09 to 0.99 by 0.02, 0.95 to 0.65 by 0.05) (c) Method II

130
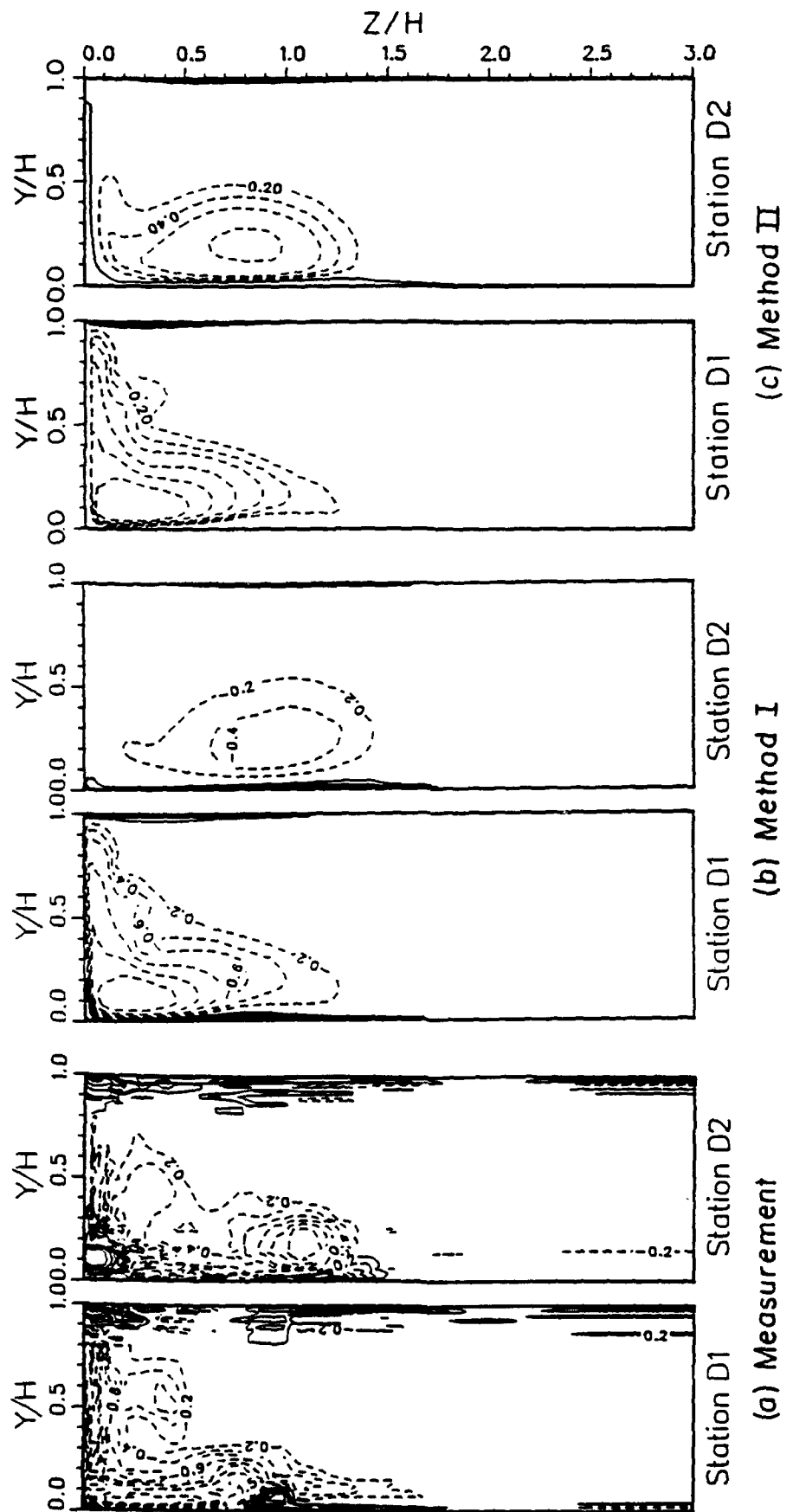
Fig. 19 Streamwise voriticity contours ($\frac{\Omega_x H}{U^o}$ = 0.2, 0.4, 0.6, 0.9, 1.2, 1.5, 2.0, 3.0)
(a) measurements (Kim, 1991); (b) Method I; (c) Method II

131

(a)

(b)
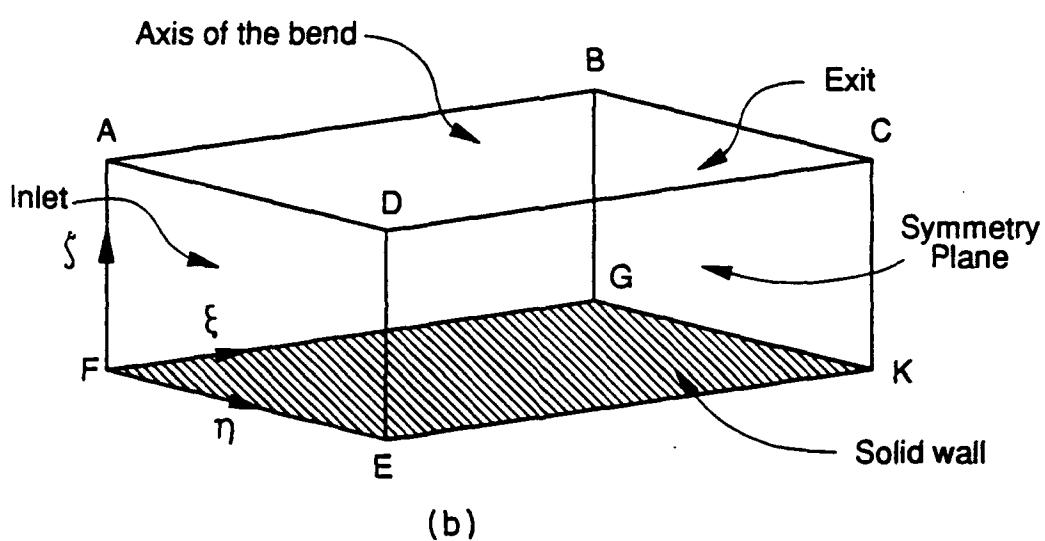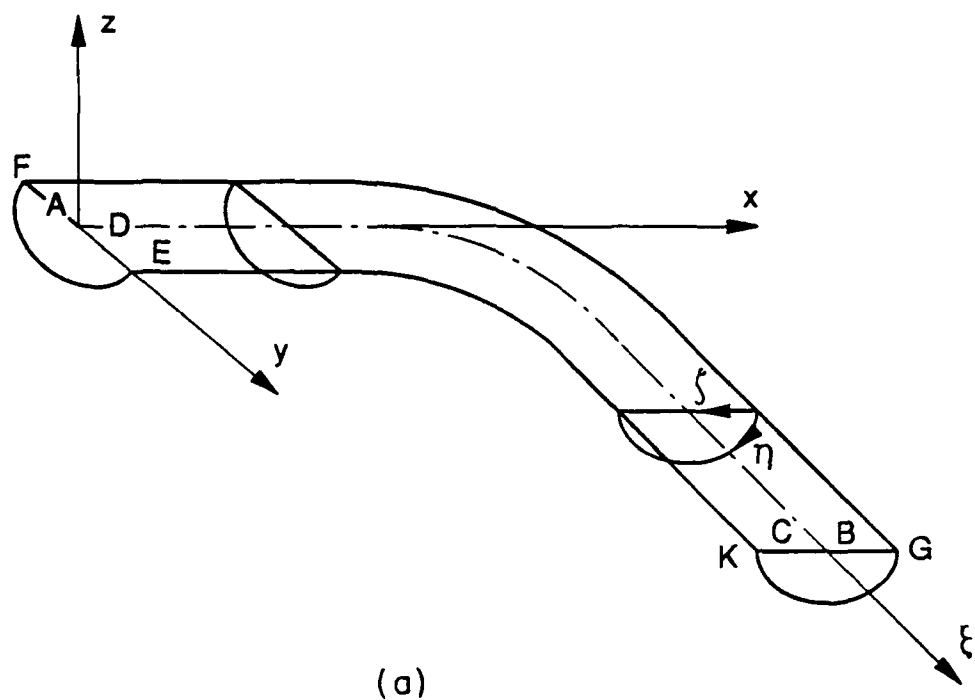
Fig. 20   Curvilinear coordinates for a typical pipe bend configuration
(a) physical solution domain; (b) transformed solution domain

132
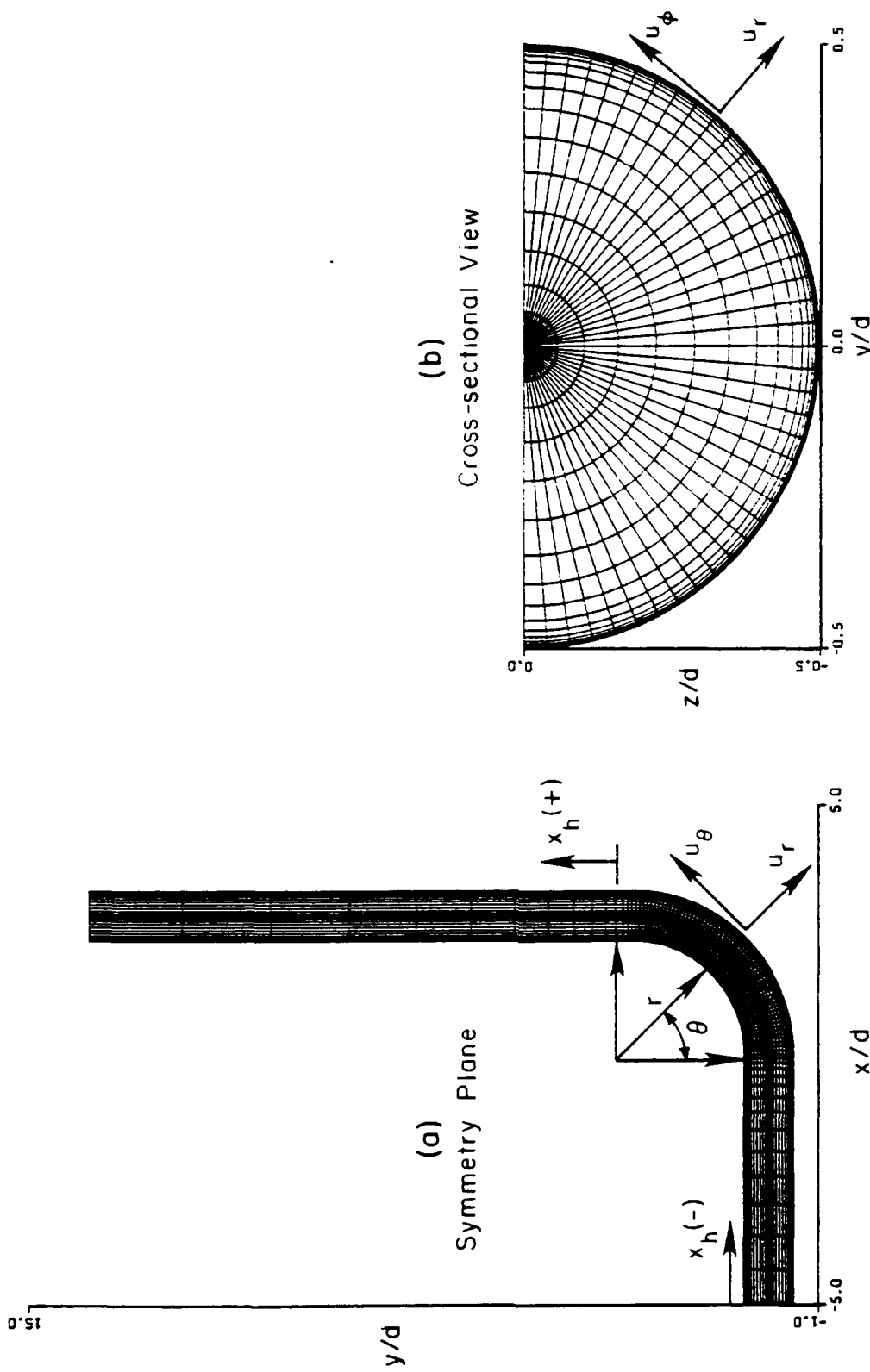
Fig. 21 Typical views of the computational grid for a pipe bend configuration
(a) plane of symmetry view; (b) cross-sectional view
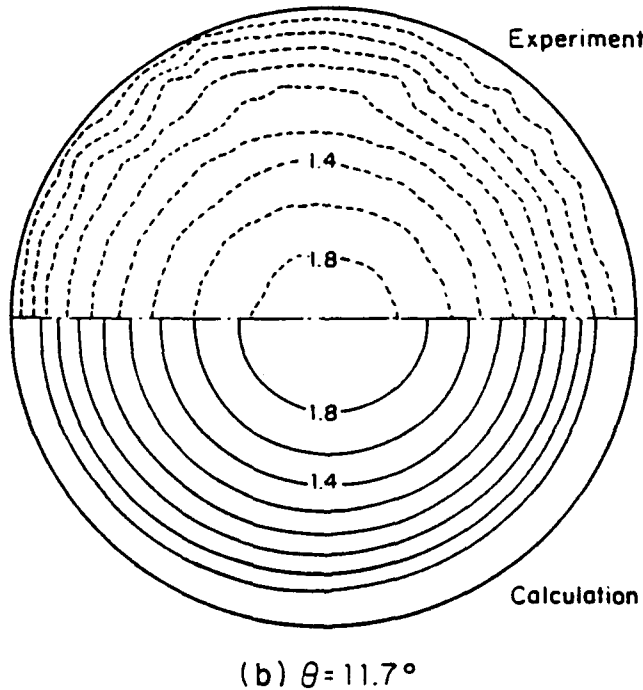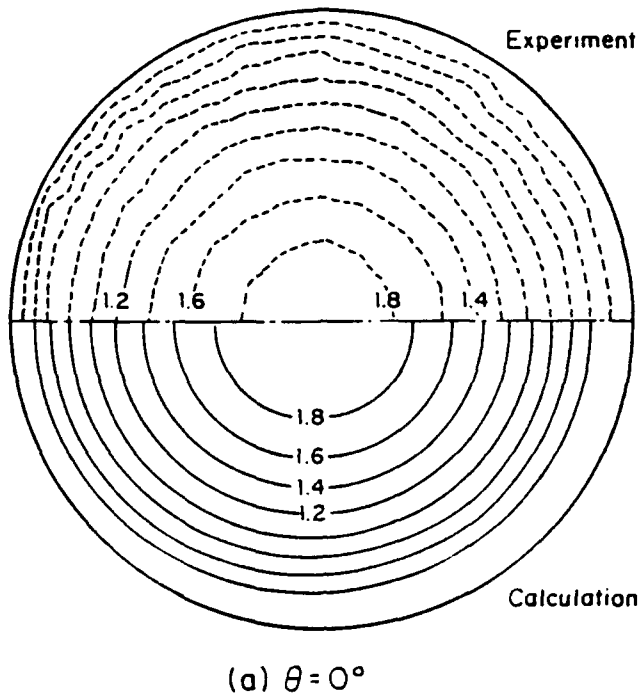
133

Fig. 22   Measured (Bovendeerd et al., 1987) and calculated streamwise velocity contours
        (a) $\theta = 0^o$; (b) $\theta = 11.7^o$
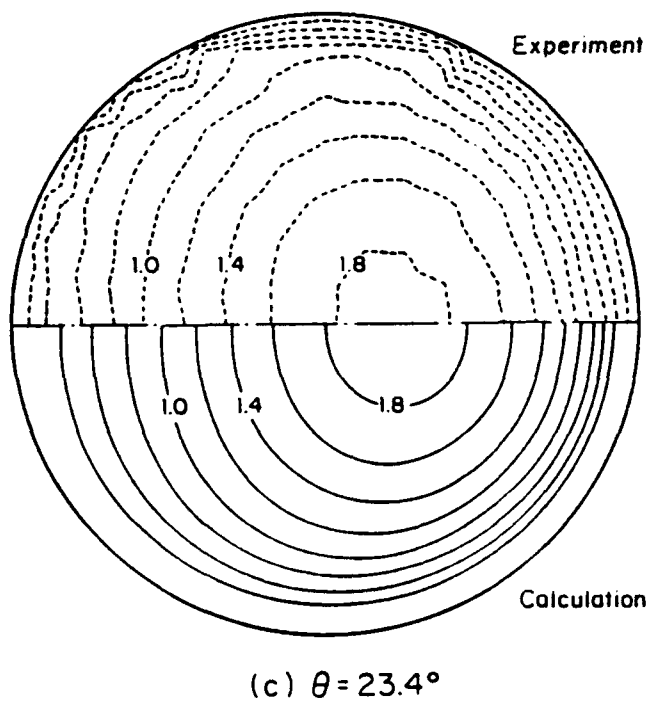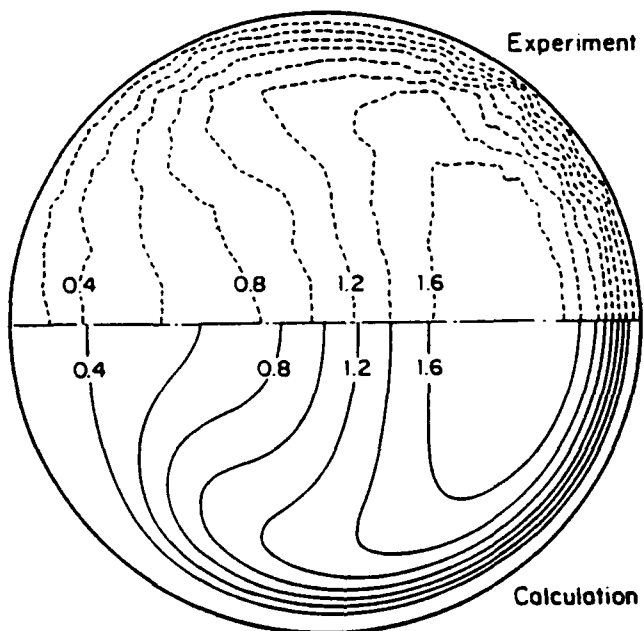
(c) $\theta = 23.4°$

(d) $\theta = 39.8°$

Fig. 22 Measured (Bovendeerd et al., 1987) and calculated streamwise velocity contours
(c) $\theta = 23.4°$; (d) $\theta = 39.8°$

135
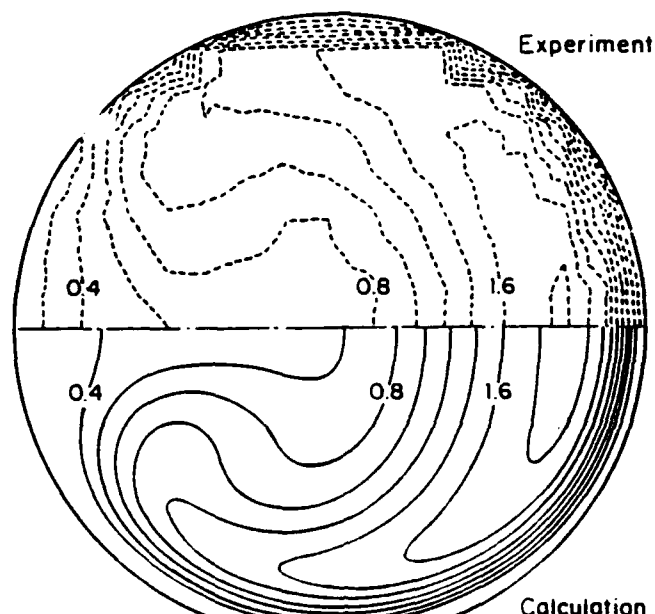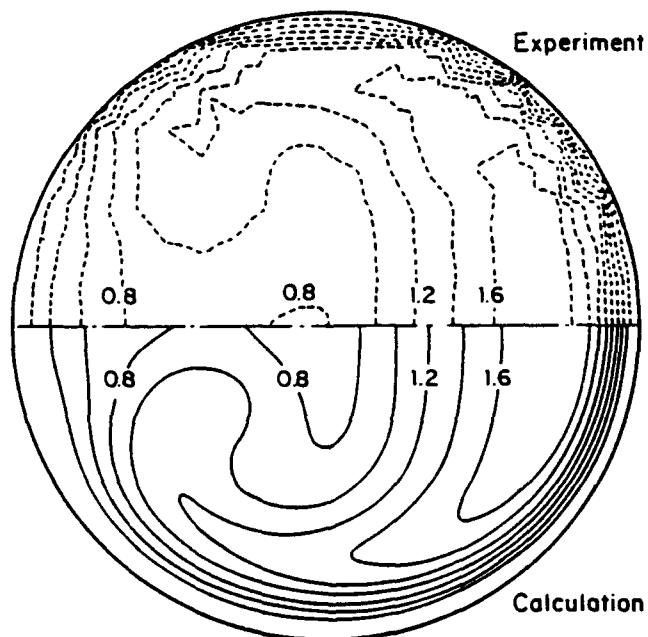
(e) $\theta = 58.5°$

(f) $\theta = 81.9°$

Fig. 22 Measured (Bovendeerd et al., 1987) and calculated streamwise velocity contours
(e) $\theta = 58.5°$; (f) $\theta = 81.9°$
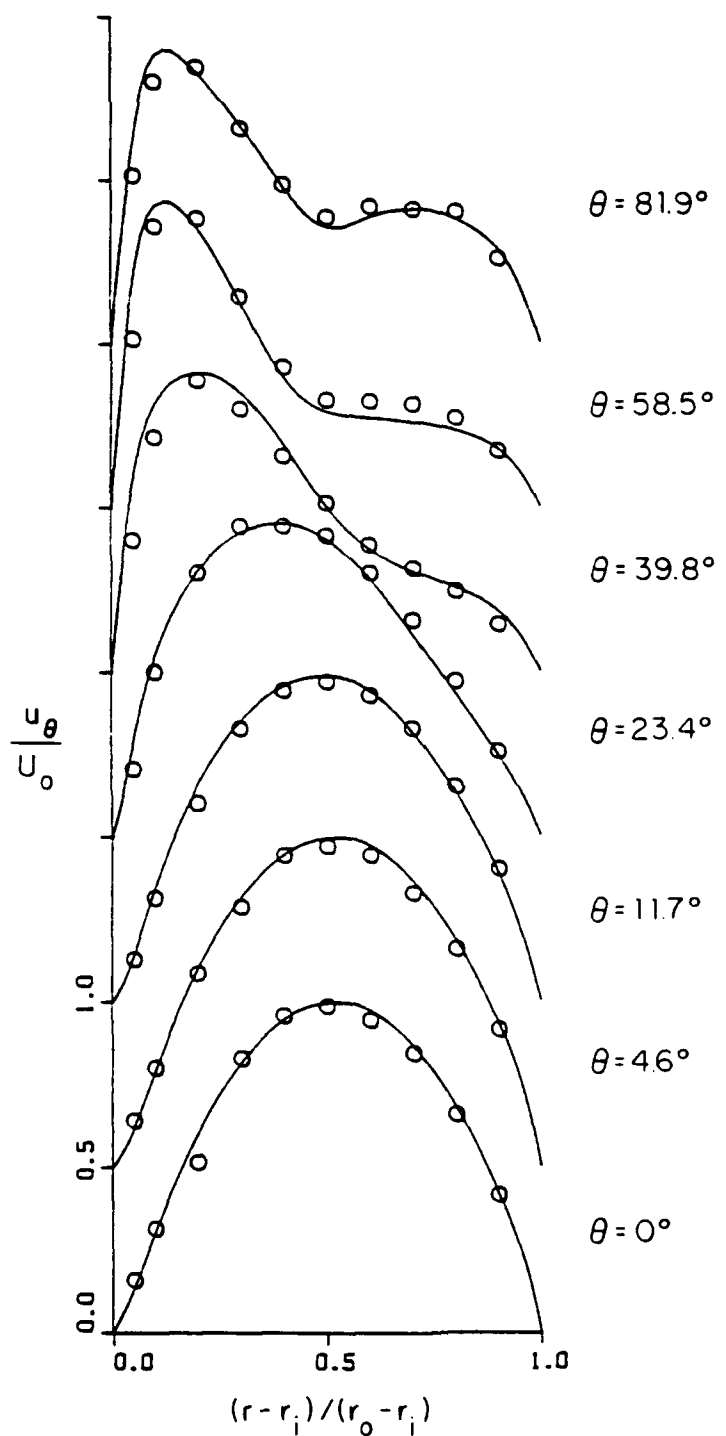
Fig. 23 Measured and calculated streamwise velocity profiles on the plane of symmetry:
o, measurements (Bovendeerd et al., 1987); —————,calculation
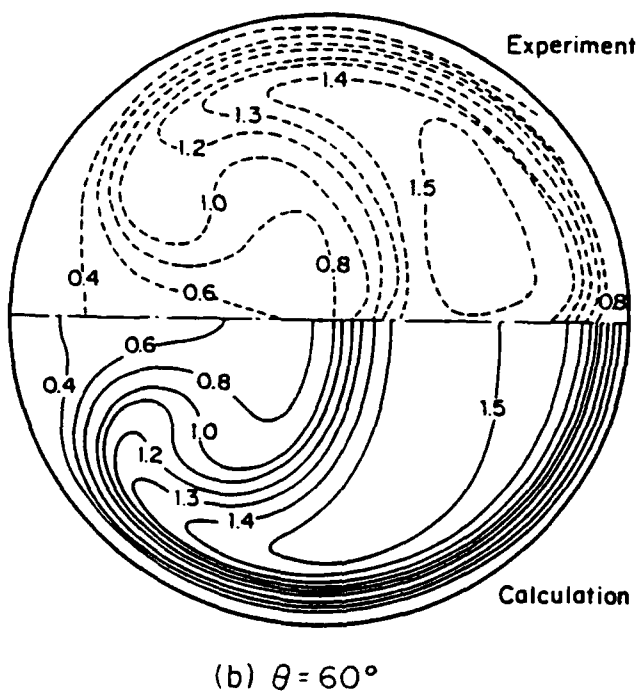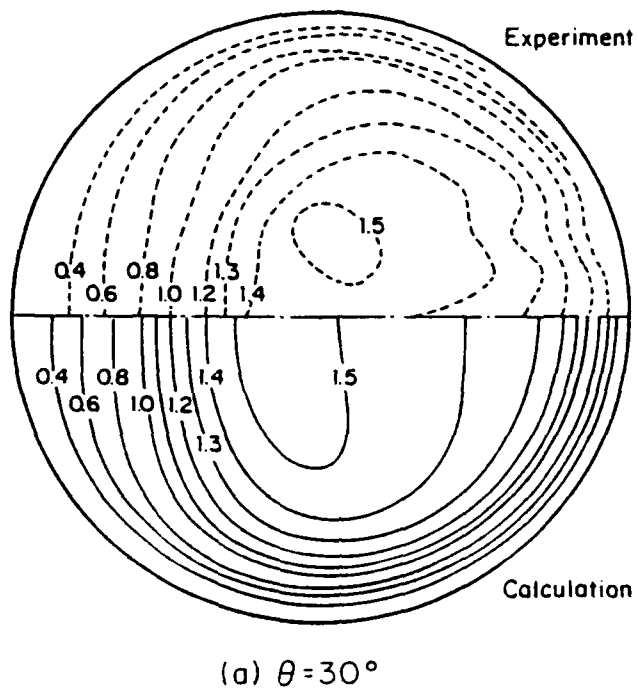
Fig. 24 Measured (Enayet et al., 1982b) and calculated streamwise velocity contours
(a) θ = 30°; (b) θ = 60°
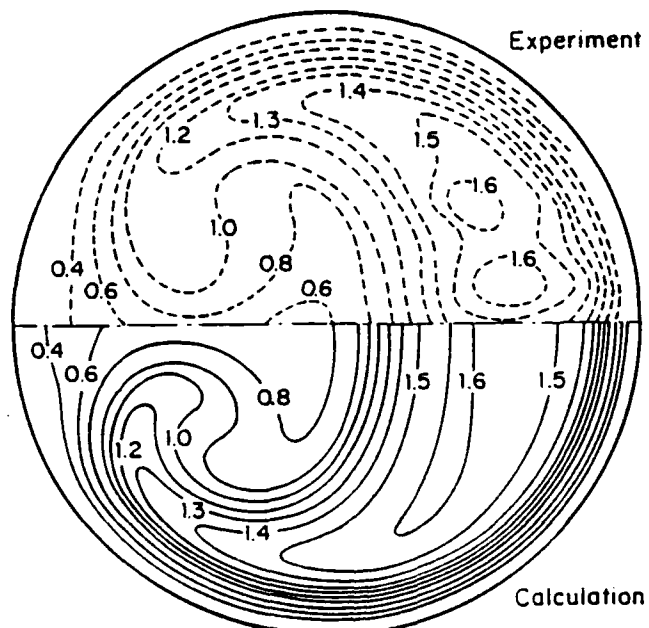
(c) $\theta = 75°$
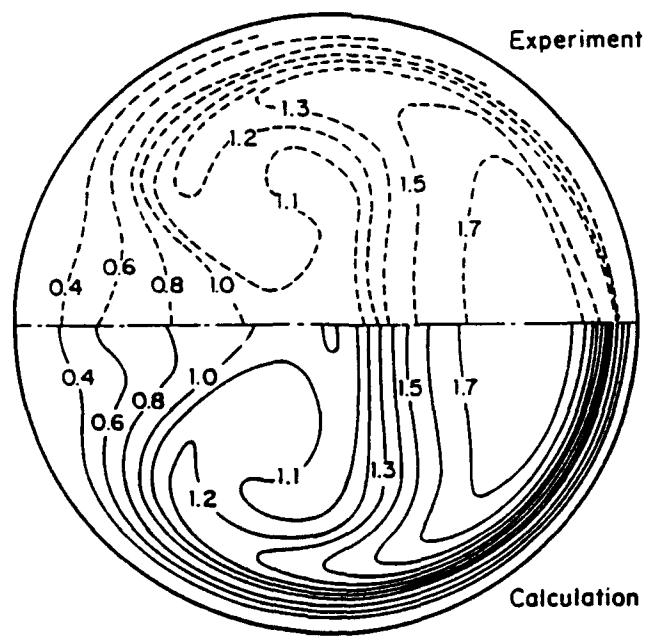
(d) $x_h = +1d$

Fig. 24 Measured (Enayet et al., 1982b) and calculated streamwise velocity contours
(c) $\theta = 75°$; (d) $x_h = +1d$

139
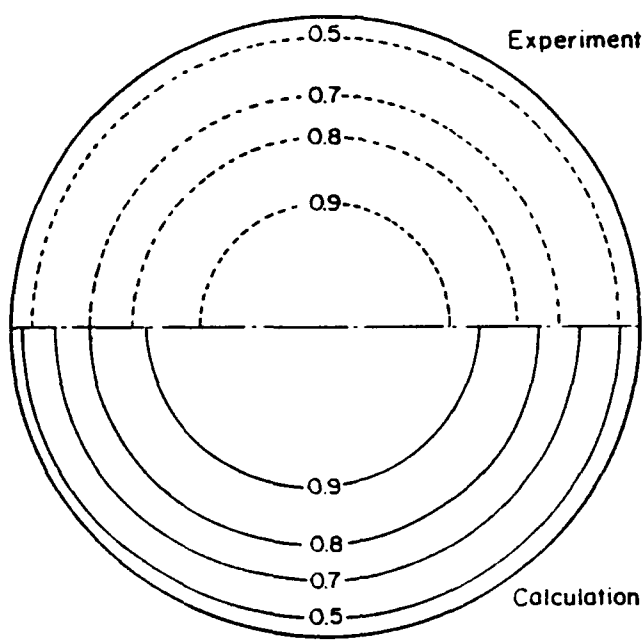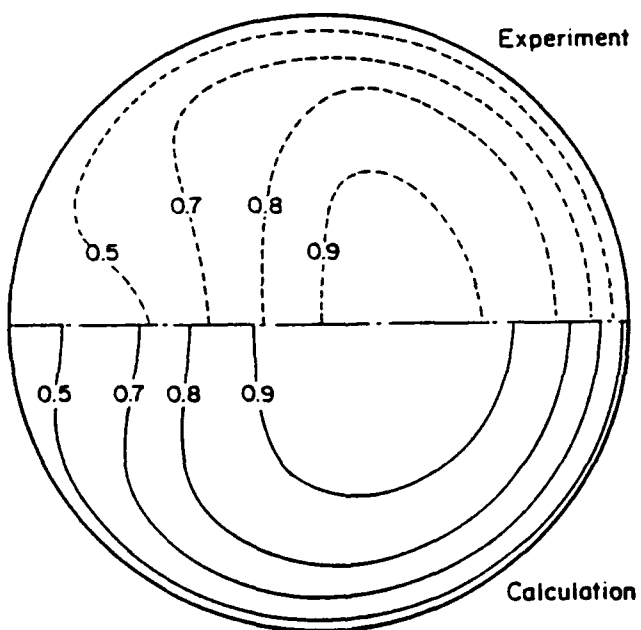
Fig. 25 Measured (Rowe, 1970) and calculated total velocity head contours
(a) θ = 0°; (b) θ = 30°

140
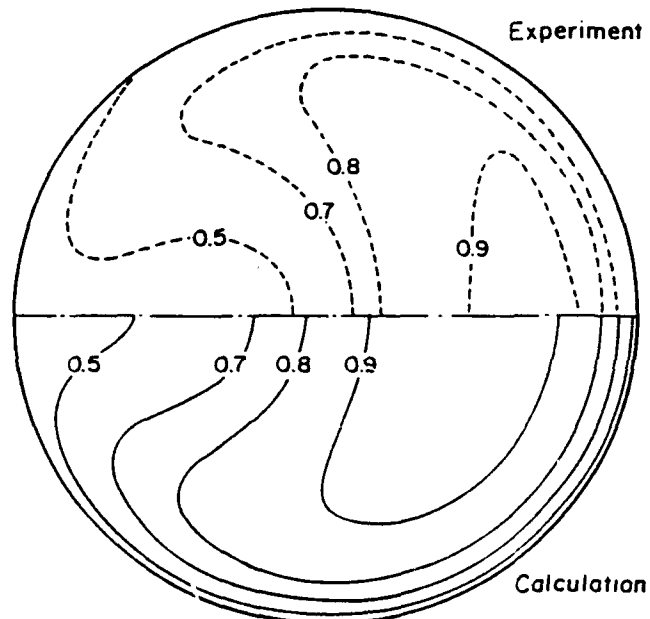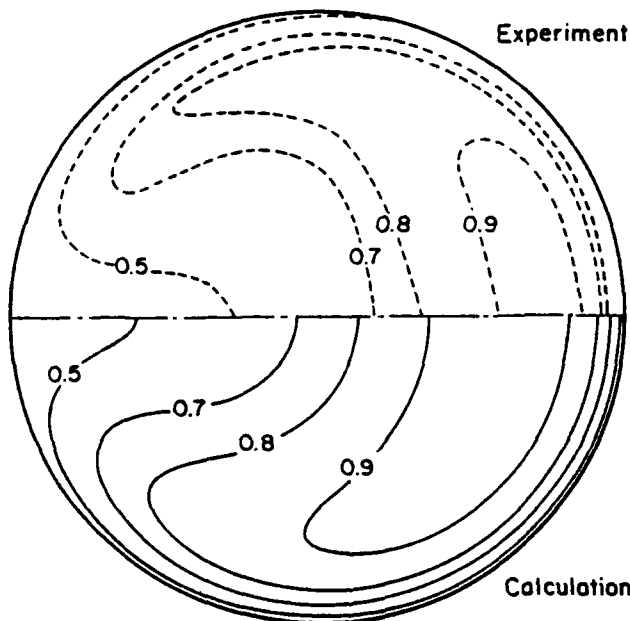
Fig. 25   Measured (Rowe, 1970) and calculated total velocity head contours
(c) θ = 45°; (d) θ = 60°

141
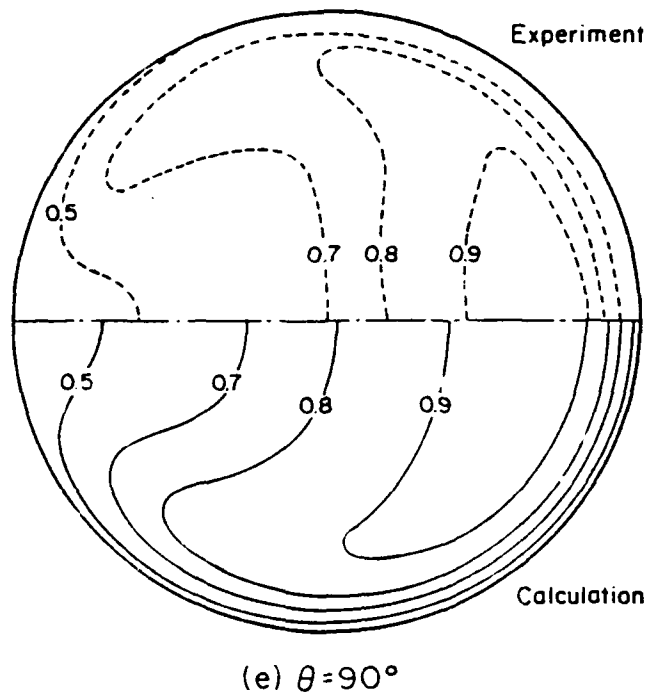
(e) $\theta = 90°$
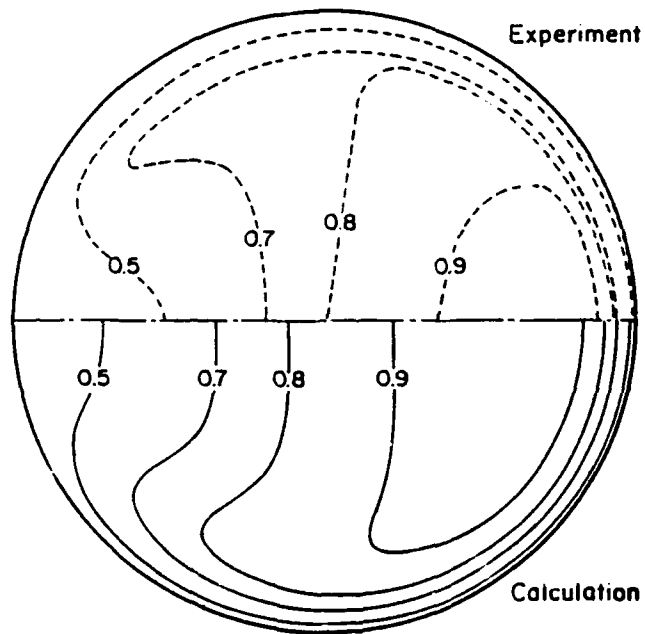
(f) $\theta = 120°$

Fig. 25   Measured (Rowe, 1970) and calculated total velocity head contours
(e) $\theta = 90°$; (f) $\theta = 120°$

142
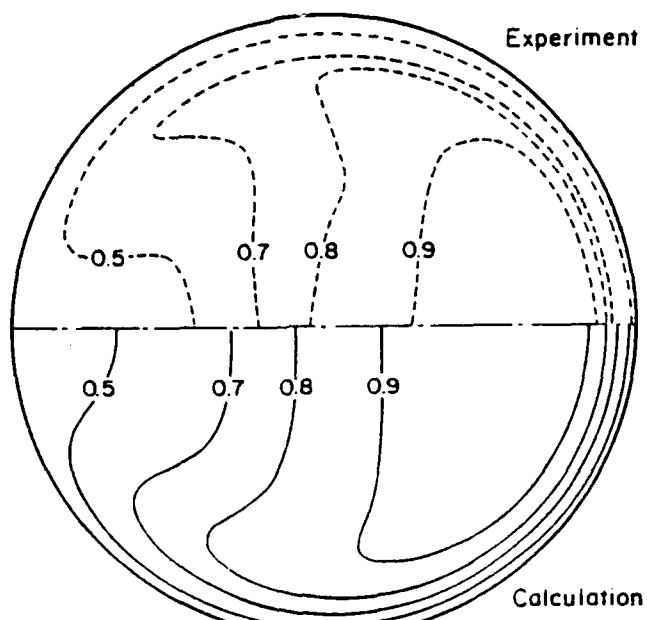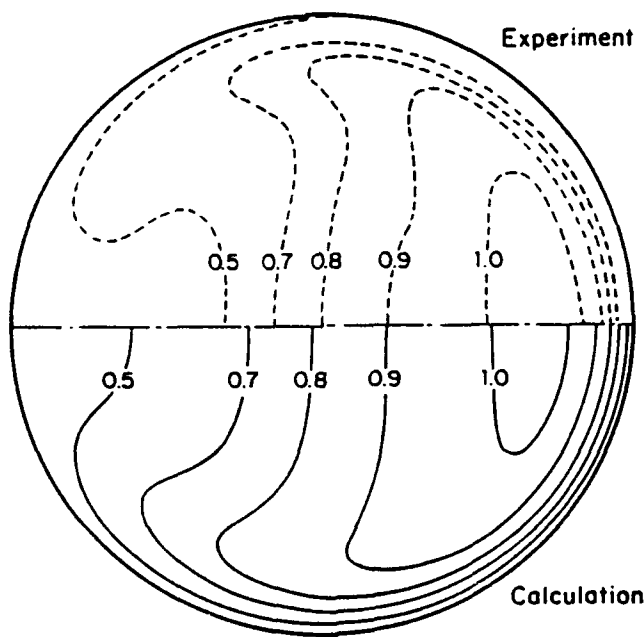
(g) $\theta = 150°$

(h) $\theta = 180°$

Fig. 25   Measured (Rowe, 1970) and calculated total velocity head contours
(g) $\theta = 150°$; (h) $\theta = 180°$

143
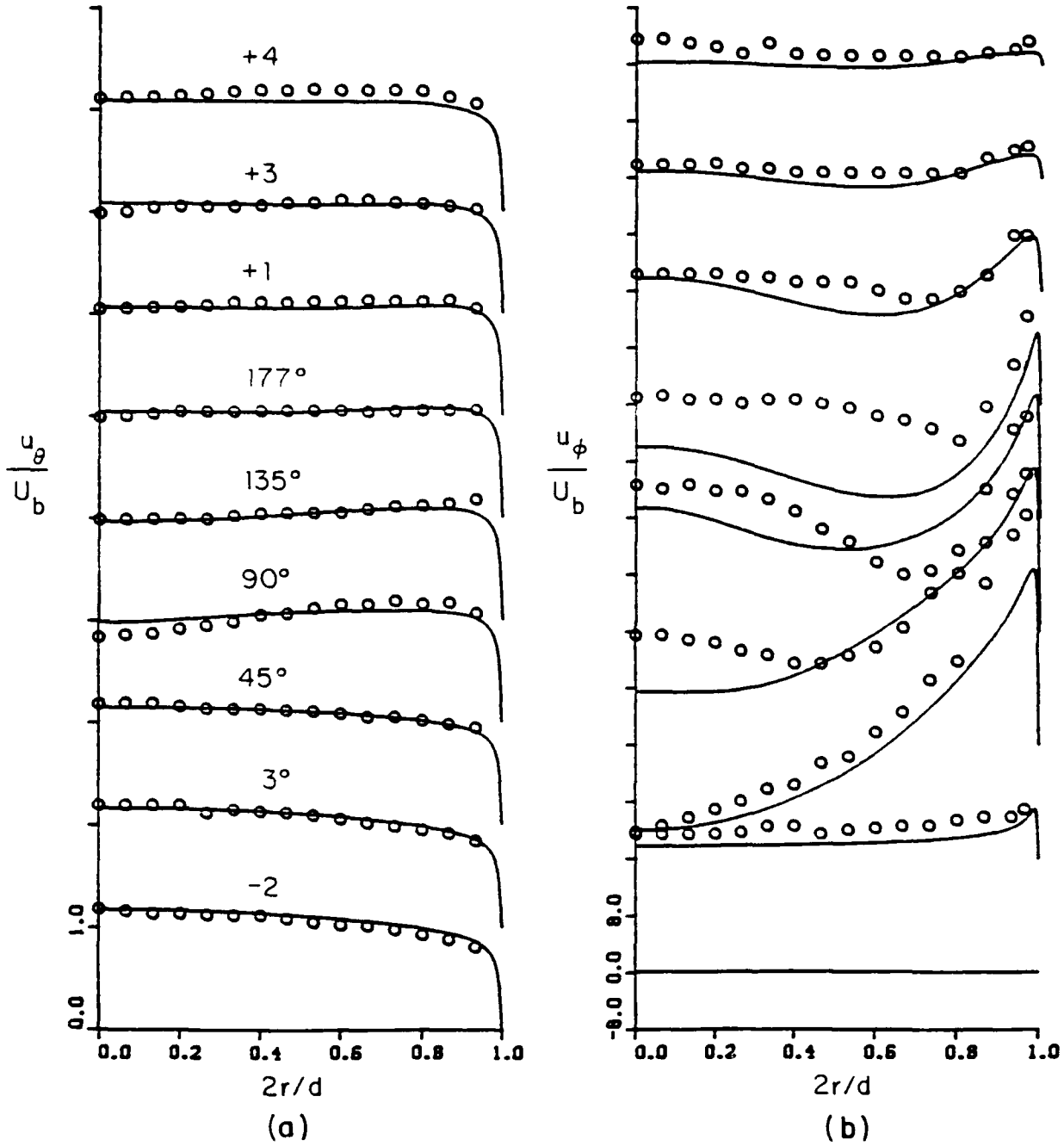
Fig. 26 Measured and calculated mean velocity profiles along the vertical radius:

o, measurements (Azzola et al., 1984); ———,calculation

(a) streamwise mean velocity; (b) circumferential mean velocity
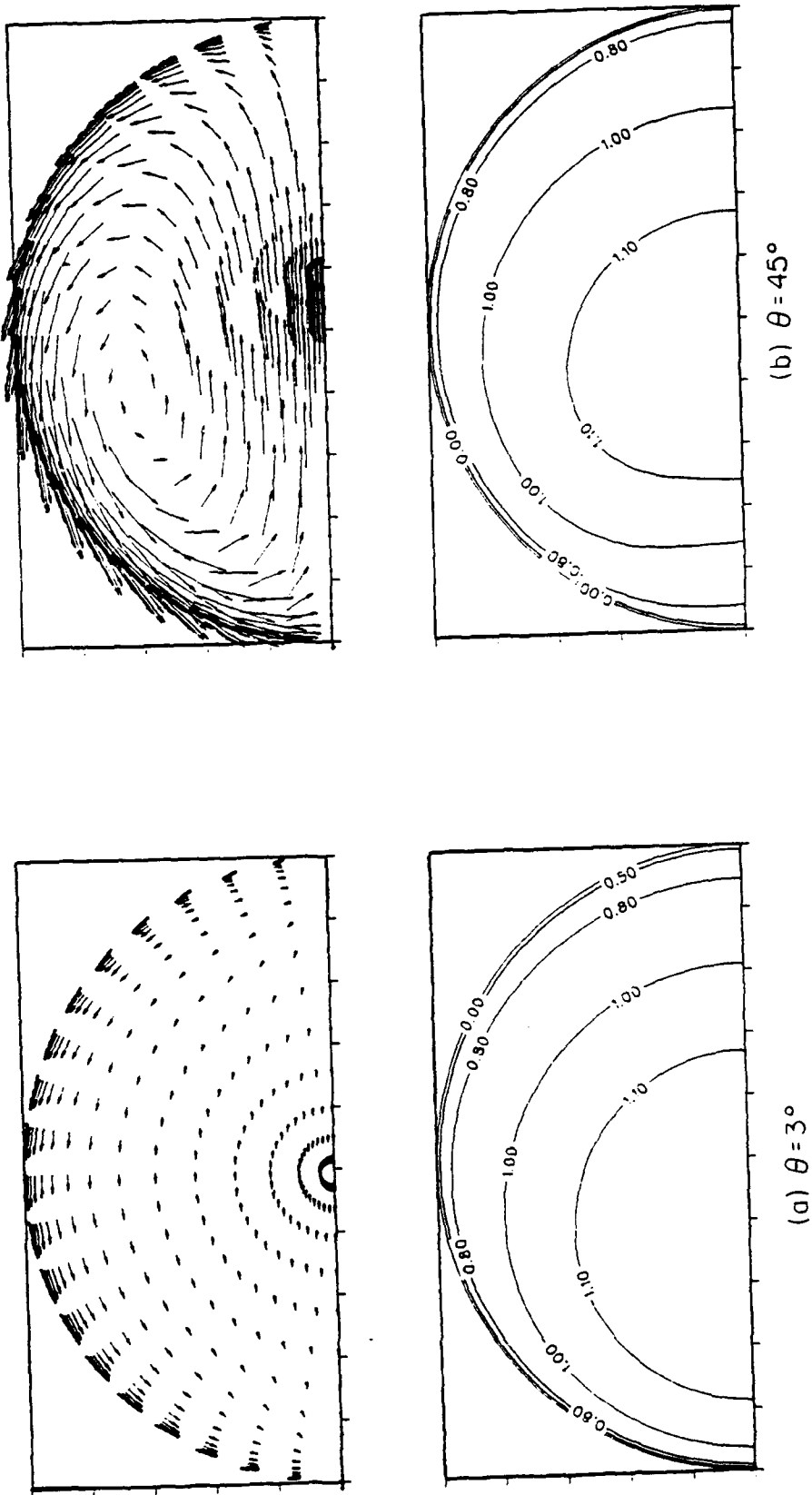
(b) $\theta = 45°$

(a) $\theta = 3°$

Fig. 27 Calculated mean secondary flow vectors and mean streamwise velocity contours
(pipe bend of Azzola et al., 1984)
(a) $\theta = 3°$; (b) $\theta = 45°$
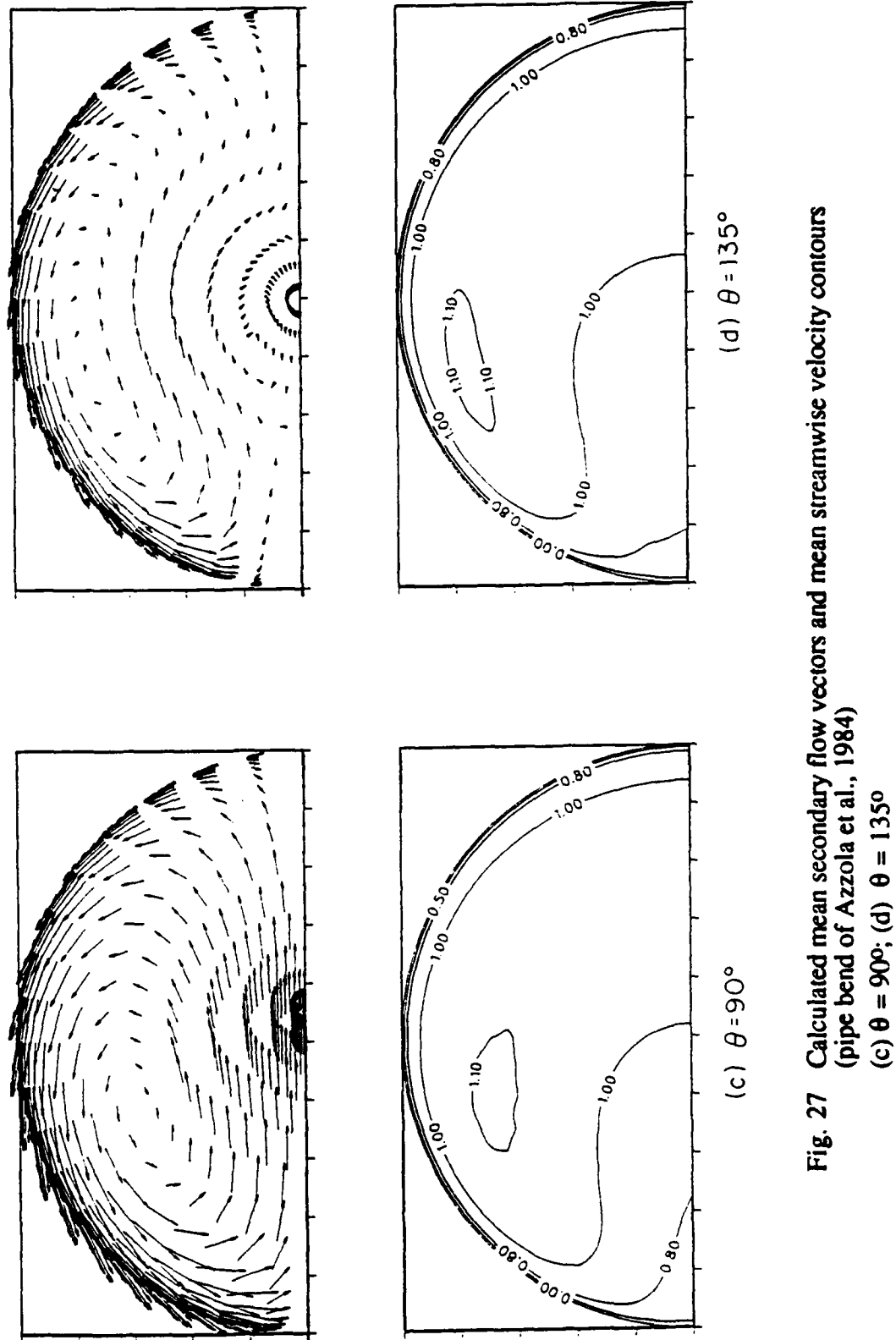
145

(c) $\theta = 90°$

(d) $\theta = 135°$

Fig. 27 Calculated mean secondary flow vectors and mean streamwise velocity contours (pipe bend of Azzola et al., 1984)
(c) $\theta = 90°$; (d) $\theta = 135°$
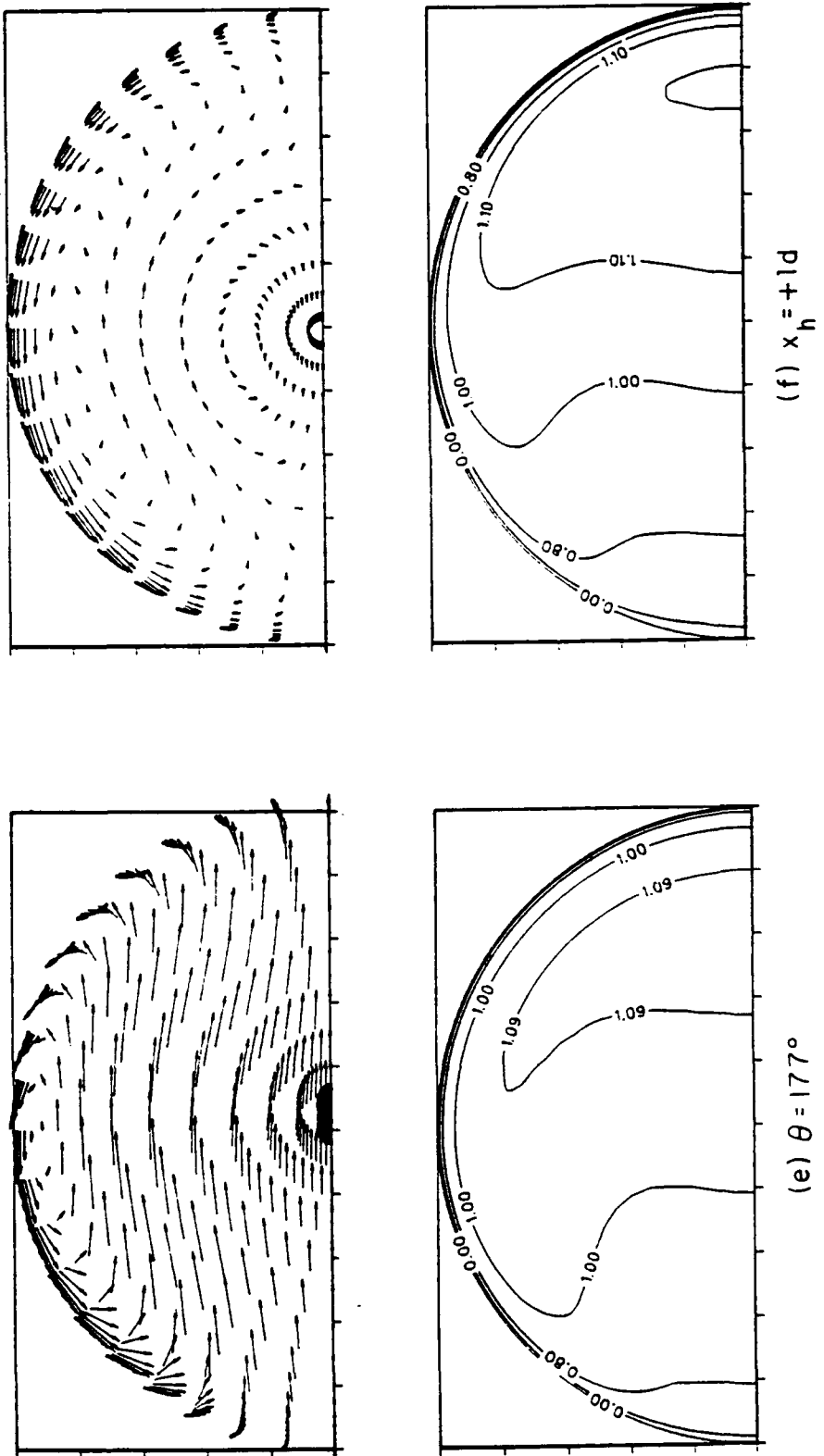
146

Fig. 27 Calculated mean secondary flow vectors and mean streamwise velocity contours
(pipe bend of Azzola et al., 1984)
(e) $\theta = 177°$; (f) $x_h = +1d$
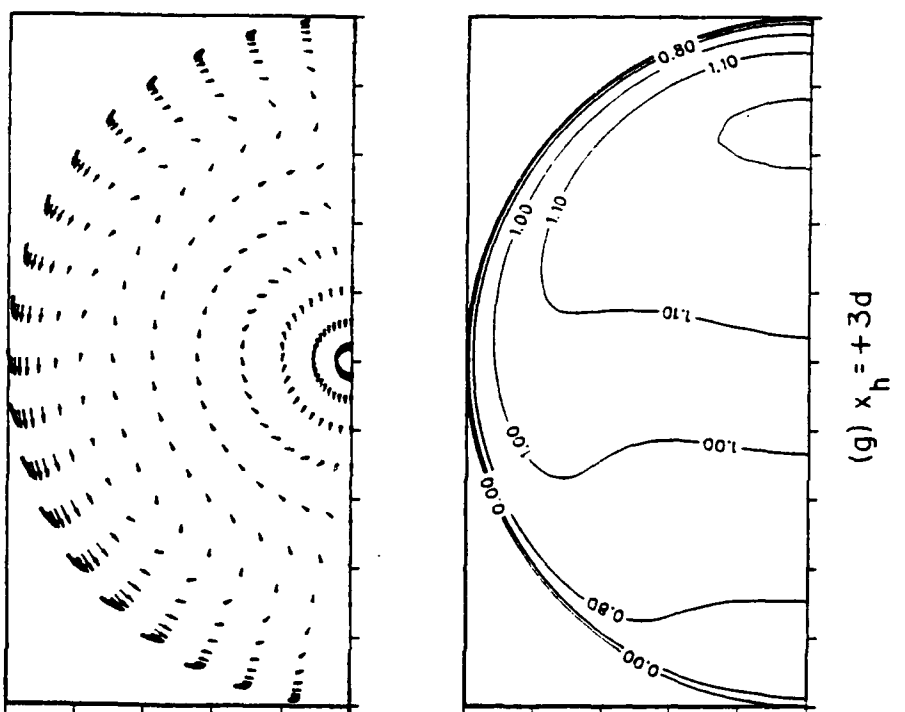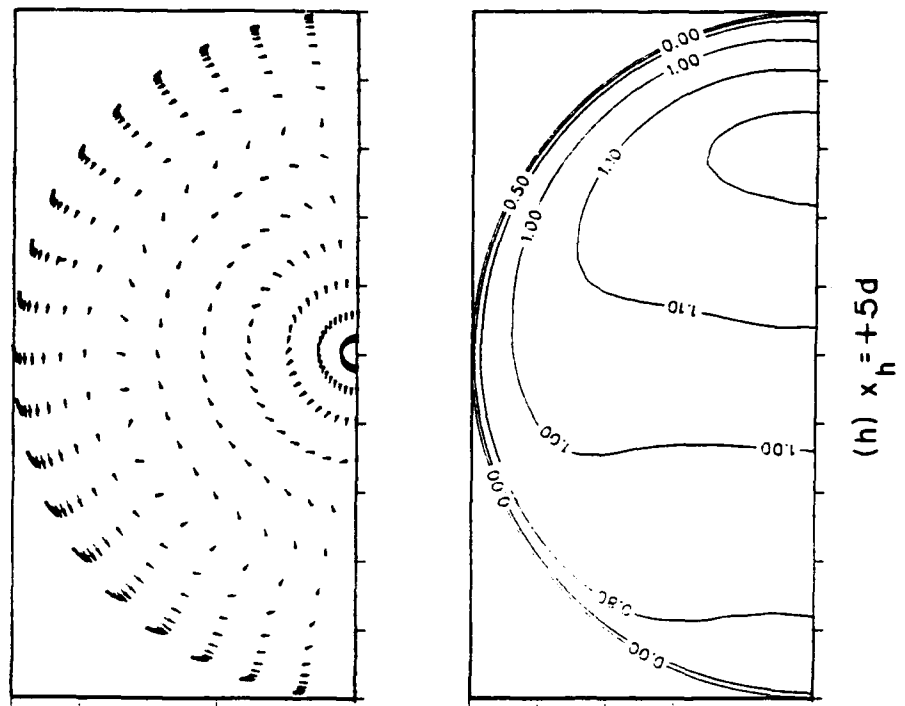
(e) $\theta = 177°$

(f) $x_h = +1d$

(h) $x_h = +5d$

(g) $x_h = +3d$

Fig. 27 Calculated mean secondary flow vectors and mean streamwise velocity contours
(pipe bend of Azzola et al., 1984)
(g) $x_h = +3d$; (h) $x_h = +5d$

148
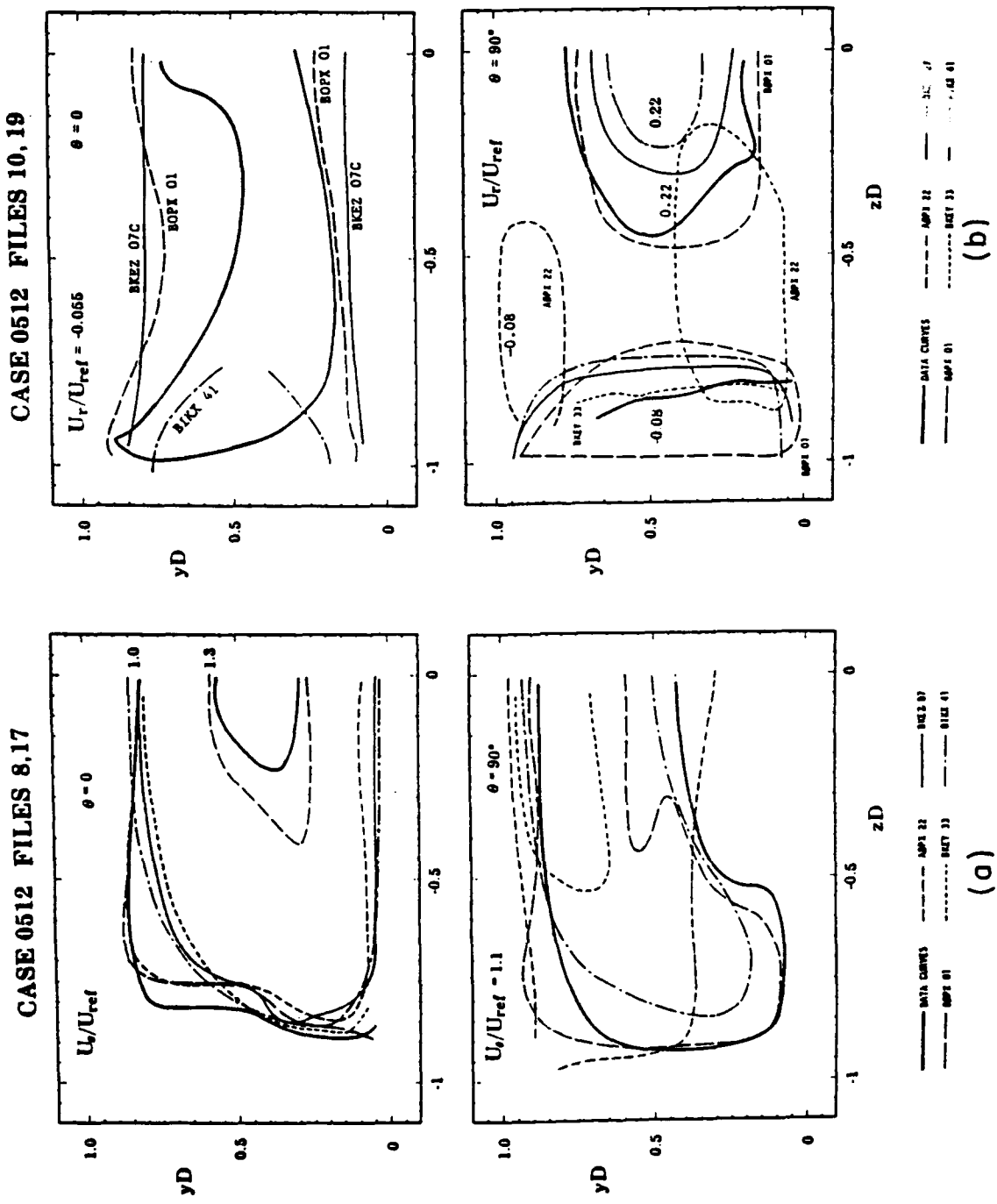
Fig. 28 Mean velocity contours presented at the "1980-81 Stanford Conference on Complex Turbulent Flows" (duct of Humphrey et al., 1981) (a) streamwise velocity; (b) radial velocity

Experiment
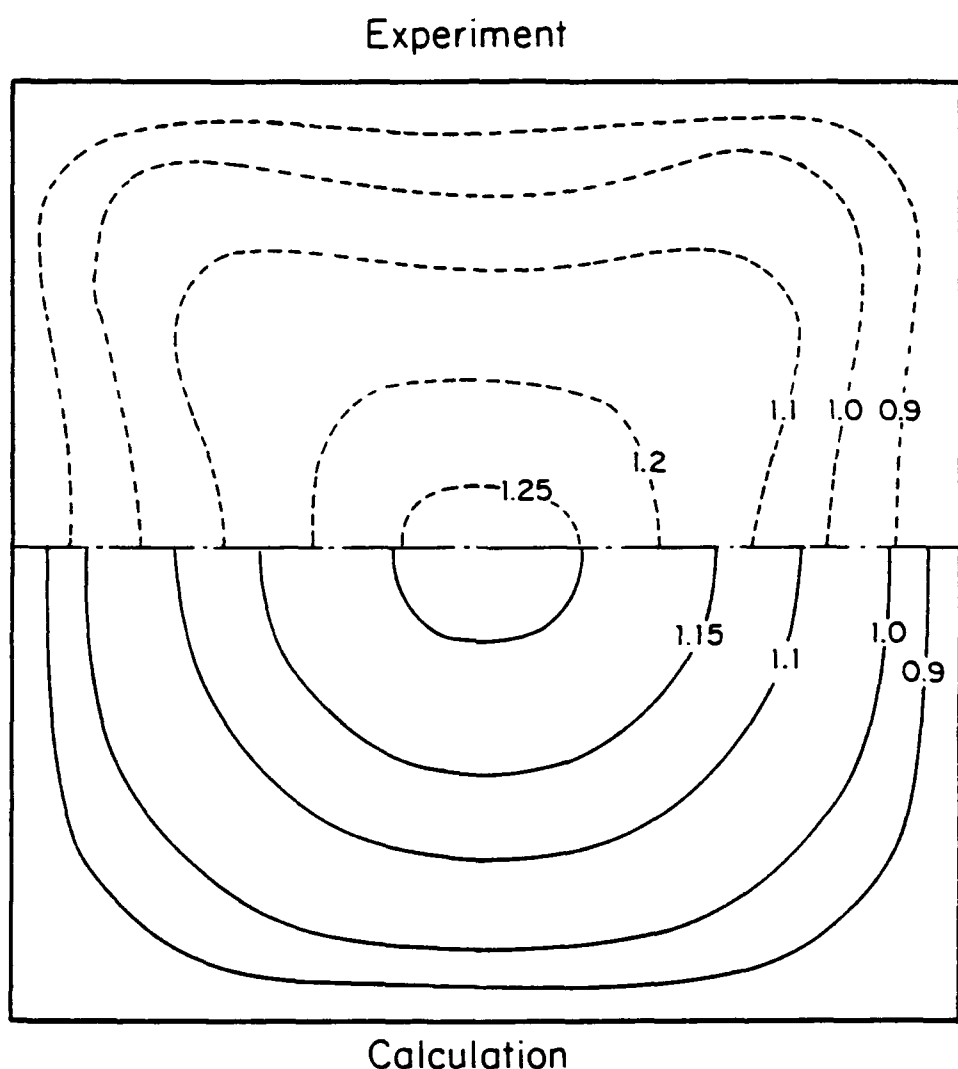
Calculation

Fig. 29 Calculated streamwise velocity contours, for fully developed straight duct flow, compared with the measurements of Humphrey et al. (1981) at $x_h = -2.5d_h$

Experiment

Calculation

(a) $\theta = 0°$

Experiment
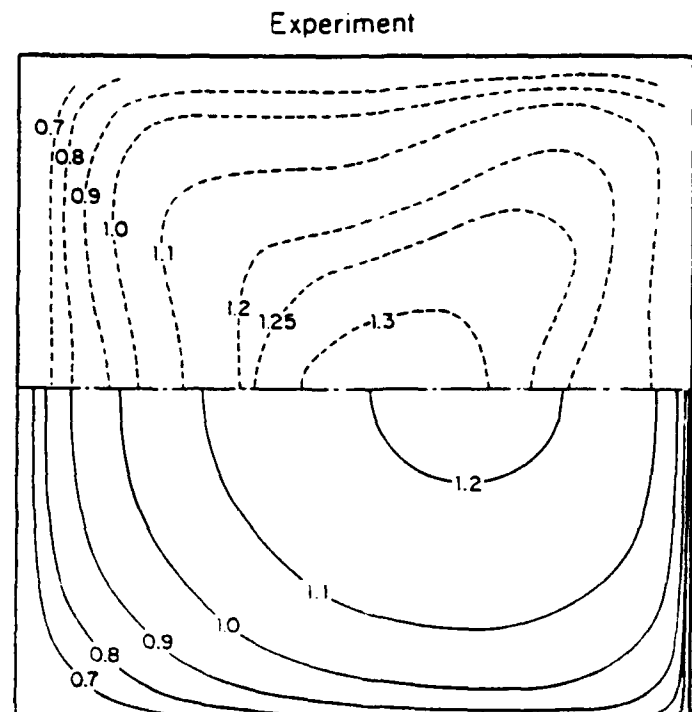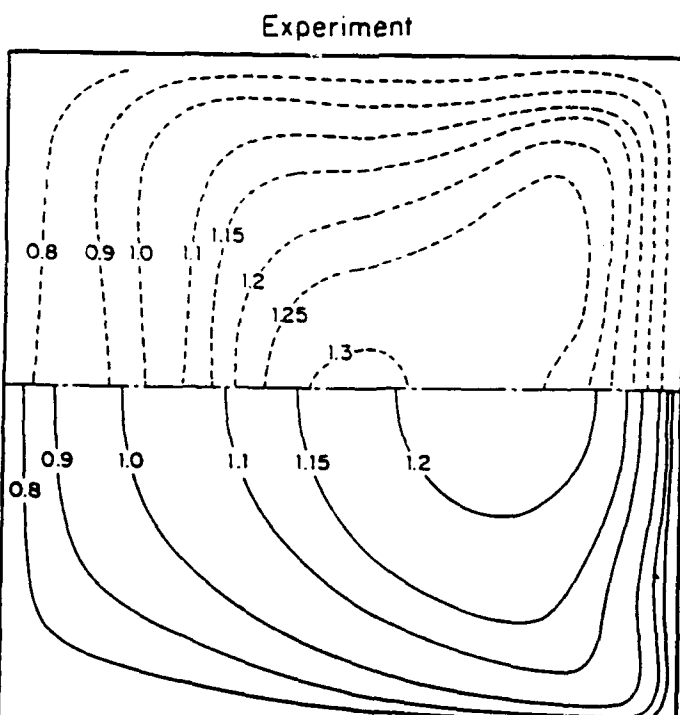
Calculation

(b) $\theta = 45°$

Fig. 30 Measured (Humphrey et al., 1981) and calculated streamwise velocity contours
(a) $\theta = 0°$; (b) $\theta = 45°$

151

Experiment

Calculation

(c) $\theta = 71°$

Experiment
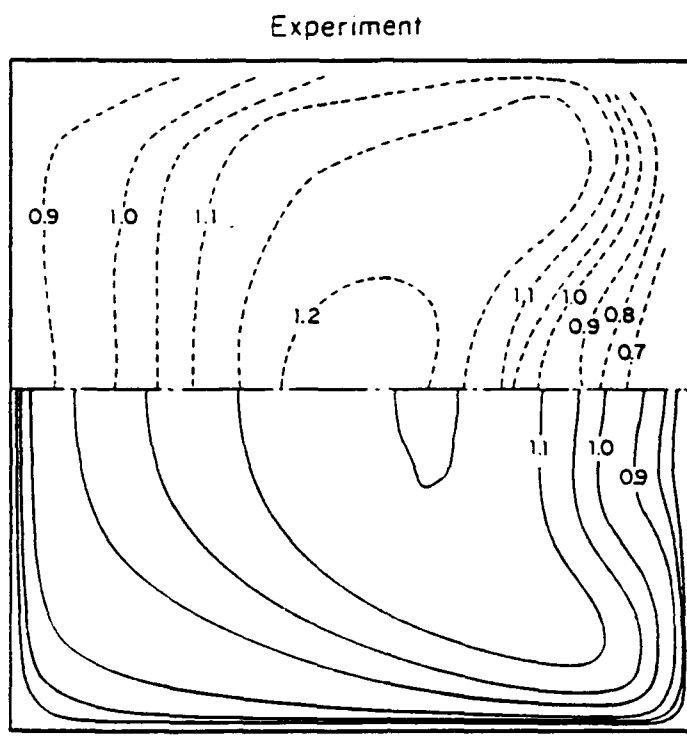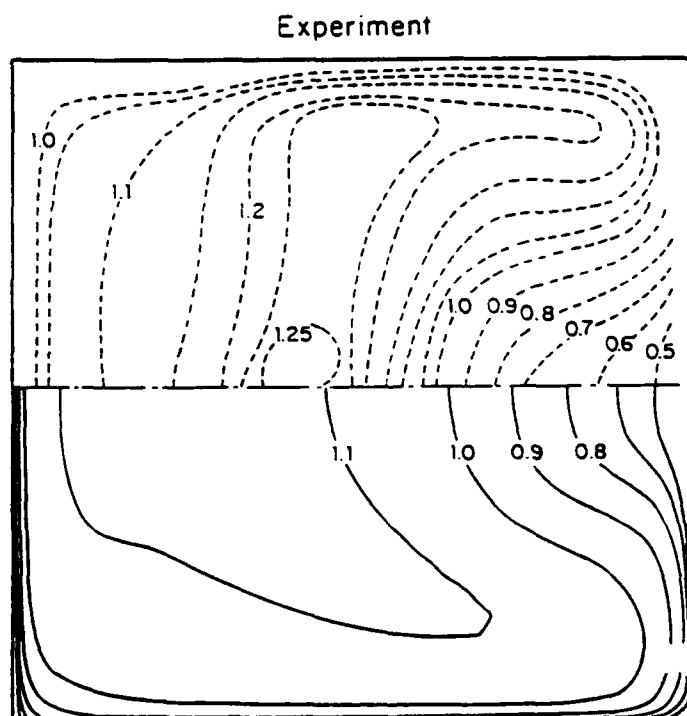
Calculation

(d) $\theta = 90°$

Fig. 30   Measured (Humphrey et al., 1981) and calculated streamwise velocity contours
(c) $\theta = 71°$; (d) $\theta = 90°$

152

Experiment
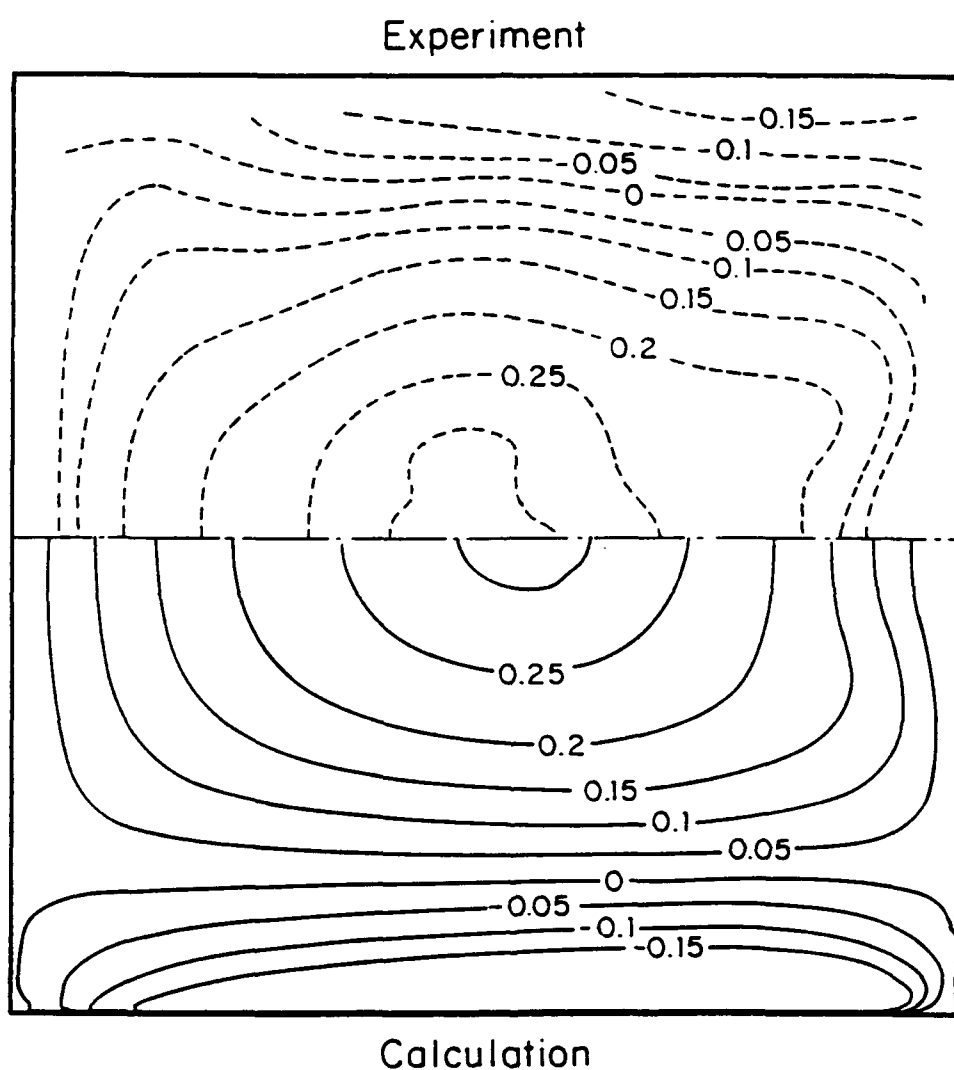
Calculation

Fig. 31 Measured (Humphrey et al., 1981) and calculated radial velocity contours
at $\theta = 90^\circ$
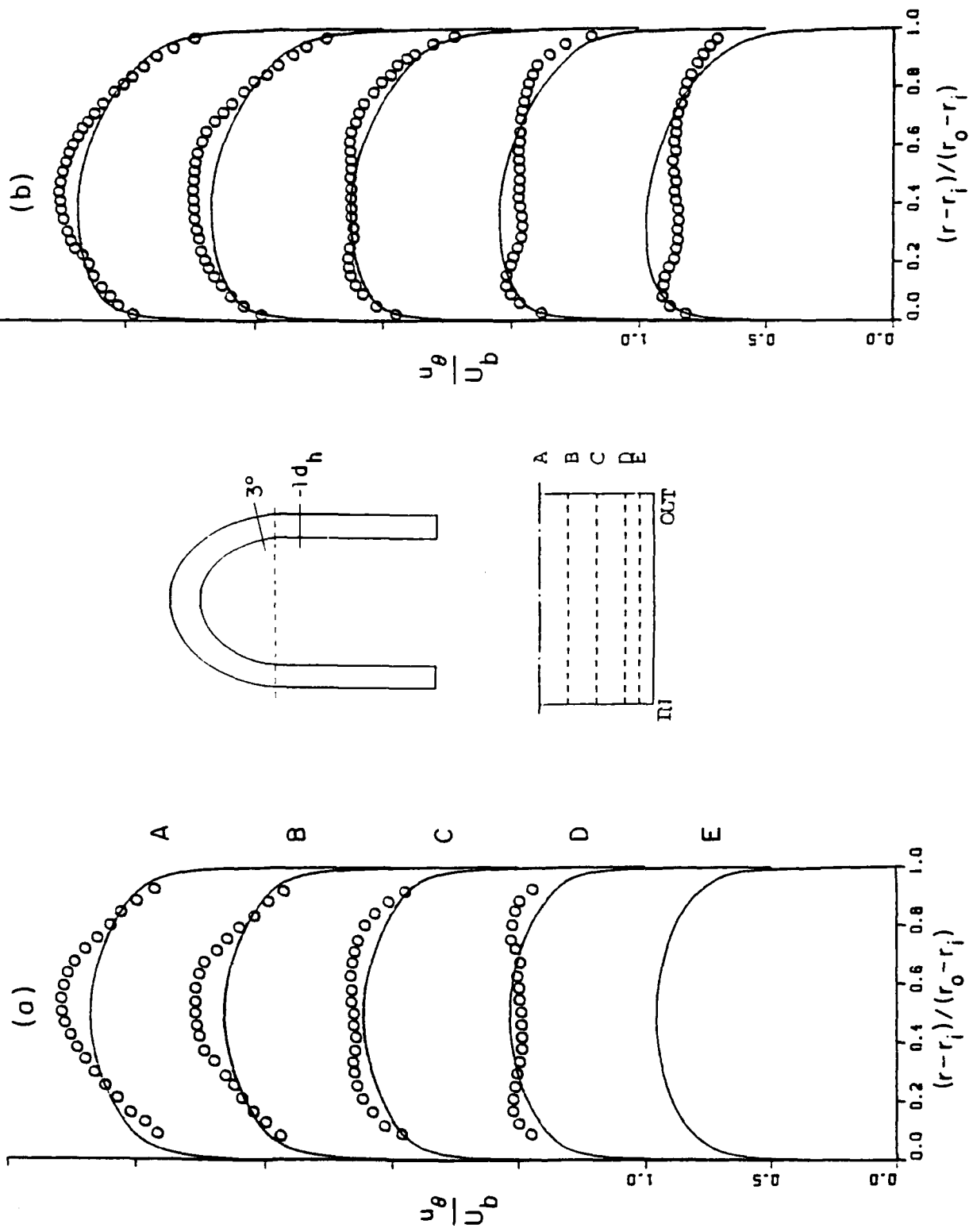
153

Fig. 32 Measured and calculated streamwise velocity profiles along radial lines:
o, measurements (Chang, 1983); ———, calculation
(a) $x_h = -1.0d_h$; (b) $\theta = 3^o$
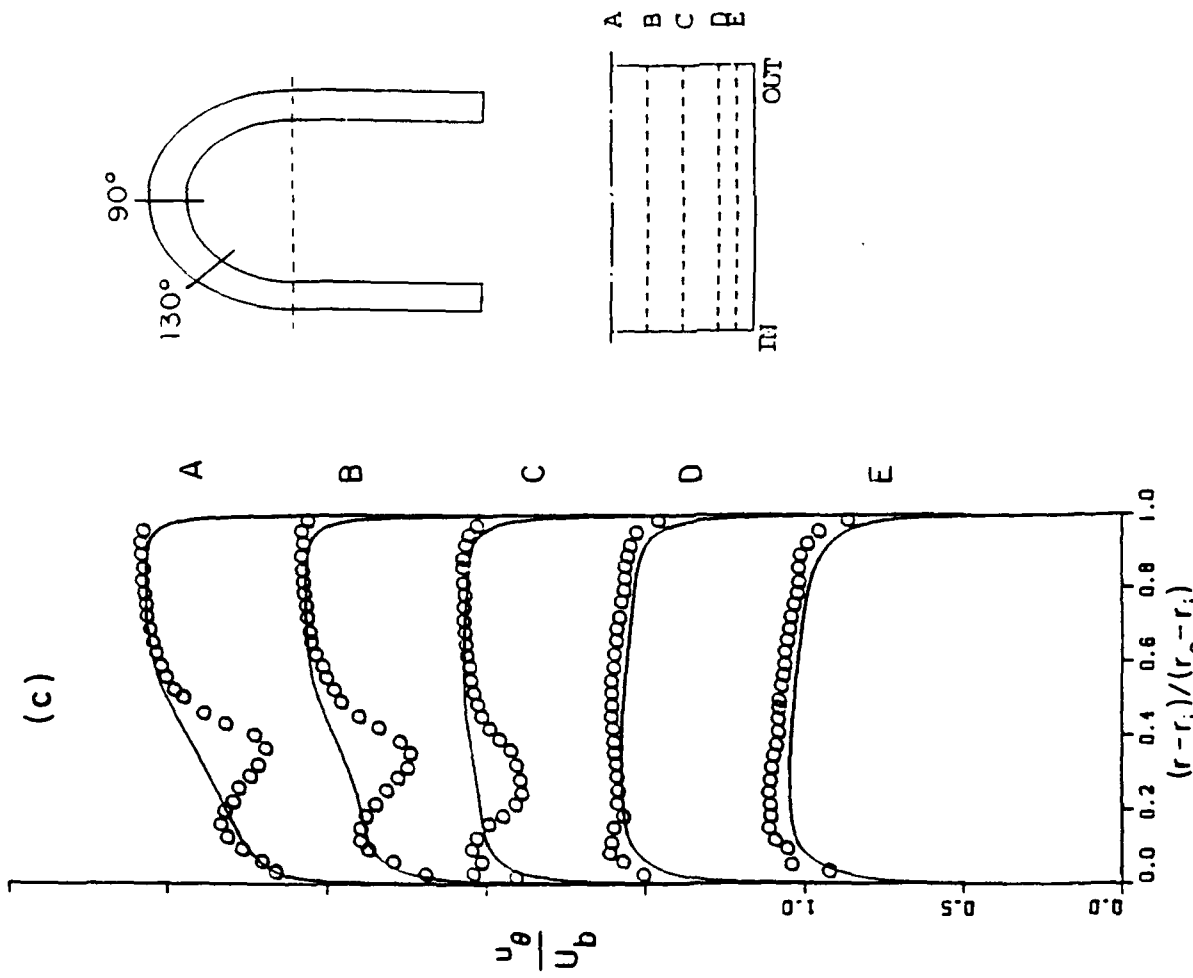
Fig. 32 Measured and calculated streamwise velocity profiles along radial lines:
o, measurements (Chang, 1983); ———,calculation
(c) $\theta = 90^\circ$; (d) $\theta = 130^\circ$

155
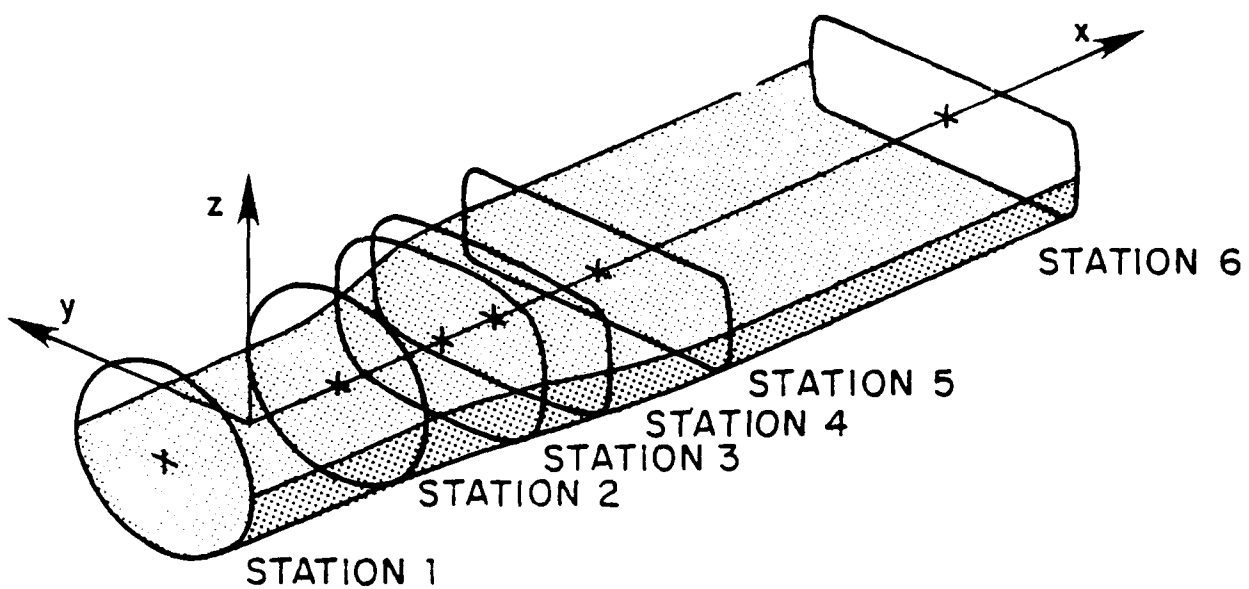
Fig. 33   Coordinates and locations of measurements stations for the transition duct of
Davis and Gessner (1992)

(a)
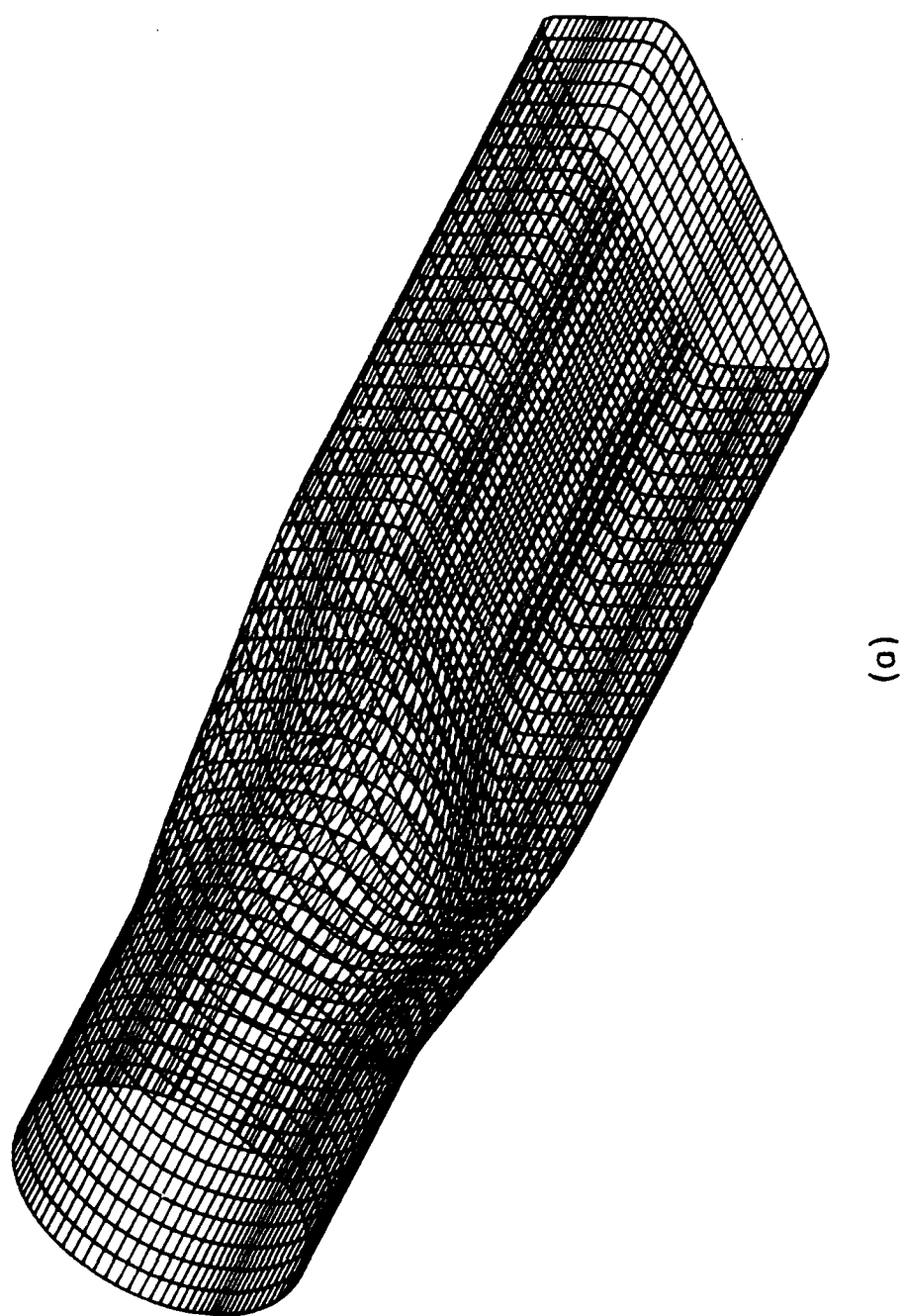
Fig. 34 Typical views of the computational grid (CR duct of Davis and Gessner, 1992)
(a) 3-D surface view

(b)
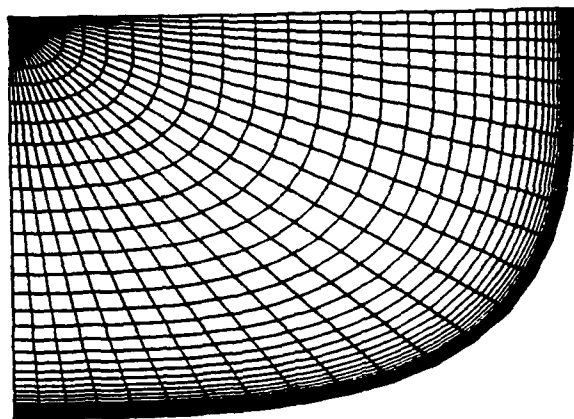
Station 3
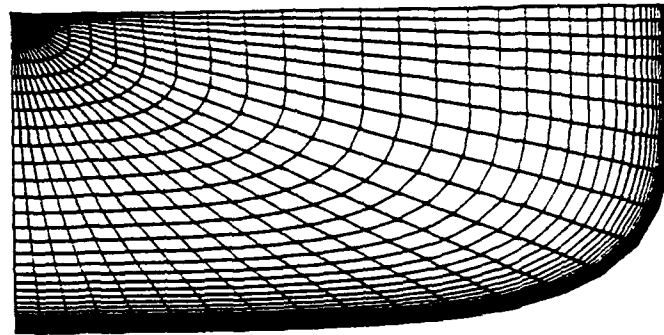
Station 4
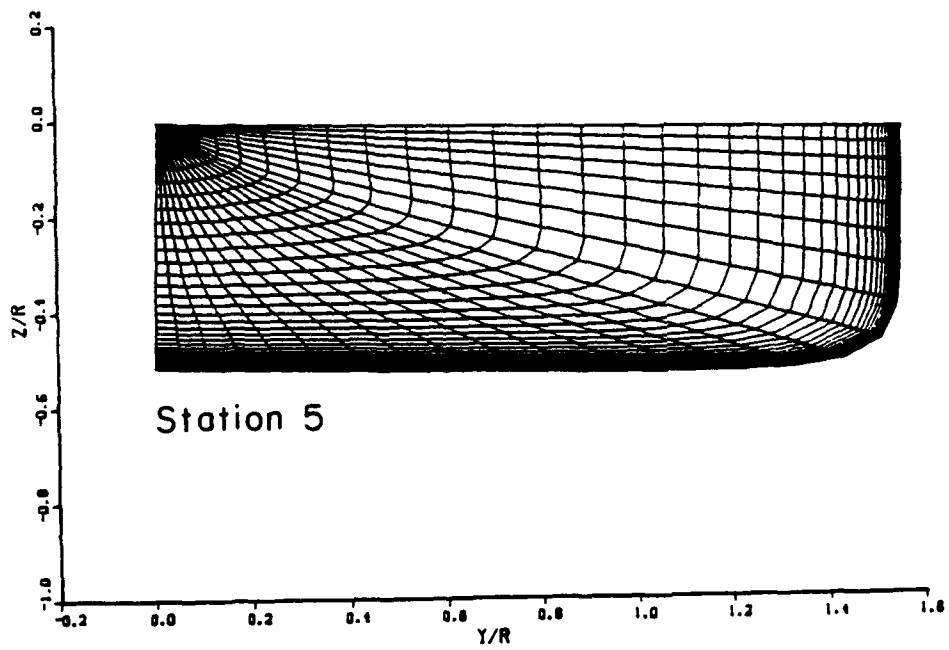
Station 5

Fig. 34 Typical views of the computational grid (CR duct of Davis and Gessner, 1992)
(b) Cross-sectional views
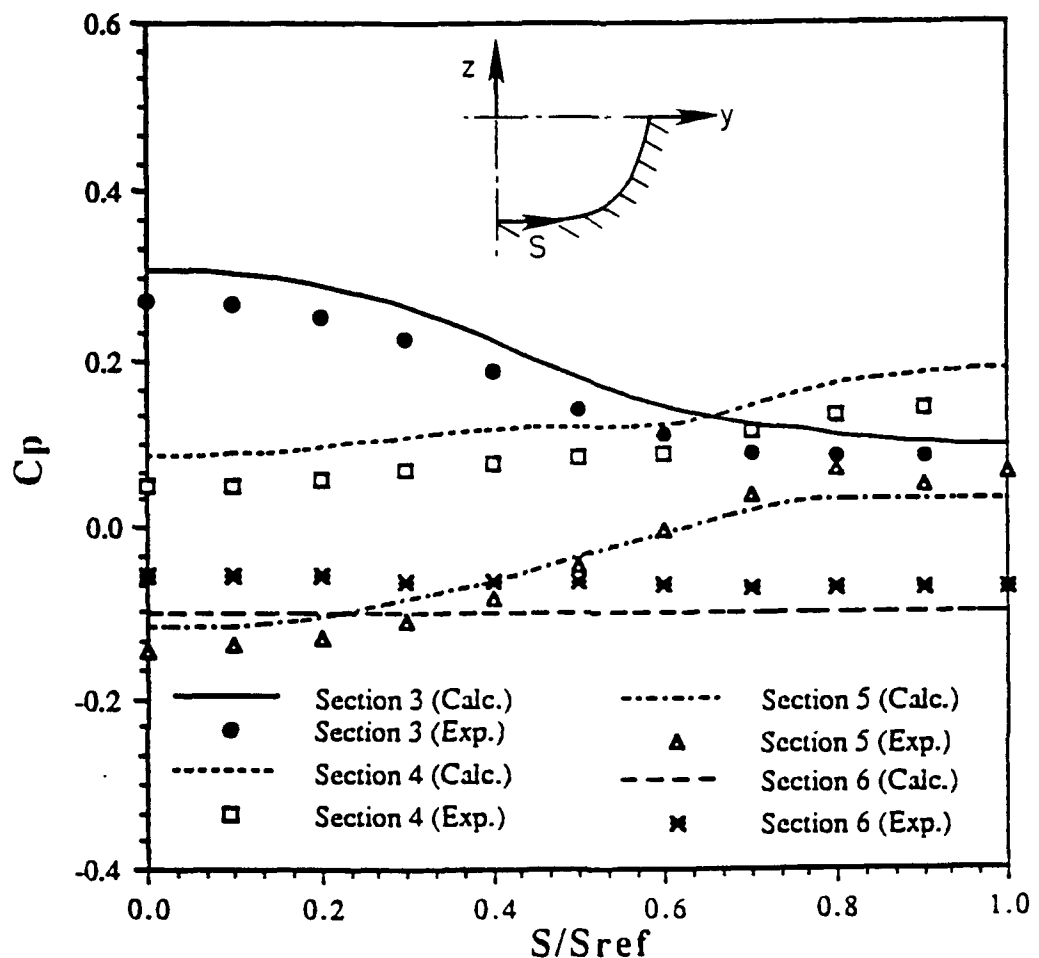
Fig. 35 Measured (Davis and Gessner, 1992) and computed peripheral wall pressure coefficient distributions
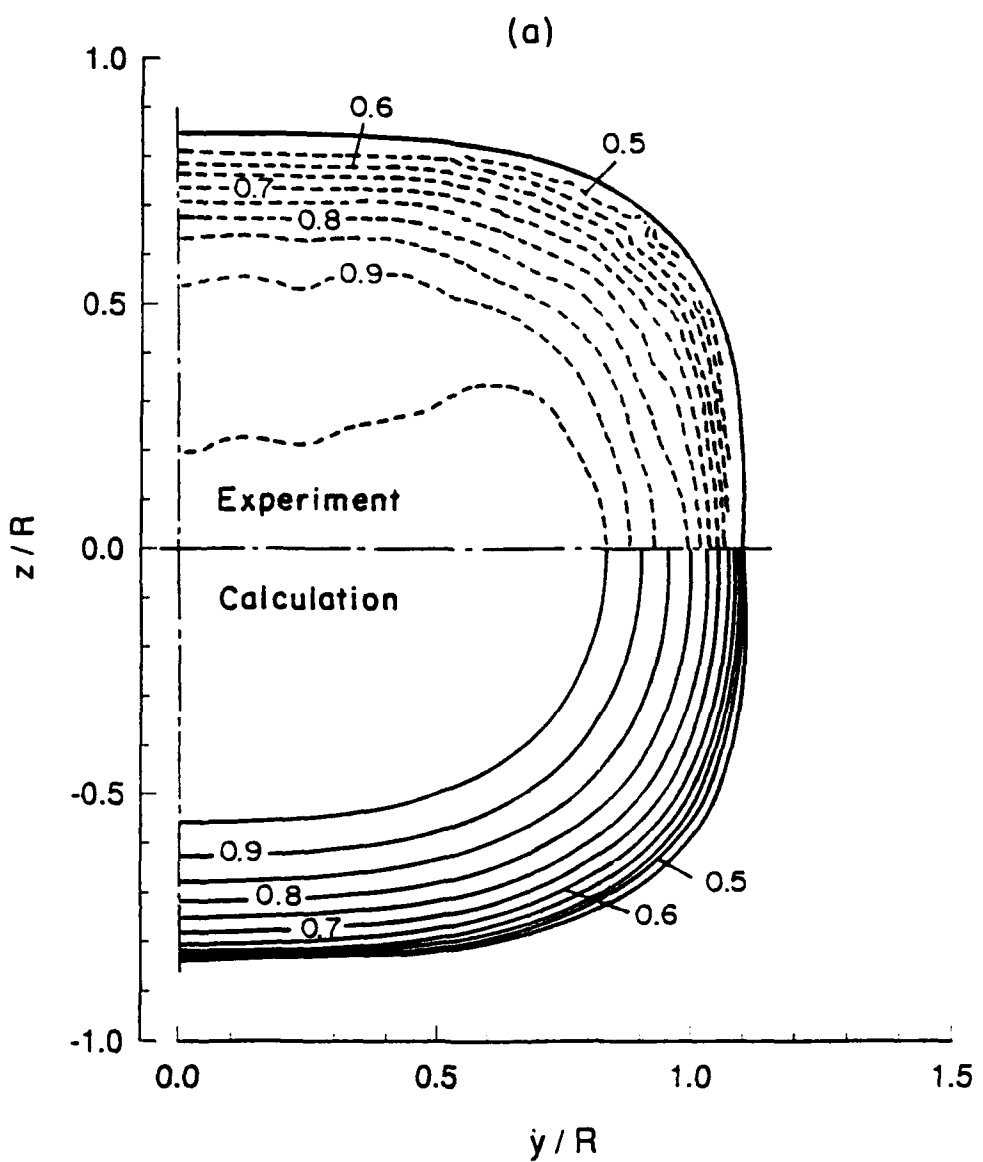
Fig. 36 Measured (Davis and Gessner, 1992) and computed axial velocity contours
(a) Station 3
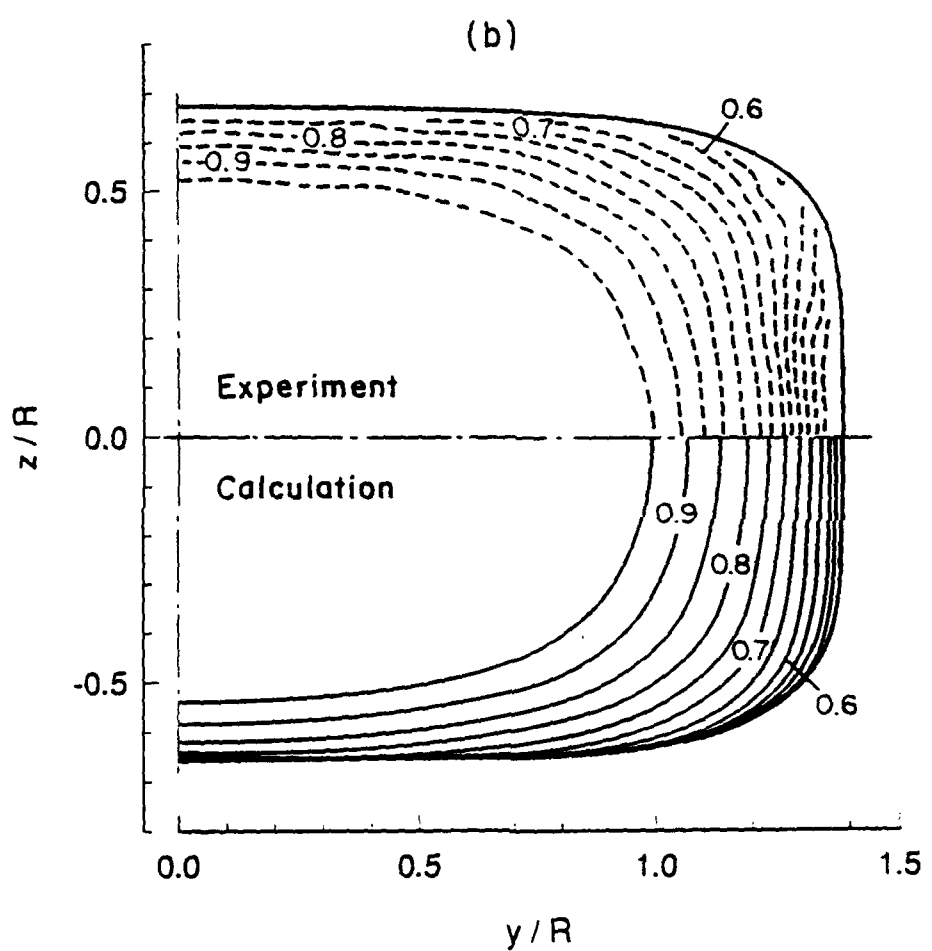
Fig. 36 Measured (Davis and Gessner, 1992) and computed axial velocity contours
(b) Station 4

161
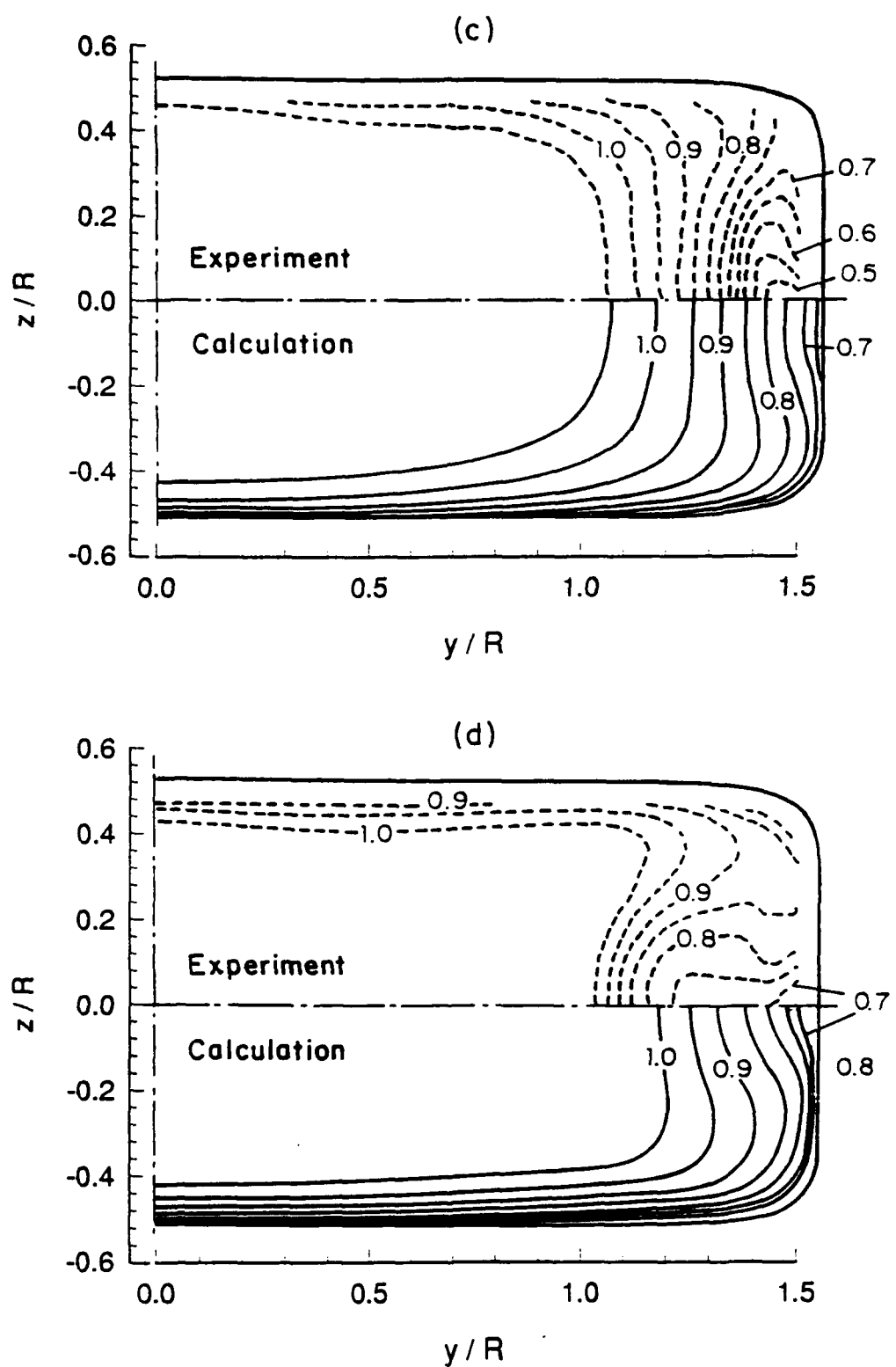
Fig. 36   Measured (Davis and Gessner, 1992) and computed axial velocity contours
(c) Station 5; (d) Station 6
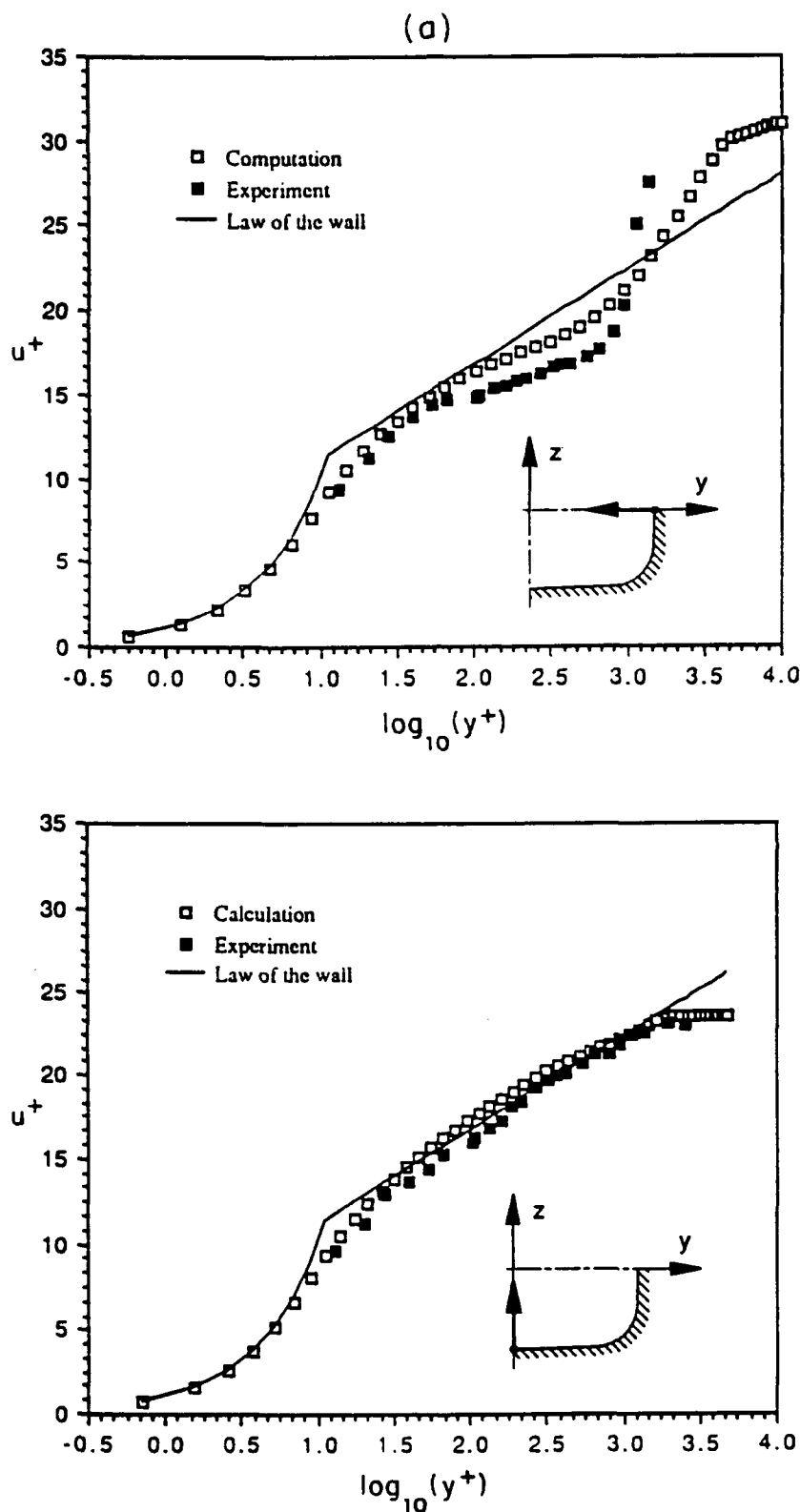
162

Fig. 37   Measured (Davis and Gessner, 1992) and computed law-of-the-wall velocity
profiles along the horizontal and vertical planes of symmetry
(a) Station 5
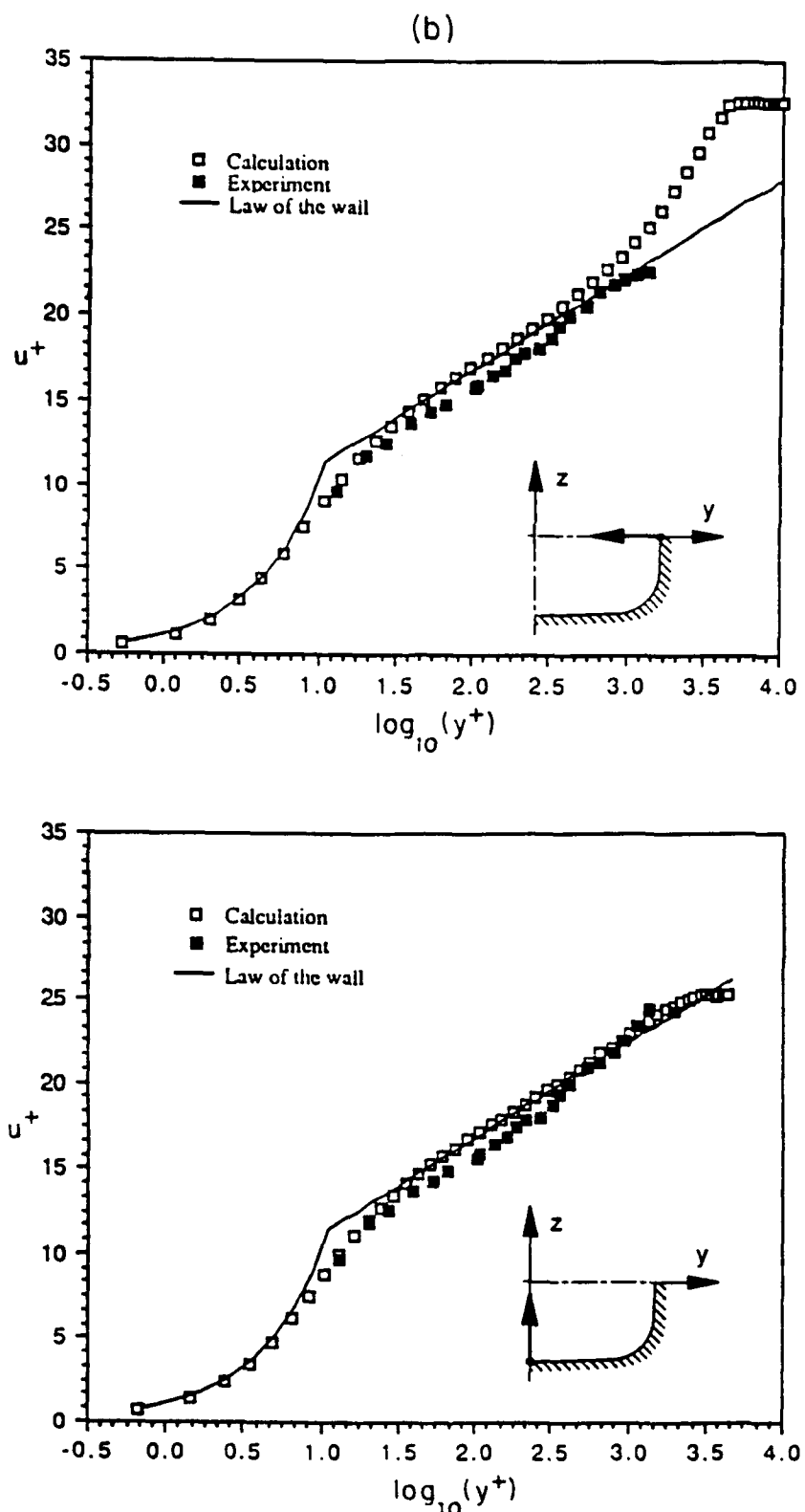
163

(b)

Fig. 37   Measured (Davis and Gessner, 1992) and computed law-of-the-wall velocity
profiles along the horizontal and vertical planes of symmetry
(b) Station 6
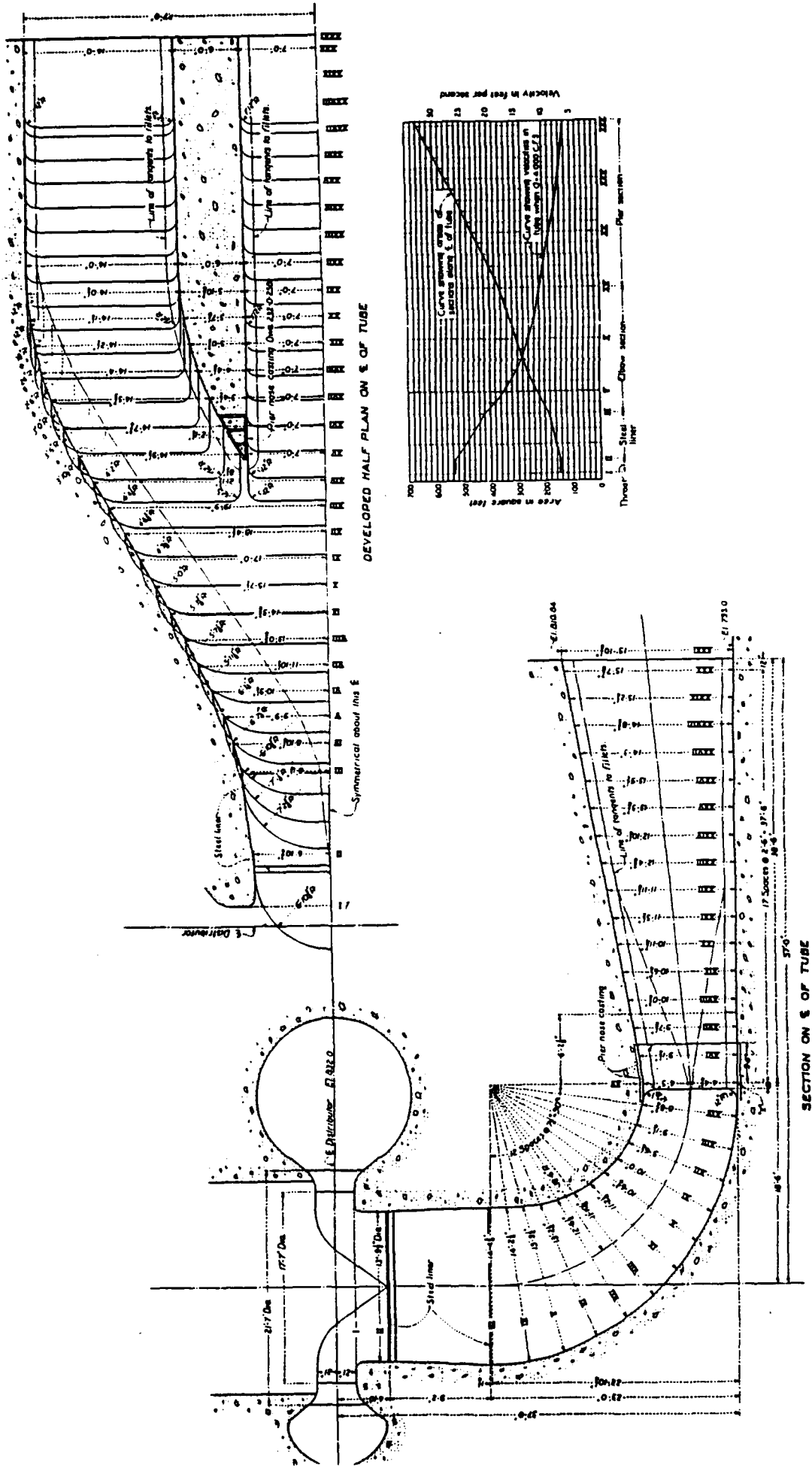
Fig. 38 Neat lines of the TVA Norris Power Plant draft tube
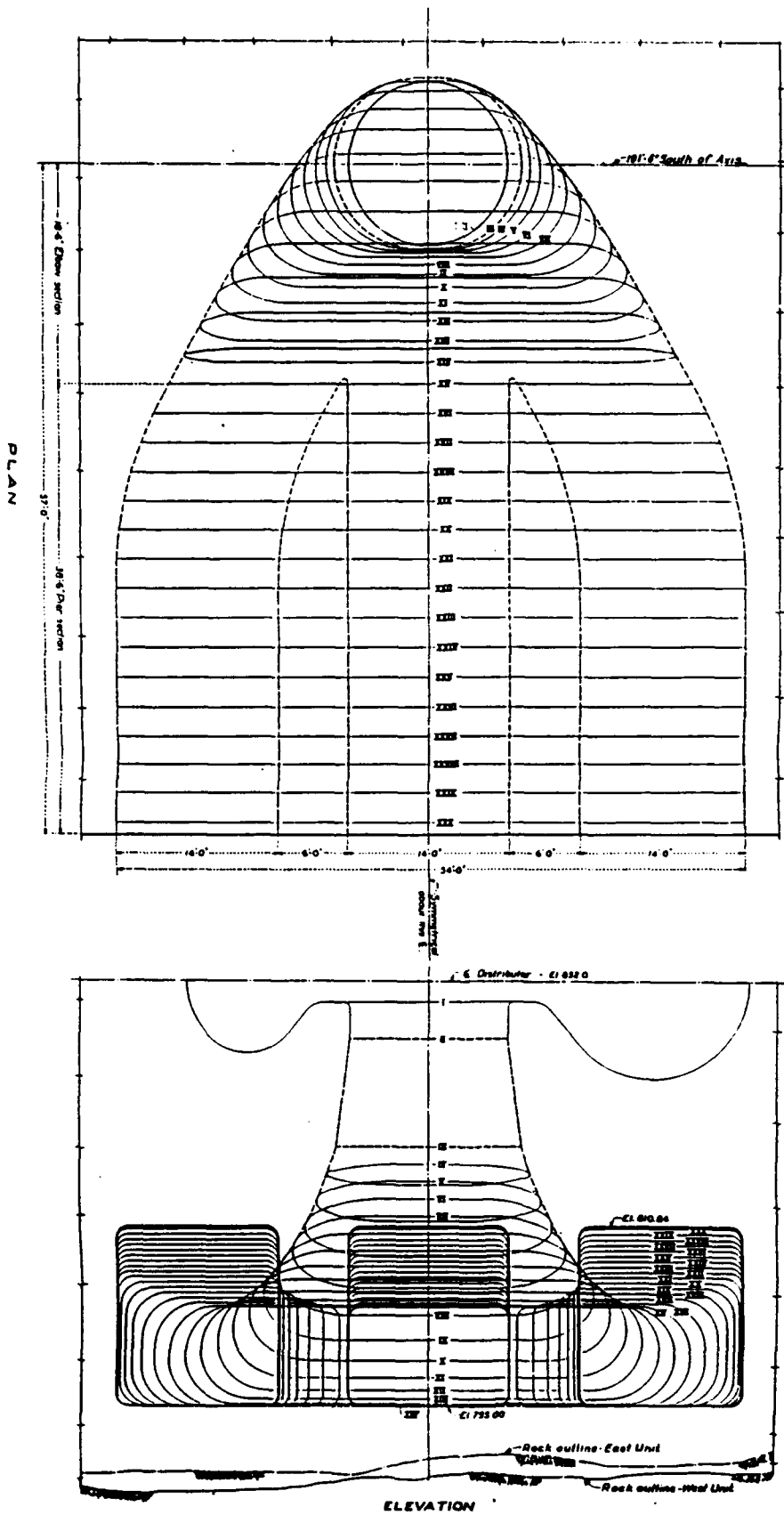
Fig. 39   Plan and elevation views of the TVA Norris Power Plant draft tube
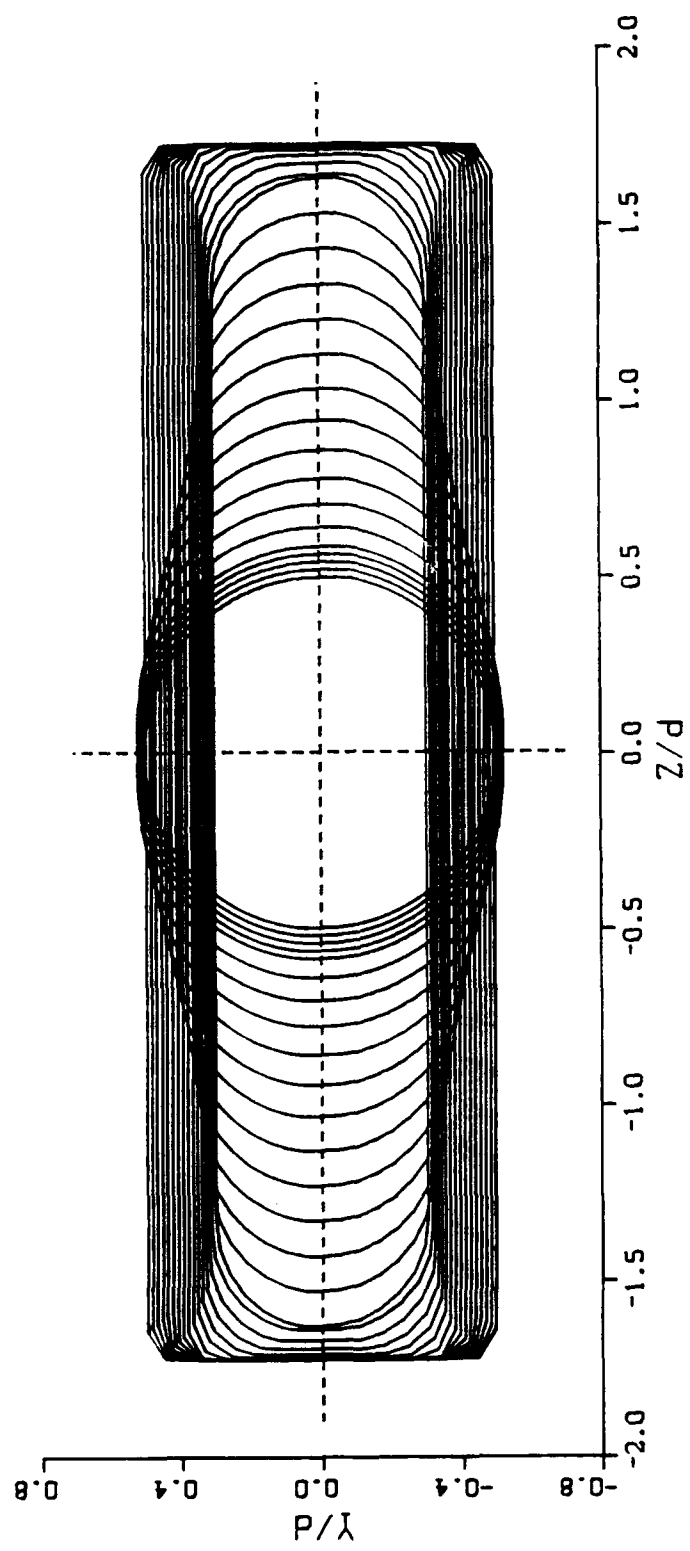
Fig. 40   Cross-sections of the scaled TVA Norris Power Plant draft tube
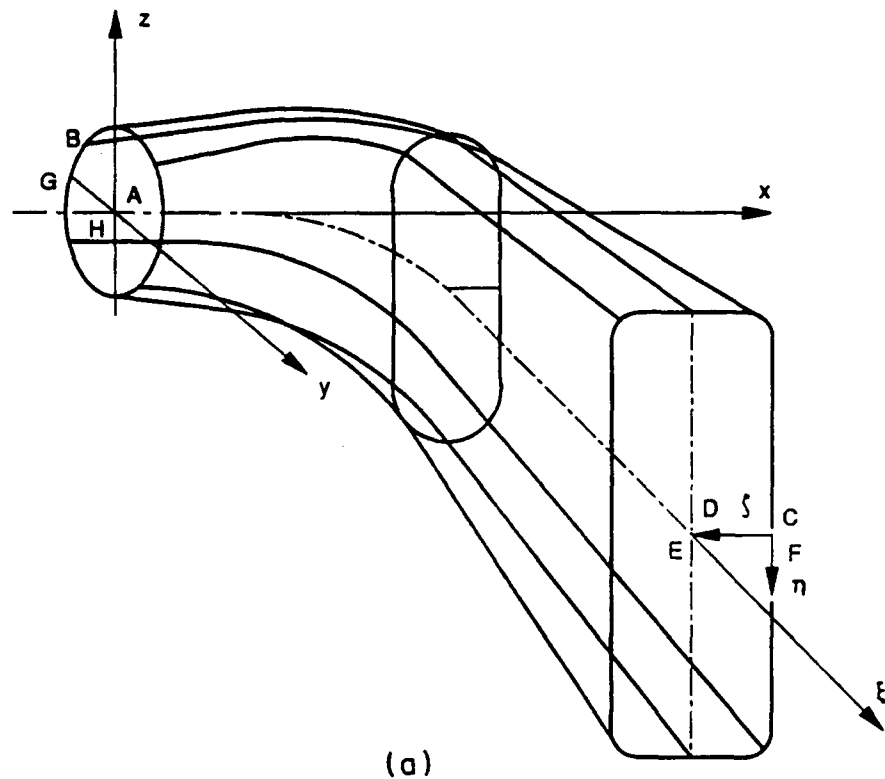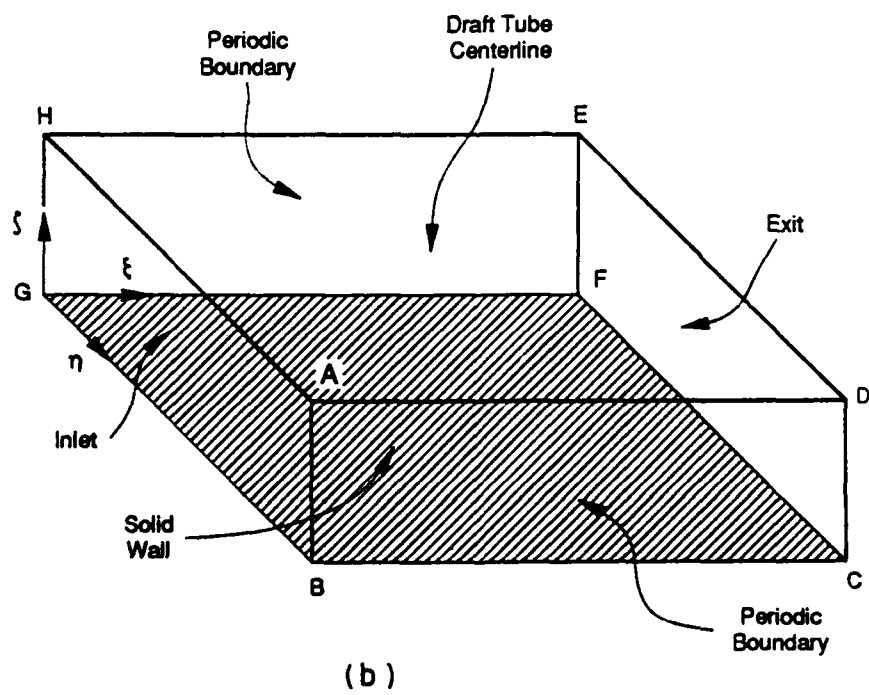
Fig. 41 Curvilinear coordinates for a typical draft tube configuration
(a) physical solution domain; (b) transformed solution domain
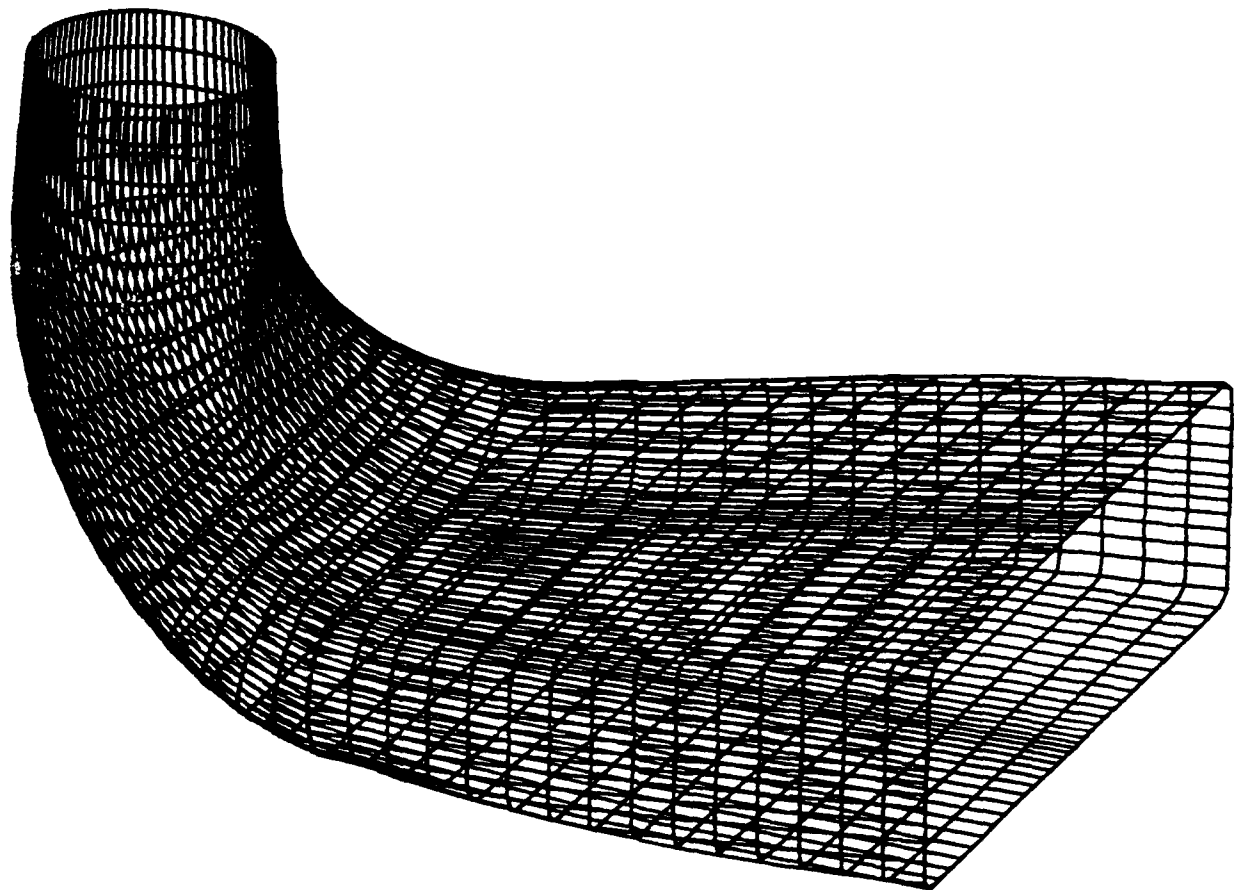
Fig. 42   Typical 3-D surface view of the computational grid for the draft tube geometry
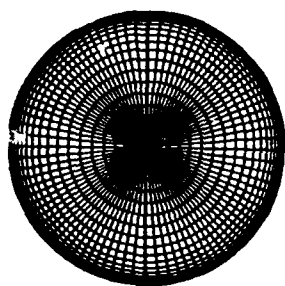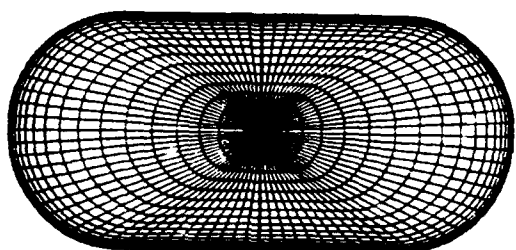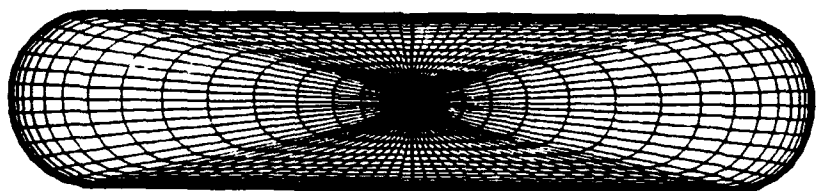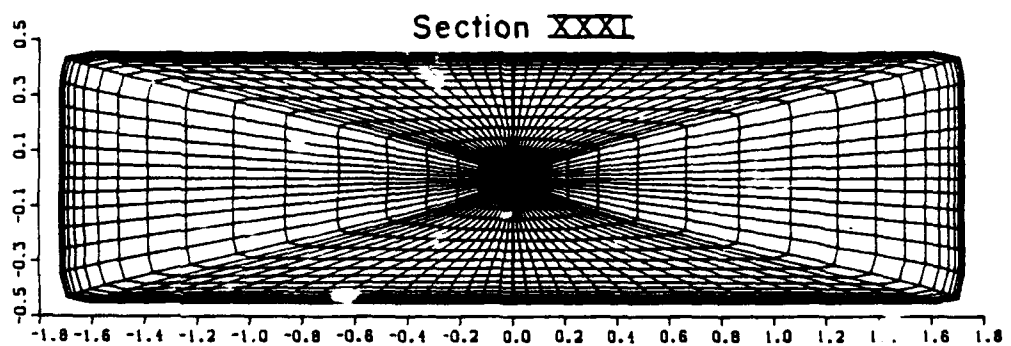
Fig. 43   Typical cross-sectional views of the computational grid for the draft tube
geometry
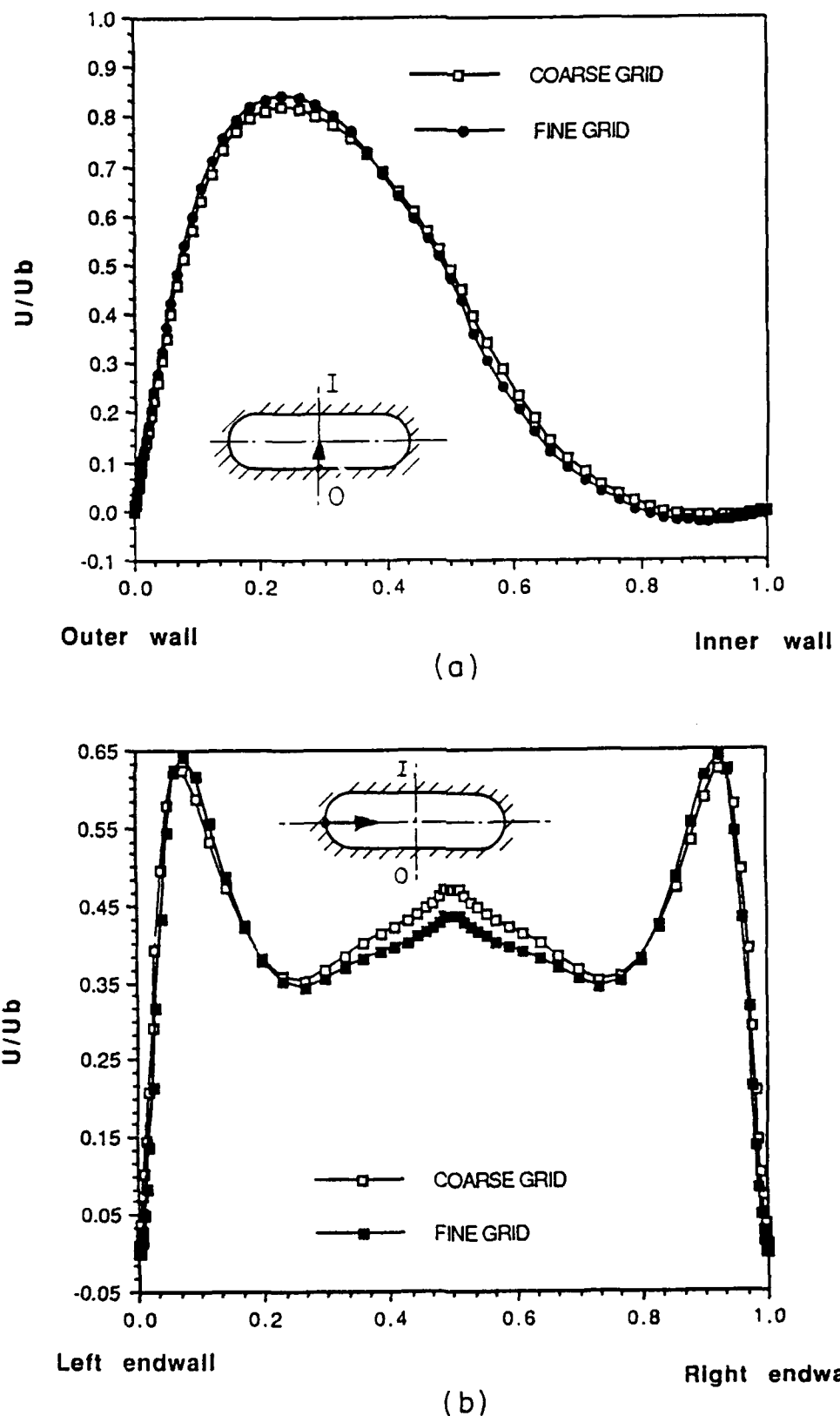
Fig. 44   Grid-dependence study (Re=1000): Streamwise velocity profiles at station XV
(a) vertical plane of symmetry; (b) horizontal plane of symmetry
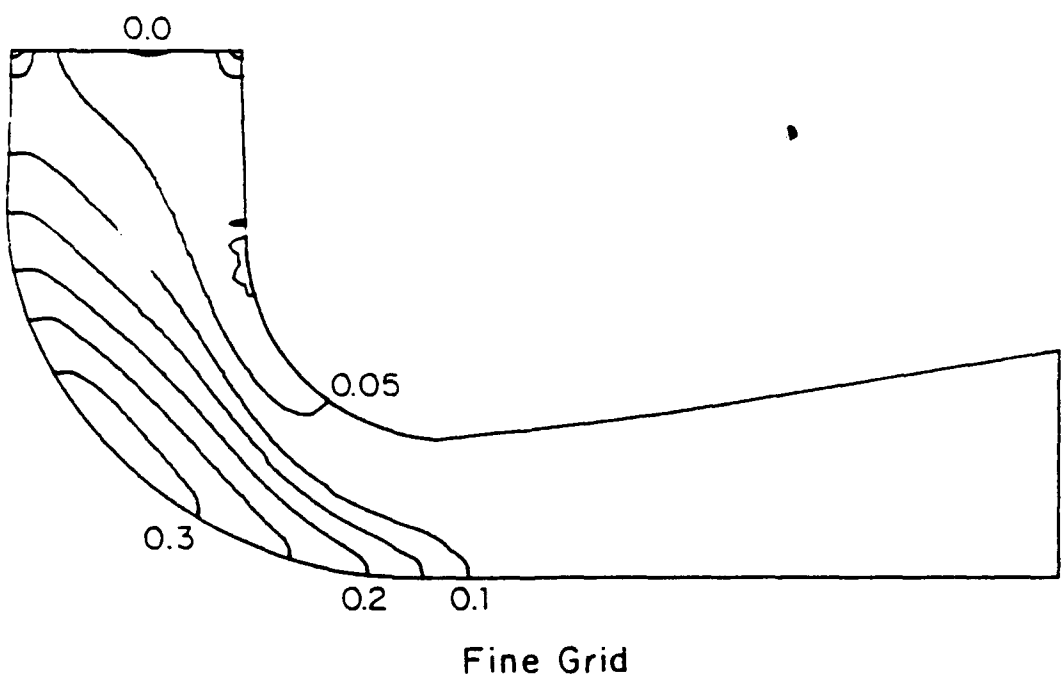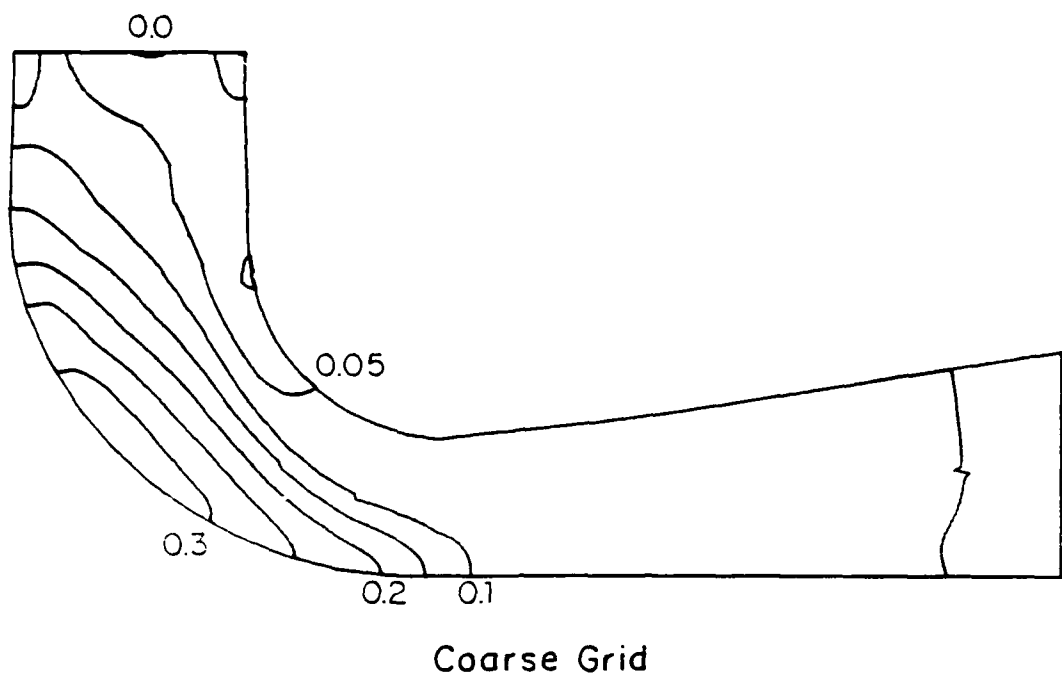
Fig. 45   Grid-dependence study (Re=1000): Static pressure contours on the plane of symmetry
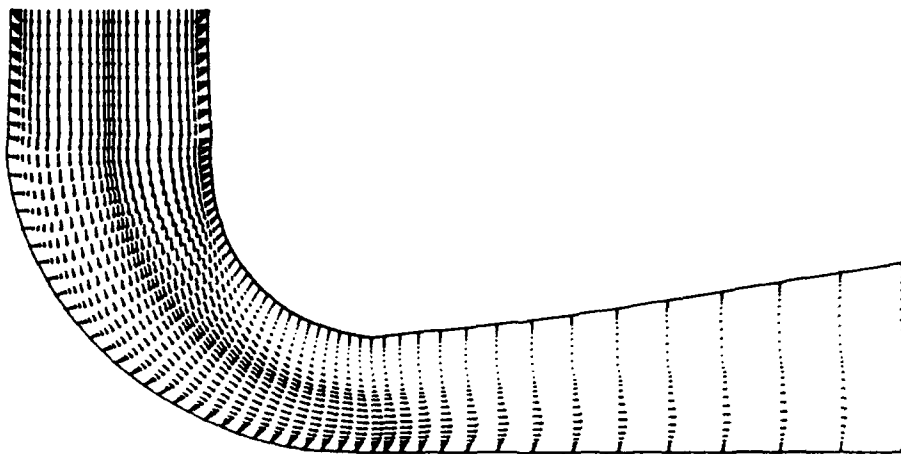
(a)
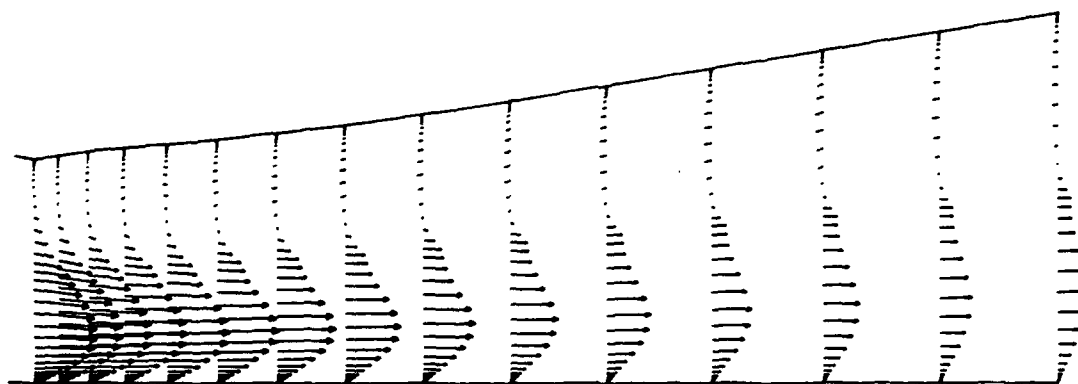
(b)

Fig. 46 Velocity field on the plane of symmetry (Re=1000)
(a) Overall view; (b) Exit region

173
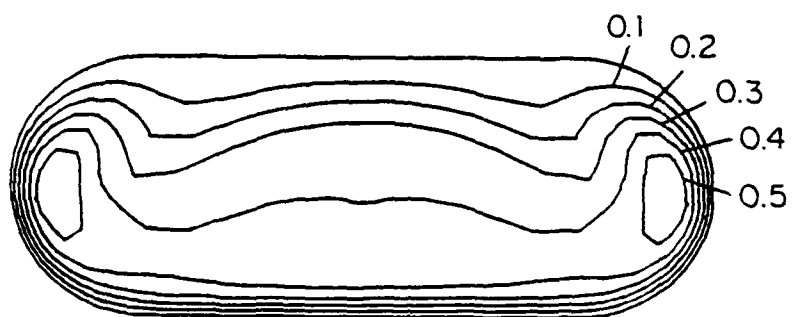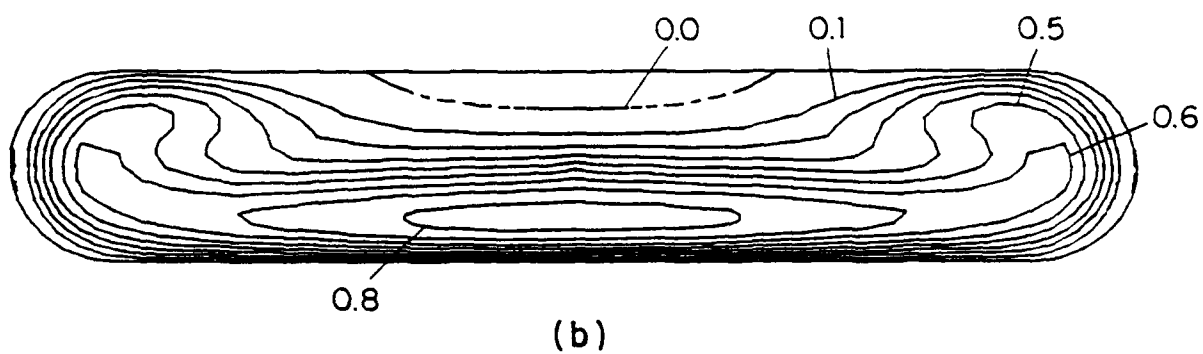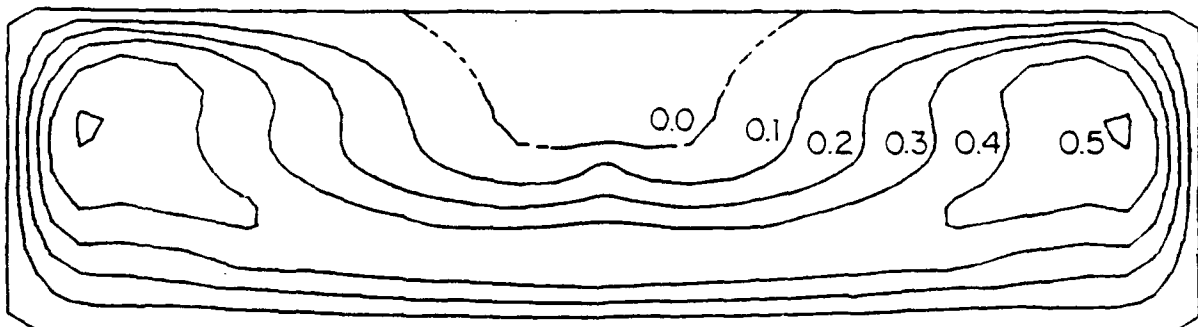
Fig. 47   Streamwise velocity contours (Re=1000)
(a) Station IX; (b) Station XV; (c) Station XXXI
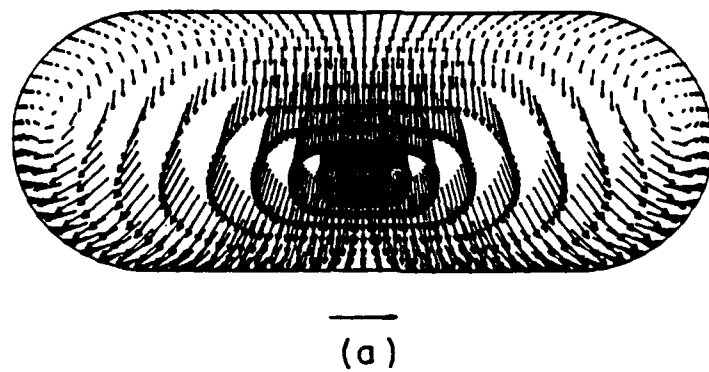
(a)
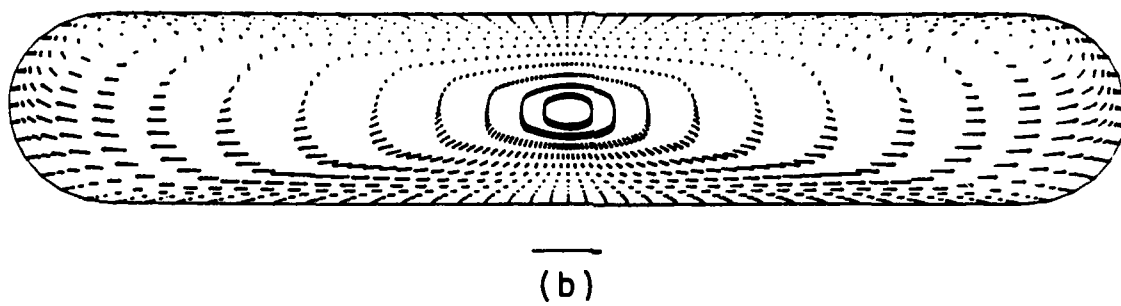
(b)
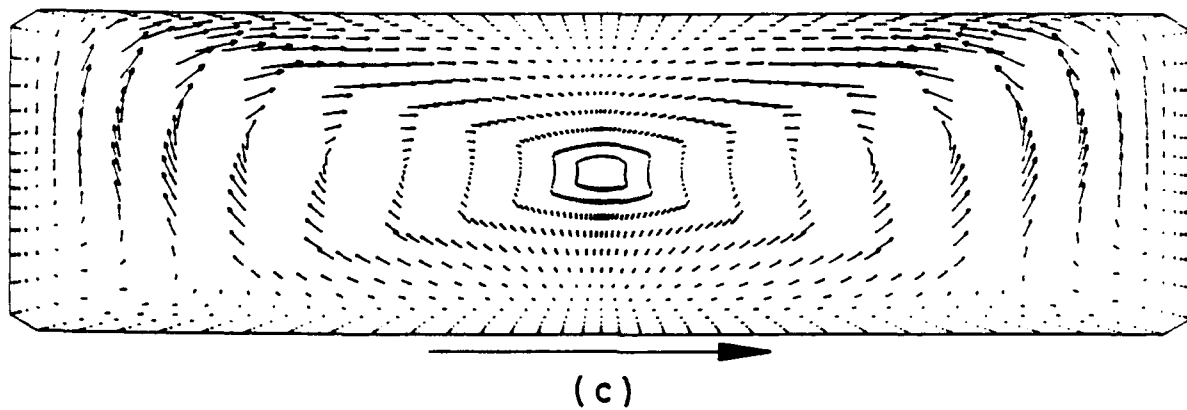
(c)

Fig. 48   Secondary flow vectors (Re=1000)
(a) Station IX; (b) Station XV; (c) Station XXXI
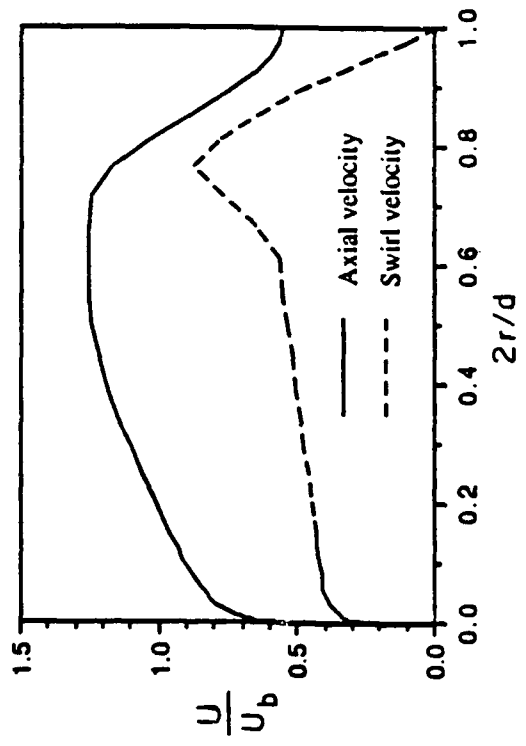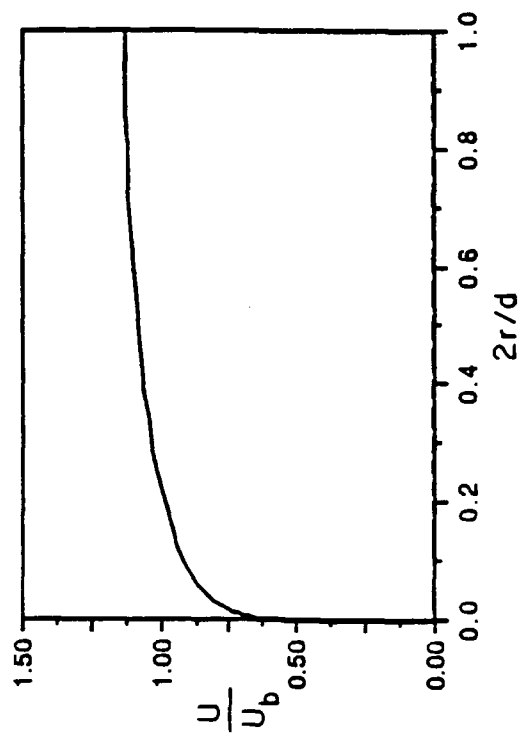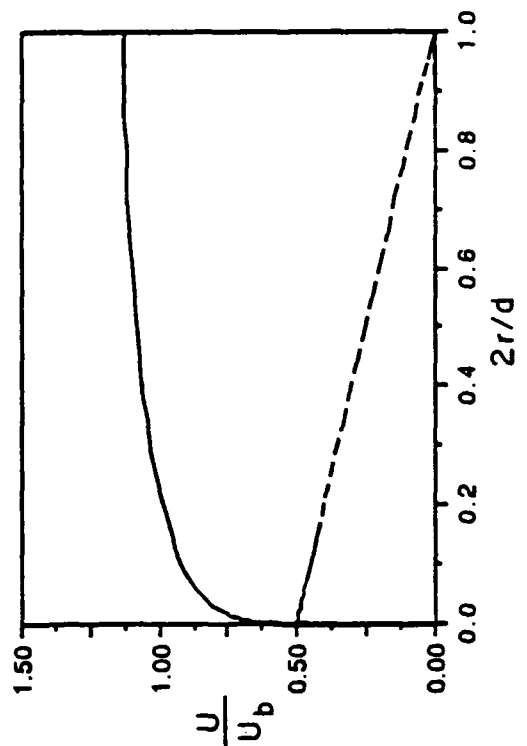
Fig. 49 Axial and swirl mean velocity profiles at the inlet of the draft tube
(a) Case FV; (b) Case S1; (c) Case S2; (d) Case S3

176
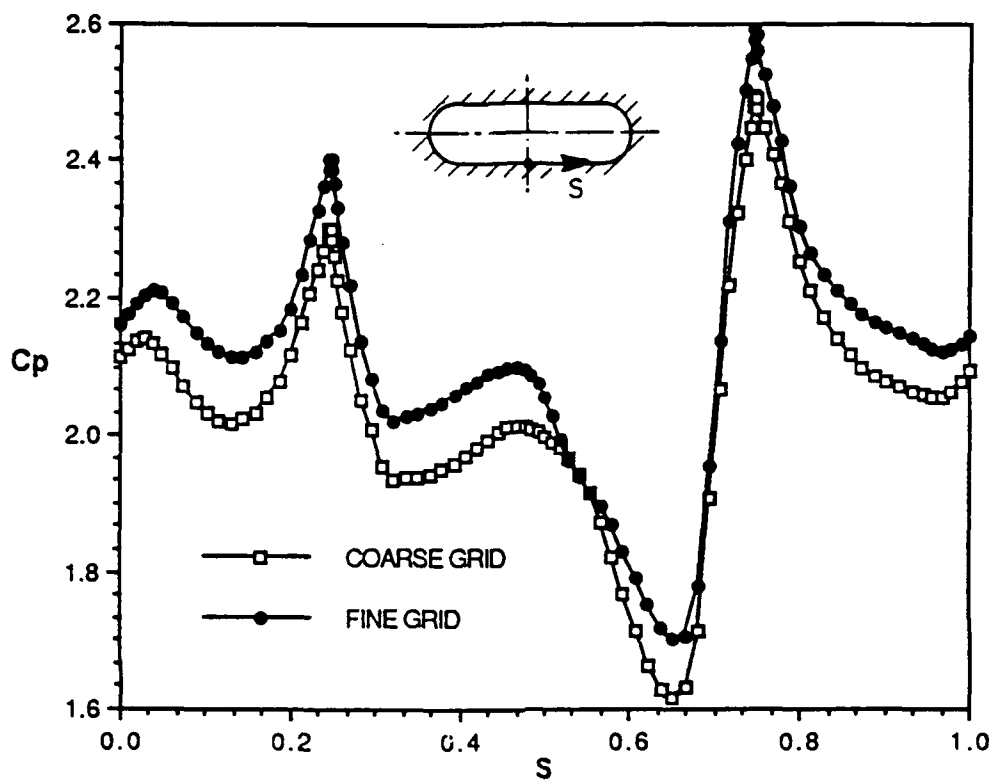
Fig. 50   Grid-dependence studies (Re=1.1x10^{6}; Case FV):
         Peripheral wall static pressure distribution at station XV
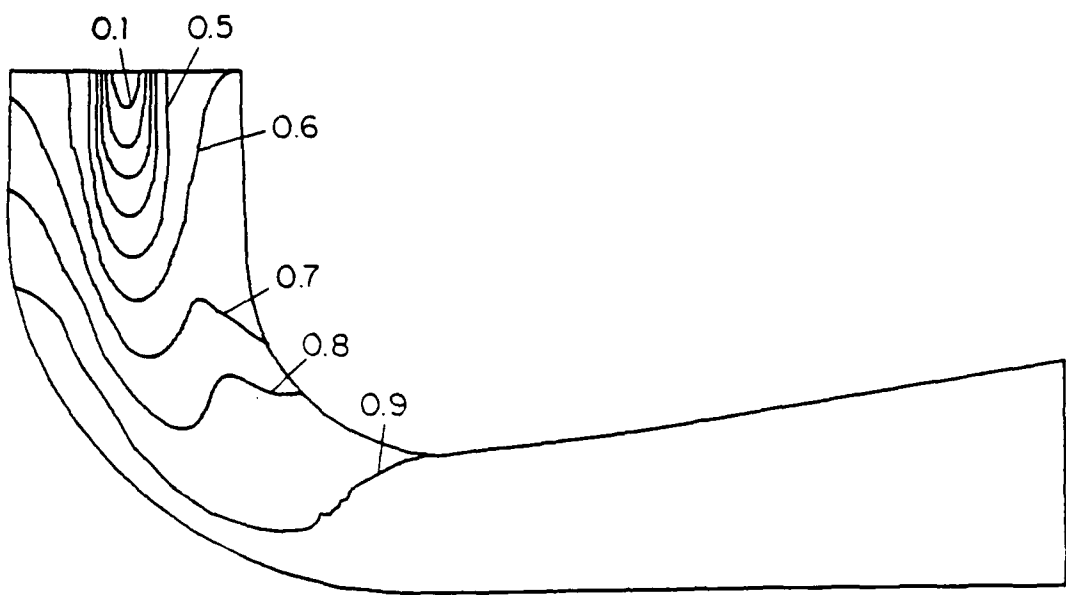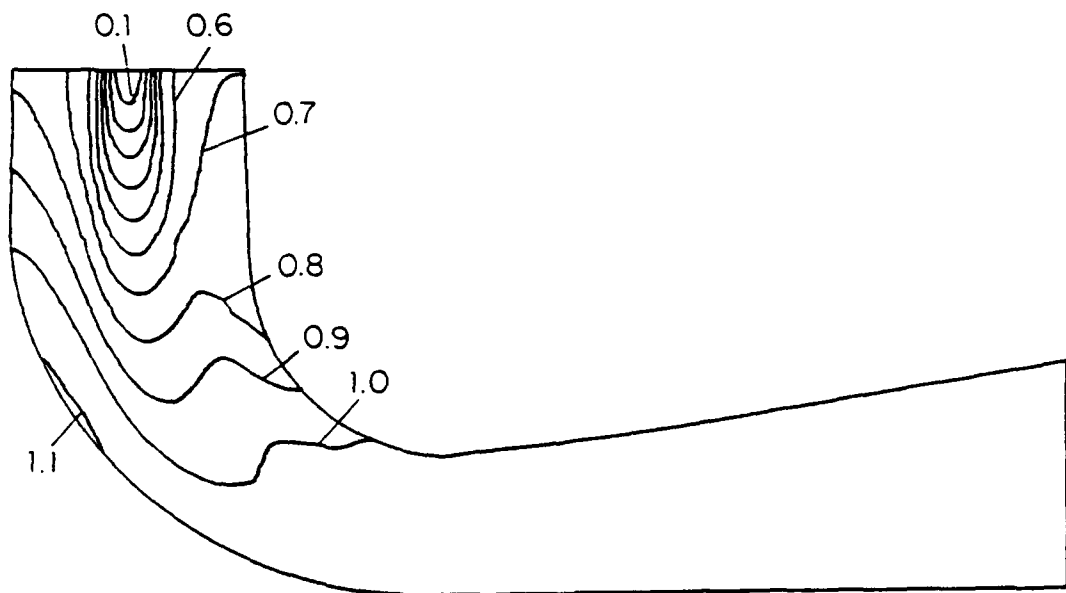
Fig. 51   Grid-dependence study (Re=1.1x10⁶; Case FV): Static pressure contours on the symmetry plane

178
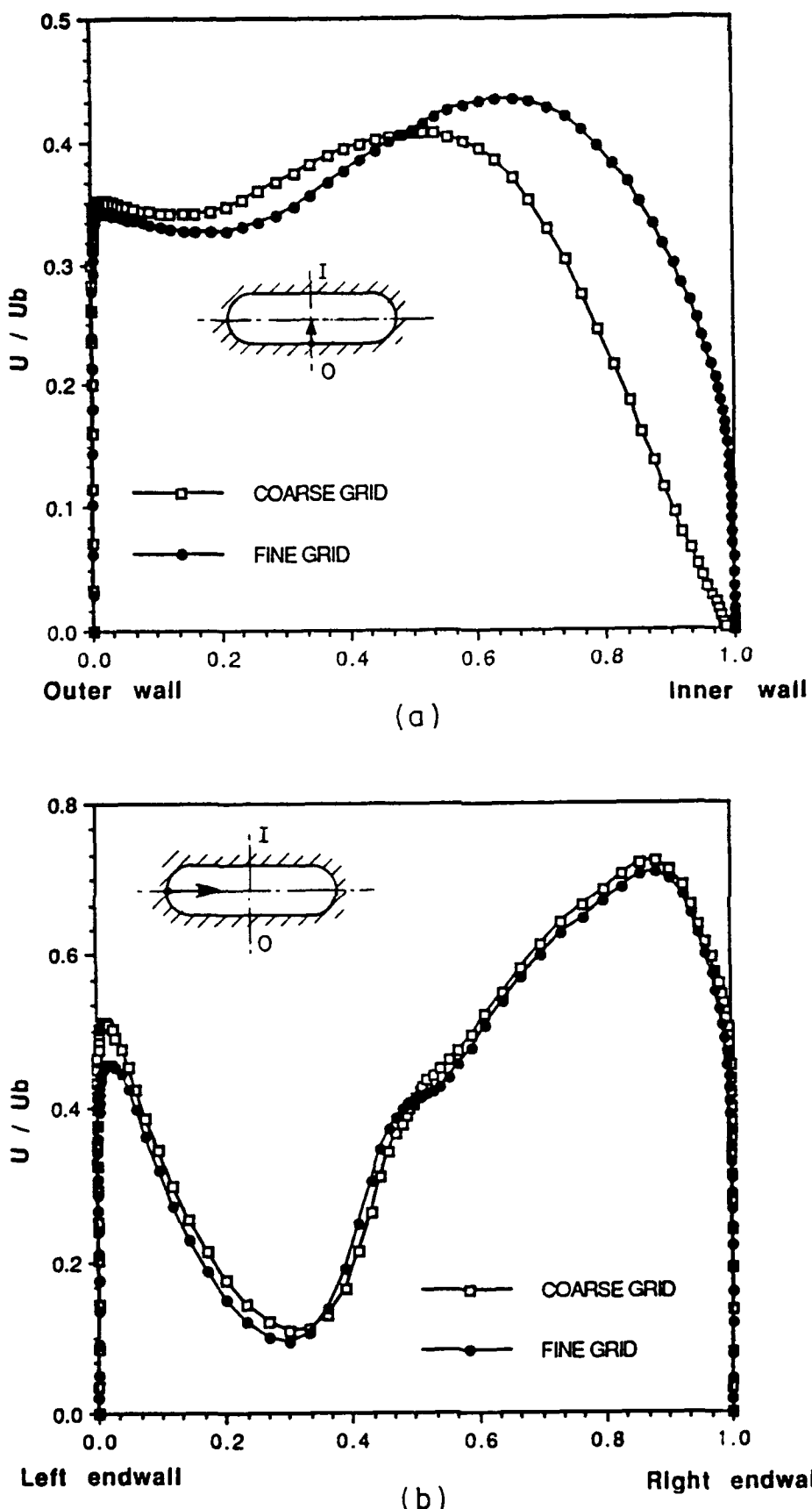
Fig. 52 Grid-dependence study (Re=1.1x10⁶; Case FV): Streamwise velocity profiles at station XV. (a) Vertical plane of symmetry; (b) Horizontal plane of symmetry

179

(a)
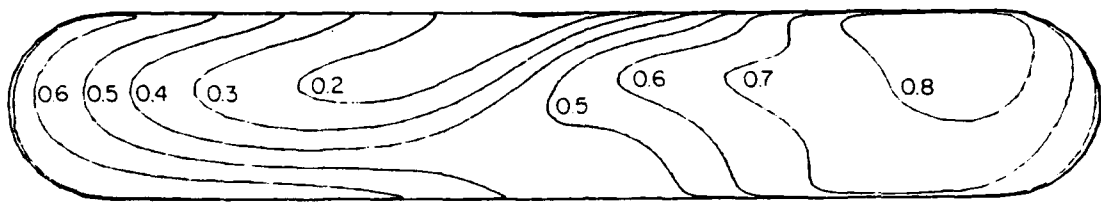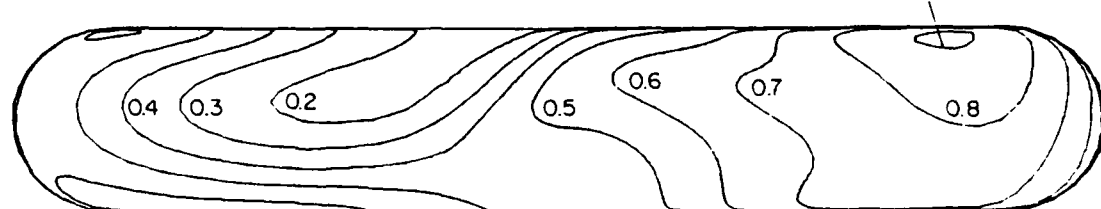
Coarse Grid

Fine Grid

Fig. 53   Grid-dependence study (Re=1.1x10⁶; Case FV): Streamwise velocity contours
(a) Station XV

(b)
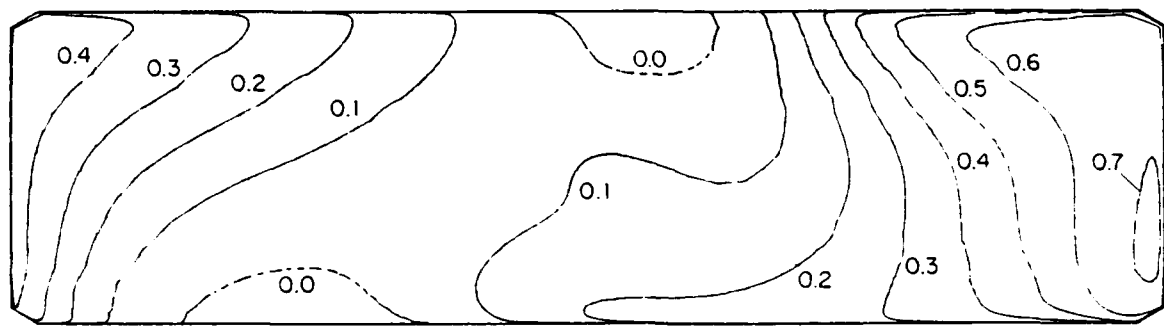
Coarse Grid
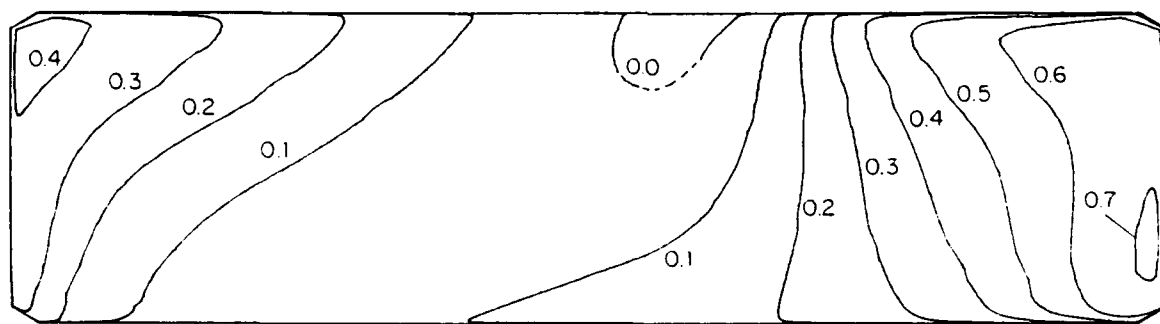
Fine Grid

Fig. 53   Grid-dependence study (Re=1.1x10^6; Case FV): Streamwise velocity contours
(b) Station XXXI

181

(a)

Coarse Grid
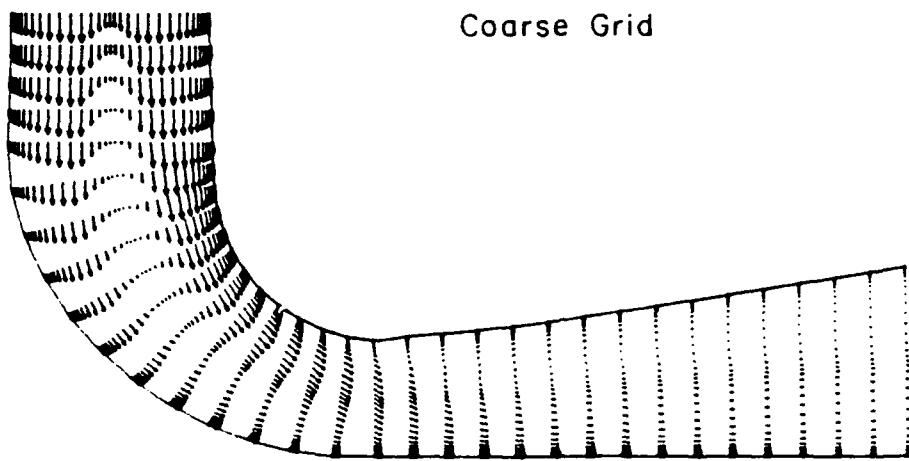
Fine Grid
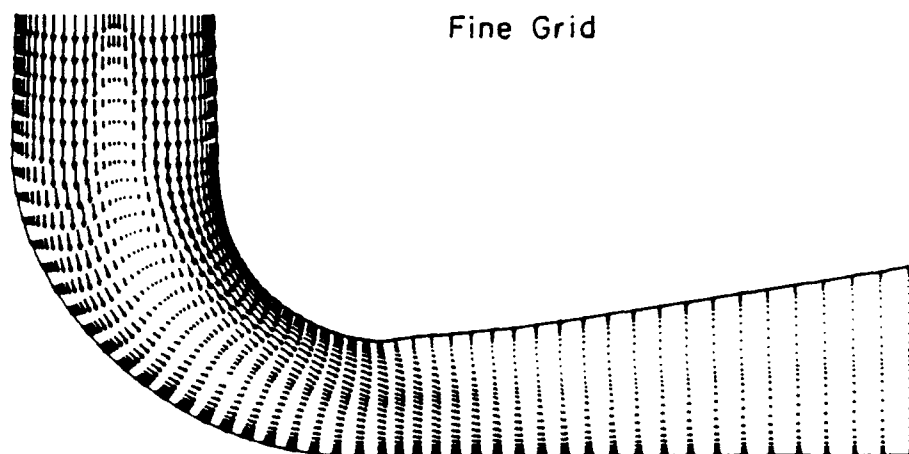
Fig. 54 Grid-dependence study (Re=1.1x10⁶; Case FV): (a) Velocity field on the plane of symmetry (overall view)

(b)

Coarse Grid

Fine Grid
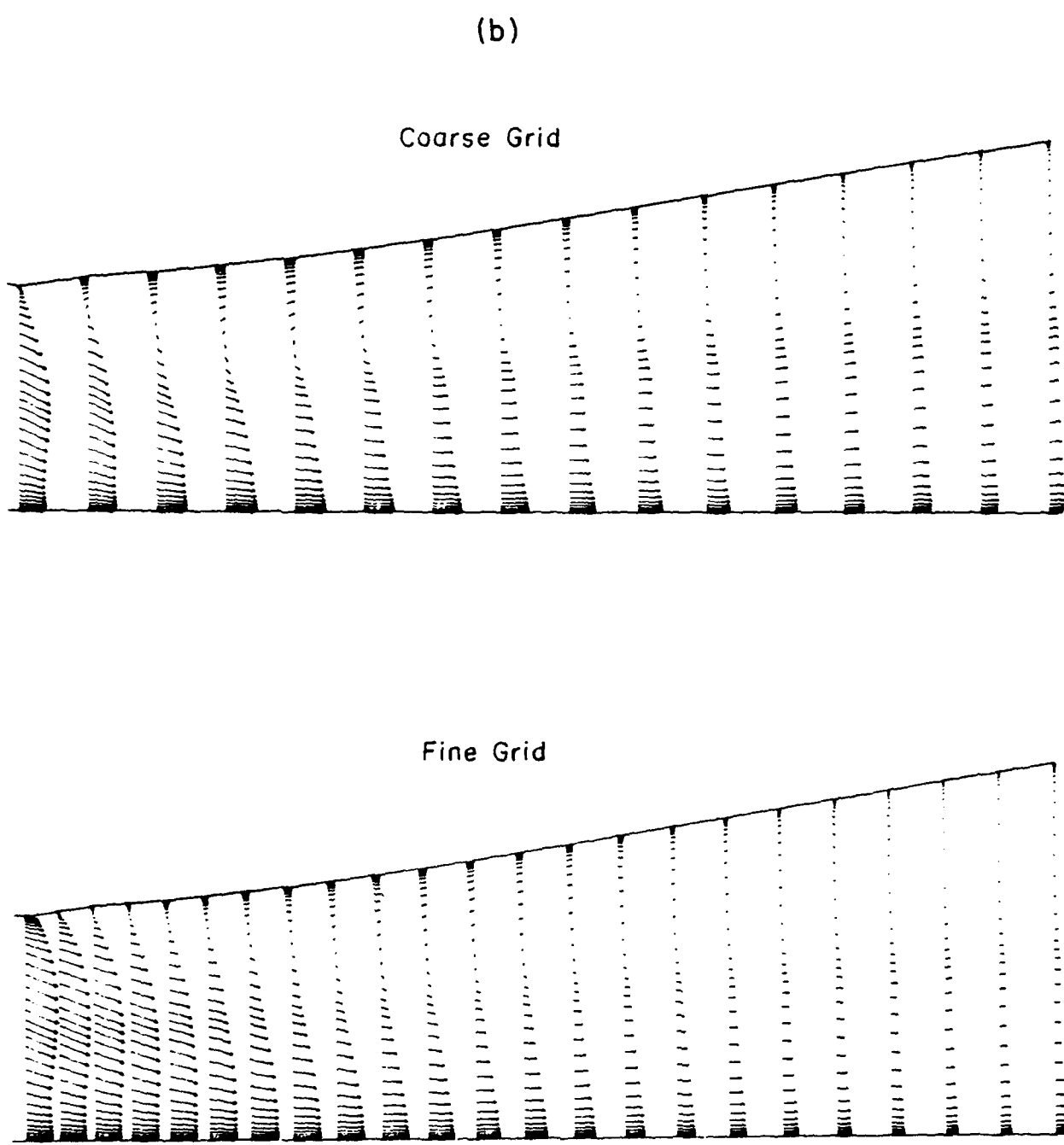
Fig. 54   Grid-dependence study (Re=1.1x10⁶; Case FV): (b) Velocity field on the plane of symmetry (exit region)
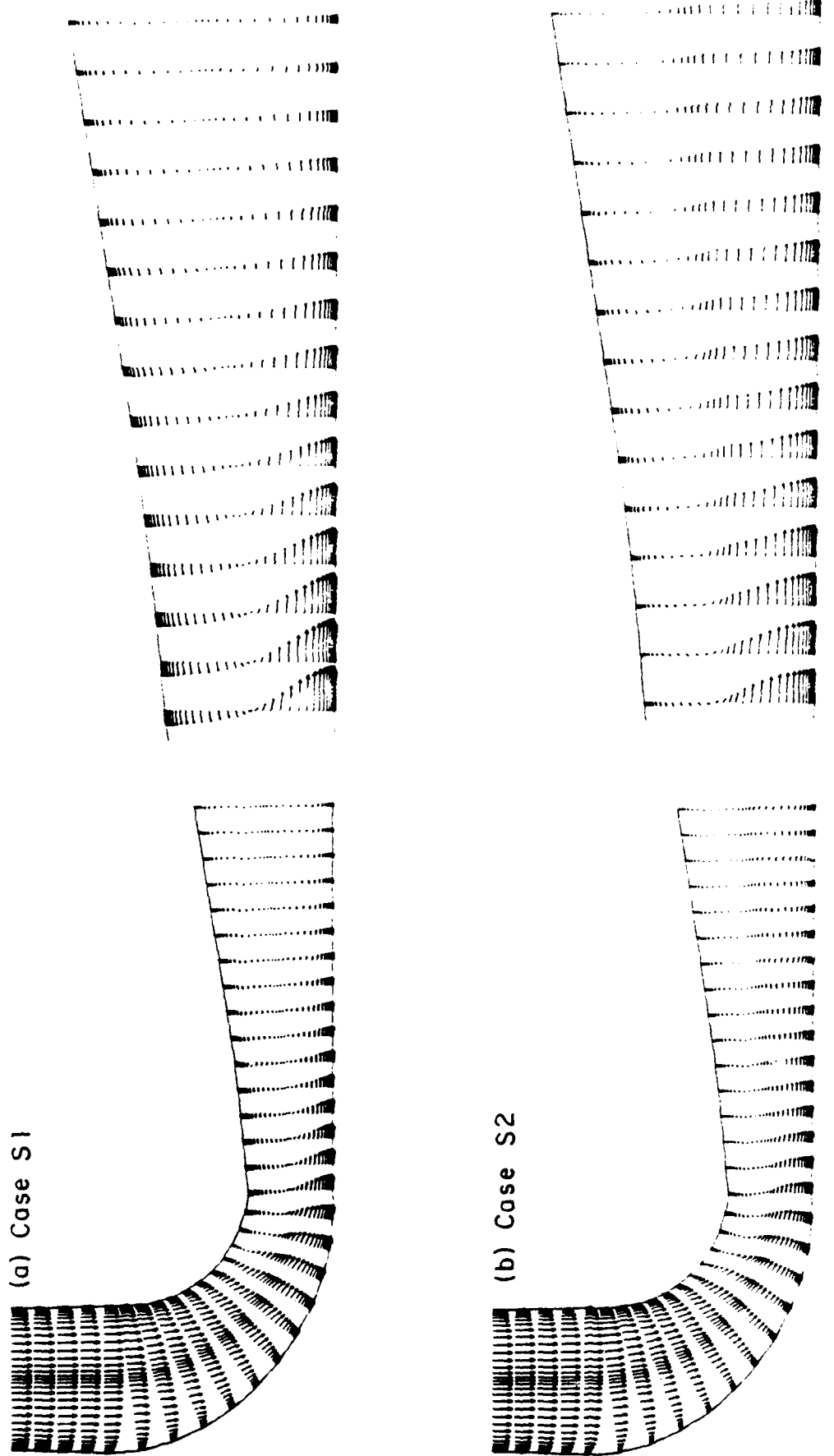
183

(a) Case S1

(b) Case S2

Fig. 55 Velocity field on the plane of symmetry for various inflow conditions
(a) Case S1; (b) Case S2

184

(c) Case S3

(d) Case FV

Fig. 55 Velocity field on the plane of symmetry for various inflow conditions
(c) Case S3; (d) Case FV

185

Fig. 56   Static pressure contours on the plane of symmetry for various inflow conditions
         (a) Case S1; (b) Case S2

186

(c) Case S3

(d) Case FV

Fig. 56   Static pressure contours on the plane of symmetry for various inflow conditions
(c) Case S3; (d) Case FV

187

Fig. 57 Streamwise velocity contours and secondary flow vectors at section IX for various inflow conditions: (a) case S1; (b) case S2

0.5 0.4   0.5 0.6 0.7 0.8 0.9

(c) Case S3

0.2

0.9

0.8

0.2

0.6

(d) Case FV

Fig. 57   Streamwise velocity contours and secondary flow vectors at section IX for various inflow conditions: (c) case S3; (d) case FV

189

Fig. 58 Streamwise velocity contours and secondary flow vectors at section XV for various inflow conditions: (a) case S1; (b) case S2

(a) Case S1

(b) Case S2

190

(c) Case S3

(d) Case FV
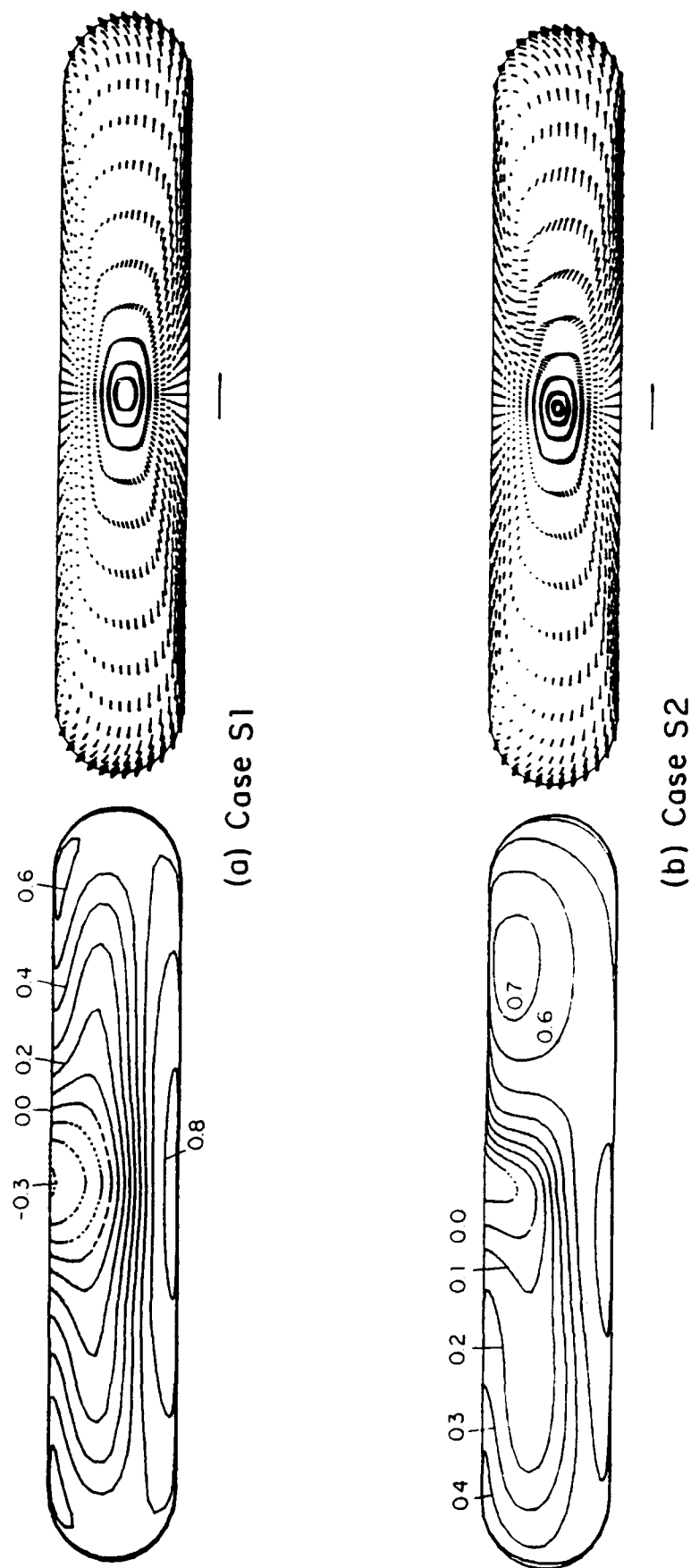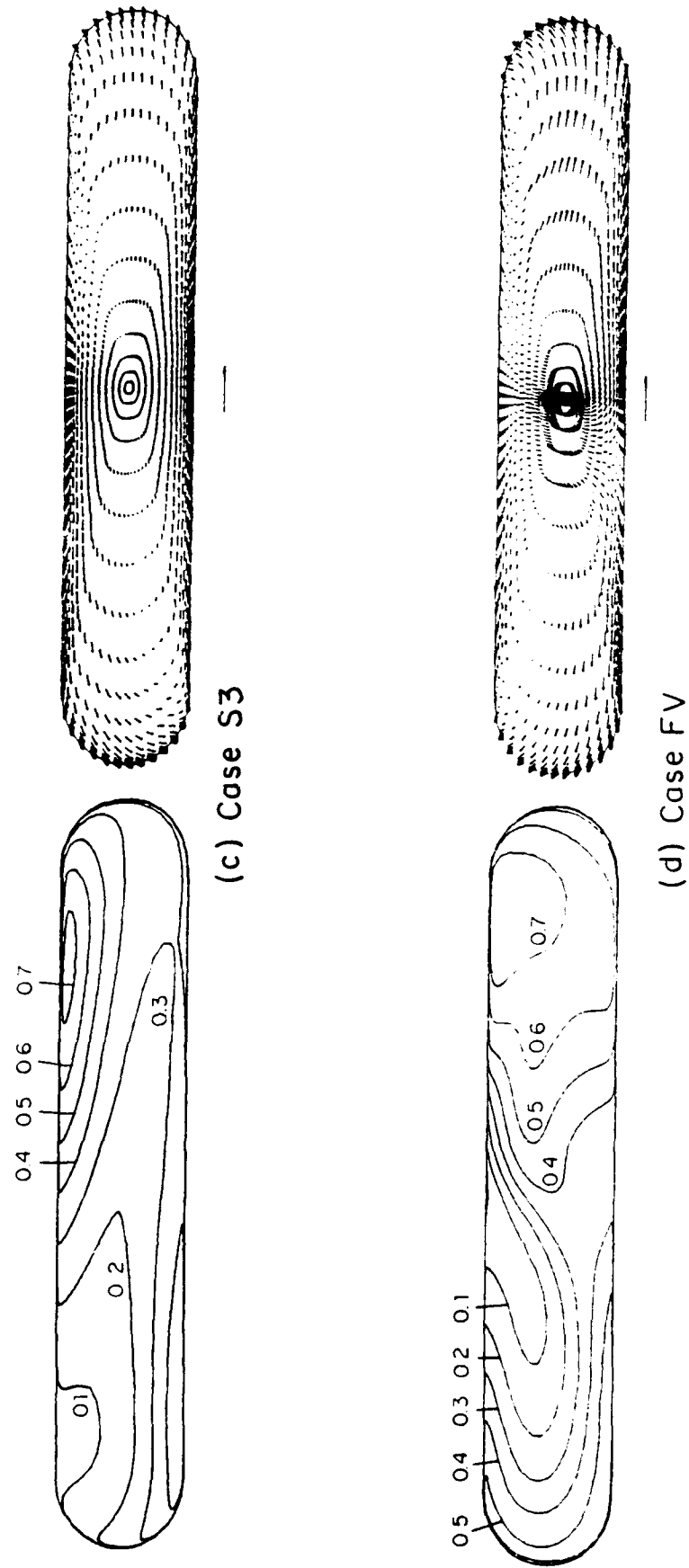
Fig. 58 *Streamwise velocity contours and secondary flow vectors at section XV for various inflow conditions: (c) case S3; (d) case FV*
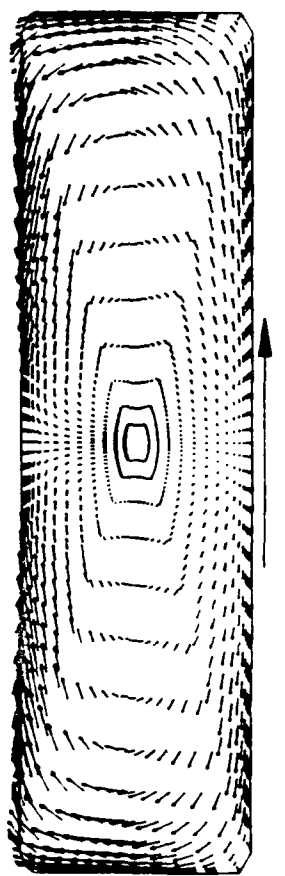
(a) Case S1
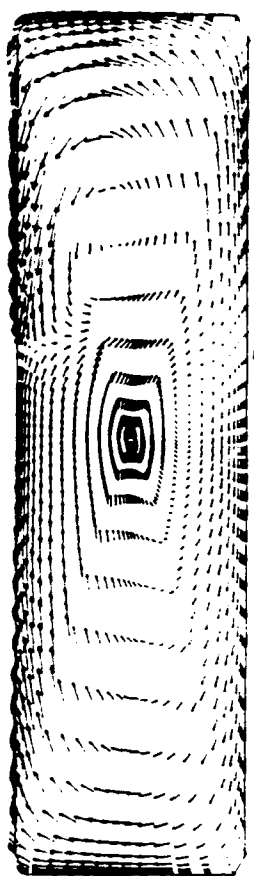
(b) Case S2
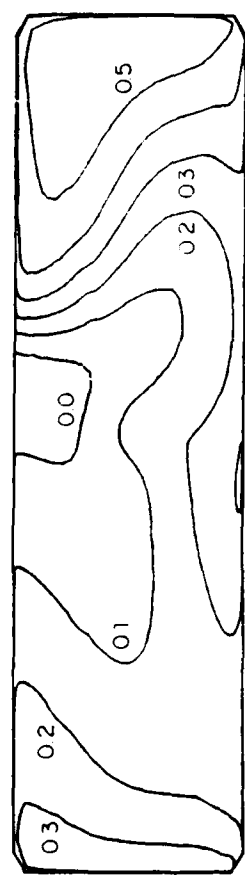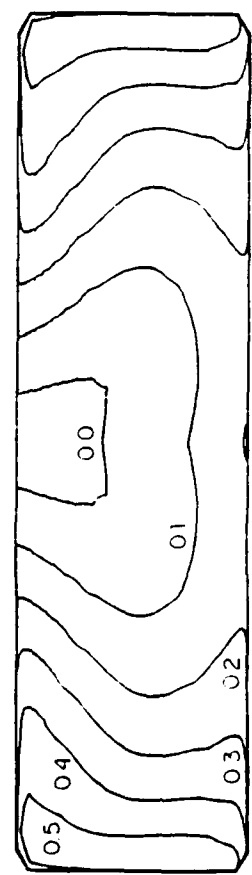
Fig. 59 Streamwise velocity contours and secondary flow vectors at section XXXI for various inflow conditions: (a) case S1; (b) case S2
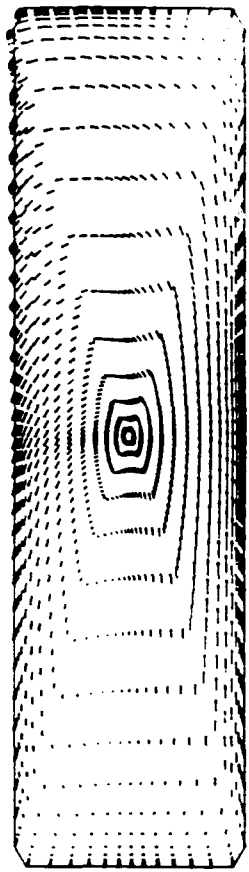
(c) Case S3
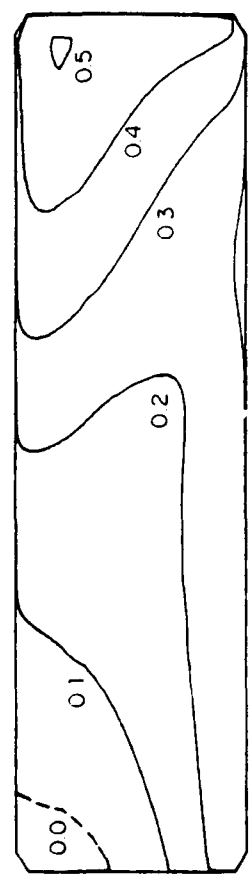
(d) Case FV
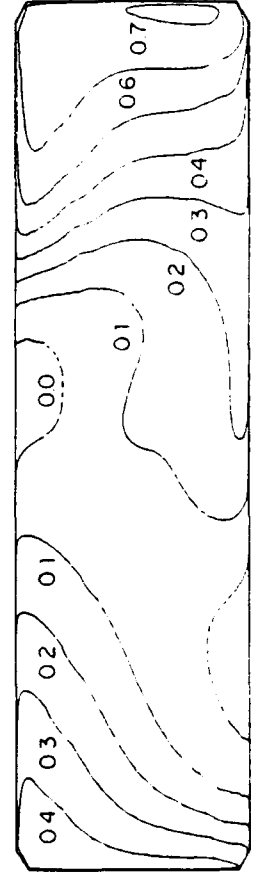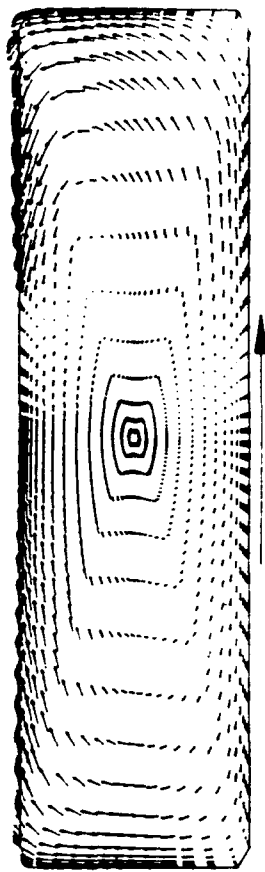
Fig. 59 Streamwise velocity contours and secondary flow vectors at section XXXI for various inflow conditions: (c) case S3; (d) case FV
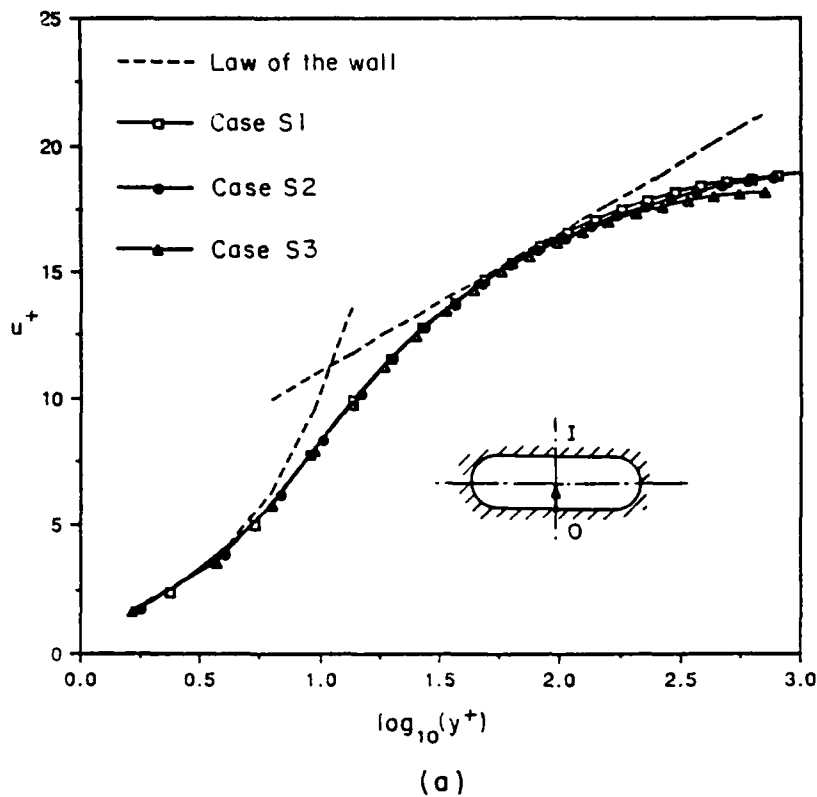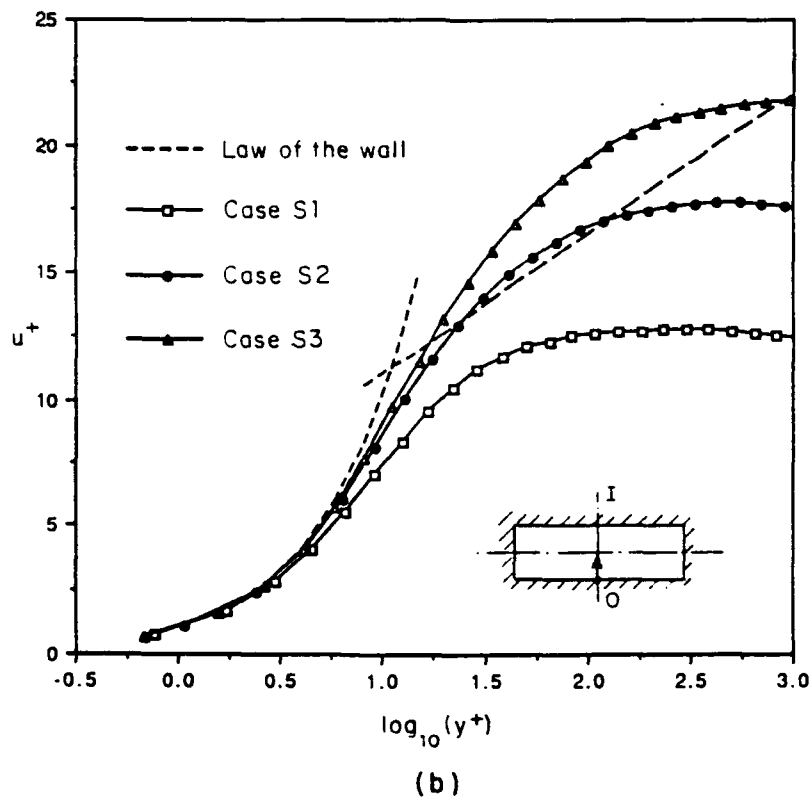
Fig. 60   Law-of-the-wall velocity profiles for various inflow conditions
(a) Section XV; (b) Section XXXI

194

U.S. DISTRIBUTION LIST

Commander
David W. Taylor Naval Ship
 R & D Center (ATTN: Code 1505)
Bldg. 19, Room 129B
Bethesda, Maryland 20084

Commander
Naval Sea Systems Command
Washington, D.C. 20362
ATTN: 05R22

Commander
Naval Sea Systems Command
Washington, D.C. 20362
ATTN:55W (R. Keane, Jr.)

Commander
Naval Sea Systems Command
Washington, D.C. 20362
ATTN: 55W3 (W. Sandberg)

Commander
Naval Sea Systems Command
Washington, D.C. 20362
ATTN: 50151 (C. Kennell)

Commander
Naval Sea Systems Command
Washington, D.C. 20362
ATTN: 56X12 (C.R. Crockett)

Commander
Naval Sea Systems Command
Washington, D.C. 20362
ATTN: 63R31 (T. Pierce)

Commander
Naval Sea Systems Command
Washington, D.C. 20362
ATTN: 55X42 (A. Paladino)

Commander
Naval Sea Systems Command
Washington, D.C. 20362
ATTN: 99612 (Library)

Director
Defense Documentation Center
5010 Duke Street
Alexandria VA 22314

Library of Congress
Science & Technology Division
Washington, D.C. 20540

Naval Underwater Weapons Research
 & Engineering Station (Library)
Newport, RI 02840

Office of Naval Research
800 N. Quincy Street
Arlington, VA 22217
ATTN: Dr. C.M. Lee, Code 432

Commanding Officer (L31)
Naval Civil Engineering Laboratory
Port Hueneme, CA 93043

Commander
Naval Ocean Systems Center
San Diego, CA 92152
ATTN: Library

Library
Naval Underwater Systems Center
Newport, RI 02840

Charleston Naval Shipyard
Technical Library
Naval Base
Charleston, SC 29408

Norfolk Naval Shipyard
Technical Library
Portmoth, VA 23709

Puget Sound Naval Shipyard
Engineering Library
Bremerton, WA 98314

Long Beach Naval Shipyard
Technical Library (246L)
Long Beach, CA 90801

Mare Island Naval Shipyard
Shipyard Technical Library (202.3)
Vallejo, CA 94592

Assistant Chief Design Engineer
 for Naval Architecture (Code 250)
Mare Island Naval Shipyard
Vallejo, CA 94592

U.S. Naval Academy
Annapolis, MD 21402
ATTN: Technical Library

Naval Postgraduate School
Monterey, CA 93940
ATTN: Library (2124)

Study Center
National Maritime Research Center
U.S. Merchant Marine Academy
Kings Point, LI, New York 11024

The Pennsylvania State University
Applied Research Laboratory (Library)
P.O. Box 30
State College, PA 16801

Dr. B. Parkin, Director
Garfield Thomas Water Tunnel
Applied Research Laboratory
P.O. Box 30
State College, PA 16801

Bolt, Beranek & Newman (Library)
50 Moulton Street
Cambridge, MA 02138

Cambridge Acoustical Associates, Inc.
54 Rindge Ave Extension
Cambridge, MA 02140

R & D Manager
Electric Boat Division
General Dynamics Corporation
Groton, Conn 06340

Gibbs & Cox, Inc. (Tech. Info. Control)
21 West Street
New York, NY 10006

Tracor Hydronautics, Inc. (Library)
Pindell School Rd.
Laurel, MD 20810

Newport New Shipbuilding and
    Dry Dock Co. (Tech. Library)
4101 Washington Ave.
Newport News, VA 23607

Society of Naval Architects and
Marine Engineers (Tech. Library)
One World Trade Center, Suite 1369
New York, NY 10048

Sperry Systems Management Division
Sperry Rand Corporation (Library)
Great Neck, NY 10020

Stanford Research Institute
Menlo Park, CA 94025
ATTN: Library

Southwest Research Institute
P.O. Drawer 28510
San Antonio, TX 78284
ATTN: Dr. H. Abramson

Mr. Robert Taggart
9411 Lee Highway, Suite P
Fairfax, VA 22031

Ocean Engr. Department
Woods Hole Oceanographic Inc.
Woods Hole, Mass 02543

Worcester Polytechnic Inst.
Alden Research Lab (Tech Library)
Worcester, MA 01609

Applied Physics Laboratory
University of Washington (Tech. Library)
1013 N. E. 40th Street
Seattle, WA 98105

University of California
Naval Architecture Department
Berkeley, CA 94720
ATTN: Profs. Webster, Paulling,
Wehausen & Library

California Institute of Technology
Pasadena, CA 91109
ATTN: Library

Engineering Research Center
    Reading Room
Colorado State University
Foothills Campus
Fort Collins, CO 80521

Florida Atlantic University
Ocean Engineering Department
Boca Raton, Florida 33432
ATTN: Technical Library

Gordon McKay Library
Harvard University
Pierce Hall
Cambridge, MA 02138

Department of Ocean Engineering
University of Hawaii (Library)
2565 The Mall
Honolulu, Hawaii 96822

Institute of Hydraulic Research
The University of Iowa
Iowa City, Iowa 52242
ATTN: Library, Landweber, Patel

Prof. O. Phillips
Mechanics Department
The John Hopkins University
Baltimore, MD 21218

Kansas State University
Engineering Experiment Station
Seaton Hall
Manhattan, Kansas 66502
ATTN: Prof. D. Nesmith

University of Kansas
Chm Civil Engr Department Library
Lawrence, Kansas 60644

Fritz Engr. Laboratory Library
Department of Civil Engr
Lehigh University
Bethelehem, Pa 18015

Department of Ocean Engineering
Massachusetts Institute of Technology
Cambridge, MA 02139
ATTN: Profs. Leehey & Kerwin

Engineering Technical Reports
Room 10-500
Massachusetts Institute of Technology
Cambridge, MA 02139

St. Anthony Falls Hydraulic Laboratory
University of Minnesota
Mississippi River at 3rd Av., SE
Minneapolis, MN 55414
ATTN: Dr. Arndt & Library

Department of Naval Architecture
   and Marine Engineering-North Campus
University of Michigan
Ann Arbor, Michigan 48109
ATTN: Library

Davidson Laboratory
Stevens Institute of Technology
711 Hudson Street
Hoboken, NJ 07030
ATTN: Library

Applied Research Laboratory
University of Texas
P.O. Box 8029
Austin, TX 78712

Stanford University
Stanford, CA 94305
ATTN: Engineering Library, Dr. Street

Webb Institute of Naval Architecture
Crescent Beach Road
Glen Cove, LI, NY 11542
ATTN: Library

National Science Foundation
Engineering Divison Library
1800 G Street NW
Washington, DC 20550

Mr. John L. Hess
4338 Vista Street
Long Beach, CA 90803

Dr. Tuncer Cebeci
Mechanical Engineering Dept.
California State University
Long Beach, CA 90840

Science Applications, Inc.
134 Holiday Court, Suite 318
Annapolis, MD 21401